POWER ELECTRONIC COMPONENTS AND HARDWARE FOR AN EXPERIMENTAL FLYWHEEL ENERGY STORAGE SYSTEM

A Thesis

Presented in Partial Fullfillment of the Requirements for the

Degree of Master of Science

with a

Major in Electrical Engineering

in the

College of Graduate Studies

University of Idaho

by

Kevin R. Ramus

May 2014

Major Professor: Joseph D. Law, Ph.D.

Authorization to Submit Thesis

This thesis of Kevin Ramus, submitted for the degree of Master of Science with a Major in Electrical Engineering and titled "Power Electronic Components and Hardware for an Experimental Flywheel Energy Storage System," has been reviewed in final form. Permission, as indicated by the signatures and dates below, is now granted to submit final copies to the College of Graduate Studies for approval.

Major Professor: ______________________ Date: __________
Joseph D. Law, Ph.D.

Committee
Members: ______________________ Date: __________
Michael J. Santora, Ph.D.

______________________ Date: __________
Christine A. Berven, Ph.D.

Department
Administrator: ______________________ Date: __________
Fred Barlow, Ph.D.

Discipline's
College Dean: ______________________ Date: __________
Larry Stauffer, Ph.D.

Final Approval and Acceptance

Dean of the College
of Graduate Studies: ______________________ Date: __________
Jie Chen, Ph.D.

Abstract

The University of Idaho Flywheel Energy Storage System (UIFESS) requires sensors and power electronics for successful operation. The UIFESS contains a Field Regulated Reluctance Machine (FRRM) to rotate the flywheel and an integrated active magnetic bearing to provide air gap control for the flywheel. The power electronics enable air gap control and rotation of the flywheel. Major hardware components required for control include eddy-current displacement sensors, current sensors, microcontrollers, and power amplifiers. Each element of the power electronics is selected and interfaced with one another. Analysis of the power electronic elements is presented. Sensor signal conditioning topologies are designed and implemented. Multiple printed circuit boards are designed using mixed-signal design principles and populated to aid in interfacing the hardware. Determination of the maximum rotational flywheel speed is discussed. An investigation on the hardware requirements to achieve a rotational speed of 500,000 rotations per minute is conducted.

Acknowledgements

I would like to thank Dr. Joseph Law for giving me the opportunity to attend graduate school and work on such an exciting project.

I would also like to extend my appreciation:

To Dr. Michael Santora for his guidance and willingness for discussion;

To Dr. Christine Berven for her guidance and feedback;

To Brent Kisling and Bridget Wimer for their feedback and friendship;

To Daniel Schneider for his fabrication assistance;

To the University of Idaho flywheel research team for feedback and interdisciplinary discussions;

And to my family for their encouragement to pursue an advanced degree.

Table of Contents

List of Figures

List of Tables

Chapter 1

Introduction

1.1 Flywheel Energy Storage Systems

Energy use is prevalent in all aspects of daily life. Many applications require the storage of energy for later use. From the cell phone carried in one's pocket to NASA's Curiosity rover on Mars, the need for efficient energy storage and energy conversion is insatiable.

Popular energy storage devices today include chemical batteries, fuel cells, superconducting magnetic energy storage, capacitors, and compressed air[1]. All forms of energy storage have advantages and disadvantages associated with its application. The major trade-offs of energy storage to consider include the cost, length of life, specific power (energy density), and scalability[2]. A concept receiving renewed interest is the mechanical storage of energy, such as a Flywheel energy storage system.

FESS Background Flywheel energy storage systems (FESS) have existed for thousands of years. The first application of the flywheel was using stone wheels attached to axles, such as potter's wheels[3][4]. The wheel is spun and energy is stored in the rotation of the wheel. Today's FESS operate on a similar principle, but carbon fiber and iron now replace the stone wheel, and electric machines are used to spin the wheel to extremely high speeds. The FESS is essentially an electromechanical battery. The electric machine acts as a motor to spin the flywheel. The electric power is converted into mechanical power and is stored in the rotation of the flywheel mass. The flywheel will simply coast or idle, maintaining the stored energy until it is required. When a load is present, the electric machine acts as a generator. Mechanical energy is removed, slowing the flywheel. The mechanical energy is then converted back into electrical energy for the load to utilize.

The kinetic energy stored in the rotating flywheel is represented by Equation (1.1). The kinetic energy is equal to one half the moment of inertia, I, multiplied by the angular velocity, ω, squared. The moment of inertia is dependent on the mass and physical characteristics of the rotating mass. Any increase in the rotational speed significantly increases the stored energy.

$$KE_{rotational} = \frac{1}{2} I \omega^2 \tag{1.1}$$

FESS Advantages The FESS offers several advantages as a storage device. Hazardous materials are not associated with FESS, as they are with chemical batteries[5]. This makes the construction and utilization of FESS environmentally friendly. Flywheel systems are capable of undergoing hundreds of thousands of charge and discharge cycles during its exceptionally long life[1]. The amount of maintenance is relatively low compared to other types of energy storage devices, such as batteries[3]. Active magnetic bearings (AMB) allow the rotating portion of the FESS to be magnetically suspended without contact, drastically reducing maintenance associated with traditional bearings. The lack of hazardous materials, ability for numerous charge and discharge cycles, and low maintenance due to the use of AMB give the flywheel a life expectancy of over 20 years. The expected flywheel lifetime is far longer than the 3 to 5 year expected lifetime of most batteries. The FESS efficiency can reach over 90%[1][5].

The specific energy of an energy storage system measures the energy stored per energy storage system mass. Flywheel energy storage system technology has a potential for using a relatively small mass to store a large amount of energy. The present specific power of FESSs are competitive with other current developing technologies, making it a viable option for applications today. It is expected that the specific energy capability of FESS will increase significantly in the next 5 to 10 years, as shown in Figure 1.1.

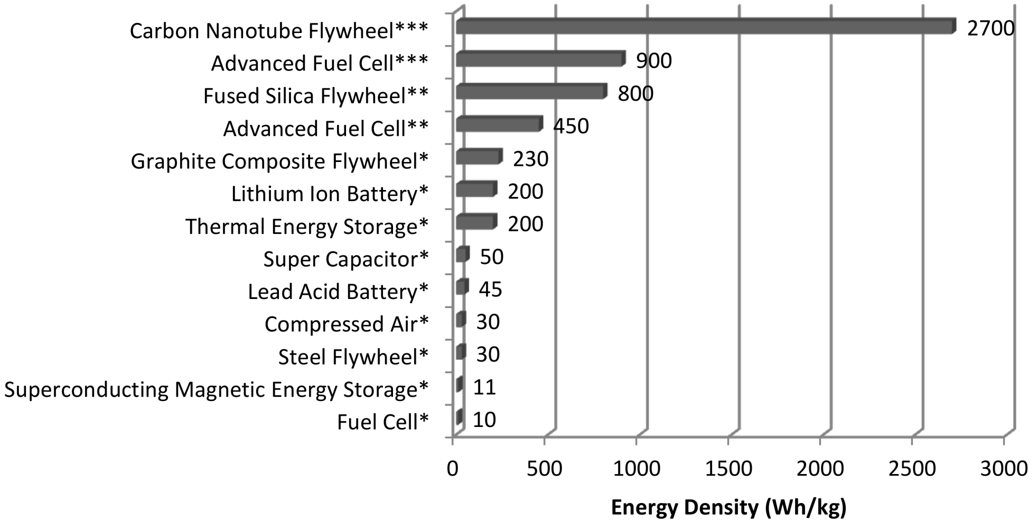

Figure 1.1: Comparison of the Specific Power in Today's and Tomorrow's Energy Storage Technologies * Current, ** Predicted Within 5 years, *** Potential Beyond 5 years [5][6][7]

FESS Applications The FESS advantages make it ideal for use in a variety of applications. Currently, FESS's are most effective in high-power systems, not high-energy systems. For example, FESS are being used to regulate frequency and mitigate power fluctuations[6]. Large scale FESS's are used to store excess power generated by wind or solar, and supply this power to the electric grid at a later time [1].

Commercial FESS are seeing increasing use in uninterruptible power supply (UPS) systems. The advantages of FESS's are best utilized for power disturbances that last less than 5 seconds. Unlike many power back-up systems, such as fuel-fired generators that take substantially longer to turn on, FESS's can respond quickly[3]. Typically, batteries are used to provide power for the time between the initial power failure, and the backup system coming online. These batteries experience many power cycles and must be replaced on a regular basis. Though FESS may have a higher initial cost, the long term benefits of replacing batteries with FESS makes economic sense. Flywheel energy storage systems have a considerably longer life span and is capable of dealing with the power cycling these intermediate power systems would experience.

Various vehicles, such as trains and experimental automobiles, have made use of the technology as well. The FESS's are used to store energy when the train or automobile is slowing down, and then use this stored energy during acceleration of the vehicle[1]. Experimental excavators used in the construction industry have been fitted with FESS to investigate the possibility of considerable fuel savings. This commercially viable product is capable of 60,000 rpm[8].

NASA Glenn has developed several models of FESS[2][9][10]. NASA Glenn is hoping to utilize high specific energy FESS for use on spacecraft. Orbital spacecraft that use solar panels as their primary energy source experience continuous cycling of light and dark, requiring the energy storage device to undergo many charge/discharge cycles. In addition to the obvious benefits, multiple FESS could be combined to also serve as the attitude control system for the spacecraft, helping to point the spacecraft in a particular direction. A system that could serve two purposes would reduce spacecraft weight and launch cost.

1.2 Project Background

The University of Idaho received funding to investigate FESS's through the NASA Steckler Space Grant. The program is intended to promote student involvement and development of technology aiding colonization of the solar system. Development of the UIFESS for Lunar Colonization includes students and faculty from the Electrical and Computer Engineering Department, the Mechanical Engineering Department, and the Physics Department. The University of Idaho's goal is to demonstrate technology that could be used to aid in providing power for a small lunar base. The lunar base would be powered by solar panels during periods of sunlight lasting 14 Earth days. Excess power generated during this time would be stored in the UIFESS. A 14 day period of darkness follows, and the base would rely on energy stored in the UIFESS during this time. This concept is shown in Figure 1.2. Nuclear energy generation is another possible source of power. However, nuclear power generation faces a similar limitation. Power production must be reduced during the light period of time due to a reduced ability to dissipate waste heat. The UIFESS could be used in a similar fashion to store excess power for use when the nuclear power generation must scale back.

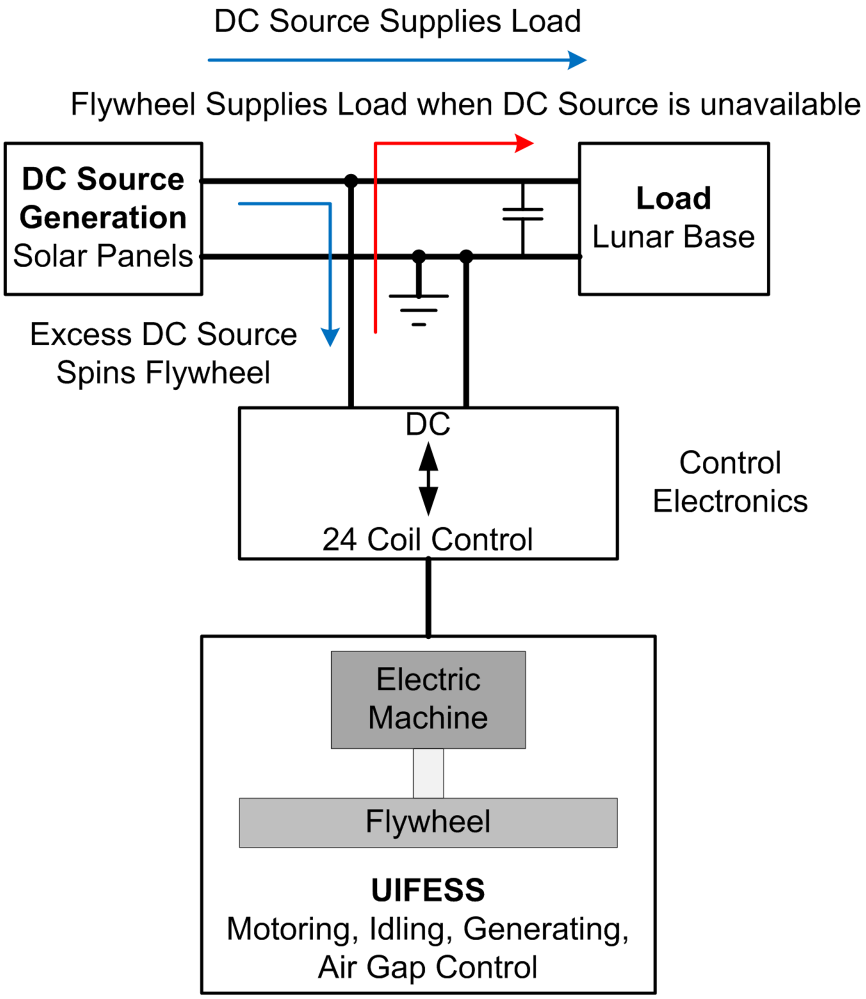

Figure 1.2: Proposed Lunar Base Energy Storage Solution

1.3 UIFESS Design

The UIFESS is intended to be a proof-of-concept, low speed flywheel energy storage system. The system is designed to rotate at 1,800 rpm. Development of the low-speed UIFESS provides researchers a fundamental understanding of FESSs before developing high speed capabilities. The UIFESS is shown in Figure 1.3. The UIFESS contains multiple subsystems resulting from effort of multiple students and departments.

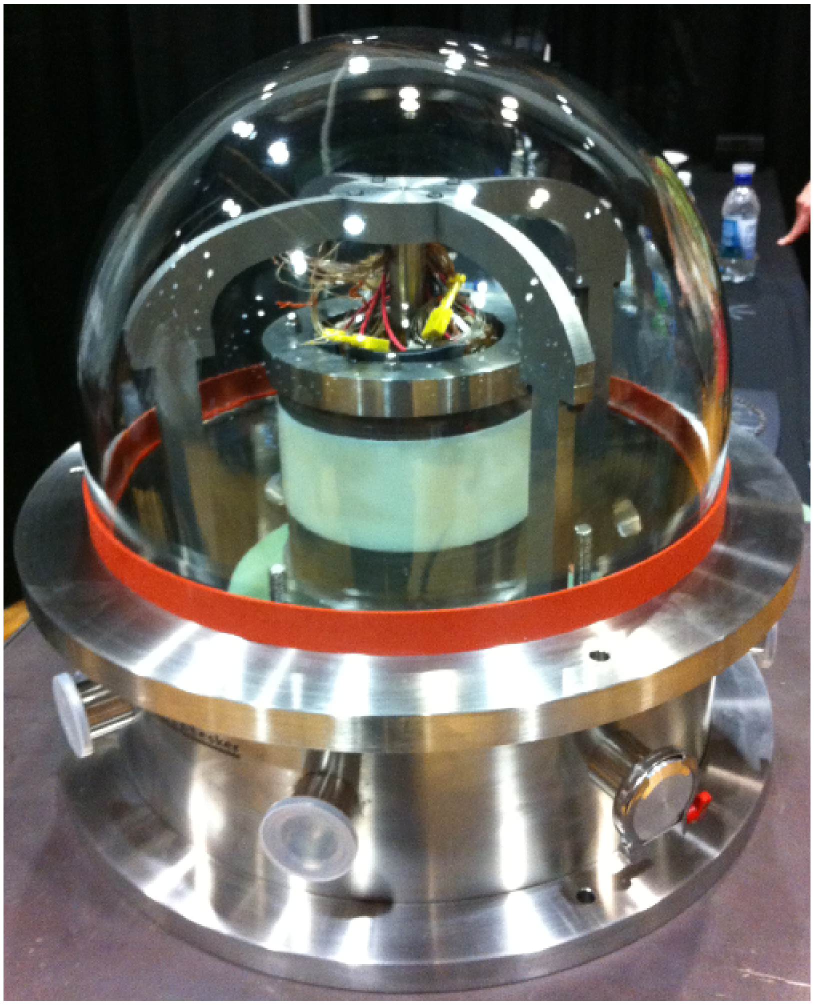

Figure 1.3: University of Idaho Flywheel Energy Storage System (UIFESS) Enclosed in Vacuum Chamber

Vacuum System The majority of the UIFESS is housed in a vacuum system, reducing windage losses as the flywheel rotates and increases efficiency. The vacuum system is capable of evacuating the chamber down to a pressure of 10^{-4} Torr. Sensors, electrical connections, liquid nitrogen, and chilled water are passed through the vacuum chamber collar. Mechanical interfaces located underneath the baseplate allow the flywheel to be lowered onto the passive magnetic bearing at the beginning of operation. The vacuum system and UIFESS can be seen in Figure 1.3.

Passive Magnetic Bearing Magnetic bearings are used to magnetically suspend the flywheel. This will reduce losses associated with traditional bearings. A passive magnetic bearing is responsible for levitating the flywheel in the z-direction. A significant radial corrective force is also generated by the passive magnetic bearing. The passive magnetic bearing utilizes High Temperature Superconductors (HTS) and a permanent magnet Halbach array built into the magnetic plate, located at the bottom of the rotor. The HTS “pucks” are mounted into the copper plate. Liquid nitrogen flows in a channel in the copper plate, cooling the HTS to 77 Kelvin. At this temperature, the HTS undergo a partial expulsion of magnetic flux, via the Meissner effect, resulting in levitation. The copper plate and the rotor magnetic plate are shown in Figure 1.5.

The Halbach Array is created by specifically orientating each permanent magnet relative to the magnets near it. The Halbach array shapes the net magnetic field at the bottom of the rotor, significantly increasing the field strength in the downward direction, while effectively eliminating the magnetic field above it. The increased strength of the downward field interacts with the HTS. The reduced field strength in the region above is ideal to reduce interference with the fields generated by the Field Regulated Reluctance Machine (FRRM).

Field Regulated Reluctance Machine The FRRM is the electric machine portion of the UIFESS. The FRRM allows motoring and generating functions. This device transfers electrical energy into mechanical energy for storage in the flywheel, then reverses the process to provide power to a load. The FRRM is designed with an inside-out topology, meaning the stationary portion (stator) of the machine is located in the center with the rotating portion (rotor) of the machine on the outside. This topology increases the energy density of the UIFESS. The FRRM design has the advantage of not requiring any wiring on the rotor. The flywheel is supported by non-contact forces, and the FRRM allows the flywheel to remain free of any physical connections.

All of the machine windings are located on the stator, which is mounted to the central hub. Chilled water flows through the hub, drawing heat out of the coils, prolonging the life of the coil insulation. The rotor and stator are constructed of magnetic steel laminates, with a 1 mm desired air gap is present between the rotor and the stator. Additional information on the UIFESS FRRM is presented in Wimer [11]. The machine stator and end windings is shown in Figure 1.4 and the machine rotor is shown in Figure 1.5.

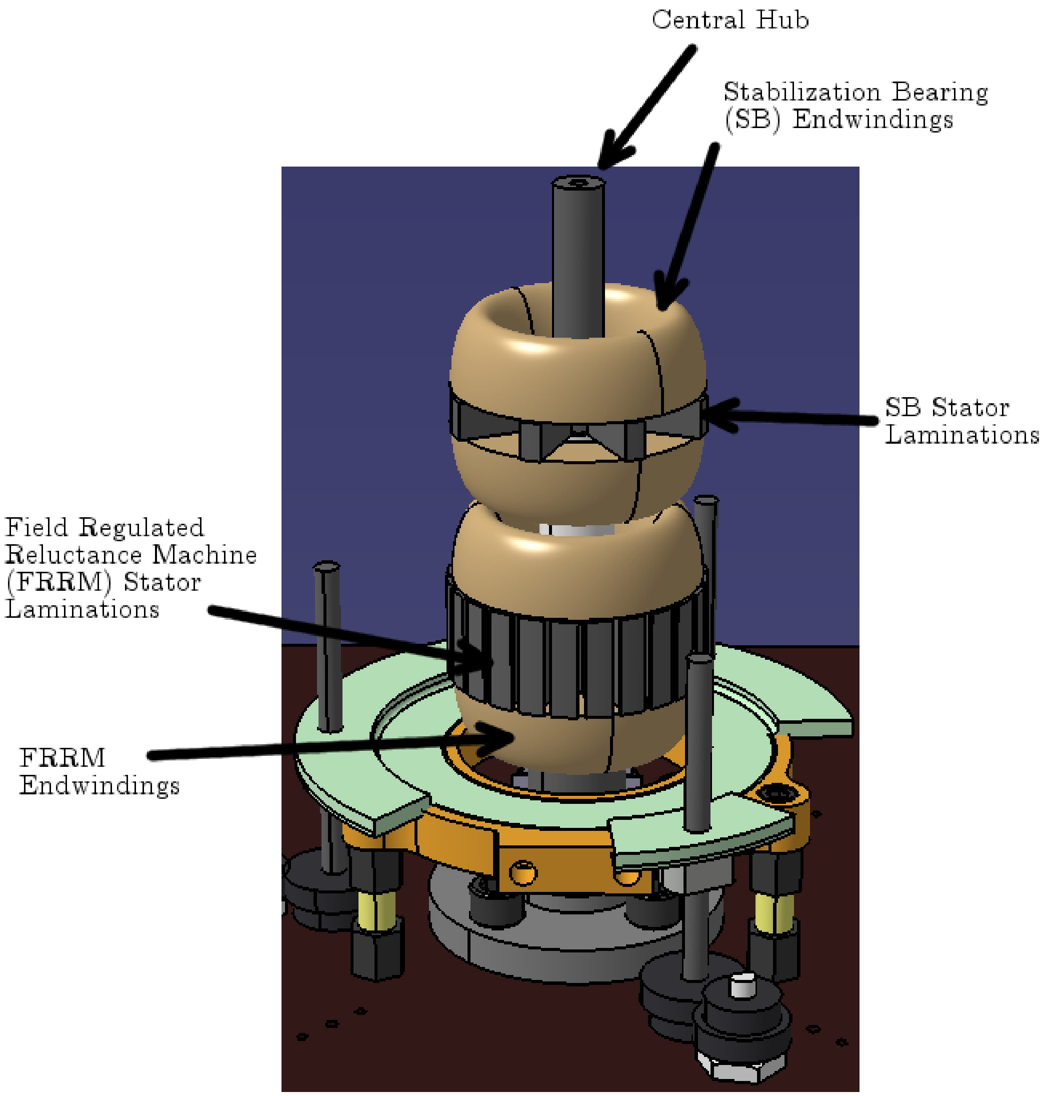

Figure 1.4: University of Idaho Flywheel Energy Storage System (UIFESS) Major Stator Components

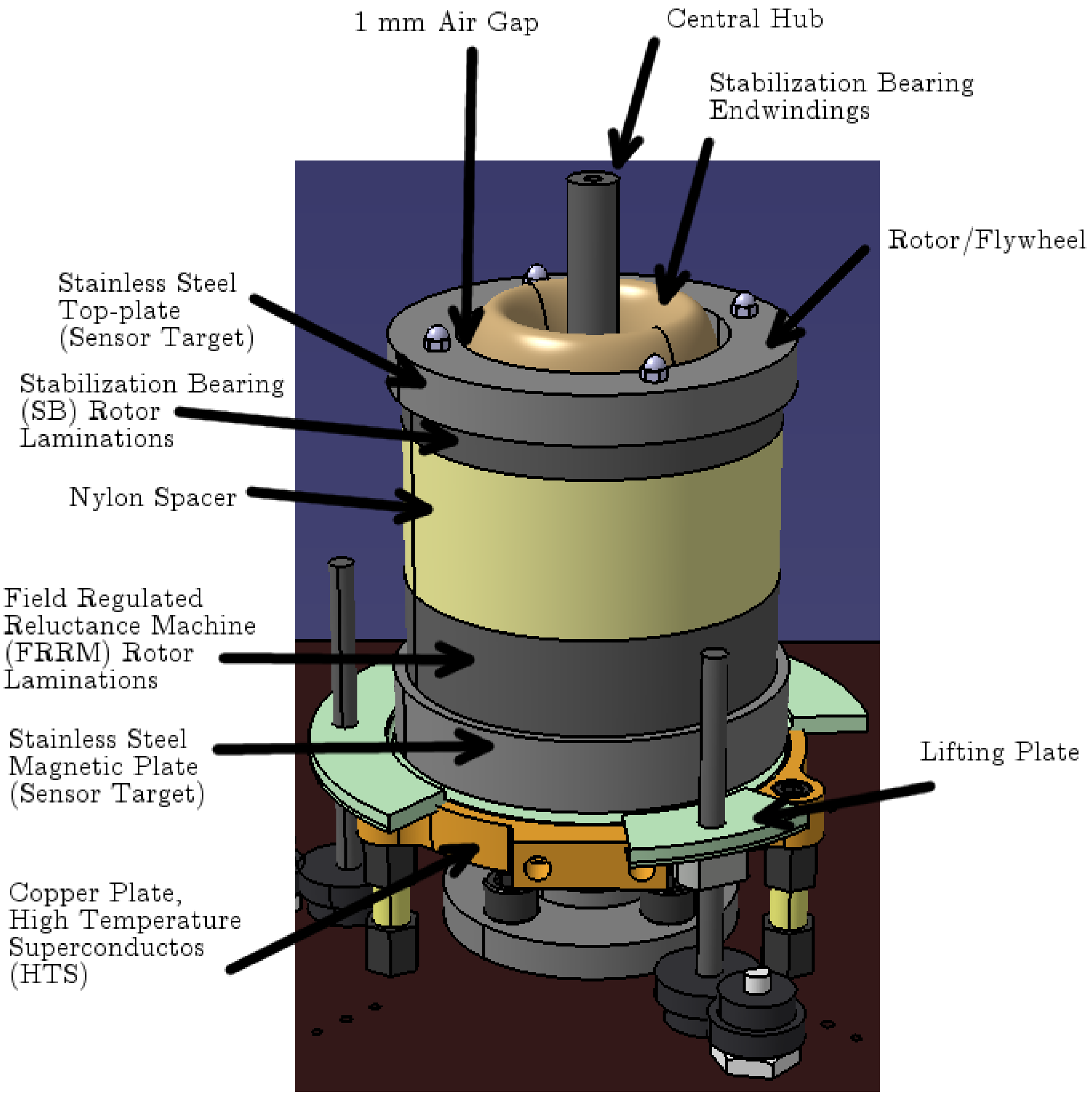

Figure 1.5: University of Idaho Flywheel Energy Storage System (UIFESS) Major Rotor / Flywheel Components

Active Magnetic Bearings To ensure the rotor does not collide with the stator, the desired 1 mm air gap must be maintained. Active Magnetic Bearings (AMB) are used to provide non-contact support to the rotor in the x-y plane. The AMB is capable of sensing a change in the rotor position with respect to the stator, and has the capability to pull the rotor in either axis direction of the x-y plane. There are two AMBs located on the UIFESS. The top portion of the flywheel has an AMB acting as a Stabilization Bearing (SB). The SB includes an eight coil stator with a round rotor, and is used to pull the top of the flywheel back into the desired position. Additional information about the SB can be found in [12]. The AMB stator and endwindings are shown in Figure 1.4 and the AMB rotor is shown in Figure 1.5.

The FRRM is also capable of acting as an AMB. This means the machine is capable of motor and generator functions as well as maintaining rotor position in the x-y plane. With this additional function, the machine is referred to as the self-bearing FRRM. The self-bearing FRRM maintains rotor position at the bottom of the flywheel. With the utilization of the SB and self-bearing FRRM, the air gap is maintained and external and tilting forces are corrected.

Control System A control system utilizing the AMB's and separate sensors is used to maintain the machine air gap. The desired and measured air gap values are compared, and the error term between the two is sent through a Proportional-Integral-Derivative (PID) controller. The controller contains a coefficient for each term, and is tuned specifically for the UIFESS. The PID controller outputs the desired current to pull the rotor back to the correct position. A simple "bang-bang" controller compares the coil current sensor reading to the desired current level, and adjusts the current as necessary. Additional information about the air gap control system is presented in Kisling[12]. The air gap control scheme is the same for the AMB located on the SB and the self-bearing FRRM. A rotational control algorithm is also discussed in Kisling[12] with a brief synopsis in Section 8.2.2.

Power Electronics Power electronics enable air gap control and rotation. Full-bridge DC-DC converters, or H-bridges, are used as power amplifiers to control the current in each coil of the SB and the self-bearing FRRM. Position and current sensors provide feedback for the control system. Signal conditioning is required to bring the sensor data into a microcontroller. The microcontroller is programmed with the control system, and uses outputs to manipulate the power amplifiers to adjust the coil current as needed. Multiple printed circuit boards (PCBs) are designed to interface the sensors, microcontrollers, and power amplifiers. The majority of this thesis discusses this topic.

1.4 Single Axis Single Bearing Unit

The Single Axis, Single Bearing (SASB) system gives the researchers a simple model to aid in conceptualization. The SASB unit features a single coil, a single distance sensor, a "U" shape iron bar, and the "flotor bar", constrained to one axis of motion. The unit is shown in Figure 1.6.

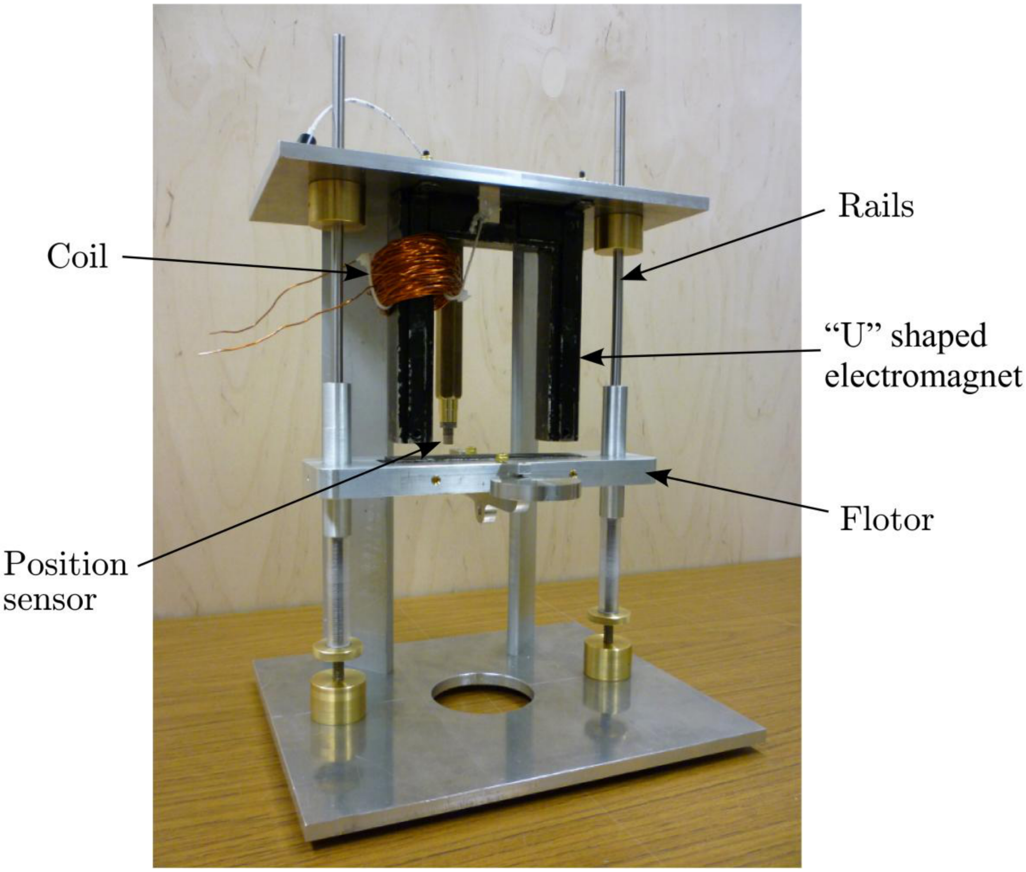

Figure 1.6: The Single Axis, Single Bearing (SASB) Demonstration Unit

The iron "U" bar, coil, and displacement sensor create an AMB. The flotor bar vertically slides up and down on rails, creating an air gap. The same principles used to control this air gap are utilized to control the air gap on the UIFESS. Essentially, the flotor mimics the rotor of the UIFESS. The distance sensor is mounted to detect displacement along the vertical axis. A stainless steel target is connected to the flotor bar. Any movement of the flotor bar will be picked up by the displacement sensor. The flotor is free to slide up and collide with the “U” bar or slide down and rest on spacers, allowing the air gap to vary from 0 mm to well beyond the 3 mm range of the displacement sensor. The SASB demonstration unit gives the researchers a test bed to practice 1 mm air gap control before attempting control on the UIFESS.

Initial testing of power electronic hardware and changes to the air gap control algorithm were first conducted on the SASB unit before being applied to the UIFESS. The simpler physical system eased troubleshooting hardware and software issues. Calibration and fine-tuning the signal conditioning topologies and the air gap control system were conducted with the SASB.

Chapter 2

Thesis Objectives

The primary objective of this effort is to enable air gap control and rotation of the UIFESS. The air gap control system, as discussed by Kisling[12], and rotation of the FRRM, as discussed by Wimer[11], require power electronics. Power electronic elements include displacement sensors, rotational position sensors, power amplifiers, current sensors, and microcontrollers. This work specified hardware and interfaces to be used in the power electronics. Considerations are taken for passing elements of the power electronics into and out of the vacuum chamber. A reliable electrical interface between all elements of the power electronics is essential to enabling air gap control and FRRM rotation. Signal conditioning topologies are designed to enable the microcontroller to sample the various sensors. The microcontroller switches the power amplifiers at a high frequency.

The secondary objective required interfacing all of the power electronic elements. Multiple custom printed circuit boards (PCBs) successfully connect all the elements of the power electronics. The custom PCB designs required mixed-signal, analog and digital, design methodologies. The PCBs connect the power electronic elements together in a single package, reducing signal noise and easing inter-connections.

The final objective investigates the speed capabilities of the power electronics. The highest rotational speed the UIFESS power electronics are capable of achieving is determined. It is hoped the power electronics could be used for the next phase of the program. A brief discussion of possible power electronics capable of achieving 500,000 rotations per minute is also presented.

Chapter 3

Scope

The work presented in this thesis represents work started in the Fall Semester of 2011 through the Spring Semester of 2014. The author spent the first year on the project as a member of the University of Idaho College of Engineering's capstone design program. The final two years were spent as a graduate student on the project. During this time, work on the UIFESS was a collaborative effort amongst many individuals. This effort was highly contingent on the work conducted by two fellow graduate students on the project, Bridget Wimer[11] and Brent Kisling [12]. Each student investigated and developed several aspects of the UIFESS.

This thesis discusses hardware used to enable air gap control and FRRM rotation. This role included defining power electronic elements including displacement sensors, current sensors, power amplifiers, microcontroller interfacing, and mixed signal printed circuit board design. Signal conditioning topologies were designed and implemented on custom PCBs. Specifics on how these elements would fit together and interface with the vacuum chamber were considered. A prediction of the UIFESS rotational capabilities concerning the power electronics was conducted.

Kisling developed a current controlled AMB model. An AMB control system was designed and implemented in software. Kisling also designed and demonstrated a custom stabilization bearing for use in the UIFESS. A foundation for the self-bearing machine control algorithms was developed by Kisling[12].

Wimer[11] was responsible for the FRRM design. Calculations determined the FRRM current stiffness and position stiffness values. Additional modeling and simulation of the UIFESS rotor dynamics was also conducted.

Chapter 4

Literature Review

Interest in developing active magenetic bearings (AMB) for new applications in rotordynamics was piqued by digital microprocessor development in the 1980's[13]. Active magnetic bearings are an enabling technology for Flywheel Energy Storage Systems (FESS). With the development of digital microprocessors, digital control could replace analog control. Digital controllers, such as Digital Signal Processors (DSP), offer greater flexibility in implementation[14]. Though digital controls replace analog controls, many of the sensors the digital controller must interface with are still analog in nature.

Digital systems grew in popularity in many industries, and interfacing analog and digital systems became widespread. The widespread use of analog and digital components being used in a single application motivated the development of mixed-signal printed circuit boards[15]. The high speed digital switching and requirement for accurate analog sensor data in FESS applications makes understanding mixed-signal design a crucial element for success.

Flywheel Energy Storage Systems is an active design topic, with groups such as NASA Glenn [9] and The Boeing Company[5] working to progress the technology. Though each facility brings a unique approach to FESS, there are some universal aspects to design. Essentially all groups use some form of digital control. NASA Glenn[9][10], including work conducted by Kascak[2], and the McTronX group of North-West University[16], implement digital control using the dSPACE Inc. real-time control system hardware. The real-time hardware is modular, meaning digital processors, analog and digital inputs and outputs are selected based on system requirements. This hardware is intended for real-time application prototype development, making it an ideal choice for FESS research. Once the prototyping phase is complete, an embedded solution capable of controlling the FESS would be developed.

Other groups initially create an embedded system to control the FESS. The AFS Trinity Power Corporation developed a system utilizing a DPS and created proprietary software and hardware[17]. The UIFESS has also created an embedded system for air gap control and flywheel rotation. Designing a custom system for control added to development time, but provided a less expensive alternative compared to purchasing dSPACE hardware.

Each FESS system includes various sensors. The most crucial sensor is the displacement sensor, responsible for determining the air gap between the rotating and non-rotating portion of the FESS. Due to the high precision required, many FESS utilize similar displacement sensors[18]. The eddy current displacement sensor offers a non-contact solution that has successfully been demonstrated on several FESS, including several NASA Glenn[2] projects and the McTronX group[16].

The digital system controls the FESS by using switches to control the current in the coils of the electric machine. IGBTs and MOSFETs have both been successfully utilized in FESS designs[2][5][16][17]. Specific use of a particular IGBT or MOSFET is dependent on several aspects of specific FESS design, such as desired rotational speed and control hardware available.

High speed FESS utilize vacuum systems to reduce windage losses that would occur at such high speeds[4]. The vacuum system is crucial to obtain a high efficiency FESS, but also introduces additional constraints. Considerations on the heat generated in the electric machine must be accounted for. All the power electronic connections made to the electric machine and AMB must pass through the vacuum chamber, adding expense and additional routing considerations. Sensor signals must also be brought out of the vacuum chamber.

The combination of these technologies has allowed flywheels to reach high speeds and begin to achieve respectable energy storage capabilities. NASA Glenn has a number of flywheels that have reached speeds ranging from 1,000 rpm[2] to 60,000 rpm[9] while demonstrating a number of concepts. The AFS Trinity Power Corporation FESS has reached speeds of 40,800 rpm and intended for use on the power grid[17]. A novel commercial product from Ricardo has demonstrated a flywheel rotating at 60,000 rpm in a hermetically sealed vacuum chamber, and does not require the use of a mechanical shaft to harness the stored energy[8].

Technological advances will enable continued development of FESS. Digital controllers continue to operate faster and gain additional features. Future control FESS hardware may include several processors in parallel, utilization of Field Programmable Gate Arrays (FPGAs), or even realizing control with analog control circuits once again [2]. These options could allow more processing to be done in parallel, and reduce the computational burden on a single processor. Power electronic efficiency will improve with the advancement of switching devices. Gallium nitride (GaN) transistors are a recent development that has the potential to reduce power losses and increase switching speeds[19]. The Boeing Company has already begun investigation into using these new devices, and claim the devices may offer up to 94.9% round trip power efficiency, compared to the 82.3% round trip power efficiency currently realized using MOSFETs[5]. These advances will allow FESS to obtain faster speeds and higher efficiencies, making them an increasingly viable option for energy storage.

Chapter 5

UIFESS Power Electronic Components

5.1 Introduction

The University of Idaho Flywheel Energy Storage System (UIFESS) can be grouped into three major subsystems. The control hardware is responsible for receiving commands from the control system and properly manipulating the electro-mechanical system. The electro-mechanical system includes components for rotation and maintaining a constant air gap between the rotating and non-rotating members of the UIFESS. The high level interaction of the subsystems is shown in Figure 5.1.

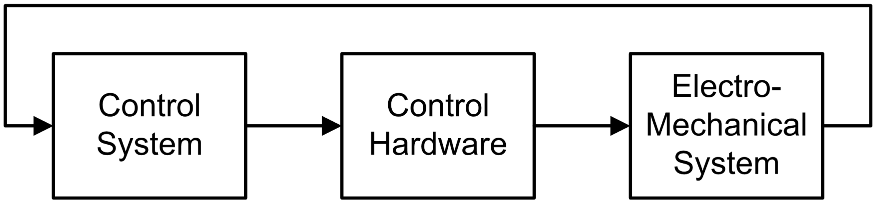

Figure 5.1: High-Level Flywheel Subsections

The electro-mechanical system consists of the rotating (rotor) and non-rotating (stator) portions of the self-bearing Field Regulated Reluctance Machine (FRRM) and the Stabilization Active Magnetic Bearing (SB), as shown in Figure 1.5. The FRRM stator contains 24 coils used for rotation and control. The SB stator has 4 coils responsible for air gap control only. The rotating portions of the self-bearing FRRM and the SB are components of the flywheel, the device which stores mechanical energy. Current passing through the stator coils is manipulated for air gap control and rotation of the flywheel.

The control system includes the air gap control and rotational algorithms coded into a microcontroller. Inputs are used to observe the electro-mechanical system and outputs are used to manipulate the electro-mechanical system. Inputs specify rotor rotation, rotor radial movement, and stator coil currents. Based on these inputs, the algorithms decide how to adjust current in each stator coil to maintain the machine air gap and rotation. The microcontroller adjusts its outputs to command the desired current for each coil.

The control hardware uses the microcontroller outputs to change the current in the coils. A Full-Fridge DC-DC converter is used to change the direction of the current in a coil. The Full-Bridge DC-DC converter adjusts the time averaged magnitude of the current. Details of operation are shown in Section 5.2. The control hardware also includes sensors. The sensors are responsible for turning real world phenomena into a measurable, time varying electric signal. Sensors give the controller an observed measurement of rotor displacement and coil current. Sensor types and specific information is given in Section 5.3.1. Major elements of the UIFESS are identified in Figure 5.2. More specific connections are shown in Figure 5.11.

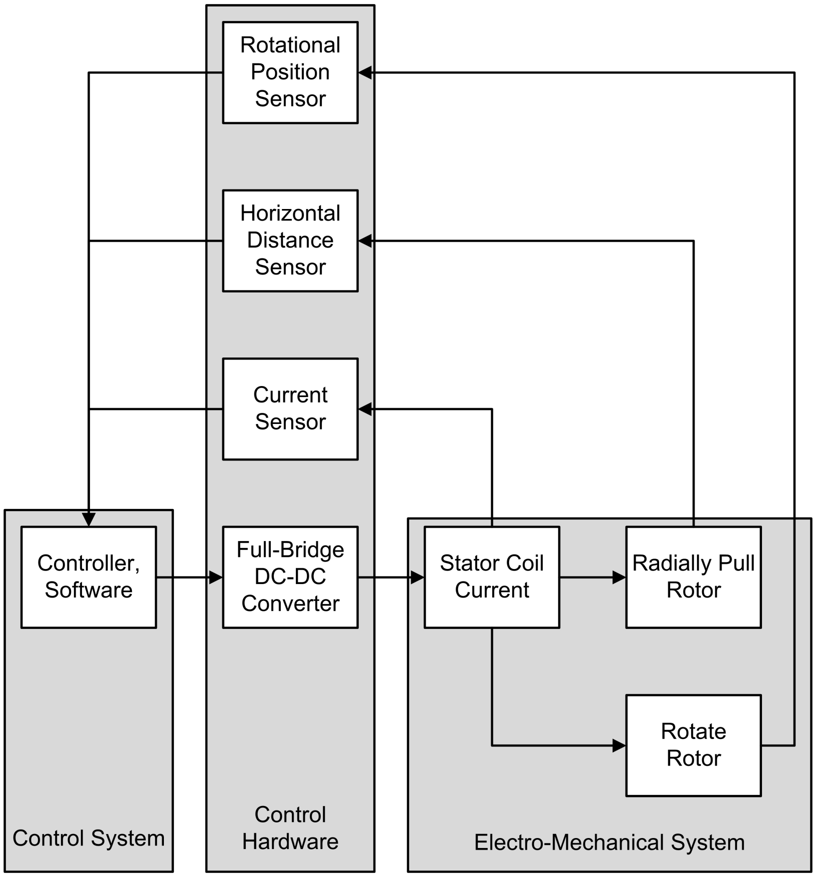

Figure 5.2: Flywheel Subsection Elements

5.2 Power Amplifier

The Full-Bridge DC-DC Converter, or H-Bridge, is typically used in DC motor drives, as shown in Figure 5.3. Converters utilize power semiconductor devices controlled by signal electronics, and typically include energy storage elements, such as inductors and capacitors [20].

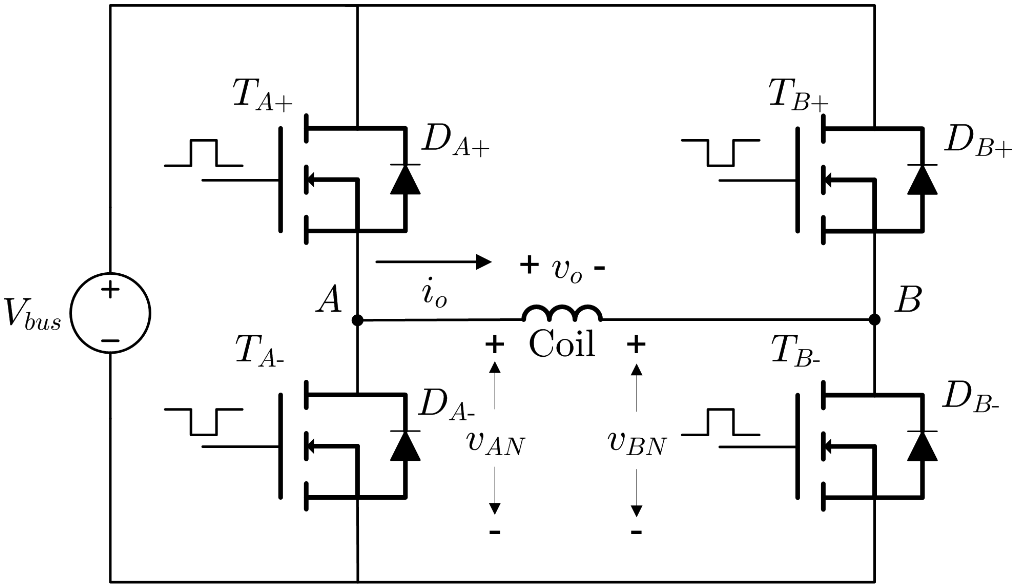

Figure 5.3: Full-Bridge DC-DC Converter or H-Bridge Using MOSFETs as Switches

The input to a full-bridge converter is a fixed-magnitude DC voltage, V_{bus}. For UIFESS application, V_{bus} varies from 12 V to 44 V. The output of the converter is a DC voltage v_o, which is controlled in magnitude and polarity. The output current i_o magnitude and direction can also be controlled [20]. The full-bridge converter can operate in all four quadrants of the i_o-v_o plane, as shown in Figure 5.4.

Opposite voltages can be placed on the load. The voltages v_{AN} or v_{BN} can be brought to V_{bus} or ground, depending on switch location, resulting in v_o, the voltage across the load, being positive or negative. The current i_o polarity is identified in Figure 5.3. Depending on the current magnitude, a change of switch positions doesn't immediately change the current direction. The load is assumed to be inductive, and current continues

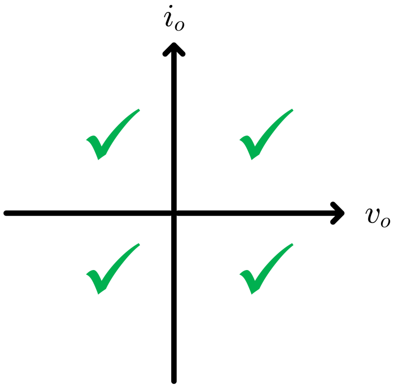

Figure 5.4: Full-Bridge Converter Can Operate in All Four Quadrants of the i_o-v_o plane

to flow in the initial direction. The body diodes of the MOSFETs allow the current to keep its direction, regardless of switch position.

Note that the converter topology includes diodes connected in anti-parallel with the switches. When a switch is in the on position, the direction of the current i_o will determine whether the switch or diode is conducting current. For the UIFESS voltages, currents, and switching frequencies, an N-channel MOSFET makes an acceptable switch. When a switch conducts current, it is in a conducting state. There are two legs in the converter topology, each with two switches and anti-parallel diodes. For each leg, an ideal case results in one switch being open and one switch being closed. Both switches are never closed at the same time, to avoid shorting the DC input. In actuality, both switches are open for a short interval, known a blanketing or dead time. This dead time ensures the DC input will not be shorted [20]. The position of the switches dictate the output voltage.

Consider switch position for leg A. With switch T_{A+} on, a positive output current flows through the switch or negative output current flows up through D_{A+}. Regardless of current direction, when T_{A+} is on and T_{A-} is off, point A is at the positive dc input terminal, as shown in Equation (5.1).

$$v_{AN} = V_{bus} \tag{5.1}$$

When T_{A-} is on, negative output current flows through T_{A-} since D_{A+} is now reversed biased. Positive output current flows through D_{A-}. Point A is now essentially at the neutral terminal of the DC input, as shown in Equation (5.2).

$$v_{AN} = 0 \tag{5.2}$$

Recall that the position of the switches dictate the output voltage, regardless of what direction i_o, the output current, is flowing. The output voltage of leg A is averaged over one switching frequency time period T_s by using the input voltage V_d and the duty cycle, $Duty_{A+}$, of switch T_{A+}, shown in Equation (5.3).

$$V_{AN} = \frac{(V_{bus} \cdot t_{on} + 0 \cdot t_{off})}{T_s} = V_{bus} \cdot Duty_{T_{A+}} \tag{5.3}$$

Similar conclusions are drawn for leg B of the converter, and a similar equation is derived, shown in (5.4).

$$V_{BN} = \frac{(V_{bus} \cdot t_{on} + 0 \cdot t_{off})}{T_s} = V_{bus} \cdot Duty_{T_{B+}} \tag{5.4}$$

The converter output voltage V_o is controlled by the duty cycle of each leg, and is independent of output current magnitude and direction, as shown in (5.5).

$$V_o = V_{AN} - V_{BN} = V_{bus} \cdot Duty_{T_{A+}} - V_{bus} \cdot Duty_{T_{B+}} \tag{5.5}$$

There are multiple ways to control the duty cycle of the switches, but one such method includes combining opposite switches from each leg into a switch pair, where T_{A+} and T_{B-} make up one pair and T_{B+} and T_{A-} make up the other pair. The switches in each pair are turned on and off at the same time. One switch pair must always be on.

Pule Width Modulation (PMW) is used to turn switch pairs on and off. This voltage switching scheme is called PWM with bipolar voltage switching. A PWM signal is sent to each MOSFET gate. Note the orientation of the pulses at each MOSFET gate in Figure 5.3. The switch pairs are always in opposite states, so when $v_{AN} = V_{bus}$, $v_{BN} =$ 0V or when $v_{AN} =$ 0V, $v_{BN} = V_{bus}$ [20].

A current being driven through a load from A to B is shown in Figure 5.5. In this situation, $v_{AN} = V_{bus}$ and $v_{BN} =$ 0V. A current flowing from B to A is shown in Figure 5.6. In this situation, $v_{AN} =$ 0V and $v_{BN} = V_{bus}$.

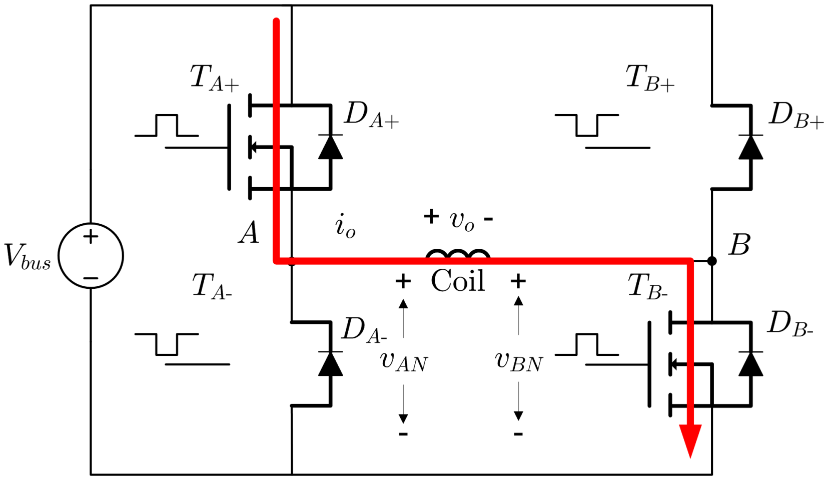

Figure 5.5: PWM with bipolar voltage switching Driving Current from A to B

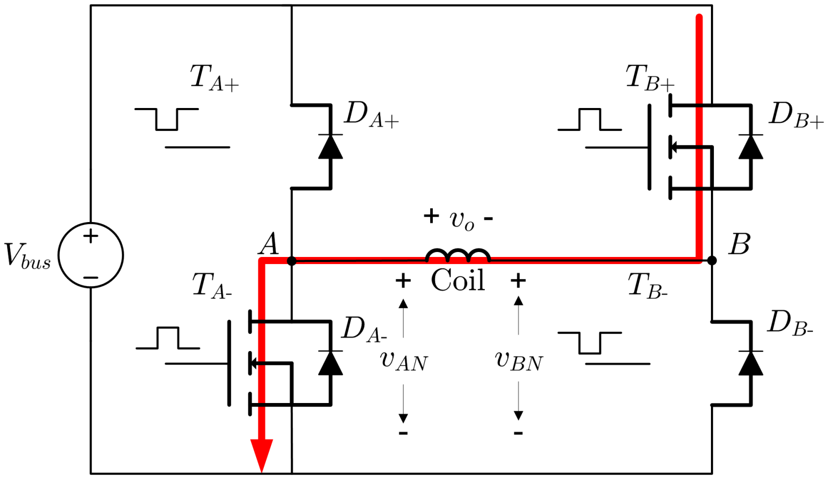

Figure 5.6: PWM with bipolar voltage switching Driving Current from B to A

The commercial Full-Bridge DC-DC converter manufactured by Pololu Robotics and Electronics is used. The Pololu High-Power Motor Driver 36v20 CS, item number 1457, uses individual discrete component to build the entire Full-Bridge DC-DC converter. N-channel Metal-Oxide-Semiconductor Field-Effect Transistors (MOSFETs) make up the switches on each leg. Specifically, the Infineon IPD048N06L3 G OptiMOS 3 Power-Transistor N-channel MOSFET is used [21]. The Pololu commercial Full-Bridge DC-DC converter is shown in Figure 5.7.

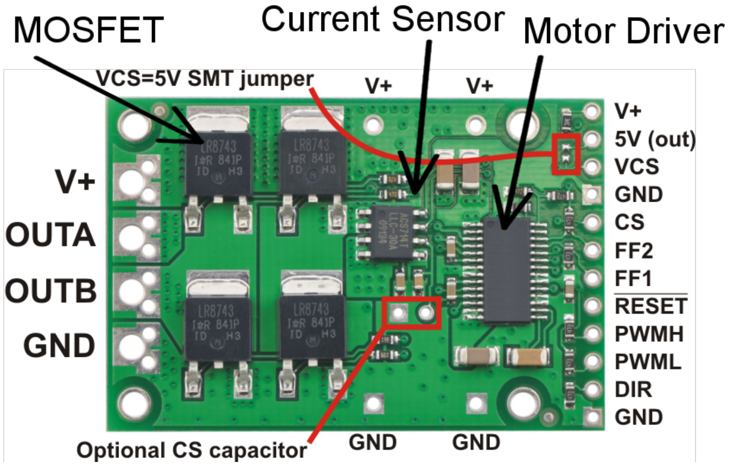

Figure 5.7: Pololu Commercial Full-Bridge DC-DC Converter or H-Bridge[22]

An n-channel MOSFET is essentially a voltage controlled switch. MOSFETs are typically used in applications requiring voltages below 200 V and switching frequencies up to the lower hundreds of kilohertz. MOSFETs have low on-state losses in low voltage ratings, fast switching speeds, and a gate that is triggered by a relatively small voltage. The MOSFET has three terminals; a drain, source, and gate. Forward current i_D flows from the drain to the source terminal. The gate-source voltage is used to turn on the device, and allow forward current to flow. If the gate voltage v_{GS} is below a threshold value $v_{GS(th)}$, typically about 2 V to 4 V, then the device acts as an open switch.

When the gate voltage surpasses the threshold voltage, then the device approximates a closed switch. When it is behaving as a closed switch, it can be modeled as a small resistor with a resistance on the order of milliohms. The forward current depends on the magnitude of the applied gate voltage [23]. The MOSFET symbol highlights major connections, shown in Figure 5.8. Drain current is able to be sourced for a certain amount of time depending on the drain to source voltage, as shown in Figure 5.9. The transfer characteristics are shown in Figure 5.10. Once the gate-source voltage becomes greater than the threshold voltage, drain current may flow.

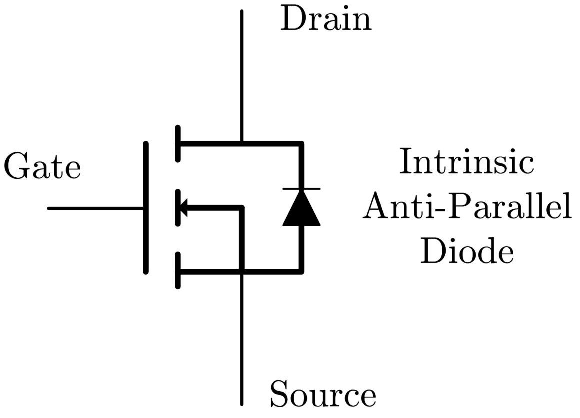

Figure 5.8: MOSFET symbol

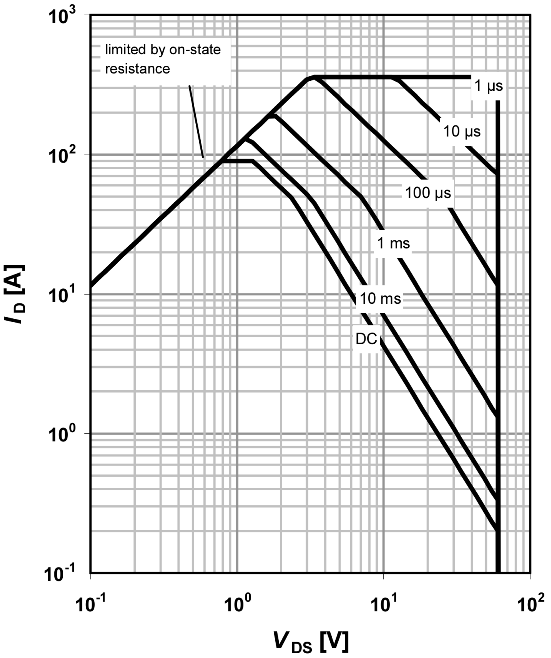

Figure 5.9: MOSFET i-v characteristic curve [21]

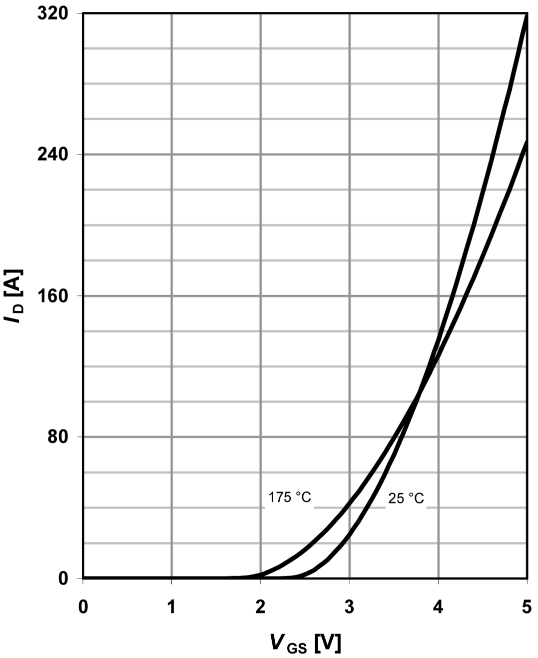

Figure 5.10: MOSFET transfer characteristic curve [21]

The commercial full-bridge converter utilizes a full bridge MOSFET driver integrated circuit (IC) as an intermediate interface between the microcontroller and the n-channel MOSFETs. The driver, Allegro Microsystems' A3941 Automotive Full Bridge MOSFET Driver, is specifically designed for high-power inductive loads, such as the inductive coils that are used in the UIFESS stabilization bearing and the self-bearing Field Regulated Reluctance Machine (FRRM)[24].

The driver IC uses the microcontroller outputs to alter MOSFET switch positions. Various MOSFET switch positions control the voltage across each coil, as well as the current direction. The driver IC also implements a dead time of approximately 1.5 μs, ensuring both switches are in the open position before closing the desired switch to ensure the input voltage is not shorted. The dead time is adjustable by changing the value of the resistance between the RDEAD pin and ground [24]. The driver IC has many options on how to drive current through the load. One such option operates on the principle of PWM with bipolar voltage switching, meaning opposite switches are paired and switch together, as discussed earlier. The documentation for the Pololu H-Bridge refers to this configuration as locked-antiphase operation. The motor driver truth table is given in Table 5.1.

Table 5.1: Motor Driver Truth Table
X = don't care (same for input H or L); Z = high impedance (outputs disconnected)[22]

PWMH	PWML	DIR	OUTA	OUTB	Operation
H	H	L	GND	V+	Forward
H	H	H	V+	GND	Backward
L	H	X	GND	GND	Brake Low
H	L	X	V+	V+	Brake High
L	L	X	Z	Z	Coast

The column titles OUTA and OUTB from Table 5.1 correspond to point A and B in Figure 5.3. The A3941 Motor Driver is the interface between the microcontroller and the individual MOSFET gates. The Pololu Full-Bridge DC-DC converter pin-out is shown in Figure 5.7. Supplying a +5 V signal to the PWMH pin will enable the MOSFETS labeled T_{A+} and T_{B+} to be turned on. Supplying a +5 V signal to the PWML pin will enable the MOSFETS labeled T_{A-} and T_{B-} to be turned on. The direction pin, DIR, determines which direction the current is forced through the load, an inductive coil for the UIFESS application. These pins are all accessible on each PCB, elaborated on in Section 6.3.3.

For initial application for the UIFESS, locked-antiphase or PWM with bipolar voltage switching is used. Both PWMH and PWML are held high with a +5 V signal. The microcontroller supplies a +5 V PWM signal to the DIR pin. A 50% duty cycle on the DIR pin will result in zero average current flow through the load. A duty cycle less than 50% will cause an average current flow from point B to point A, as shown in Figure 5.6. This method was the simplest to implement and required the least amount of microcontroller GPIO pins.

The Pololu documentation mentions that the driver supports PWM frequencies as high as 40 kHz. The PWM rates can be higher, though the switching losses will be considerably higher. The 40 kHz rate includes using the duty cycle, so for a 50% duty cycle, the MOSFETs are actually switched at 80 kHz, which is further discussed in Section 8.2.1.

Unfortunately, the driver IC requires 5 V high logic, while the microcontroller is capable of only supplying 3.3 V. A level-shifting IC is required to interface the devices. The n-channel MOSFET itself has a gate threshold voltage of approximately 2.2 V. A gate-source voltage of 4.5 V allows a forward current of approximately 45 A to flow, more than acceptable for UIFESS applications. The worst case drain-source on-state resistance is 8.2 mΩ [21].

Table 5.2: Pololu Full-Bridge DC-DC Converter Specifications

Parameter	Symbol	Rating	UIFESS
Drain-Source Voltage	V_D	50 V	V_{bus}
Continuous Drain Current	I_D	20 A	12 A
MOSFET Gate-Source Voltage	V_{GS}	±20V	5V
Switching Frequency[22]	f_{sw}	40 kHz, 50% Duty	80 kHz
Switching Dead Time	t_{dead}	1.5 μs (Adj.)	1.5 μs

The V_{bus} rail supplies the voltage across the coils of the stabilization bearing and the self-bearing FRRM. The vacuum electrical feed-throughs are rated to 12 A. A logic level shifter will have to be used to interface the microcontroller and the commercial full-bridge converter. A switching frequency of 80 kHz will be used on the DIR pin. The default motor driver IC switching dead time will be kept the same. The interface between the control system, control hardware, and the coils is shown in Figure 5.11. The specific pin connections discussed to utilize the power amplifier are shown as well. This diagram shows all the possible connections. Each UIFESS Driver Boards will not interface with the displacement sensors. The PCB shown is discussed in Section 6.3.

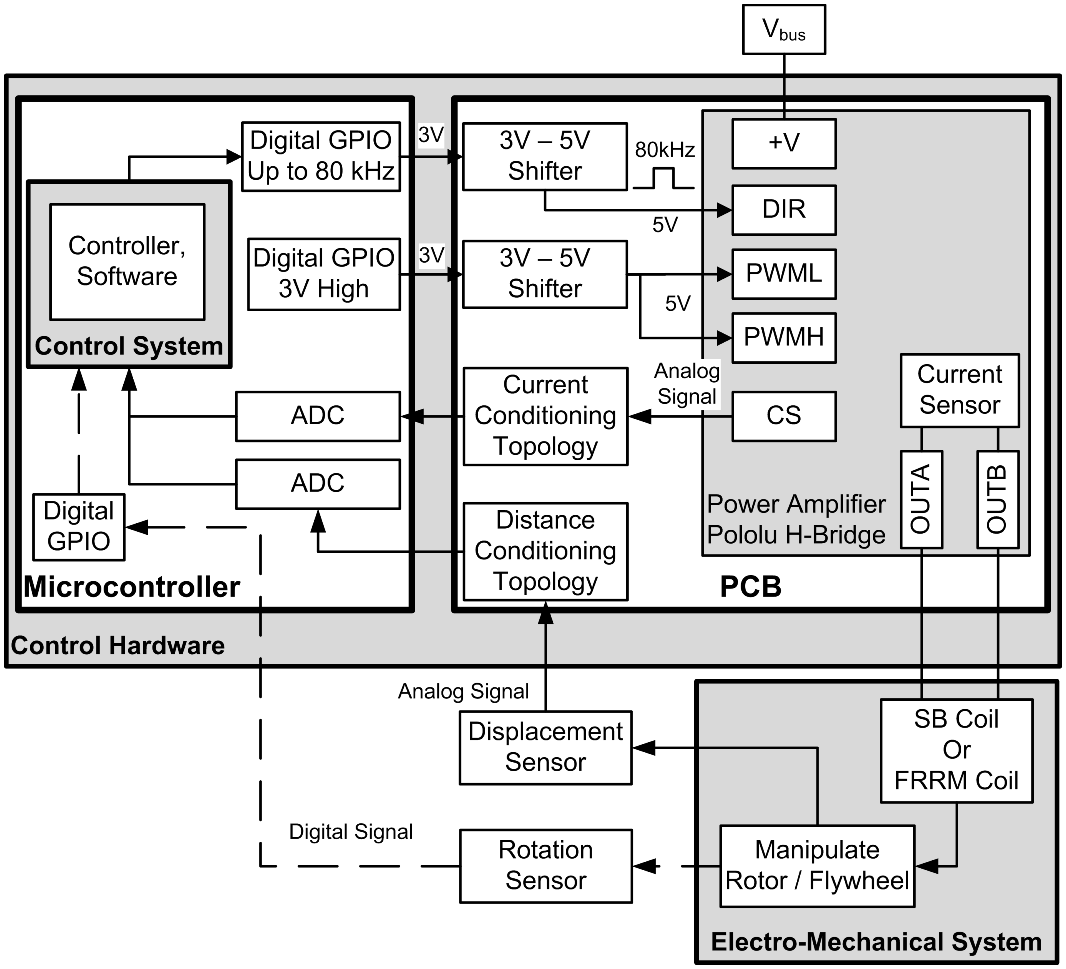

Figure 5.11: Block Diagram Showing the Interface Between the Control System, Control Hardware, and the Electromechanical System

5.3 Sensors

5.3.1 Introduction

The UIFESS uses several analog sensors to turn real world phenomena into a measurable, time varying electric signal. Radial displacement sensors are used to determine how much the flywheel has moved in the xy-plane. Rotational position sensors determine the rotor pole positions of the FRRM. Hall effect current sensors determine the current flowing in each coil of the FRRM and AMB. Thermocouples monitor the temperature of the coils. These analog sensors are read by the microcontroller analog to digital converter (ADC) for use in the control system algorithms. The various sensors and the UIFESS is shown in Figure 5.12.

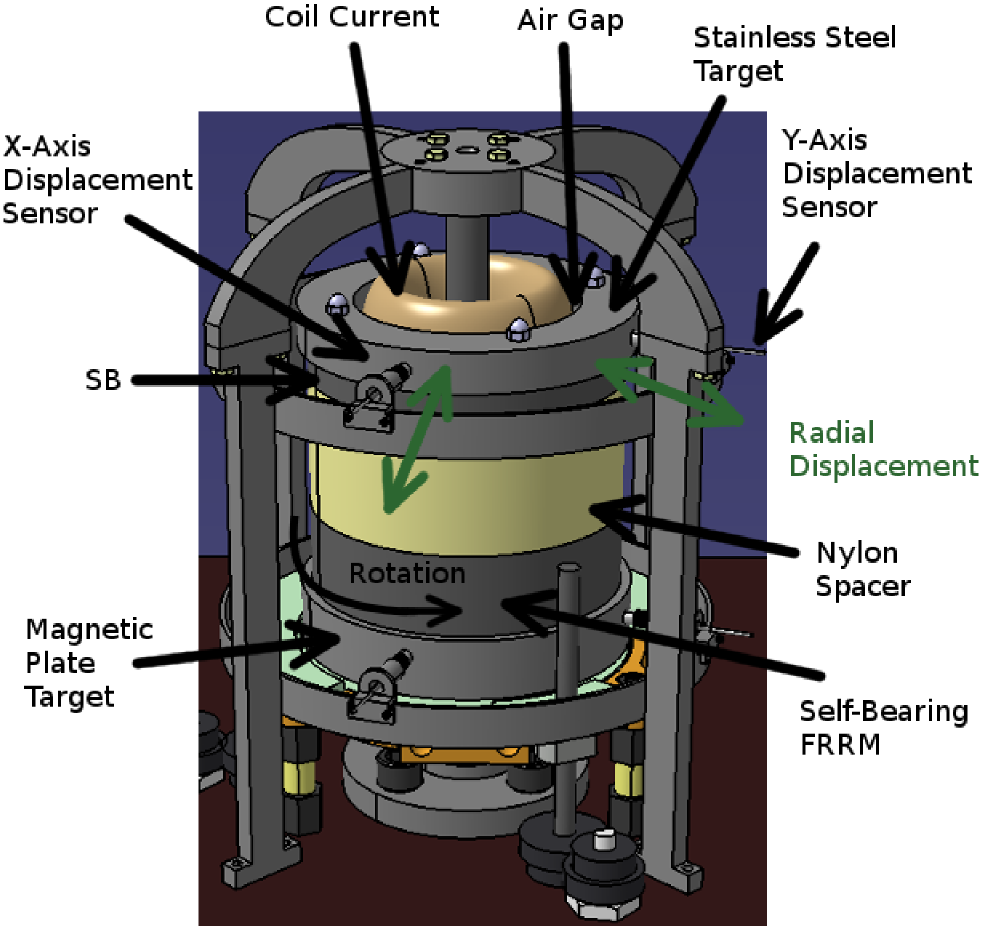

Figure 5.12: Sensors Monitoring Various Phenomena of the UIFESS

5.3.2 Radial Displacement Sensor

The radial displacement sensor is responsible for determining how much radial displacement the rotor has experienced at a given time. The sensor relates the movement of the rotor to the air gap, the distance between the rotor and the stator. It is desired to maintain a 1.00 mm air gap between the rotor and the stator. The rotor has five axes of freedom, so it has the ability to tilt and move radially, causing the air gap to increase or decrease. A sensor is needed to determine radial motion of the rotor, so the air gap can be determined. It is crucial to have an accurate portrayal of the air gap so the control system can maintain the 1.00 mm air gap. The smaller displacement the sensor can determine, the more quickly the control system can respond. The faster the response, the smaller corrective action is needed, and system stability is maintained. In addition, recall the rotor is essentially free-floating, so a non-contact sensor must be used to determine the rotor displacement.

5.3.2.1 Displacement Sensor Selection

A variety of sensor types are capable of determining rotor displacement. These sensors operate on various principles, therefore offering differences in sensing range, accuracy, and resolution. Common non-contact measuring techniques include inductive displacement sensors, magnetic displacement sensors, capacitive displacement sensors, and eddy current sensors [18][25].

Inductive Displacement Sensors This sensor type uses a coil inductor with a ferromagnetic core. The coil is driven with an oscillator. When the target ferromagnetic material is in range and moves, the target material will perturb the inductance of the coil. This perturbation of the inductance is sensed by electronics, and converted into a time varying voltage output. Ideally, the output voltage will vary linearly with the displacement. If the magnetic bearings are driven by switching amplifiers, such as what is done with the UIFESS, significant disturbances will occur when the switching frequency of the bearings are near the modulating frequency [18]. Since UIFESS uses switching amplifiers, it is decided to not pursue this type of sensor.

Magnetic Displacement Sensors A constant current is passed through a magnetic loop with a coil and an air gap. The target material must be magnetic. The flux density, B, at the air gap is used to determine the air gap. Flux density is measured with a Hall sensor. These sensors are inexpensive, but susceptible to magnetic interference [18][25]. The possibility of magnetic interference is high, so this sensor type is not investigated.

Capacitive Displacement Sensor A high frequency current flows through the sensor. The sensor itself is a plate capacitor, and includes one electrode plate of the plate capacitor. The other plate is the target made of a conductive material. The distance between the two plates affects the capacitance, and supporting electronics turn the distance into an output voltage signal. Their accuracy is affected by contamination between the plates, which would alter the dielectric constant, and give unreliable capacitance measurements. Capacitive displacement sensors may require a grounding connection to the target material, which would be difficult to implement in a non-contact sensing solution. Capacitive sensors are typically more costly compared to other displacement sensor types [18] [25]. Due to cost issues and a possible grounding connection required, it is decided to find a more suitable sensor type.

Eddy Current Displacement Sensors Megahertz frequency current is passed through an air-core coil. The high frequency current generates an electromagnetic field. This field induces eddy currents in the target material. These induced eddy currents create their own opposing electromagnetic field, shown in Figure 5.13.

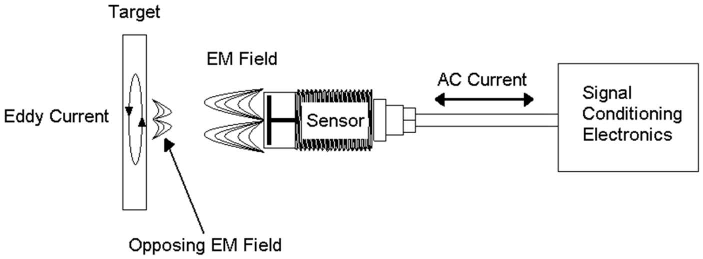

Figure 5.13: Eddy Current Displacement Sensor Operation[25]

The interaction of the generated EM field and the opposing EM field is called the coupling effect. The intensity of the coupling effect is dependent on the distance between the coil and the target material. The coupling effect will alter the impedance of the coil. Signal conditioning electronics translate the varying impedance into a displacement signal. The eddy current sensors are not affected by contaminants and can be used in a vacuum. The sensors have a frequency response range into the tens of kHz. Target material imperfections may cause noise-like disturbance. High frequency magnetic fields have the possibility to introduce error as well [18] [25]. Eddy current sensors offer relatively high resolution, accuracy errors that can be solved, and have an acceptable cost for our budget. It was decided to find a solution that uses this type of sensor.

Eddy Current Displacement Sensor Selection To determine the best solution for the UIFESS, various manufacturers were contacted. Eddy current displacement sensor solutions from multiple manufactures are compared in Table 5.3. The desired solution would have a sensor range of 3 mm, sub-micrometer resolution, linear output, and have a vacuum feed-through solution. The rotor can only move radially a total of 2 mm before the rotor collides with the stator. A sensor with a 3 mm range would guarantee that the entire range of radial motion would be sensed.

Table 5.3: Eddy Current Displacement Sensor Comparison

Solution	Range	Res.	Output [V]	Vacuum
Kaman KD-2446, 9C [26]	5.08 mm	0.3 μm	0-22, nonlin.	Bulkhead
Kaman KD-2306, 9U [27]	4 mm	0.4 μm	0-10, lin.	Bulkhead
Lion Prec. ECL114, U12C [28]	3.5 mm	0.35 μm	0-10, lin.	Bulkhead
Micro-Epsilon Eddy 500, U3 [29]	3 mm	0.3 μm	0-10, lin.	Custom
GE 3300 XL, 11 mm [30]	4 mm	100 μm	(-1)-(-17), lin.	Custom

In all cases, each solution requires an eddy current displacement sensor, or probe, which is located in close proximity to the rotor target. The probe is attached to a signal conditioning electronics box, responsible for conditioning the signal into a usable output voltage, essentially turning the sensed change in impedance into an output voltage, and may linearize the change in impedance and output voltage relationship.

It is desired that the rotor moves a maximum of ±100 μm. The less movement the rotor undergoes, the less the controller has to work to maintain a constant air gap. In order for the controller to maintain such a small air gap, the controller must have a displacement reading multiple orders of magnitude smaller than the air gap tolerance attempting to be maintained. It is decided that a sensor reading two orders of magnitude finer than the maximum desired air gap movement was a fair balance of sensor cost and controller robustness. For the UIFESS, this means a sensor solution requires a resolution down to single micrometers.

Linear output from the sensor requires less microcontroller computation time to determine the displacement reading. A single linear equation turns the linear displacement output into a number directly representing the physical displacement of the rotor. A nonlinear sensor output requires a look up table and precise knowledge of the nonlinear behavior of the sensor.

The displacement sensors are located inside the vacuum chamber where the rotor is located. The electronic boxes and the rest of the control hardware are located outside of the vacuum chamber. A solution is required to pass the cable that leads from the sensor probe to the electronics box.

The Kaman KD-2446 was significantly cheaper than the Kaman KD-2306 solution. The UIFESS budget was large enough to purchase a linear output solution. The Kaman KD-2446 solution is eliminated from contention. The KD-2306 and Lion Precision's ECL114 solutions offer very similar benefits, but Lion Precision's solution is significantly more expensive. The solution offered by Micro-Epsilon has comparable specifications. However, additional effort is required to obtain a vacuum feed-through solution, eliminating the Micro-Epsilon solution from contention. The solution offered by General Electric Bently Nevada (GE) does not have high enough resolution and still requires additional effort for a vacuum feed-through solution. The GE solution is eliminated from contention.

Industry partners at NASA Glenn Research Center are contacted for their recommendation about displacement sensors. NASA Glenn has successfully used the Kaman DIT-5200 in their flywheel designs, and they recommend the Kaman brand. The DIT-5200 specifications are beyond the UIFESS requirements, so this specific solution is not considered. However, NASA's positive experience with Kaman persuaded the UIFESS team to invest in Kaman sensors. The KD-2306 Eddy Current Displacement Sensor is selected. These sensors are the most expensive of the required sensors. Costs of the various discussed solutions ranged from $4,000 to $9,000.

5.3.2.2 KD-2306 Eddy Current Displacement Sensor

The Kaman KD-2306 Eddy Current Displacement Sensor with 9U probe was purchased[27]. The sensor probe range is large enough to capture the entire range of motion the rotor is possible of encountering, but small enough to maintain significant resolution. A vacuum feed-through bulkhead is spliced into the cable that connects the sensor probe to the electronics box. A single KF-40 flange is capable of passing all four displacement sensors through.

Calibration of the displacement sensor solution was conducted by Kaman. The solution required an accurate 0 mm to 3 mm range. The target material is 303 stainless steel, a non-magnetic steel already present on the flywheel. The top plate and the magnetic plate of the flywheel are both this material. The target must be an inch or more in height for optimal performance. The SB displacement sensors are aimed at the center of the stainless steel top-plate of the flywheel, identified in Figure 1.5. The FRRM displacement sensors must be centered on the upper one inch of the stainless steel magnetic plate, identified in Figure 1.5.

In addition, the sensors are calibrated to have a 1 mm offset. When the 9U probe is 1 mm away from the target, it gives a reading of 0 mm. This allows the full range of the sensor to be used without risking a collision between the 9U sensor probe and target.

The 9U sensor probe is aimed at the flywheel top plate stainless steel target in Figure 5.14. The interface between the distance sensor and the control hardware is shown in Figure 5.11.

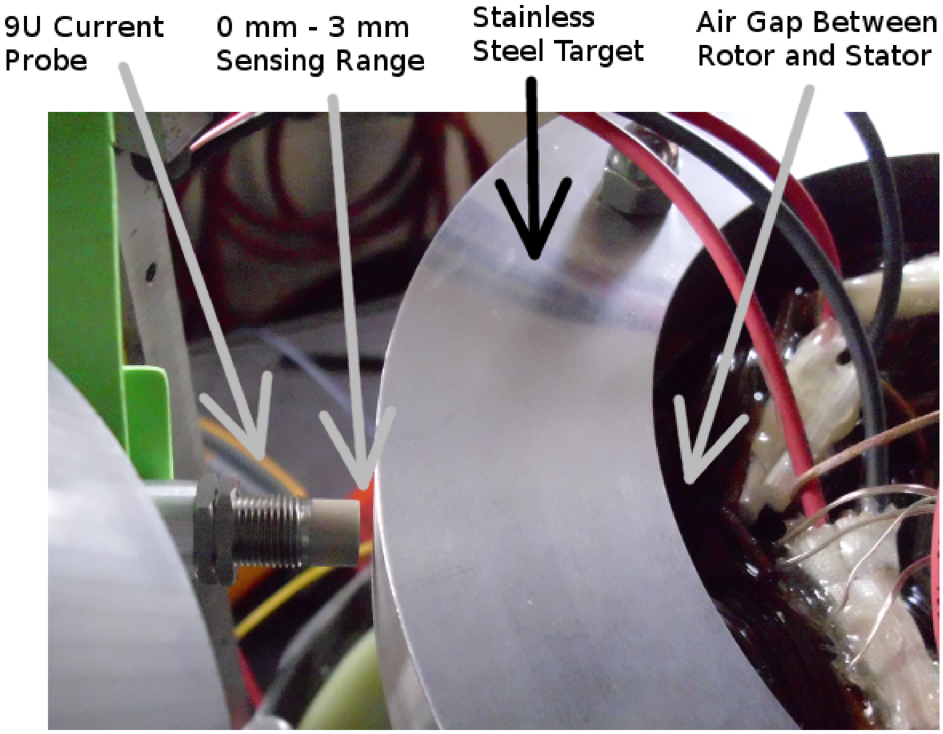

Figure 5.14: KD-2306 9U Eddy Current Sensor Probe aimed at the upper Stainless Steel Target of the UIFESS

5.3.3 Current Sensing

The control system requires driving the current in a coil to a desired magnitude and direction. In order to ensure the current reaches the desired magnitude, a current sensor is needed. After investigation, the commercial full-bridge converter is discovered. The commercial product includes an on-board Hall Effect-Based Linear Current Sensor in an IC package[31]. This sensor is the ACS714ELCTR-30A-T, manufactured by Allegro MicroSystems, Inc. The on-board current sensor IC is shown in Figure 5.7. The interface between the current sensor and the control hardware is shown in Figure 5.11.

5.3.3.1 Hall Effect-Based Linear Current Sensor

The sensor is capable of sensing bi-directional AC and DC currents, and is typically used in motor control applications[31]. A copper conduction path runs through the IC. The current the user desires to monitor must be passed through this conduction path. The conduction path is located near a precise, low-offset, linear Hall circuit. When a current is passed through the conductor, a magnetic field is generated. The Hall circuit will turn this magnetic field into a linear, proportional output voltage. As the sensed current increases, the output voltage will also increase.

The ACS714ELCTR-30A-T is intended for sensing currents in the ±30 A range. The IC requires a 5 V supply and will create a linear output voltage that ranges from 0.5 V to 4.5 V for currents ranging from -30 A to 30 A. The output voltage has 66 mV/A sensitivity and has a 2.5 V offset, see Figure 5.15. Typical output error is 1.5%. The current sensor is located on the commercial full-bridge converter. The converters are all located outside of the vacuum chamber, so no vacuum feed-throughs or specialized hardware implementation is required.

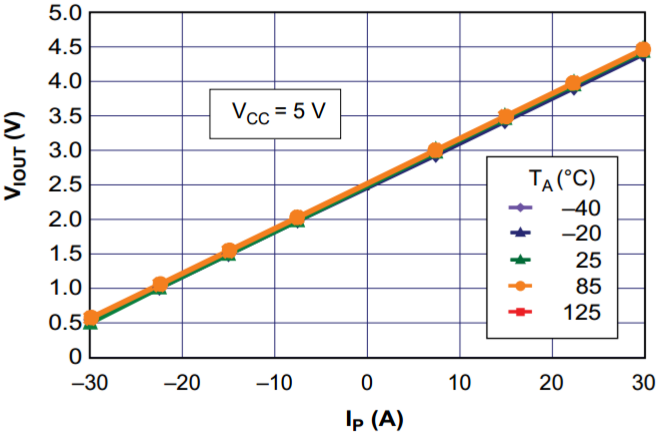

Figure 5.15: Current Sensor Output Voltage Relationship[31]

5.3.4 Rotational Position Sensor

The self-bearing FRRM includes a rotor with salient poles, meaning the inner circumference of the rotor is not round. An overview of machine rotation is given in Section 8.2.2. Additional details are discussed in Wimer[11] and Kisling[12]. Due to time constraints, a specific rotational sensor is not selected. It is expected this will be a digital sensor, and will output pulses as the rotor rotates. Discussion on placing marks on the plastic spacer of the flywheel is discussed. The marking has to be accurately placed, and safe for use in the vacuum chamber. The rotational sensor would have to be an optical device that would use reflected light to determine when a mark on the rotor passes by. Another option discussed involves connecting a counter wheel to the flywheel. The rotational sensor could count marks on the wheel as it spun. Lowering the flywheel after the HTS's have cooled complicates this option.

5.3.5 Thermocouples

The self-bearing FRRM stator has 24 coils and the stabilization bearing has 4 coils, all of which are passing a significant amount of current at all times. A significant amount of heat is generated by the coils. Excessive heat will degrade the life of the coil winding insulation, and could cause shorting in the windings. The machine operates in a vacuum, so convection does not take place.

The only effective means to pull heat from the coil windings is through conduction. The center hub of the stator is hollow, and a baffle has been installed so that chilled water may pass through the hub, and draw heat from the self-bearing FRRM stator. Thermocouples have been placed at various positions in the windings to monitor the temperature, and ensure the temperature does not reach a level where the insulation could be damaged.

Thermocouples convert thermal energy into electrical energy. Thermocouples are constructed of two dissimilar metals connected at one end. The other ends are known as the "cold junction" ends, which is where the voltage measurement is taken. Three thermoelectric effects are responsible for a thermocouple's operation: the Seebeck, Peltier, and Thomson effects [32].

The Seebeck effect describes that when two dissimilar metals are connected in a series circuit, and each junction is at a different temperature, an electric current will be observed. The amount of current is dependent on the temperature difference between the two junctions and the specific metals used. The Seebeck effect is a combination of the Peltier effect and the Thomson effect[32][33].

The Peltier effect demonstrates that when a current is passed through two dissimilar metals in series, one junction will rise in temperature while the other will fall, depending on the current direction[32][33].

The Thompson effect essentially describes how the temperature gradient of a single metal changes when a current is passed through it[32][33].

A thermocouple exploits these three effects to accurately determine a temperature at one of its junction locations. The temperature sensing junction is typically spot welded. The two metals are each individually insulated, and both of these insulated wires are covered by a protective jacket. The color of the individually insulated jacket identifies the type of metal. Different combinations of metal yield different temperature ranges. A voltmeter is used at the other junction to measure the voltage. The electromotive force generated in on the order on millivolts. An amplifier circuit may required to increase the magnitude of the voltage to be measured.

5.3.5.1 Type K Thermocouples

Type K thermocouples are constructed by joining Chromel and Alumel. Chromel typically has a yellow jacket and Alumel typically has a red jacket. This metal combination yields a useful temperature range of -200°C to 1250°C.

Type K thermocouples are located in multiple windings of the UIFESS. The stabilization winding has thermocouples located in several coils. The self-bearing FRRM coils have thermocouples located in multiple coils of the machine. Vacuum feed-throughs for 2 Type K thermocouples were purchased.

The stabilization bearing has a single coil with multiple thermocouples installed in it, as shown in Figure 5.16. Thermocouple #1 is located at the top of the coil, opposite of the leads. Thermocouple #2 is located in the middle of the coil. Thermocouple #3 is located at the bottom of the coil. Thermocouple #4 is located at the top of the coil, near the leads coming out of the coil.

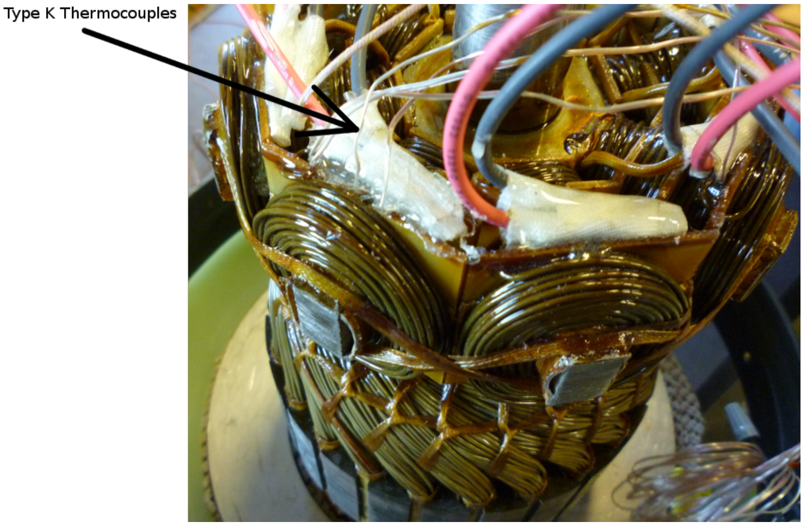

Figure 5.16: Type K Thermocouples in the Stabilization Bearing Coil

A large, continuous current can be passed through the coil, and each thermocouple can be monitored. The thermocouple that senses the highest temperature should be monitored. Using this coil as a reference, the other coils with only a single thermocouple can be monitored, and the highest temperature of each coil will be known. A similar approach can be used for the self-bearing FRRM coils.

5.3.5.2 Type T Thermocouples

Type T thermocouples are constructed by joining Copper and Constantan. Copper typically has a blue jacket and Constantan typically has a red jacket. Type T thermocouples are intended for use in cryogenic applications. The metal combination yields a useful temperature range of -250°C to 350°C. These thermocouples will enable temperature monitoring of the copper cold plate and the HTS. The HTS must be cooled with liquid nitrogen, which has a temperature of -196.15°C. Vacuum feed-throughs for 2 Type T thermocouples were purchased.

5.3.5.3 Thermocouple Data Logger

The OM-CP-QUADTEMP2000, a 4-channel data logger from Omega Engineering is used to record temperatures[34]. Once the stabilization bearing and the self-bearing FRRM coils have been characterized, a single Type K thermocouple from each bearing can be brought through the vacuum chamber for monitoring and data logging. This will allow monitoring of the coil temperatures during operation of the UIFESS. The data logger has the ability to simultaneously monitor Type T thermocouples, which will monitor the HTS temperature. It must be ensured the HTS remain cool to maintain rotor levitation.

5.4 Microcontrollers

5.4.1 Introduction

The microcontroller is responsible for reading sensor signals, using the sensor data in the control algorithm to determine which coils and currents are required to provide corrective forces or produce torque for machine rotation.

From a control and rotational standpoint, the self-bearing FRRM and the stabilization bearing are separate systems. Each system is similar in concept, but has a different number of coils and the coil function differs with rotor position in the self-bearing FRRM. A separate microcontroller is used for each system. A different microcontroller model is used for each system to more closely match the needs of the particular system.

Each system requires two horizontal rotor position sensors to determine the air gap in its system. Each system operates on a decentralized principle, meaning one horizontal rotor position sensor is responsible for sensing air gap along the x-axis while a second sensor is responsible for sensing air gap along the y-axis. Each horizontal rotor position sensor requires its own analog input. Each system must be capable of monitoring the current in every coil. Each system requires a significant amount of analog and digital channels and fast computation times to enable control. Texas Instruments' Delfino microcontroller family offers floating-point performance and analog integration for real-time control applications, making the family an ideal product to use for the UIFESS.

5.4.2 Stabilization Bearing Microcontroller

Based on requirements below, the TMS320F28335 microcontroller from Texas Instruments' Delfino microcontroller family is selected to enable control of the stabilization bearing. The Experimenter Kit, shown in Figure 5.17, is used to aid in programming and accessing the microcontroller pins[35]. The microcontroller is programmed using Texas Instrument's Code Composer Studio.

Analog Requirements The stabilization bearing only has four coils to use for maintaining the sensed air gap at the top of the rotor, so four currents are monitored using analog inputs. In addition, two displacement sensors are also monitored. A

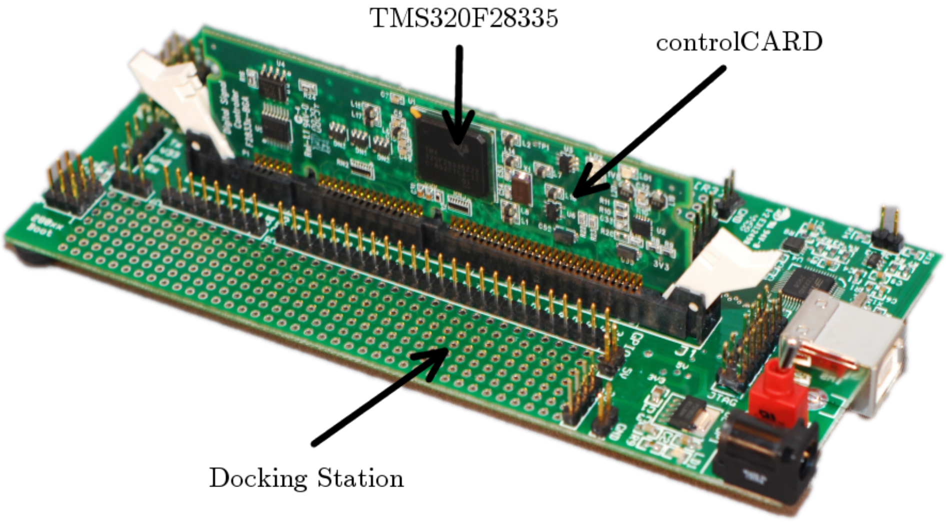

Figure 5.17: TMS320F28335 Experimenter Kit [35]

minimal control scheme uses 6 ADC channels, see Table 5.4. Since 16 channels are available, it is decided to read each analog sensor using two ADC channels, for a total 12 channels. The tests conducted on the SASB and the AMB of the UIFESS are conducted in this manner. The readings are averaged together to obtain a more accurate value. Additional ADC channels could be used to oversample the analog sensors, but the increased sample time may reduce performance.

Table 5.4: TMS320F28335 Delfino Microcontroller I/O Requirements for Stabilization Bearing Control[36]

Specification	Available	Minimal Control	Optimized Control
Digital I/O	88	4	24
12-bit ADC	16	6	16

Digital Requirements Each coil requires its own full bridge DC-DC converter. For minimal control, a single digital output pin is required to interface with each Full-Bridge DC-DC converter direction, DIR, pin. The PWMH and PWML pins would be tied to +5 V, and the converter would drive the current using locked-antiphase operation. This will provide control of coil current magnitude and direction. Optimized control would interface with all six of the converter digital pins. The microcontroller features are presented in Table 5.5.

Table 5.5: TMS320F28335 Delfino Microcontroller Features[36]

Feature	
CPU	C28x, 32-Bit DSC, FPU
CPU Frequency	150 MHz (6.67 ns Cycle Time)
RAM	68 KB
Flash	512 KB
Digital I/O	3.3 V
Digital I/O pins	88 General Purpose I/O (shared)
12-Bit ADC	16 Channel
ADC Conversion Time	80 ns
ADC Conversion Type	Single or Simultaneous

5.4.3 Self-Bearing FRRM Microcontroller

Based on the requirements below, the Texas Instrument TMS320F28377D is selected to enable self-bearing FRRM rotation and control. The TMS320F28377D is also from the Delfino family of microcontrollers, but has a dual core processor with additional integrated analog features[37]. Due to time constraints, the F28377D Delfino Experimenter Kit shown in Figure 5.18 is purchased, but not programmed or utilized in any testing [38]. The microcontroller uses Texas Instrument's Code Composer Studio.

Analog Requirements The FRRM has 24 coils that must be used for rotation and control. Each of these coil currents must be monitored and requires an analog channel. Additionally, two displacement sensors are also monitored with analog channels. This requires 26 analog channels. A multiplexer, or mux, is considered to interface the microcontroller with all the necessary analog sensors. A total of 26 analog channels is required for rotation and control. However, due to the high expected number of current control algorithms to be run, it is logical to use a separate microcontroller to obtain the x-axis and y-axis displacement readings. These readings are sent to the main

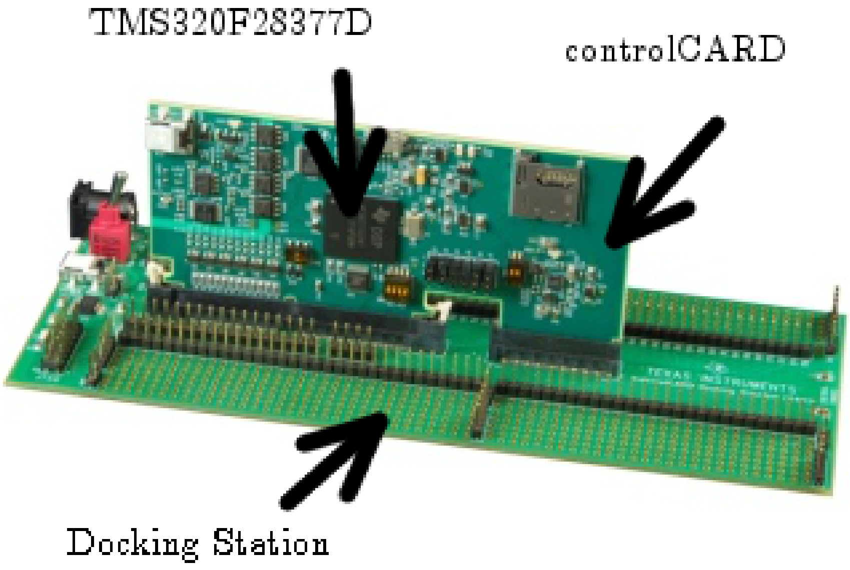

Figure 5.18: F28377D Delfino Experimenter Kit [38]

microcontroller using 12 digital lines in parallel. A proposed solution is given in Section 8.2.3. The microcontroller features are summarized in Table 5.6.

Table 5.6: TMS320F28377D Delfino Microcontroller Features[37]

Feature	
CPU	Dual C28x, 32-Bit DSC, FPU
CPU Frequency	200 MHz (5-ns Cycle Time)
SRAM	204 KB
Flash	1024 KB
Digital I/O	3.3V
Digital I/O pins	169 General Purpose I/O (shared)
12-Bit ADC	24 Channel
ADC Conversion Time	286ns
ADC Conversion Type	Single or 4 Simultaneous

Digital Requirements Each coil requires its own full bridge DC-DC converter. For minimal control, a single digital output pin is required to interface with each Full-Bridge DC-DC converter direction, DIR, pin. The PWMH and PWML pins would be tied to +5V, and the converter would drive the current using locked-antiphase operation. This will provide control of coil current magnitude and direction. The proposed parallel communication channel requires 12 digital pins and 2 handshaking pins. Additional digital input pins would be required for each rotational sensor used in the UIFESS. Rotational sensor specifics have not been defined. It is assumed that 2 rotational sensors are used. The total digital pins required include 2 rotational sensor pins, 12 parallel communication pins, 2 handshaking pins, and 24 DIR pins for each power amplifier, resulting in 40 pins.

Optimized control would interface with all six of the converter digital pins. This results in 144 pins for the power amplifiers, 12 parallel communication pins, 2 handshaking pins, and 2 rotational sensor pins, a grand total of 160 pins. The microcontroller I/O requirements are summarized in Table 5.7.

Table 5.7: TMS320F28377D Delfino Microcontroller I/O Requirements for the Self-Bearing FRRM Rotation and Air Gap Control[37]

Specification	Available	Minimal Control	Optimized Control
Digital I/O	97	40	160
12-bit ADC	24	24	24

5.4.4 UIFESS Custom Printed Circuit Boards

The UIFESS power electronic components are interfaced with custom designed Printed Circuit Boards (PCBs). Specifics of these PCBs are discussed in Section 6.3.

5.4.5 Proposed Power Electronic Hardware Setup

The major hardware components required for air gap control and flywheel rotation are shown in Figure 5.19. The UIFESS project has all the required hardware to conduct a full rotational test. However, unresolved issues with the High Temperature Superconductors (HTS) made levitation of the flywheel not possible by Spring 2014. A first pass at developing the rotational algorithm is discussed in Kisling[12]. Due to time constraints, the rotation algorithm was not coded or tested. Air gap control using the

SB is successfully demonstrated using the TMS320F28335 and the UIFESS Driver Version 1 PCB. The PCB design is discussed in 6.3.3.2.

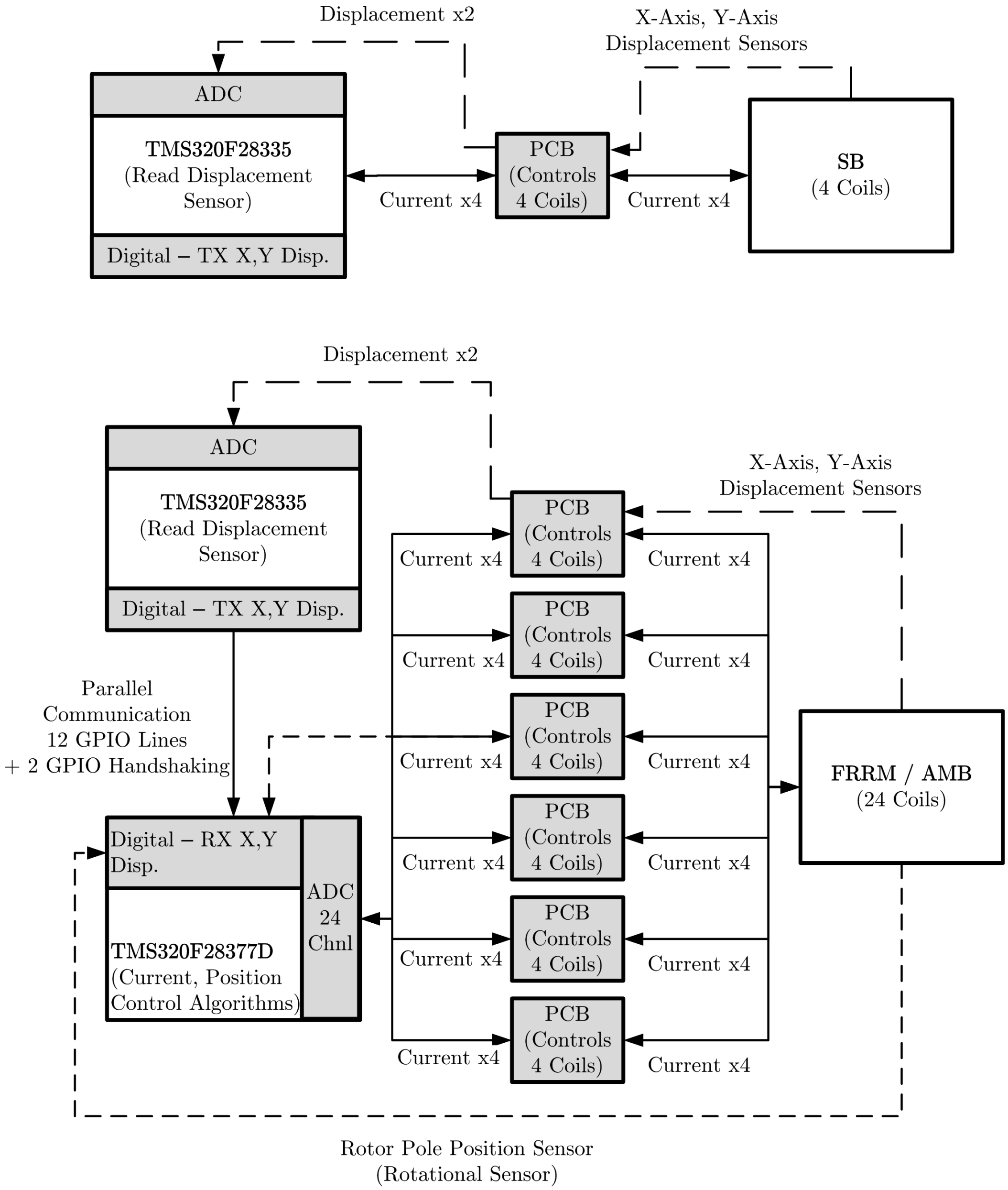

Figure 5.19: Proposed UIFESS Power Electronic Hardware Setup

Chapter 6

Signal Conditioning and PCB Design

6.1 Introduction

The number of sensors, Full-Bridge DC-DC converters, analog and digital connections, and microcontrollers required makes hardware implementation a non-trivial issue. Preservation of the analog sensor data is of utmost importance. The control system requires feedback that reflects an accurate portrayal of what is truly happening in the system for successful and robust control. It is decided to design and fabricate printed circuit boards to optimize successful control.

This chapter addresses the design considerations and methodology for designing analog sensor signal conditioning topologies. These topologies will filter, shift, and scale the displacement sensor and current sensor output voltages to levels that are read by the microcontroller analog to digital converter (ADC).

Printed circuit boards (PCBs) are designed to interface displacement and current sensor outputs with signal conditioning topologies and the microcontroller ADC. In addition, the power amplifiers also connect to the PCB. The PCB also includes logic level shifting components to enable communication between the microcontroller and the power amplifier. The main function of the UIFESS PCBs is to serve as a convenient interface between the microcontroller, sensors, and coils. Major connections between the controller, coils, and various sensors are displayed in Figure 6.1. The entire flywheel control hardware system comprises of two microcontrollers, four horizontal displacement sensors, 28 current sensors, 28 Full-Bridge DC-DC Converters, and rotor rotation sensors. The entire power electronic hardware setup is shown in Figure 5.19.

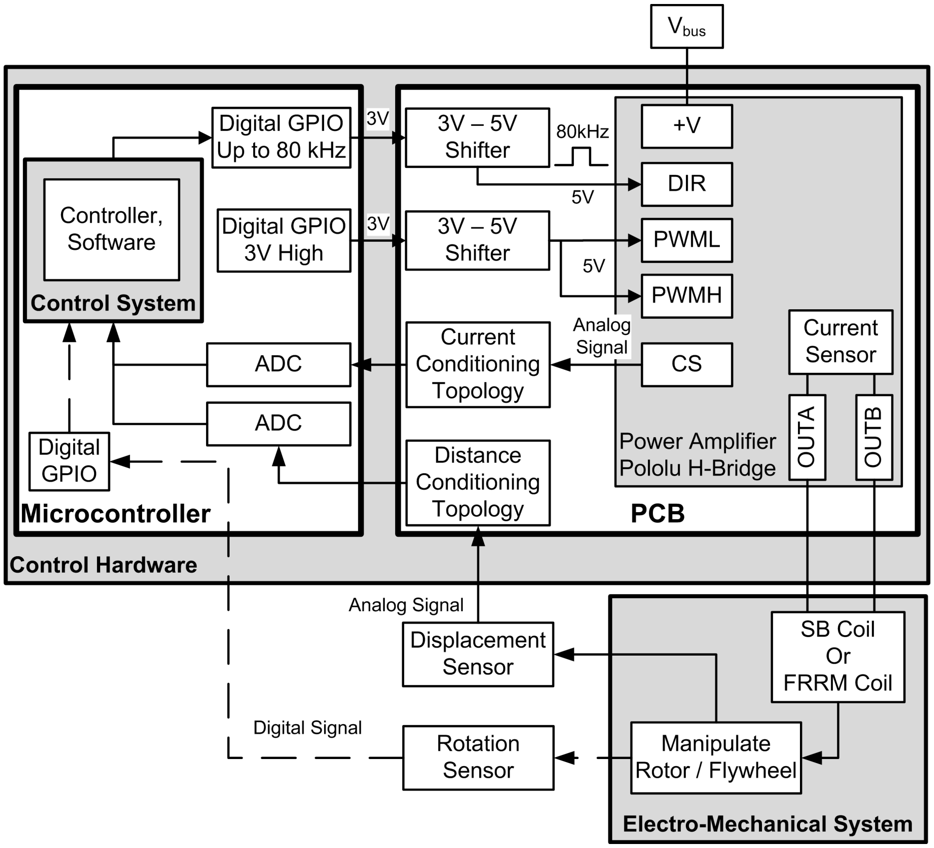

Figure 6.1: Block Diagram of PCB Interface and Connections

6.2 Sensor Signal Conditioning

The UIFESS control hardware contains two analog sensor types. The Hall Effect-Based Linear Current Sensor is an analog sensor that is located on the commercial Full-Bridge DC-DC converter, discussed in Section 5.3.3. There are 28 of these sensors responsible for sensing the current in each coil of the UIFESS. The Kaman horizontal displacement sensor, discussed in Section 5.3.2, is an analog sensor responsible for sensing the change in rotor position, allowing determination of the air gap.

The microcontroller analog to digital converter (ADC) can only read voltages up to 3 V. Attempting to use the ADC to read voltages above 3 V causes inaccurate ADC readings or damage the microcontroller[39]. Each of these linear sensors outputs a voltage that is proportional to the phenomena being sensed. Each sensor is capable of outputting a voltage over 3 V, so a solution is required to properly scale the output voltages to a level the microcontroller ADC can read and use as inputs for the control algorithm.

When scaling a voltage, one may conclude a simple voltage divider would suffice. Though this would scale the voltage down, the ADC has its own impedance which would affect the voltage divider, and introduce significant error in the reading. A voltage divider is not a solution to shifting the voltage level.

Common practice involves adding an operational amplifier (op-amp) for signal conditioning and buffering [39]. The sensor output would be sent through the op-amp circuit for scaling, shifting, and buffering before being sampled by the ADC.

The op-amp is an ideal device to use since it features an extremely large input impedance. Care must be taken when selecting external resistors for various shifting and scaling topologies. Depending on the topology, the external resistances determine the input resistance, and an appropriate current is drawn. If designed properly, the op-amp topology does not load the sensor output, and the signal integrity is maintained. The op-amp output can be modeled as a low-impedance source, and charges the ADC sampling capacitor [39]. The low-impedance op-amp output will not load the ADC, and signal integrity is maintained, and successful ADC sampling can occur.

Op-Amp Investigation A specific op-amp is required to implement a circuit capable of shifting and scaling the sensor data. An initial parts search yielded Texas Instrument's LM318 High-Speed Operational Amplifier. The LM318 has a slew rate of 70 V/μs, which is very high [40]. The slew rate measures how quickly the op-amp would be able to change its output voltage. Initially, it was thought that any amount of significant delay would compromise the horizontal displacement sensors' ability to accurately determine the air gap when rotating. Timing specific microcontroller actions and functions had not been done at this time, so it was unsure what speed was needed, so one of the High-Speed Op-Amps were investigated to see its limitations.

Samples of the LM318 are obtained and breadboarded to further investigate the device. Implementation is difficult and unsuccessful. The high slew rate made the device rather unstable, and test voltages at expected sensor frequencies show the output is not representative of the input. The LM318 is not practical for UIFESS applications, and another solution is needed.

A professor mentoring the project recommended Texas Instrument's OPA277 or TI's INA129 Instrumentation Amplifier. The professor feels their specifications are appropriate for the application.

OPA277 High Precision Operational Amplifier The OPA277 High Precision Operational Amplifier has a slew rate of 0.8 V/μs, so it is considerably slower than the LM318. However, the maximum change the output voltage would be required to do is 3 V, but a step change in the actual distance or current would not occur during normal operation of the UIFESS. Even if a step change needed to be detected, Equation (6.1) shows how long it would take the OPA277 to reflect the step change.

$$Time_{StepChange} = \frac{3V}{0.8\frac{V}{\mu s}} = 3.75\mu s \tag{6.1}$$

The microcontroller will be sampling the current at an 80 kHz rate, which is every 12.5 μs and the position is sampled at a 10 kHz rate, which is every 100 μs[12]. If the sampling does occur when the op-amp output is attempting to catch up to the phenomena it is monitoring, the microcontroller does not have an accurate representation of the system for one control cycle. The control algorithm needs to be robust enough to correct for this once the next sample is taken.

The OPA277 requires a dual power supply for operation. It is decided to not pursue single supply op-amps, to ensure the output could be driven all the way down to ground if needed. It is desired to ensure the entire sensor output range is appropriately shifted.

The OPA277 also features a common-mode rejection ratio (CMRR) of 140 dB. CMRR measures an op-amp's ability to block undesired signals that are present on both the positive and negative input terminals. The OPA277 comes in a variety of surface mount packages, including a single, dual, or quad op-amp package.

INA129 Instrumentation Amplifier Typical instrumentation amplifiers (in-amp) are constructed of three op-amps, see Figure 6.2. The positive and the negative terminals of the device each feature a buffer op-amp that passes the common-mode signal through at a unity gain. However, the signal is amplified. Both buffers are then connected to a subtractor or difference amplifier. The difference amplifier will amplify the differential signal while the common-mode voltage is heavily attenuated[41]. For the INA129, the differential signal gain is set by an external resistor value, shown as R_G in Figure 6.2 [42].

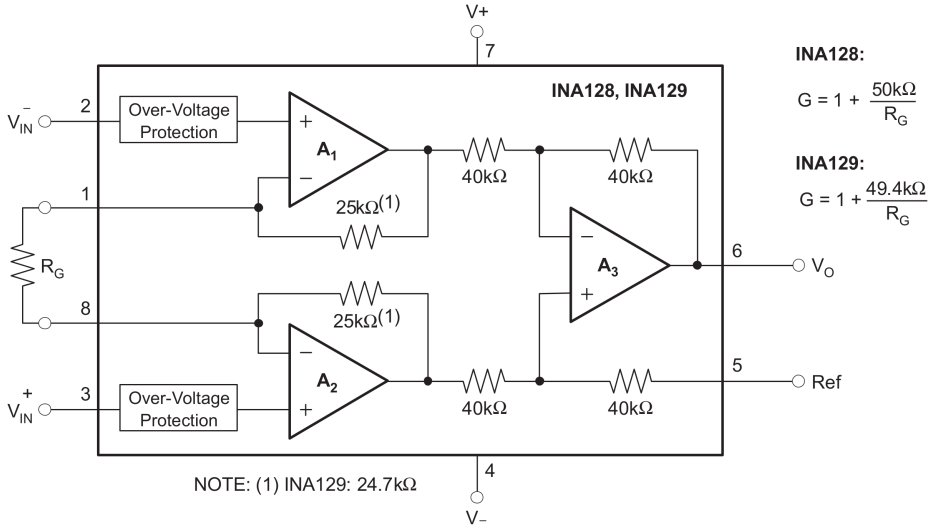

Figure 6.2: INA129 Instrumentation Amplifier Block Diagram [42]

The in-amp is suited for detecting small signals which must use long transmission lines[43]. The main advantage of the in-amp is the fact that it amplifies the difference between its input terminals while rejecting signals common to both input terminals [41]. This essentially means that the desired sensor signal will be passed and amplified, if desired, and noise picked up along the path from the sensor to the in-amp is cancelled out. This makes the INA129 ideal for shifting and scaling sensor signals.

The INA129 requires a dual power supply for operation. It features a CMRR of at least 120 dB. The slew rate is 4 V/μs, so the in-amp output will be able to adjust its output quickly enough to keep pace with even the largest sensor changes. In-amps are more stable when compared to op-amps [44]. The cost of the INA129 is considerably more than the cost of a typical op-amp, but offers better performance.

6.2.1 Distance Sensor Output Signal Conditioning

The displacement sensor is discussed in detail in Section 5.3.2. The displacement measurement used to determine the air gap between the rotor and the stator is a crucial measurement to successfully operate the UIFESS. The displacement is sampled at a 10 kHz rate, compared to the coil current sampling rate of 80 kHz. The distance sensor is sampled less, so it is desired to obtain the best possible representation of the air gap to give the control algorithm the best chance of success. The desire for the best possible representation of the air gap means the INA129 Instrumentation Amplifier should be the main product used in the conditioning of the displacement sensor output.

The Kaman eddy current sensor outputs a voltage that ranges from approximately 0-10 V for a displacement of 0-3 mm. This output is too large for the ADC. It is desired to scale the output voltage so that the ADC will see a 0-3 V signal for a displacement of 0-3 mm.

Consider Kaman non-contact displacement sensor #1. Additional money was spent to have the sensors factory calibrated over a 0-3 mm range with a target of 303 Stainless Steel. The factory calibration for Kaman displacement sensor #1 is shown in Table 6.1. The factory calibration is plotted to see the linear relationship between displacement and output voltage, as shown in Figure 6.3. The linear equation associated with the factory calibration is shown in Equation (6.2).

Distance [mm]	Output [V]
0	-.008
0.3	.982
0.6	1.988
0.9	2.999
1.2	4.008
1.5	5.011
1.8	6.009
2.1	7.005
2.4	8.004
2.7	9.012
3	10.041

Table 6.1: Kaman Displacement Sensor #1 Factory Calibration

$$Displacement[mm] = 0.298841 \left[\frac{mm}{V}\right] Kaman_{Output}[V] + 4.411644 \cdot 10^{-3}[mm] \qquad (6.2)$$

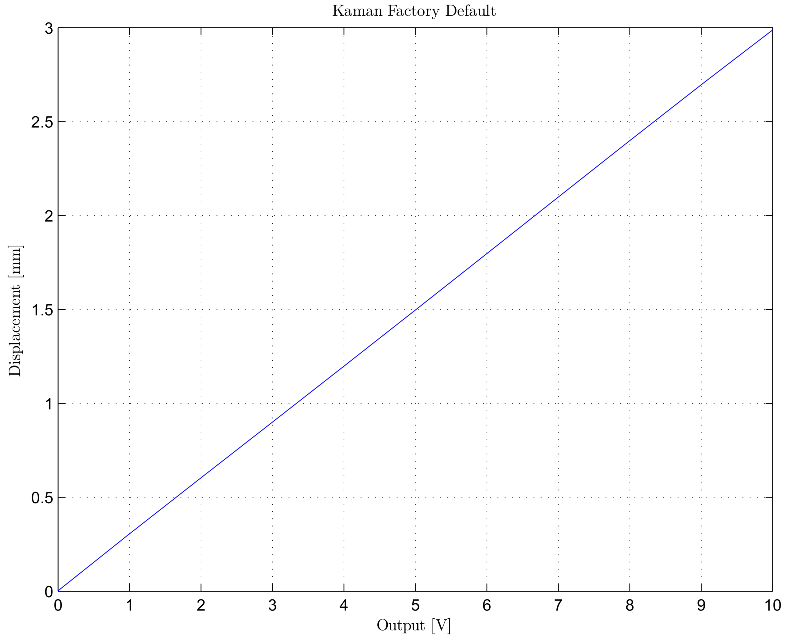

Figure 6.3: Kaman Displacement Sensor #1 Factory Calibrated Linear Relationship

The INA129 Instrumentation Amplifier is used for scaling the voltage. High frequency noise, such as noise beyond 1 MHz, can be introduced in the connections from the sensor to the in-amp. In-amps have a difficult time dealing attenuating the high frequency noise. Many datasheets, including the INA129, do not specify a CMRR above 1 MHz [44]. The in-amp may distort the high frequency signals as they pass through, and as a consequence, introduce lower-frequency noise in the frequency range of interest, or present itself as a DC-offset error[43][44].

To reduce the effects of high frequency noise, a low-pass filter should be added to the front end of the in-amp. This will attenuate the high frequency voltages before they reach the in-amp[43][44].

A cutoff frequency for the low-pass filter is chosen. The displacement sensor will be sampled at a 10 kHz rate. According to the Nyquist Theorem or Shannon Theorem, harmonic signals cannot be reconstructed properly if sampled at a rate lower than twice the signal frequency[18]. For a 10 kHz sample rate, only rotor oscillations of 5 kHz or less will be accurately represented. The rotor is a slow moving system, since the rotor has a significant amount of inertia to overcome before significant movement capable of affecting controller performance would be present. Any useful information regarding the rotor movement will be contained below 5 kHz. For this reason, a low-pass filter cutoff frequency of 5 kHz was selected. A digital filter will be added to the software[12]. With this additional filtering, a first-order analog filter suffices. A first or second order analog filter is typically acceptable[18]. A single-order low pass filter topology[43][44] is shown in Figure 6.4.

Resistors, R, add noise, and keeping the resistor value smaller will introduce less noise[44]. The differential capacitor, C_d, is chosen to set the differential filter cutoff slightly higher than the signal of interest. The differential cutoff frequency is calculated as shown in Equation (6.3). The common-mode capacitors, C_C, match each other very closely to keep each terminal of the in-amp as closely matched as possible. Choose a R and C_C ratio to attenuate the desired frequencies, shown in Equation (6.4). A rule of thumb says the common-mode capacitors should be one tenth the differential capacitor value, as shown

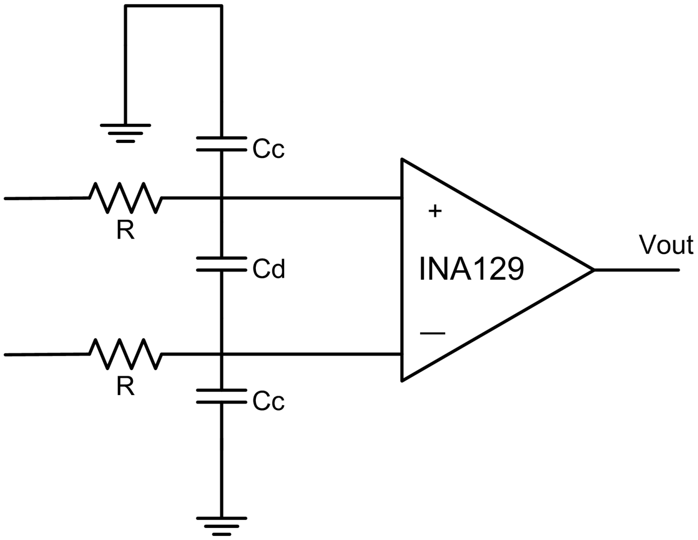

Figure 6.4: In-Amp First-Order Low Pass Filter

in Equation (6.5)[44].

$$Cutoff_{Differential} = \frac{1}{2\pi R(2C_d + C_C)} \tag{6.3}$$

$$Cutoff_{Common-Mode} = \frac{1}{2\pi RC_C} \tag{6.4}$$

$$C_C = C_d(\frac{1}{10}) \tag{6.5}$$

The following values and theoretical cutoff frequencies are selected and displayed in Table 6.2. The differential cutoff frequency is slightly above 5 kHz, which is the maximum frequency that is accurately represented with a 10 kHz sample rate.

Table 6.2: In-Amp Low Pass Filter Values

Component	Value
R	1.5 $k\Omega$
C_D	10 nF
C_C	1 nF
$Cutoff_{Differential}$	5.053 kHz
$Cutoff_{Common-Mode}$	106.103 kHz

In addition, the INA129 requires an input bias current return path. The inputs are high impedance, but approximately ±2 nA will need flow in each terminal. A common solution calls for adding a resistance to ground path on each terminal to give the bias current a path to return to ground[42]. A complete topology, including the component values to be used, is shown in Figure 6.5. An in-amp building block has been developed that will attenuate the high, unwanted frequencies and provides a path for the bias current to flow.

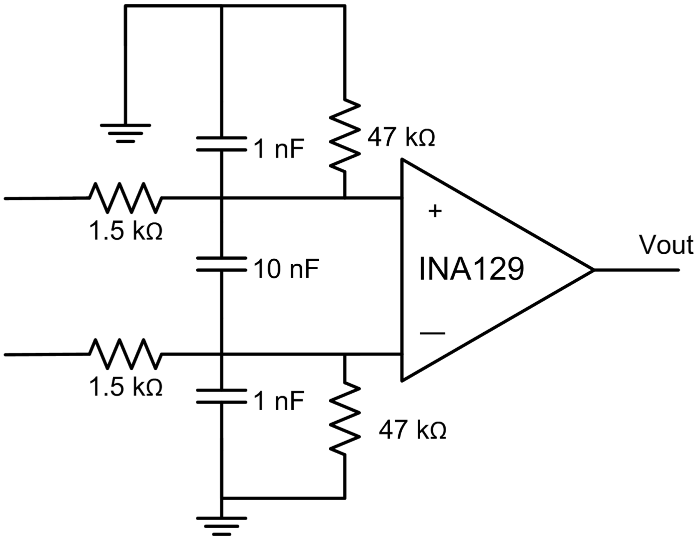

Figure 6.5: In-Amp Low Pass Filter with Bias Current Path

6.2.1.1 Full Range Displacement Sensor Topology

It is desired to scale the displacement sensor output so the microcontroller ADC can sense rotor position over the entire 3 mm sensor range. The Kaman displacement sensor outputs 10.8 V when the target is greater than 3 mm away. The distance sensor may be powered on when the target is not in place, so this large voltage could be present at the sensor outputs for a substantial time. The topology must step this 10.8 V down to 3 V to be successfully read by the microcontroller ADC.

The INA129 does not have the ability to create a gain less than 1. A topology containing cascaded op-amps and in-amps is utilized. The first stage is responsible for scaling the voltage down, and the second stage can contain the in-amp for filtering and common-mode rejection, as shown in Figure 6.6.

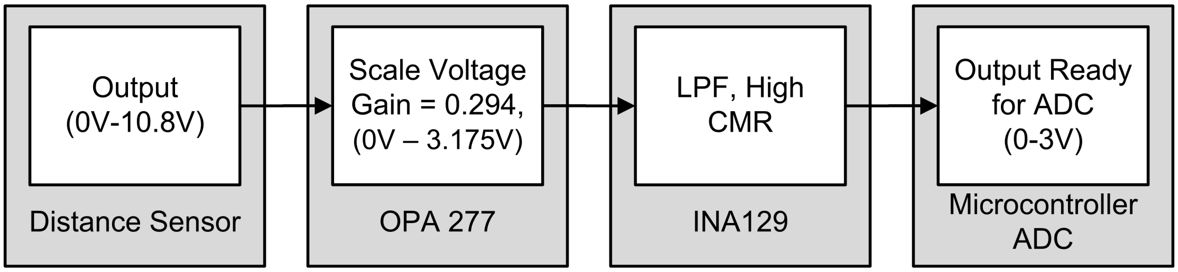

Figure 6.6: Full Range Displacement Sensor Topology Block Diagram

The first stage requires a method of stepping the voltage down. The simplest solution uses a voltage divider to obtain a gain of less than one, and buffers the voltage using a voltage follower or unity buffer amplifier. Both voltage divider resistors determine the input impedance. The first stage can use the OPA277 for the voltage follower. The voltage divider resistances selected are used in Equation (6.6). These resistor values result in gain shown in Equation (6.7).

$$V_{Div} = 10.8V \frac{100\,k\Omega}{(100\,k\Omega + 240\,k\Omega)} = 3.176\,V \tag{6.6}$$

$$Gain_{FullDistanceDesired} = \frac{100\,k\Omega}{(100\,k\Omega + 240\,k\Omega)} = 0.294\,\frac{V}{V} \tag{6.7}$$

Note the scaled voltage is slightly over 3 V. The microcontroller ADC can handle voltages up to 3.3 V before sampling accuracy is affected[39]. This value can be sampled by the ADC and will not introduce any accuracy issues. The INA129 will not have a gain resistor in place so the voltage present at its terminals will not be amplified.

Circuit Simulation Texas Instrument's TINA-TI is a circuit design and simulation tool. This SPICE-Based Analog Simulation Program allows users to bring in specific TI parts to simulate a design before investing time and money in purchasing parts, breadboarding, and PCB fabrication. The simulations in this thesis are conducted using Version 9.3.50.40 of the TINA-TI software.

The block diagram from Figure 6.6 is realized in schematic form using the simulation software, as shown in Figure 6.7. The frequency sweep result using the AC transfer characteristic simulator is shown in Figure 6.8. The low pass filter passband shows a gain of -10.9 dB, which is approximately a gain of 0.2851 V/V, which is a near match for the desired gain in Equation (6.7). The cutoff frequency, or 3 db-down point, of the low pass filter is approximately 5 kHz, the desired frequency dictated by the ADC sample rate.

$$Gain_{FullDistanceSimulated} = -10.9\,dB = 0.2851\,\frac{V}{V} \tag{6.8}$$

The topology should scale the distance sensor voltage to a level that is safe for the microcontroller ADC. The topology attenuates high frequency voltages, which reduces the amount of interference the signal encounters.

After the signal passes through this topology, it is sampled by the microcontroller ADC. A new linear equation is needed to convert the sampled voltage back into a displacement distance in millimeters.

Recall Equation (6.2) shows the linear relationship for displacement and output voltage. The gain from Equation (6.7) will scale the output voltage from the Kaman sensor to a level for ADC sampling, shown in Equation (6.9), where $Gain_{FullDistance}$ is a general gain term for the Full Range Distance topology.

$$Kaman_{Output}[V] = \frac{ADC_{DistFullRange}[V]}{Gain_{FullDistance}} \tag{6.9}$$

A general equation to relate the displacement to the ADC reading is required. Substitute Equation (6.9) into Equation (6.2) to obtain the linear relationship to turn the ADC voltage reading into a displacement measurement, Equation (6.10). Results of implementing the design on a PCB are given in Section 7.2.1.1.

$$Displacement[mm] = \frac{0.298841\left[\frac{mm}{V}\right]}{Gain_{FullDistance}} ADC_{DistFullRange}[V] + 4.411644 * 10^{-3}[mm] \tag{6.10}$$

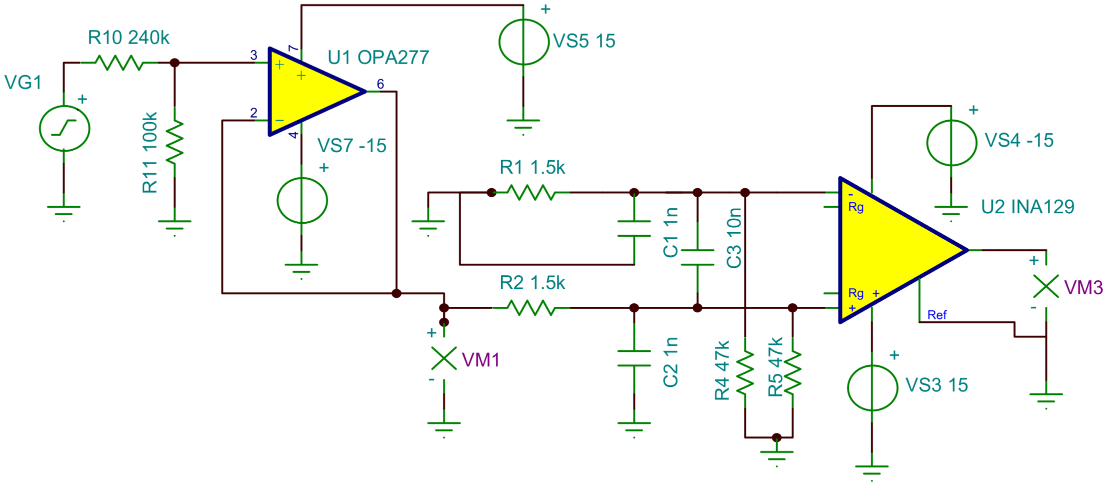

Figure 6.7: Full Range Displacement Sensor Topology Schematic

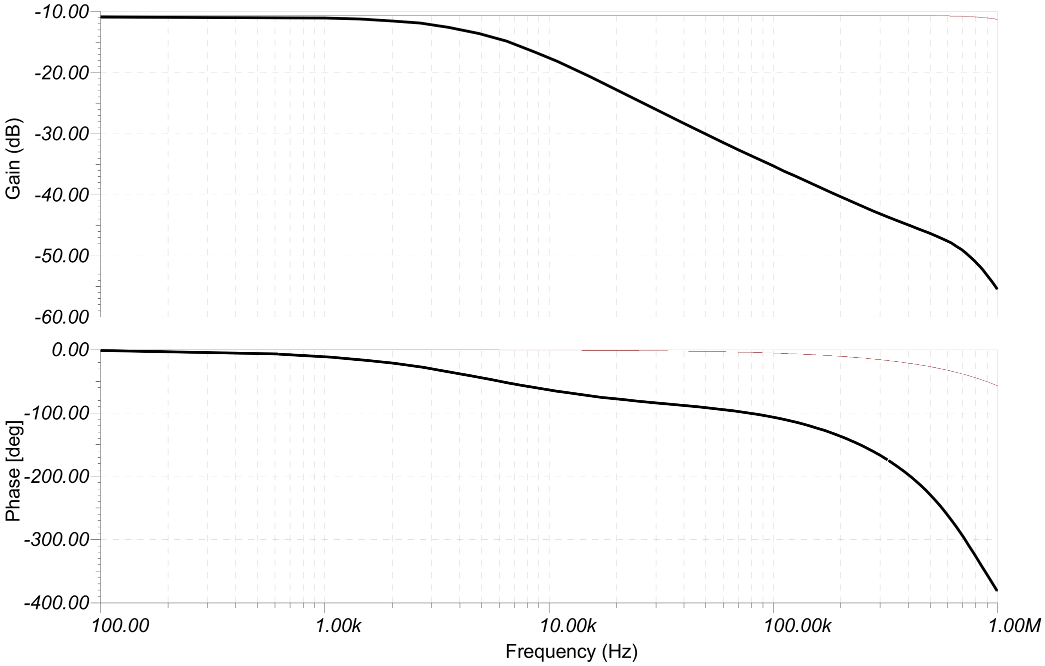

Figure 6.8: Full Range Displacement Sensor Topology Schematic

6.2.1.2 Short Range Displacement Sensor Topology

Concerns existed about the displacement sensor resolution if the full displacement range is used. A second topology is designed that was capable of sensing only a 0.5 mm range. This short range distance sensor topology is only capable of outputting ADC level voltages for displacements from 0.75 mm to 1.25 mm. A similar low-pass filter topology with level shifting is used. If the shifting topology received power, but the displacement sensor is not turned on, a large negative voltage would be maintained at the output of this topology, damaging the microcontroller ADC. In order to ensure this did not occur, a diode clamp circuit was placed on the output to ensure the output did not drop below 0 V or rise above 3 V. See the circuit topology in Figure 6.9.

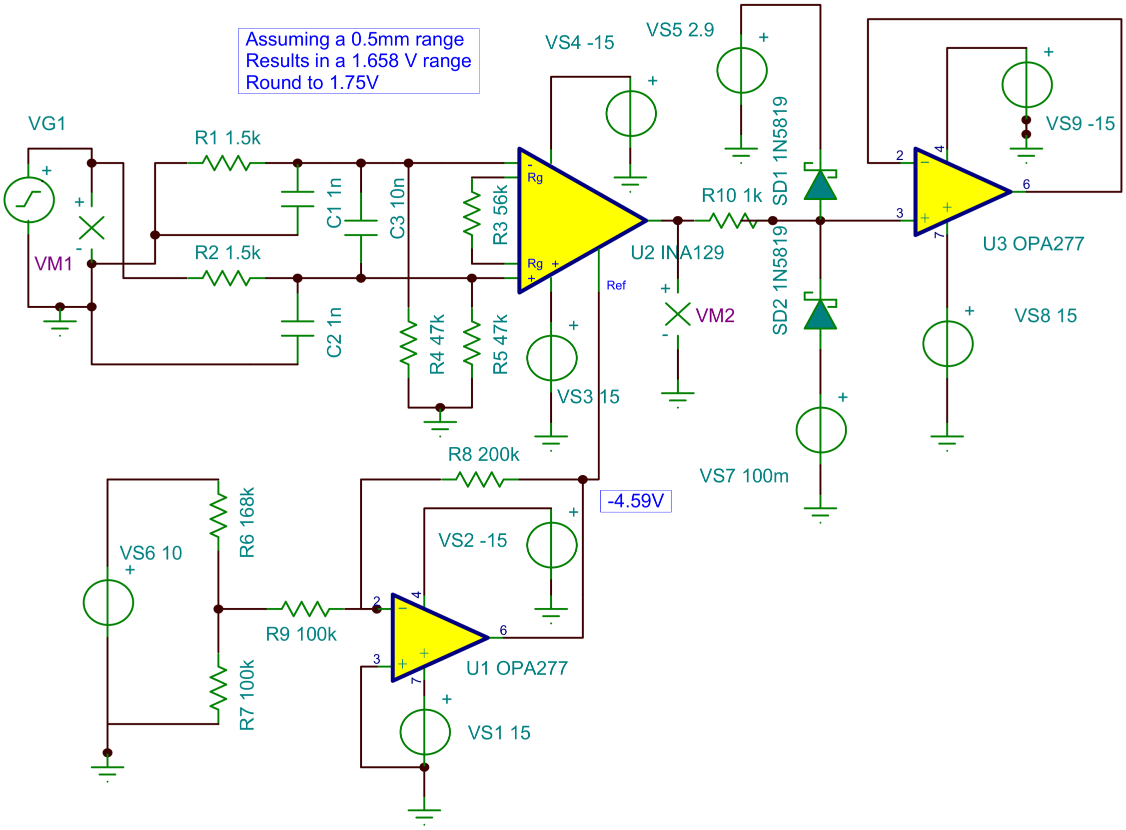

Assuming a 0.5mm range
Results in a 1.658 V range
Round to 1.75V

Figure 6.9: Short-Range Displacement Sensor Signal Conditioning Topology

Circuit Simulation TINA-TI was again used to simulate the circuit. Note the additional hardware required to shift the voltage and the diodes required to protect the ADC from extended periods of out-of-range voltages. Figure 6.9 shows the short-range distance sensor signal conditioning topology. Results of implementing the design on a PCB are given in Section 7.2.1.2.

6.2.2 Current Sensor Output Signal Conditioning

The current sensor is discussed in detail in Section 5.3.3. Recall the current sensor is an IC device on a commercial Full-Bridge DC-DC converter. The coil current is sampled at an 80 kHz rate. The current is sampled more often than the displacement sensor, and the current reading does not have to be as precise as the distance measurement. A smaller error in the current does not have as large an effect when compared to a small error in the displacement. It is decided that two topologies should be tested, one topology capable of better performance using the INA129, and the other with the OPA277.

The current sensor is capable of sensing a current from -30 A to 30 A, and outputs a voltage from 0.5 V to 4.5 V. The current and output voltage have a linear relationship due to the Hall sensor circuit. The current sensor claims an output error of 1.5%. The datasheet linear relationship is shown in Equation (6.11)

$$CS_{Output}[V] = 0.66\left[\frac{mV}{A}\right] * I_{Coil}[A] + 2.5[V] \tag{6.11}$$

A single Full-Bridge DC-DC converter was purchased initially, and it was desired to see how well the current sensor operated. The Full-Bridge DC-DC converter is attached to a small load, and the load voltage is adjusted and measured. The corresponding currents are measured by a Tektronix AM503A Current Probe Amplifier. The AM503A also uses the Hall effect to determine the current travelling through a wire. The AM503A contains a probe that clamps around the wire and electronics housed in a separate box amplify the probe output and display the measurement on an oscilloscope [45]. The recorded measurements are shown in Table 6.3, and are plotted in Figure 6.10.

Table 6.3: Recorded Current Sensor Measurements

Current [A]	Output [V]
-4.25	2.2165
-3.875	2.23801
-3.545	2.2619
-3.18	2.2823
-2.88	2.3052
-2.53	2.3281
-2.165	2.3512
2.145	2.6421
2.525	2.6645
2.82	2.684
3.2	2.7059
3.575	2.7232
3.925	2.7436
4.245	2.7635

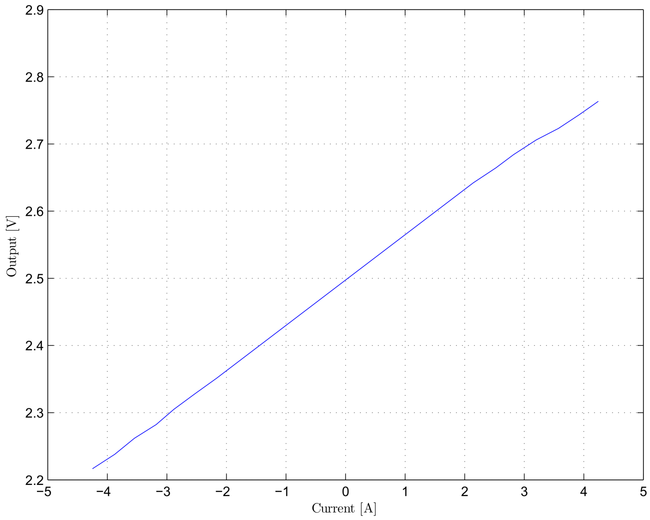

Figure 6.10: Experimentally Derived Current Sensor Verification

The experimentally derived data confirms a linear relationship between the measured current and output voltage. The linear relationship from the experimental results of

Table 6.3 is represented by Equation (6.12).

$$Output[V] = 65.410 \left[\frac{mV}{A}\right] * I_{Coil}[A] + 2.494[V] \tag{6.12}$$

The experimental results represented by Equation (6.12) closely match the current sensor's theoretical output shown in Equation (6.11). The current sensor output is verified, and it is decided the sensor would fulfill the needs of the UIFESS project.

The experimentally obtained data that results in Equation (6.12) is close enough to Equation (6.11) from the datasheet. The equation for shifting and scaling the sensor output is represented by Equation (6.11).

The UIFESS does not experience currents over ±12 A. The vacuum feed-throughs are limited to 12 A, and there are concerns about the winding insulation integrity for currents over 12 A. The current sensor is capable of sensing ±30 A, so the entire sensor range is not needed. It is desired to allow the ADC to read a current range of ±15 A, which will allow sensing in the ±12 A range, plus a small margin. Expected sensor output voltage for the desired current range is represented by Equations (6.13) and (6.14). The output voltages are rounded to 1.5 V and 3.5 V for currents of -15 A and 15 A respectively.

$$Output[V] = 66 \left[\frac{mV}{A}\right] * -15[A] + 2.5[V] = 1.51\,V \tag{6.13}$$

$$Output[V] = 66 \left[\frac{mV}{A}\right] * 15[A] + 2.5[V] = 3.49\,V \tag{6.14}$$

6.2.2.1 In-Amp Current Sensor Topology

The in-amp is the main component for the current sensor shifting and scaling. Developing a topology for the current sensor uses similar principles as stated for the distance sensor topology of Section 6.2.1. The high frequencies are again attenuated [44]. To reduce the effects of high frequency noise, a low pass filter should be added to the front end of the in-amp. This will attenuate the high frequency voltages before they reach the in-amp. A first order filter will be used. A digital filter is not be used on the current sensor readings. A first or second order analog filter is typically acceptable[18].

A cutoff frequency for the low-pass filter must be chosen. The current sensor is sampled at a 80 kHz rate. According to the Nyquist Theorem or Shannon Theorem, harmonic signals cannot be reconstructed properly if sampled at a rate lower than twice the signal frequency. For a 80 kHz sample rate, only current changes of 40 kHz or less will be accurately represented.

A cutoff frequency of around 70 kHz is selected. It is desired to have minimal attenuation up to 40 kHz. The maximum switching frequency the Full Bridge DC-DC converter will experience is 80 kHz, so the current sensor output will have a strong DC component, and contribution from signals up to around 80 kHz.

Using similar logic as presented in Section 6.2.1, the following component values are selected to obtain the cutoff frequency, as shown in Table 6.4 and Figure 6.11.

Table 6.4: In-Amp Low Pass Filter Values for Current Sensor

Component	Value
R	100 Ω
C_D	10 nF
C_C	1 nF
$Cutoff_{Differential}$	75.788 kHz
$Cutoff_{Common-Mode}$	1.592 MHz

The in-amp has a low-pass filter that attenuates frequencies higher than the switching frequency of the current. This ensures high frequency noise does not enter the in-amp, while allowing the frequency range of interest through.

Recall that the current sensor will be outputting a voltage of 1.5 V to 3.5 V for the current ranges expected on the UIFESS. The ADC can only handle voltages up to 3 V, and the current sensor output is not taking advantage of the ADC's ability to read voltages in the 0 V - 1.5 V range.

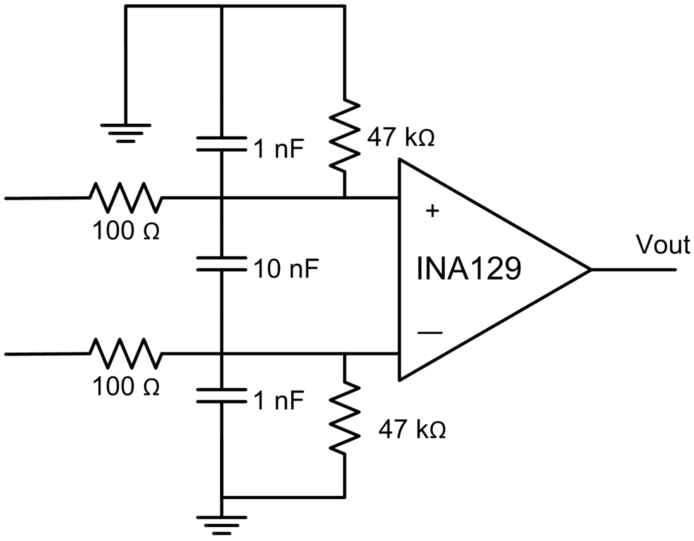

Figure 6.11: In-Amp First Order Low Pass Filter with Bias Current Path for Current Sensor

The current sensor output must be scaled and shifted to take advantage of the ADC's 0 V - 3 V range. See Figure 6.12 for an overview of the shifting and scaling techniques used to prepare the current sensing output for ADC sampling.

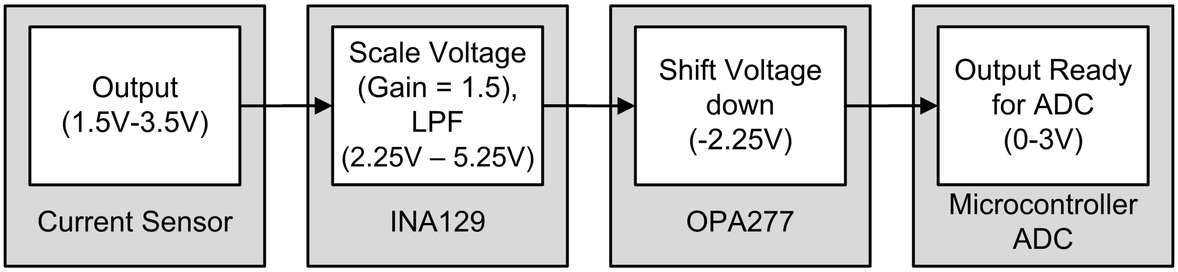

Figure 6.12: Current Sensor In-Amp Topology Block Diagram

A gain is placed on the in-amp to scale the current sensor output. The 2 V range on the current output must be increased to a 3 V range. The desired gain of 1.5 V/V for the circuit is derived using Equation (6.15) and (6.16).

$$2\,V * CurrentSenseGain_{Desired} = 3\,V \tag{6.15}$$

$$CurrentSenseGain_{Desired} = \frac{3\,V}{2\,V} = 1.5\,\frac{V}{V} \tag{6.16}$$

The INA129 can have a gain that ranges from 1 to 10,000 [42]. The gain calculation equation is shown in Equation (6.17).

$$Gain_{INA129} = 1 + \frac{49.4\,k\Omega}{R_G} \tag{6.17}$$

Using standard resistor values, a value of 100 kΩ should be used as the gain resistor to obtain a close match to the desired gain value of Equation (6.16). The theoretical gain of an in-amp with a gain resistance of 100 kΩ is shown in Equation (6.18).

$$Gain_{INA129} = 1 + \frac{49.4\,k\Omega}{100\,k\Omega} = 1.494\,\frac{V}{V} \tag{6.18}$$

The circuit with the gain resistor in place is shown in Figure 6.13. This circuit will now scale the output voltage from a 1.5 V to 3.5 V signal to a 2.25 V to 5.25 V signal.

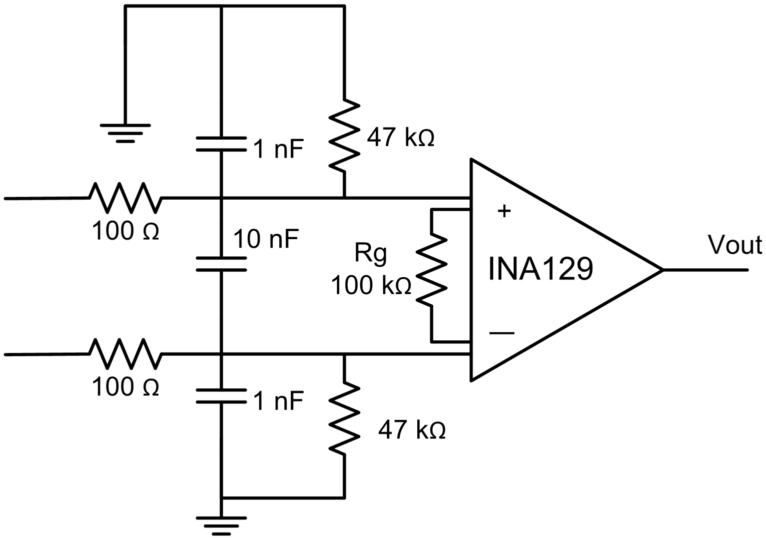

Figure 6.13: Current Sense In-Amp Topology with Gain

This signal must now be shifted to an appropriate level for ADC sampling. The voltage is currently 2.25 V to 5.25 V, which is the desired 3 V range. This range is shifted down to 0 V - 3 V, a shift of -2.25 V.

A 10 V supply is used in the shifting topology. A voltage divider circuit scales the voltage down. This scaled voltage is passed through an inverting op-amp topology. The OPA277 is used in this topology. See Figure 6.14 for the topology.

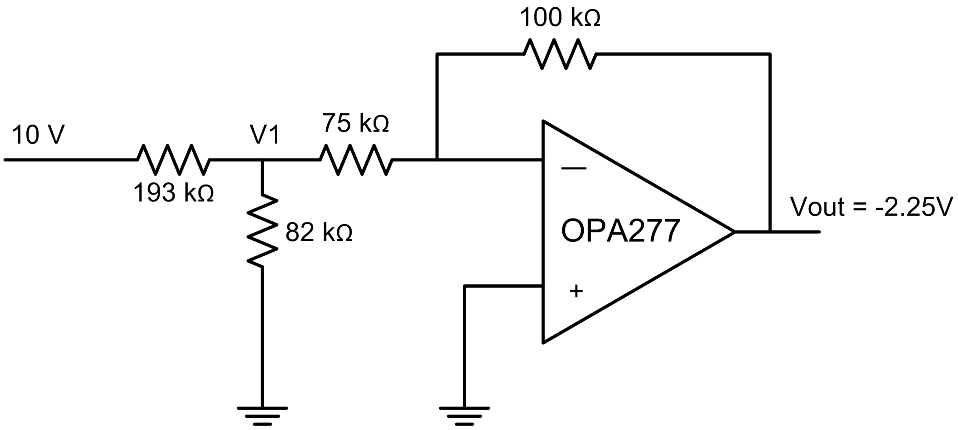

Figure 6.14: Shifting Topology for Use with the In-Amp Current Sensor Topology

Note that the 82 kΩ and the 75 kΩ resistors are in parallel. The equivalent resistance is shown in Equation (6.19).

$$R_{Eq} = \frac{82\,k\Omega * 75\,k\Omega}{82\,k\Omega + 75\,k\Omega} = 39.172\,k\Omega \tag{6.19}$$

Now a voltage divider is formed with R_{Eq} and the 170 kΩ resistor. The voltage V1 is calculated as shown in Equation (6.20).

$$V1 = 10\,V * \frac{R_{Eq}}{R_{Eq} + 193\,k\Omega} = 1.690\,V \tag{6.20}$$

Now a scaled voltage is at the negative input terminal of the inverting op-amp topology. The inverting op-amp gain equation, and the output voltage to be used for shifting, is shown in Equation (6.21).

$$V_{Shift} = -\frac{100\,k\Omega}{75\,k\Omega} * V1 = -2.250\,V \tag{6.21}$$

This shifting voltage is connected to the reference pin on the INA129, and will provide the DC bias to offset the scaled voltage and allow the current sensor to be sampled by the ADC. See Figure 6.15 and Figure 6.16 for the entire circuit and the simulated results.

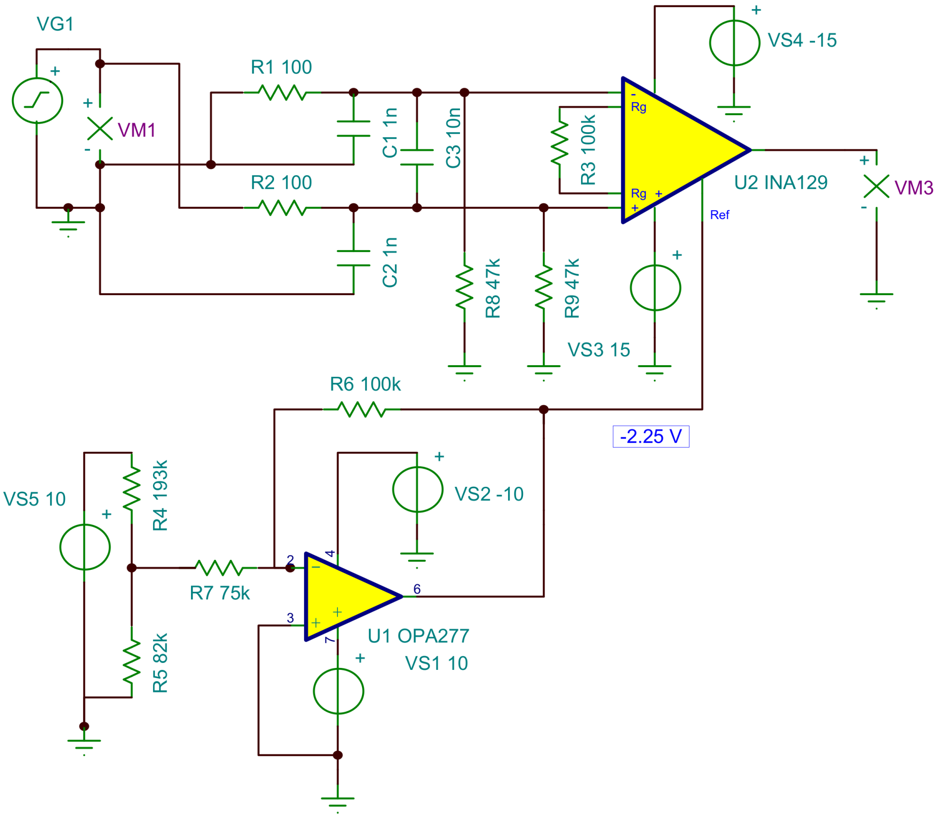

Figure 6.15: Current Sensor Signal Conditioning Topology using the INA129 In-Amp

The simulation results show a gain of 3.47 dB in the passband, which is a magnitude gain of 1.491 V/V, which is close to the desired gain. This is shown in Equation (6.22). Results of implementing the design on a PCB are given in Section 7.2.1.3.

$$Gain_{CurrentSim} = 3.47\,dB = 1.491\,\frac{V}{V} \tag{6.22}$$

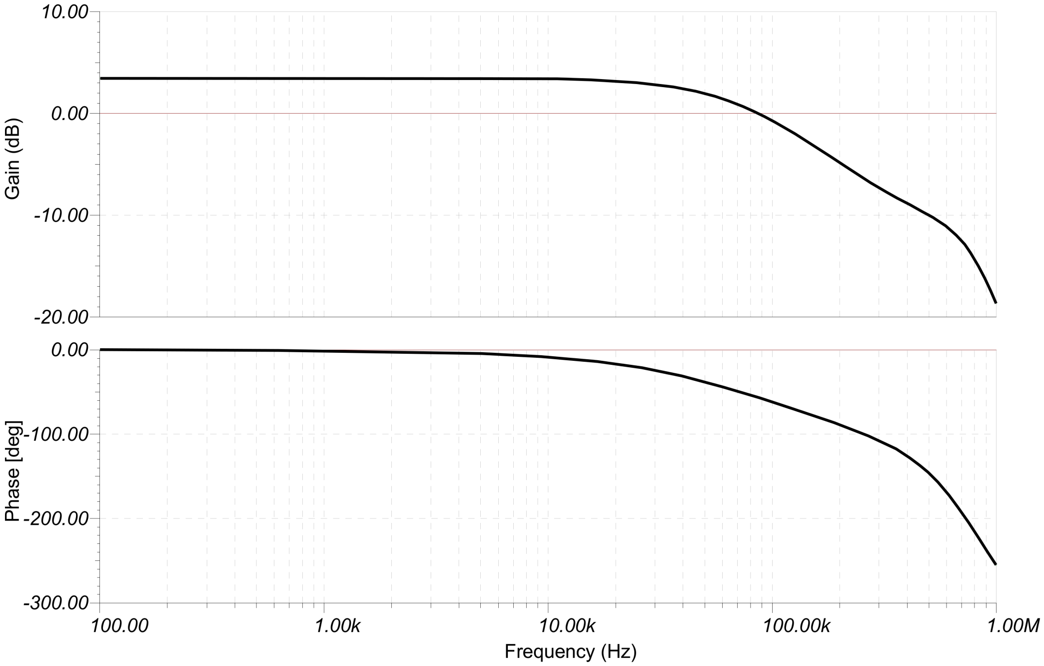

Figure 6.16: Shifting Topology

6.2.2.2 Op-Amp Current Sensor Topology

The INA129 is a fairly expensive IC, and 28 currents require monitoring. A topology using the OPA277 and a Sallen-Key filter topology is designed to see if a cheaper solution exists. The topology is still be responsible for turning the currents in the ±15 A range into a 0 V to 3 V signal to be sampled by the microcontroller ADC.

Simulation Results The TINA-TI software is again used to simulate the op-amp current signal conditioning topology, shown in Figure 6.17. Results of implementing the design on a PCB are given in Section 7.2.1.4.

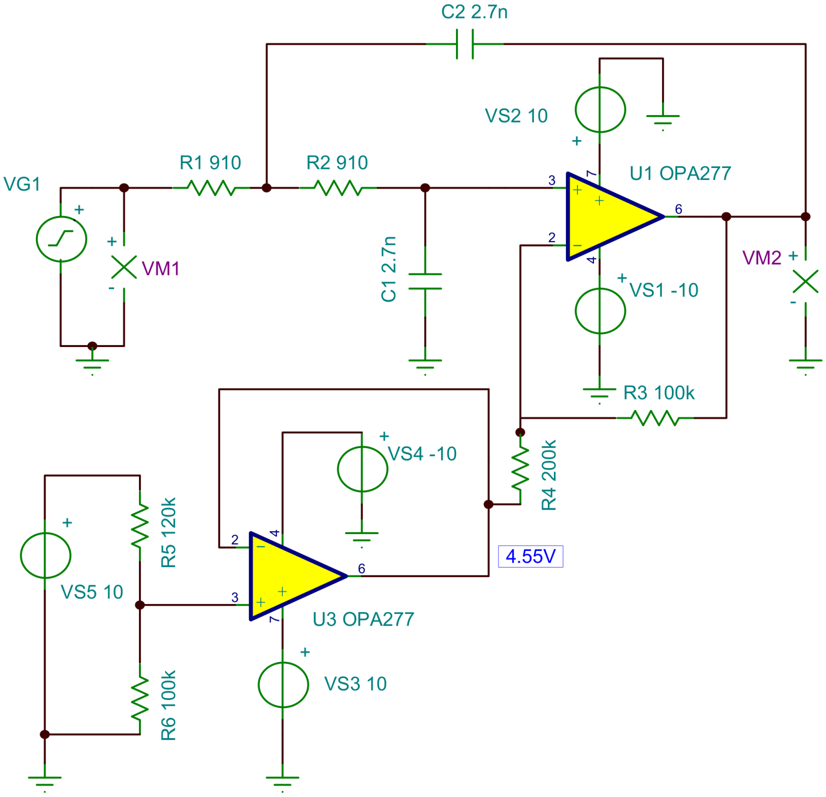

Figure 6.17: Op-Amp Current Sensor Topology

6.3 PCB Design

A Printed Circuit Board (PCB) is an electronic packaging device where electronic components are formed into an electronic system. The PCB structure is typically made out of FR-4, a non-conductive composite of epoxy resin with woven fiberglass reinforcement. Conductive copper foil is electrodeposited onto the FR-4, and etched to create traces according to custom circuit requirements. Components are then added to the PCB to create a final electronic system [46]. Implementing an electronic system by placing components on a PCB is a reliable and cost effective solution, and is widely used. Typical, smaller scale PCB designs can contain 2 to 4 copper layers. Components are placed on the top and bottom of the PCB, using two layers. The components are connected to each other by copper traces. If a 4 layer board is used, the inner layers are typically used for power and ground connections. A via is used to electrically connect inner layers to the other layers of the PCB.

6.3.1 Design Constraints

PCB Fabrication It is decided to use a board-house to manufacture the PCBs. Previous experiences with Advanced Circuits have been positive overall, so it is decided to send the gerber files there for PCB fabrication. Advanced Circuits has special pricing for universities available. Single or multiple quantities of 4-layer PCBs up to 30 in^2 in size can be purchased for \$66 if it is shipped to a university address.

The 30 in^2 size became a design constraint when designing the PCBs. It is determined that 4 commercial Full-Bridge DC-DC converters and the associated signal conditioning could fit on a PCB of this size. The UIFESS requires 24 Full-Bridge DC-DC converters for the self-bearing machine and an additional 4 Full-Bridge DC-DC converters for the stabilization bearing. A minimum of 7 PCBs must be purchased and fabricated. Before investing significant resources, it is desired to apply design principles to a single PCB and ensure a working design is achievable. A Prototype PCB is first fabricated, populated, and tested before making additional board revisions and purchases.

PCB Population Once the PCB is designed, the manufacturing files are sent to the board-house, and a PCB is then shipped to the University. The PCB does not come with any parts on it, shown in Figure 6.18. Populating the PCB is the technique of placing all of the ICs, resistors, capacitors, and other parts on the PCB. Many of these parts are small, surface mount devices. The University of Idaho Electrical and Computer Engineering Department has a small operation capable of populating PCBs. However, the quantities that the UIFESS would require are beyond the ability of the facility.

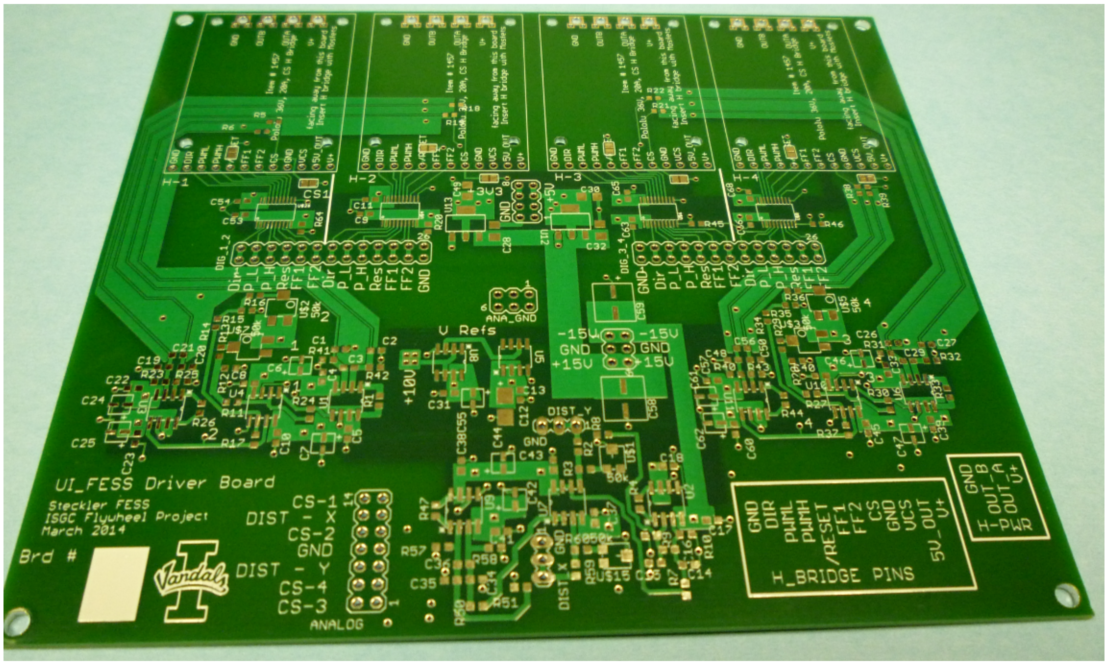

Figure 6.18: A Printed Circuit Board After Boardhouse Fabrication. The PCB is Blank Must be Populated with Components.

Many board-houses offer a population service based on the number of parts per board, and the quantity of boards. After investigation, it is decided that the cost was high enough to investigate an alternate means of populating the PCB.

Investigation found it is possible to reflow solder using an everyday toaster oven. Solder paste can be applied to the pads of the PCB using a syringe-like applicator. The surface mount parts are placed manually using a fine set of tweezers and a microscope to ensure accurate placement. Once the parts are all placed, the toaster oven reflows the solder, and the surface mount parts are attached to the board. The solder reflow setup is shown in Figure 6.19.

Successful reflow of the solder is achieved under the following conditions using a Hamilton Beach Type O47 1050 Watt Toaster Oven. The temperature was set to 300 °F. The PCB with solder paste and surface mount components is loaded and centered in the toaster oven. The oven is then be turned on. After approximately 2 minutes and 30 seconds, the solder begins to wick.

Figure 6.19: Solder Applicator and Solder Reflow Toaster Oven Used for In-House PCB Population

Once the solder begins to wick, its color turns from its usual gray paste appearance into a bright, metallic appearance. Once this transformation occurs, it should be left in the oven for an additional 20 seconds or so, then the toaster oven should be turned off so the board may begin to cool.

The toaster oven does not offer the most ideal solder reflow process. Proper solder reflow calls for ramping the heat applied by a steady amount so the PCB and parts are not warmed up too quickly. The temperature would then be increased substantially, with a quick spike in temperature to initiate solder reflow, then the cool-down process can occur. For the relatively small quantity of boards and parts the UIFESS requires, the toaster oven do-it-yourself approach is sufficient.

Placement of resistors and capacitors with an “0603” (1608 metric) package size have been repeatedly successful without significant difficulty. This package size is 0.063” L x 0.031” W (1.60 mm x 0.80 mm). ICs with pins as fine as 0.65 mm pitch have been placed with no major issues. An occasional short may occur between two pins, but touch-up with a fine tipped solder iron will quickly eliminate the problem.

Thorough continuity testing should be conducted after the board is populated to ensure an accidental short was not introduced. A recommended method for PCB population follows.

Once the PCB is received from the board-house, continuity testing should be conducted to ensure no shorts exist. For example, check for shorts between the ground plane and power planes. Ensure the pads that are grounded are correct. Ensure the pads that should be getting a specific voltage will receive it. Test major connections to ensure no issues exist. A quick visual inspection of the PCB should also be done. There are instances where a trace was not entirely etched out of the top copper layer for instance, causing a short. Any undesired shorts found during this testing are due to an error in the PCB design, or a manufacturing error.

Once it is known the PCB is free of manufacturing and design errors, the PCB is populated. Populating the entire PCB at once can be done if it is desired, but it makes tracking down an issue much more difficult. It is recommended to initially place only the power related components. The cost of ICs add up quickly, and ensuring power is going to the correct locations before placing expensive ICs on the PCB is a great investment of time. All the power components can be placed, and put in the toaster oven to reflow the solder. After applying power to the PCB, a voltmeter is used to test voltage levels. Placing only the power components verifies voltage regulators are working, capacitors are placed with proper polarity, and that other ICs to be placed later receive the correct voltage. This testing does not risk any ICs.

Once it is verified proper voltages are at the desired locations, other components may be added. For the UIFESS, there are a small enough number of parts that they are placed all at once. Since the toaster oven does not ramp the heat as slowly as a commercial reflow oven does, the parts are exposed to a harsher thermal cycle. It is desired to expose the PCB and parts to as few thermal cycles as possible.

Considerable effort is made when designing the PCBs to place all components on the top layer. There are no surface mount parts on the bottom layer. Adding parts to the bottom layer would have added complexity and possibly another thermal cycle to the population process. The maximum allowable PCB size was large enough to allow utilizing the top layer. This would also increase the ease of troubleshooting the PCBs.

After the rest of the parts are placed, continuity testing should be conducted again before power is applied. Ensure no shorts are created in the latest soldering reflow process. Conduct continuity tests on all IC pins. A solder bridge may occur in a location not easily visible with the microscope. Visually inspect all of the pads that have been soldered. Ensure the solder stayed on the desired pad, and did not flow to another pad or location. The more thorough the testing is, the less chance of there being a serious issue when power is applied. Once the power is applied, the damage may be unrepairable. Once the power has been applied, and no shorts are present, then further testing can conducted.

Once one becomes comfortable with the process, about 35 unique parts an hour can by placed manually. Obviously, this number is dependent on the package size, IC pin pitch, and number of different components being placed.

6.3.2 Printed Circuit Board Design Methodology

It is desired to first design, fabricate, and test a prototype PCB to ensure the entire process is understood. A working design is desired before investing further time and resources. Cadsoft's Easily Applicable Graphical Layout Editor (EAGLE) was used as the PCB layout software. Mixed-signal, analog and digital, design considerations are investigated to ensure digital high speed switching would not interfere with the analog signals from the current and displacement sensors.

PCB Layout Software Cadsoft's Easily Applicable Graphical Layout Editor (EAGLE) was used as the PCB layout software. EAGLE enables users to create custom PCB designs, and can output gerber files. The gerber files are sent off to a board house. The board house in turn fabricates the users custom PCB.

EAGLE has a Schematic Editor that is used for drawing electrical wiring diagrams. This is where the user defines specific electrical connections of the various ICs and components used in the custom design.

EAGLE also has a Layout Editor, where all the parts and connections specified in the Schematic Editor are brought into the Layout Editor. The user specifies how large a PCB is desired, where parts and components are placed, and traces for electrical connections.

EAGLE also has a Library Editor that is used to add or modify parts. A part is represented by three elements in EAGLE; the package, symbol, and device. The package is used in the Layout Editor, and provides the information on how the part physically interfaces with the PCB. For example, a surface mount resistor package would include information on how large the surface mount pads should be, and how far apart they need to be from one another. The symbol is used in the schematic editor. The symbol allows a user to define electrical connections for the part. For example, which pin should receive power or be grounded for a particular part. A device connects the symbol with the package. The device element allows the user to map a pin from the symbol to a specific pin in the physical package. Many EAGLE parts are found in the EAGLE default EAGLE library collection or online. Many manufacturers offer a .bxl CAD file type. This file type is developed by Accelerated Designs and the Ultra Librarian software is used to convert the manufacturer file into an EAGLE library file. Texas Instruments provides .bxl files for the majority of their parts. These files are used on multiple occasions without issue.

Once the user has added all parts and components, and done the physical layout of the PCB, EAGLE generates the appropriate manufacturing files. The CAM processor is capable of generating Excellon files for drilling and gerber files for plot data [47].

The University of Idaho has 5 Professional Edition Licenses of Version 6.5.0 available for student use. The Professional Edition can generate PCBs up to 150 inches by 150 inches, with 255 layers; far more than enough for the UIFESS's intentions. The Professional Edition comes with the Schematic Editor and the Layout Editor, as well as the ability to generate the manufacturing files.

Mixed Signal Design Techniques Many PCBs feature either ICs or microcontrollers with both analog and digital features. For instance, the microcontroller features an internal ADC to read the sensors, and uses digital outputs to adjust the electromechanical system. The microcontroller can potentially be switching the digital outputs at a rate of 80 kHz. Higher speeds could be used in the future, as discussed in Section 8.2.

The digital outputs are attempting to transition from one state to another as quickly as possible. The sudden transitions will generate sharp pulses of digital current [48]. These sharp current pulses may interfere with the analog signals, and the ADC sampling will not reflect what the sensor has actually observed. It is important to consider what return paths each analog and digital signal will take.

Current flow is only achieved when there is a complete path. For example, current can originate from a power supply, flow through a circuit, then must return back to the power supply through the electrical ground. The current return paths in the electrical ground have the potential to cross one another and cause interference. The board designer must take into account current return paths when placing analog and digital components, as well as placing components relative to each other.

It is important to note the return currents follow the path of lease impedance. The DC and low frequency return currents essentially travel in a straight line through the ground plane back to their source. Typically the DC power supply is capable of supplying the DC and low frequency currents. High frequency currents do not follow the same behavior. The path of least impedance for the return currents to follow is actually under the trace itself. The high frequency currents are sourced by bypass capacitors that are typically located near the IC. Sometimes a combination of different capacitor types are used to optimize sourcing currents across frequencies. An electrolytic capacitor helps source current for lower frequencies and a tantalum or ceramic capacitor type sources the higher frequency currents.

Consider an example to better illustrate the return current paths[48]. Consider a multi-layer PCB. Typically, one layer is dedicated ground plane. A different layer, typically called the component layer, contains signal traces. A ground plane with a signal trace on a different layer of the PCB is shown in Figure 6.20. The trace is 10 mils above the ground plane. Point A is the source and point D is the load.

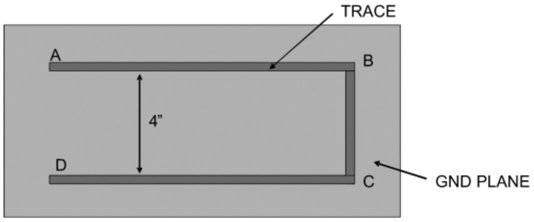

TRACE TOTAL LENGTH = 22"
TRACE IS 10 MILS WIDE, 1 MIL THICK, 10 MILS ABOVE GND PLANE

Figure 6.20: Example Trace Physical Geometry. Point A is the source and point D is the load.[48]

Now various currents are passed from the source to the load through the signal trace. In order to complete the circuit, the current must return to the source. The return current flows through the ground plane following the path of least impedance. The path of least impedance depends on the frequency of the current.

Consider when a low frequency current of 1 kHz is passed through the trace. An electromagnetic simulation of the current return path is shown in Figure 6.21. For the low frequency current, the majority of the current flows in a straight line from the load back to the source. A small amount of current actually follows under the trace back to the source.

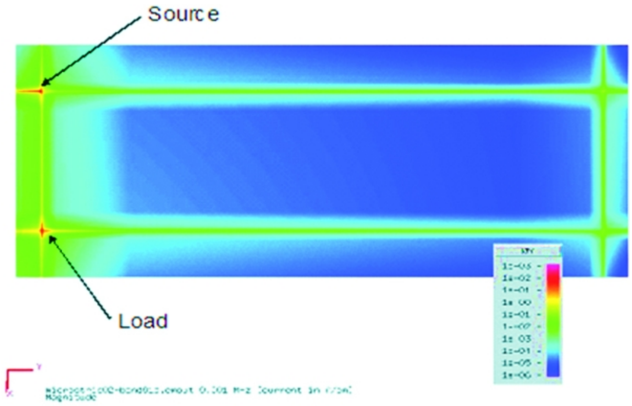

Figure 6.21: 1kHz return current flowing through ground plane. Note the majority of the return current flows from the load directly back to the source.[48]

Now consider when a medium range frequency current of 50 kHz is passed through the trace. An electromagnetic simulation of the medium range frequency current return path is shown in Figure 6.22. In this case, the path of least impedance is not so straightforward. A small amount of current also flows in a straight line from load back to source as well.

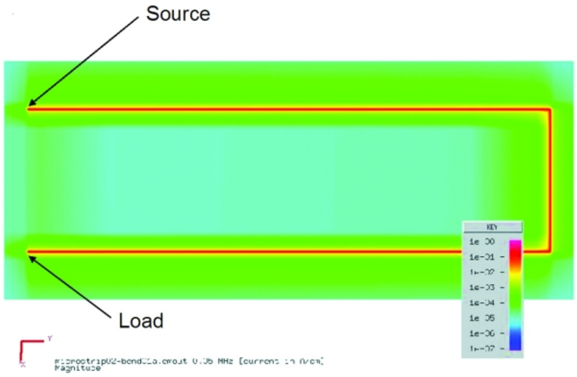

Figure 6.22: 50kHz return current flowing through ground plane. Note that some of the return current flows from the load to the source, but most of it actually follows under the trace back to the source.[48]

Finally, consider the case when a high frequency current of 1MHz is passed through the signal trace. An electromagnetic simulation of the high frequency current return path is shown in Figure 6.23. Virtually all of the return current flows back to the source by following under the signal trace.

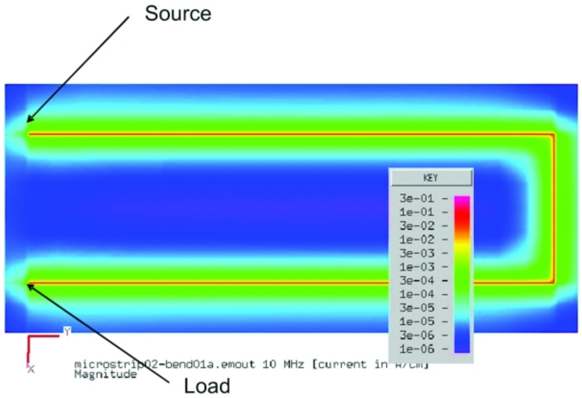

Figure 6.23: 1MHz return current flowing through ground plane. Note that virtually all of the return current returns to the source by following under the signal trace.[48]

These examples help visualize how return currents of various frequencies flow in the ground plane. Board designers are possibly tempted to separate the analog and digital grounds, to ensure no crosstalk occurs. The grounds still need to have a common point however. Inserting cuts into the ground plane while maintaining a single point ground, or ground bridge, is a method to reduce return current interference.

An example cut is shown in Figure 6.24. The cut separates the analog and digital pins. The figure shows red traces being routed to other devices, and orange high frequency current return paths returning to the IC through the ground plane under the signal trace.

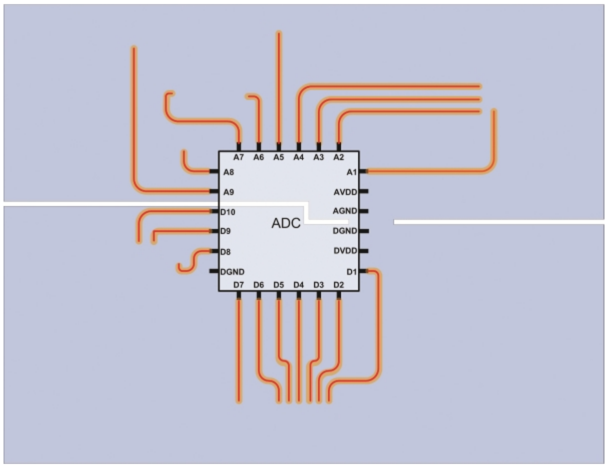

Figure 6.24: Analog and digital IC with cuts in the ground plane.[48]

If a digital trace had to pass over the cut and into the analog side, both the low and high frequency components of the current would be forced to travel all the way to the ground bridge and then back to the appropriate digital pin. The ground return path would be a much longer route and introduce additional voltage drop in the signal.

Typically, an off-board power supply is used to power the PCB. There is usually a single location where the power supply voltage and ground is brought in. Ground return paths from other components on the PCB must ultimately return to this power supply ground to complete the circuit. Ground connections from components on the analog side of the board all have to pass through the ground bridge before returning to the power supply ground, shown in Figure 6.25. Forcing the ground return currents to funnel through the ground bridge will lengthen the return current path, and introduce additional voltage drop in the signals.

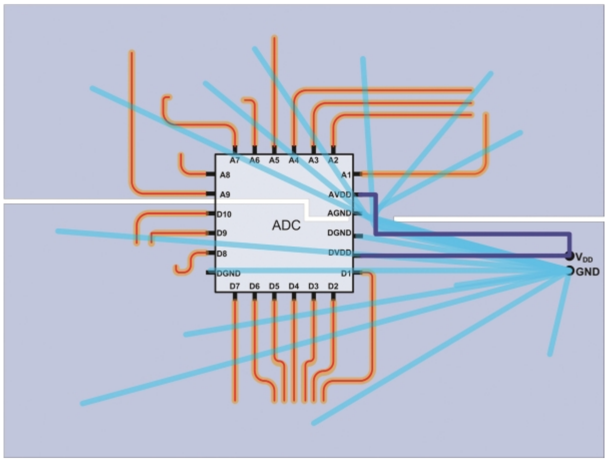

Figure 6.25: Ground return paths from other component ground connections on the PCB to an off-board power supply funneling through the ground bridge[48]

Ultimately, if care is taken when placing the components on the PCB, the ground plane cuts can be removed to provide shorter return current paths to the power supply. The return current paths with the cut in the ground plane is shown in Figure 6.26.

A successful PCB design keeps the analog and digital return current paths as separated as possible while providing the shortest return paths for all signals and power. A proper board layout does not require the use of cuts in the ground plane.

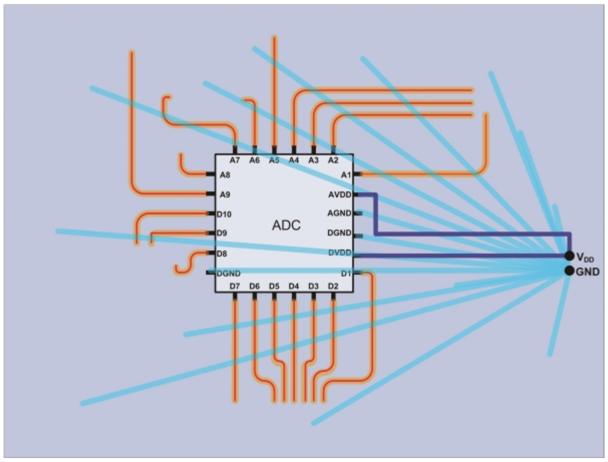

Figure 6.26: Ground return paths from other component ground connections on the PCB to an off-board power supply with the ground bridge removed[48].

6.3.3 PCB Design Implementation

The implementation of the mixed signal design theory for each specific PCB manufactured for the UIFESS is discussed. The Prototype PCB is designed, fabricated, populated, and tested before the UIFESS Driver PCB Version 1 is designed. Results generated from each PCB design are found in Section 7.1.

6.3.3.1 Prototype PCB

Purpose Recall the motivation for building a PCB as stated in Section 6.1. The PCB acts as the interface between the sensors, Full-Bridge DC-DC converter, and microcontroller. It is desired to first design and build a prototype PCB to verify the mixed-signal design methodology explained in Section 6.3.2 and ensure the population techniques of Section 6.3.1 are achievable. The time and resources in developing multiple PCBs for use on the actual flywheel are then spent.

In addition, this prototype PCB is used on the Single-Axis, Single Bearing (SASB) Demonstration Unit. The SASB is a test setup that will verify the airgap control algorithm, the electromechanical model, the sensors, the commercial Full-Bridge DC-DC converters, and the power electronics PCB interface. A detailed description of the SASB and its purpose is given in Section 1.4.

Functions The PCB is capable of multiple functions. The commercial Full-Bridge DC-DC converter must be mounted to the PCB. Analog circuitry for converting the current sensor output of the converter into a level for ADC sampling is required. Analog circuitry to convert the displacement sensor output into a level for ADC sampling is also required. A simple interface between the microcontroller and the PCB is desired. A simple interface between the converter and coil is also desired. The PCB must interface with a 24 V rail for the converter and coil, as well as ±15 V rails for the analog circuitry. Reference voltages to be used for the shifting portions of the analog circuits is needed. Additional features and access points are included to aid in troubleshooting and fine-tuning various functions of the PCB.

The prototype PCB design is judged on a variety of aspects. Most importantly, the analog portion of the PCB must convert the sensor data into voltage levels that are capable of being read by the microcontroller while still accurately portraying the phenomenon being measured. Analog filter performance is investigated. The analog signals cannot be affected by the digital switching associated with the converter on the same PCB. The analog circuitry responsible for filtering, shifting, and scaling must all be demonstrated. The PCB must be able to handle the coil current that passes through the converter. Interface between the PCB and sensors, microcontroller, and coil must all be easy to implement. The ease of troubleshooting will also be considered. This PCB is intended for learning, and lessons learned can be applied to the final PCB designs.

Analog Hardware The topologies used for adjusting the displacement and current sensor outputs are discussed in Section 6.2.1 and Section 6.2.2, respectively. Additional hardware is required to successfully implement these topologies. The analog hardware is responsible for adjusting the displacement and current sensor outputs into levels the microcontroller ADC can read.

Full-Range Distance Signal Conditioning Topology This topology is discussed in detail in Section 6.2.1.1. The displacement sensor topology converted the entire sensing range of the displacement sensor. The topology included an OPA277 op-amp to scale the output voltage, a low-pass filter to remove the high frequency noise, and an in-amp for high common-mode rejection. A potentiometer is placed in the scaling portion so the gain of the topology could be adjusted. The low-pass filter is designed to have flexibility with minimal additional effort. The resistor and capacitor values from simulations of Section 6.2.1.1 are placed in the topology, and are used in initial testing. If the low-pass filter did not meet expectations, or the cut-off frequency had to be adjusted, two resistors could be removed, and 0 Ω resistors could be installed to bring potentiometers into the low-pass filter topology. Various resistor values and a potentiometer allow significant cutoff frequency adjustments if needed. The topology is shown in Figure 6.27.

In-Amp Current Signal Conditioning Topology This topology is discussed in detail in Section 6.2.2.1. The current sensor topology included a low pass filter, INA129 in-amp, and an OPA277 intended for voltage shifting. The same reasoning is applied for the current sensor's low pass filter as used for the displacement sensor's low-pass filter. In addition, the INA129 gain resistor could be adjusted to include a potentiometer if desired. The shifting circuit is responsible for reducing the INA129 output voltage magnitude. Any noise in the shifting voltage will not be filtered by the INA129, so a quiet voltage source is desired. Texas Instruments commonly uses the REF102 for various applications. In addition, the output of the REF102 is passed into a unity gain OPA227 op-amp so that the precision output is not be loaded.

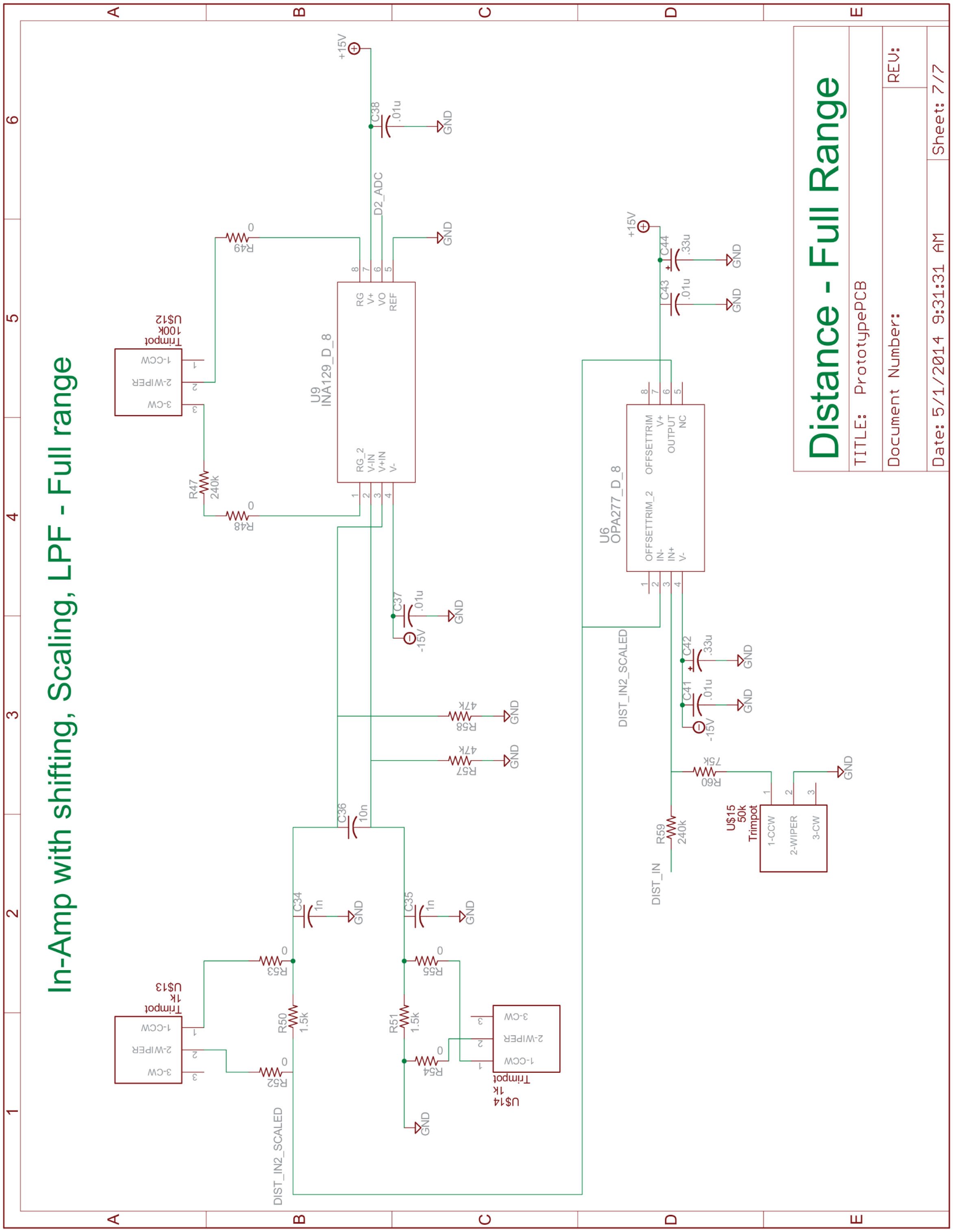

Figure 6.27: EAGLE Schematic View of Full-Range Distance Signal Conditioning Topology

The REF102 is a precision 10 V reference. The 10 V output is low noise, on the order of 5 μV peak to peak. The device also features a wide input supply voltage range of 11.4 V to 36 V. The REF102's 10 V output voltage is voltage divided to provide the desired offset voltage for the current sensor topology. A precision potentiometer is included in the voltage divider to allow an accurate offset bias voltage to be achieved.

Short-Range Distance Signal Conditioning Topology This topology is discussed in detail in Section 6.2.1.2. Concerns about the full range displacement sensor resolution existed. A second topology is placed on the PCB that was capable of sensing only a 0.5 mm range. This short range distance sensor topology is only capable of outputting ADC level voltages for displacements from 0.75 mm to 1.25 mm. A similar low pass filter topology, INA129 in-amp, and level shifting is used in this topology. If the shifting topology received power, but the displacement sensor is not turned on, a large negative voltage is maintained at the output of this topology, which can damage the microcontroller ADC. In order to ensure this did not occur, a diode clamp circuit is placed on the output to ensure the output does not drop below 0 V or rise above 3 V.

Op-Amp Current Signal Conditioning Topology This topology is discussed in detail in Section 6.2.2.2. A second, cheaper, current sensor topology is present. The INA129 is a fairly expensive IC, and 28 currents require monitoring. A topology using the OPA277 and a Sallen-Key filter topology is used. Flexibility of the filter cut-off frequency and the offset voltage is once again obtained with the use of potentiometers. Since this topology requires the use of two OPA277s, the OPA2277 package is used. This is simply a package that contains two OPA277s, making for a smaller footprint and fewer required connections.

Power Both the INA129 and the OPA277 require positive and negative voltage rails. Implementing a single rail design is not considered, since it is desired each topology output reaches 0 V if needed. The maximum input voltages for both parts is ±18 V while the REF102's input voltage range is 11.4 V to 36 V. The supply for the op-amp and in-amp positive input voltage rails is also used for the REF102. The Full-Bridge DC-DC converter requires 5 V to power the analog current sensor.

Digital Hardware

Digital I/O The microcontroller uses digital signals to adjust switches on the Full-Bridge DC-DC converter. The switching rate of the digital signals varies with the required current, but the switching rate could be as high as 80 kHz. The digital switches control the average voltage across a coil, and how much current will flow in the coil. The coil may require up to 12 A and switching at a high frequency.

The microcontroller digital outputs are capable of outputting a high state of 3 V. The commercial Full-Bridge DC-DC converter driver requires 5 V logic. Its minimum high input signal threshold is 3.5 V, so the microcontroller would be unable to reliably switch the converter.

Logic Level Shifting Texas Instrument's TXB0108 has been successfully used in previous projects. The TXB0108 is a Bidirectional Voltage-Level Translator that is capable of converting a 3 V microcontroller signal to a 5 V signal required by the converter. It is bidirectional, so it can also turn 5 V outputs from the converter down to 3 V to be read by microcontroller. The device is capable of level shifting 3 V to 5 V or 5 V to 3 V in at most 4 ns. Recall that the dead time between switching on the converter is 3 μs, so the device's switching time is acceptable. The TXB0108 requires two voltage rails, one for each side of the shifter. For the UIFESS's application, a 3 V and a 5 V rail is required. The microcontroller development board has both 3.3 V and 5 V supplies, so the required voltages are sourced from the microcontroller. The lower voltage rail must be in the range of 3.3 V ± 0.3 V, so having a 3.3 V rail. In order to properly shift the voltage level to 5 V, a voltage in the range of 0.8 V to 4 V is required, which the microcontroller is capable of.

Full-Bridge DC-DC Converter and Power Supply The Full-Bridge DC-DC converter input rail has a 5.5 V to 50 V range. It is decided the coils would be run off of a 24 V supply. This 24 V supply attaches to the converter, and is responsible for sourcing the significant current for the coil. During operation, the microcontroller will be switching digital outputs to adjust the current in the coil. The rapidly switching microcontroller outputs as well as the switching current itself must be kept separate from the analog portion of the PCB. The converter does include the analog current sensor, so connections between the analog and digital side will exist.

Common-Mode Choke A common-mode choke is placed on the PCB. The ACM1513 is intended to introduce high common-mode impedance and noise suppression for high current applications. The choke suppresses high frequency noise that the coil or leads may pick up before reaching the PCB. Testing is conducted with or without the choke to see if it is effective and worth the considerable board space.

Microcontroller Interface The PCB interfaces with the microcontroller. Analog sensor data must be delivered to the ADC and the microcontroller digital outputs must be delivered to the on-board Full-Bridge DC-DC converter. Male header pins are used to interface with the signals on the PCB. The microcontroller also possesses male header pins, so female-to-female cables can be used to make the appropriate connections.

Schematic Design The parts required to fulfill the boards intentions are all declared above. Supporting parts such as bypass capacitors for the ICs will be added. Recall the schematic layout defines all of the electrical connections in the entire PCB. For example, this defines what a specific pin of a given IC is connected to. Power and ground connections are defined, as well as where the resistors and capacitors are connected.

An EAGLE library part must exist for every part used in the design. Some parts are imported using the Ultra Librarian software and other parts are created manually.

Parts were systematically brought into EAGLE's Schematic Editor and their electrical connections are defined. Package sizes must be determined at this stage. It was decided to attempt using the 0603 (1608 metric) package size for the resistors and capacitors. The package size is 0.063" L x 0.031" W (1.60 mm x 0.80 mm) and is small enough to not take up excessive board space yet large enough to place during in-house population. The entire PCB schematic is shown in Appendix A.

Board Layout After the schematic is complete, the board layout follows. The mixed signal design methodology discussed in Section 6.3.2 will is implemented.

Layout Considerations Some initial design parameters are discussed. A 4-layer board is used. There are enough parts in the design that attempting a 2-layer board is not practical. The 4-layer board allows additional flexibility in the board design. It is desired to keep all the parts on the top layer of the board. Keeping the parts on the top layer simplifies the population process to be done in-house. The second layer is inside the PCB. This layer is dedicated to the voltage rails. The voltages are brought in from the top layer and the voltage will be distributed through power planes, large polygons of copper. The ±15 V rails and 10 V precision reference will use this layer. The 24 V plane is placed on the top layer to better see if the high currents cause too much heating in the traces. The third layer is dedicated to the ground plane. This plane should ideally be as large as possible and have as few cutouts as possible. The bottom layer is used if an additional layer is required for running signal traces.

As parts are added to the Schematic Editor, they are also added to the Layout Editor. All of the parts will be spread out in an area not on the board layout. The first step for the board layout is to group all the parts that are connected. For example, all the resistors, capacitors, potentiometers, and ICs that make up each analog filter are grouped. Once all the parts are grouped, the parts could be laid out for their physical orientation on the PCB. The layout must take into account several factors.

The parts in each group are placed to minimize the trace length between parts. If the part placement is optimized, the group takes up a smaller area, and the goal of keeping all the parts on the top layer of the board is achieved. Shorter trace lengths also result in a shorter current return path, and additional interference is avoided. A view of the Layout Editor is shown in Figure 6.28, showing the Full Range Distance sensor topology of Figure 6.27 as it appears on the physical PCB.

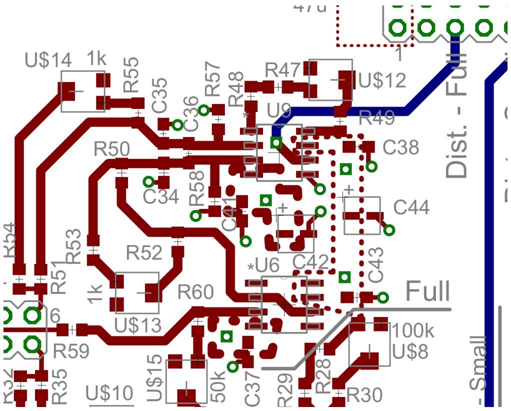

Figure 6.28: EAGLE Layout Editor Full-Range Displacement Sensor Topology. The pads for surface mount components and the signal traces are displayed.

The voltage requirements of each part must be considered. Many of the ICs require ±15 V. Three of the four analog topologies also require the 10 V precision voltage for shifting the topology's output. The ±15 V source will be brought to the PCB in one location only. The parts must be placed so that each part has access to the voltage sources, and each source does not need to take a complicated path to each IC or part.

A block diagram of the layout is shown in Figure 6.29. The parts are sized relative to one another. The analog and digital parts are placed on different sides of the PCB. The microcontroller interface is in the middle, with digital outputs towards the top and analog inputs on the bottom. The ±15 V are brought into the analog portion of the PCB. The analog topologies should be placed such that each IC has access to the ±15 V rails, and the +10 V precision source can be accessed for the shifting portions where necessary.

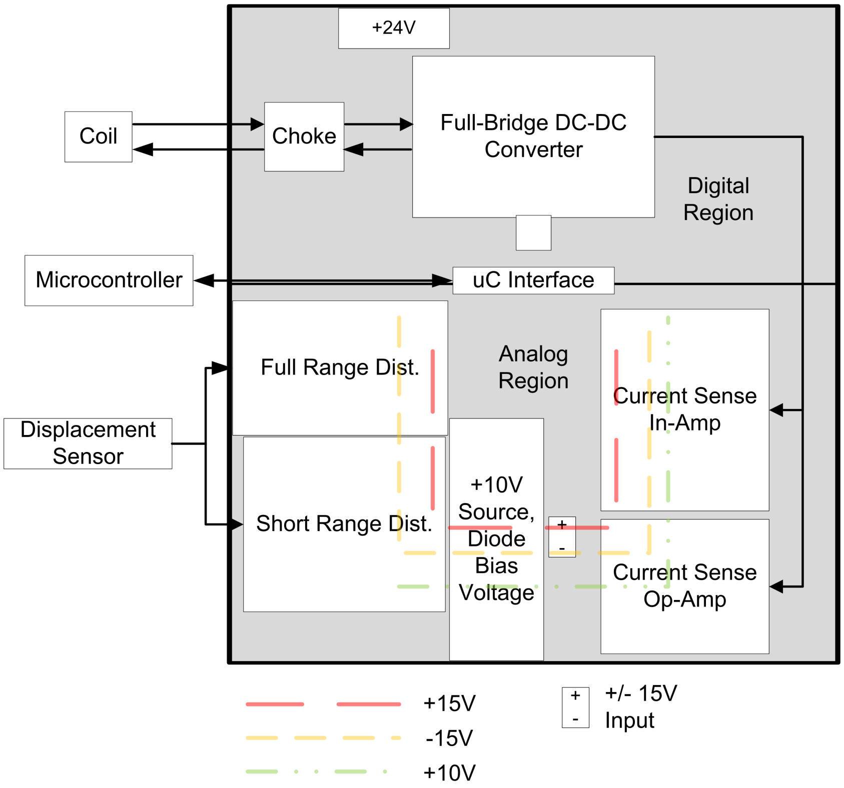

Figure 6.29: Prototype PCB Layout Block Diagram Showing Approximate Placement of Major Components

For each topology, optimizing the trace length between parts must be considered, as well as placement of the parts relative to other topologies and voltage rails on the PCB. Considerable time is spent orientating the parts to achieve small trace lengths and have each topology situated to allow the voltage rails to have ease of access. Once the parts are placed relative to each other, the group is thought of and moved as a modular block until a satisfactory configuration is found.

The block diagram layout of Figure 6.29 follows the major rules for mixed signal design. The upper region of the board is dedicated to digital hardware, while the lower region is dedicated for analog hardware. The microcontroller interface is strategically placed at the border of the two regions. The return paths for currents from the 24V source are not near the analog parts, as shown in Figure 6.30.

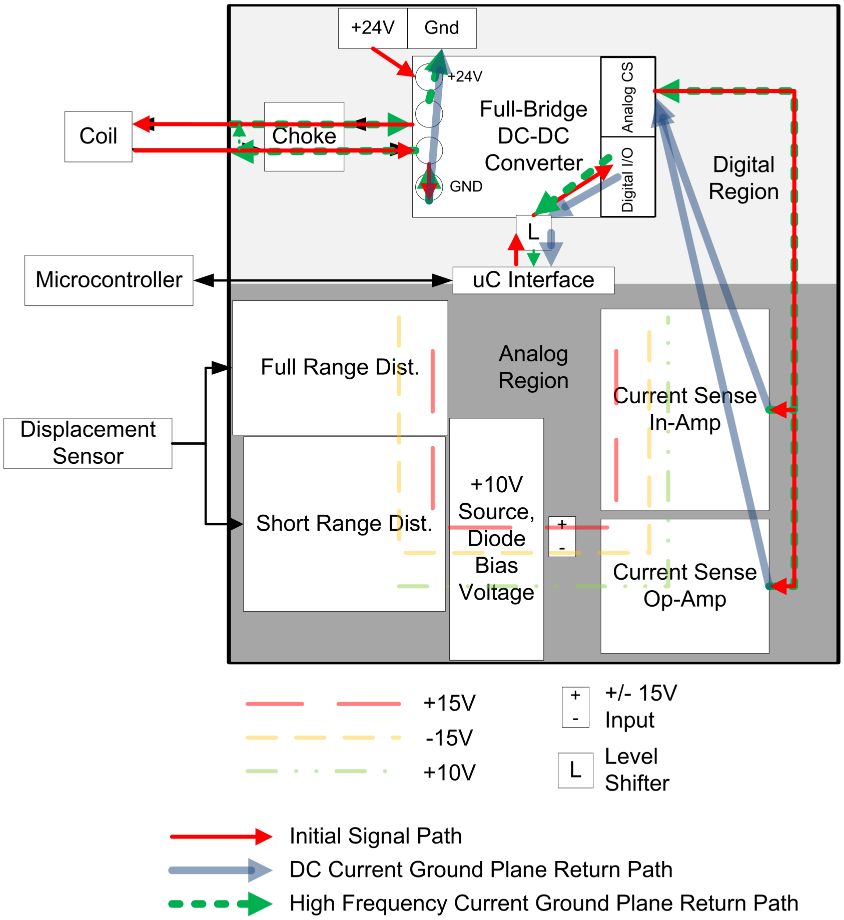

Figure 6.30: Prototype PCB Layout Block Diagram Showing Major Current Return Paths

The analog sensor is located on the Full-Bridge DC-DC converter and the current sensor analog output had to be brought from the digital side to the analog side. This route was longer than desired, and it is possible noise could get picked up in such a long trace, or cross-coupling interference could be introduced in the traces. To mitigate these concerns, a guard trace was implemented. An additional copper pour, or guard trace, is placed on the top layer between traces that run near each other. The guard trace is grounded along its path and will protect sensitive parts of the circuit, such as the analog sensor trace[49].

First Layer The completed design for the top layer of the PCB is shown in Figure 6.31. Red polygons represent power planes and red lines are traces. This figure shows the actual traces on the physical PCB. Note the upper left quadrant contains the 24 V plane and large traces responsible for delivering large currents between the Full-Bridge DC-DC converter and the coil. The converter itself is centered in the upper portion of the digital region. The analog current sensor traces with the guard traces are located on the right hand portion of the PCB. The level shifter is located between the microcontroller interface and the digital inputs and outputs of the DC-DC converter. Note that the 3.3 V and 5 V planes are located on the microcontroller interface and are required to power the level shifter.

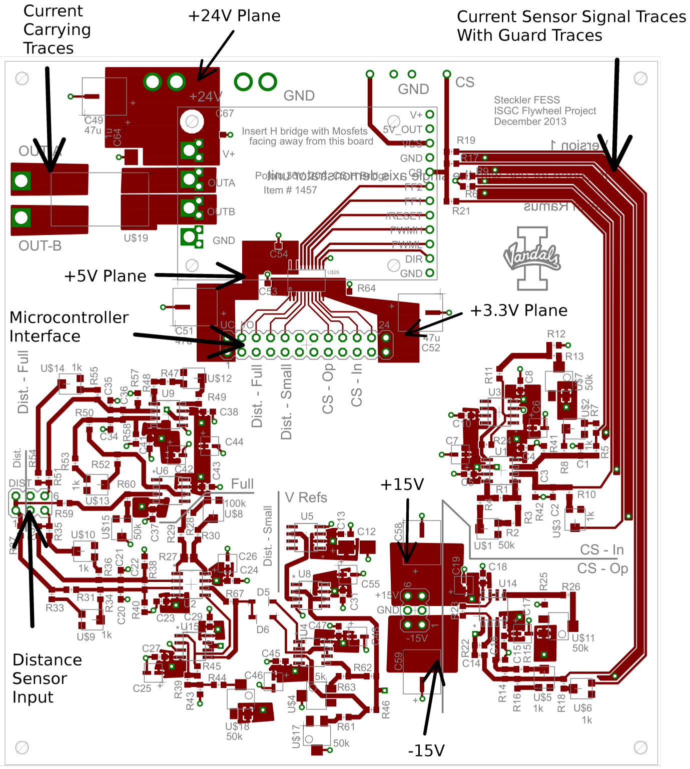

Figure 6.31: Prototype PCB Component (Top) Layer - EAGLE Layout View

The four topologies that are being investigated in the prototype design are located on the lower portion of the PCB. Note the header pins in the analog region responsible for bringing in ±15 V. The displacement sensor signals are brought into header pins on the left hand portion of the PCB.

Second Layer The second layer of the PCB is shown in Figure 6.32. This is the power plane layer. The ±15 V copper planes exist in this layer, as well as a plane for the 10 V precision voltage reference. The +15 V plane is the inner-most copper plane, the -15 V plane is located outside the +15 V plane and closely follows the +15 V outer boundary. Notice the ±15 V planes each pass under the ICs used in the analog topologies. The large copper plane allows a path of less resistance to the ICs that are located far away from where the voltage rails are brought into the PCB. To bring power up to the component or top layer, a via is needed. The via makes connections possible between different layers of the PCB.

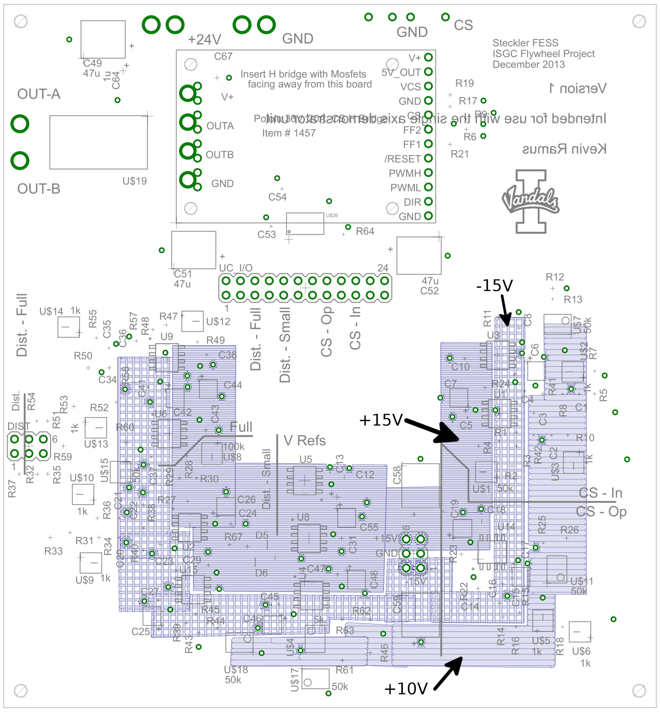

Figure 6.32: Prototype PCB Power Plane (Second) Layer - EAGLE Layout View

A trace on the top layer connects the via to the appropriate pad, delivering the desired voltage to the desired pin of the IC. Experienced EAGLE users may realize the -15 V plane appears to be a hatch-type copper pour. The polygon was set to a hatch type pour so that it could be easily distinguished between the other layers on the PCB. The -15 V plane is also a solid copper pour. This is illustrated in the copper layer image shown in Figure 6.33.

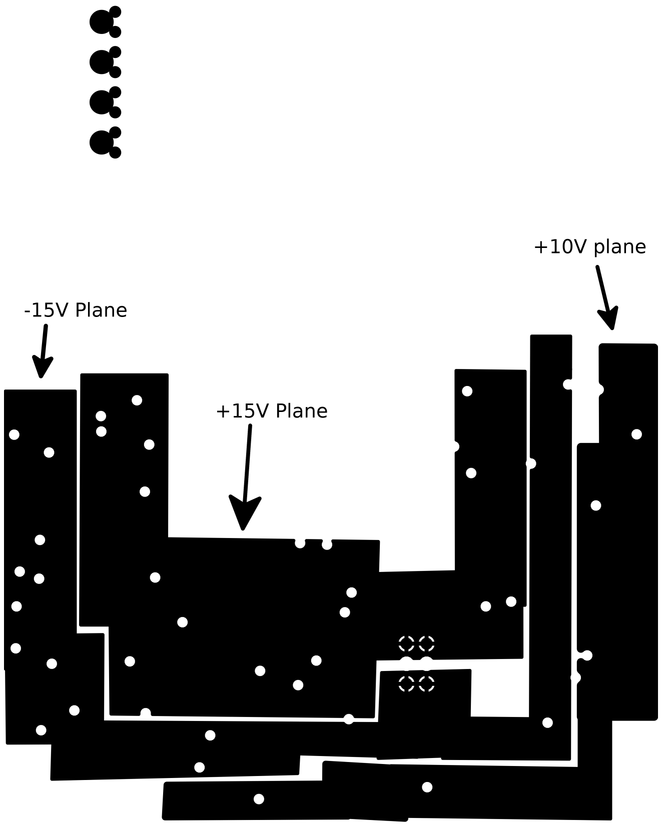

Figure 6.33: Prototype PCB Power Plane (Second) Layer - Copper Layer View

Third Layer The third layer of the PCB is dedicated to the ground plane. This ground plane is where all currents, analog and digital as well as low and high frequency currents, must flow to complete the intended circuit path. As stated in Section 6.3.2, cuts in the copper plane are not required for a successful design. However, a cut in the copper plane is placed on the left hand side to see how well the cut would turn out in case a cut had to be used in later designs. There are no traces that pass over the cut, so there are no increased lengths of return paths. The EAGLE Layout Editor View of the ground plane is shown in Figure 6.34. The red polygon is the ground plane.

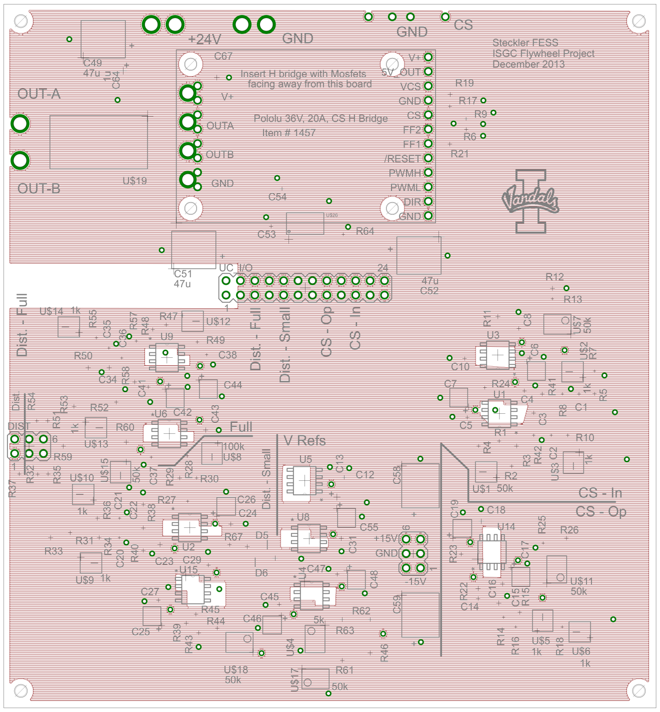

Figure 6.34: Prototype PCB Ground Plane (Third) Layer - EAGLE Layout Editor View

The physical copper layer view is shown in Figure 6.35. Recall that the +24 V power plane is in the upper left hand region. This region contains the return currents that are of the highest concern. By putting a cut in the left hand region, this ensures any return currents straying beyond the intended paths do not pass into the analog portion of the PCB. Any surface mount pad that needed to be grounded requires a trace connected to a via.

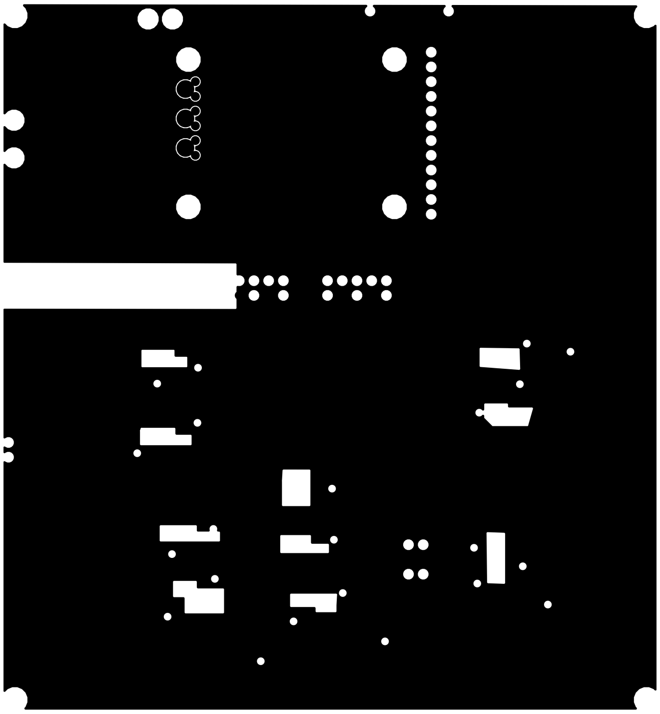

Figure 6.35: Prototype PCB Ground Plane (Third) Layer - Copper Layer View

Fourth Layer The fourth layer of the PCB is typically intended for additional components placed on the backside of the PCB. The bottom layer can also be referred to as the solder side. One of the design requirements of the prototype PCB is not placing components on the back layer, which makes the in-house population process more difficult. The fourth layer is used for additional trace routing area. For the prototype PCB, the analog sensor conditioning topologies are compact. The topology output intended for the ADC is not be routed to the microcontroller interface using the top layer. The signals are brought to the bottom layer through a via, shown in Figure 6.36.

Manufacturing Files The board design is complete, and the gerber files are sent to the manufacturer. The blank PCB is received, and extensive continuity testing is conducted to ensure there are no manufacturing or design errors. Once it is determined there are no errors, the population process is conducted. The population process requires roughly 5 hours of time to place all surface mount parts. The toaster oven was used for the

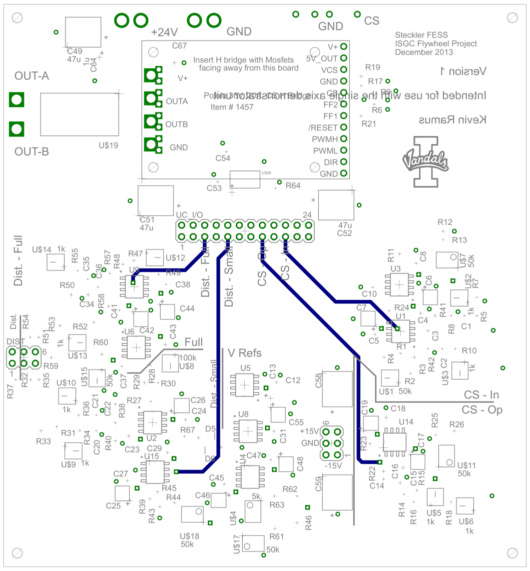

Figure 6.36: Prototype PCB Solder (Forth) Layer - EAGLE Layout Editor View

solder reflow process. An excessive amount of solder paste is accidentally used for placing some of the ICs, and shorting resulted between multiple pins. A typical solder iron is all that is required to remove the shorts. Thorough continuity testing is done before applying power to the PCB for the first time. See Appendix B for a complete Bill of Materials for the Prototype PCB. The completed Prototype PCB is shown in Figure 6.37. The Prototype PCB results are discussed in Section 7.2.

6.3.3.2 UIFESS Driver Version 1

Purpose Recall the motivation for building a PCB as stated in Section 6.1. The PCB acts as the interface between the sensors, Full-Bridge DC-DC converter, and microcontroller. This PCB design leverages the knowledge gained from the successful prototype PCB. This PCB is capable of driving 4 coils belonging to either the stabilization bearing or the FRRM self-bearing.

It is decided to only purchase 2 PCBs initially to ensure the new design would be successful in working with the coils in the UIFESS. After ensuring the design worked, minor changes could be made and the rest of the required PCBs could be ordered.

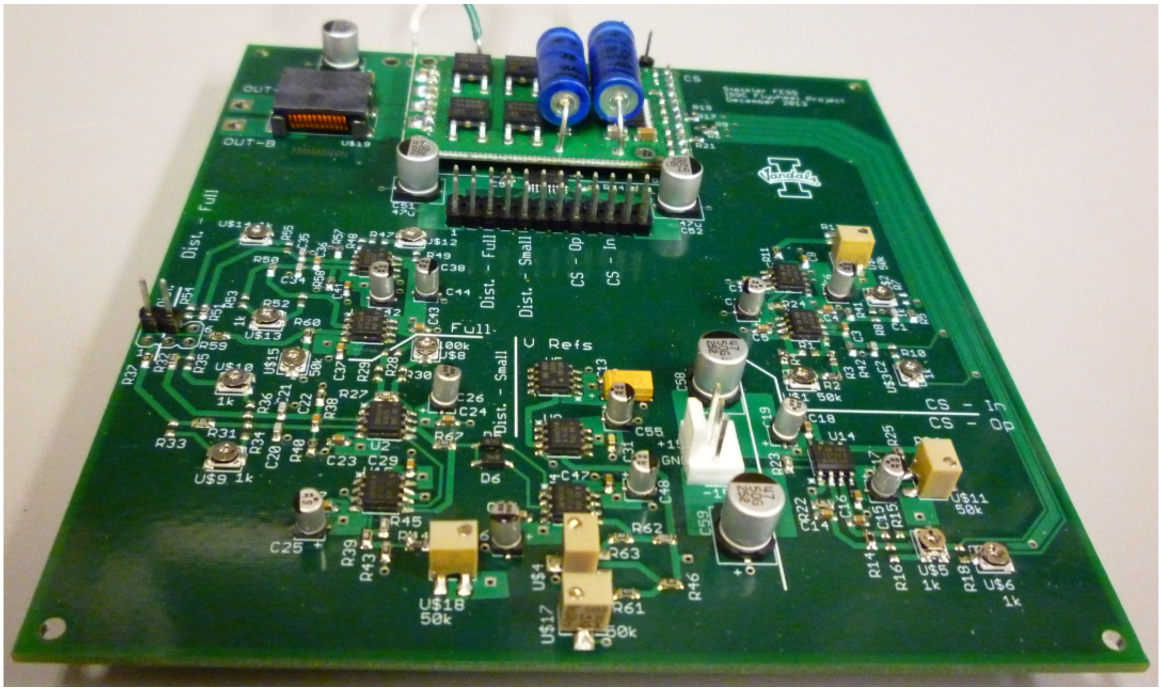

Figure 6.37: The Fully Populated and Functional Prototype PCB

Functions The UIFESS Driver Version 1 PCB is intended to be used in the actual UIFESS, not for test setup as the Prototype PCB was intended. The UIFESS Driver Version 1 PCB will be capable of controlling 4 separate coils, providing 4 conditioned coil current signals, providing 2 conditioned displacement signals, and provide a microcontroller to PCB interface. In addition, the UIFESS Driver Version 1 PCB requires digital logic level shifting. The microcontroller digital outputs provide a 3 V signal while the full-bridge driver requires 5 V to properly control the converter.

The UIFESS Driver Version 1 PCB requires ±15 V to power the analog electronics. On board regulators will step the +15 V source down to 3.3 V and 5 V for use with the logic level shifter. The commercial Full-Bridge DC-DC converters require interfacing with the +24 V rail. The displacement sensor outputs will need to be brought on board for signal conditioning before being sent to the microcontroller ADC. Design considerations for troubleshooting and enabling waveform capture will be implemented.

The UIFESS Driver Version 1 PCB is judged on its ability to control 4 separate coils, deliver accurate analog current and distance sensor signals to the microcontroller

ADC, enable interface and control of the commercial Full-Bridge DC-DC converters, and the ease of troubleshooting and signal capture access points. The UIFESS Driver Version 1 PCB must maintain the mixed signal design practices discussed in Section 6.3.2 and enable ease of surface mount population.

Design The design of the UIFESS Driver Version 1 PCB borrows heavily from the Prototype PCB. Much of the same hardware is used, and the physical layout is similar. The population process for the Prototype PCB went smoothly, so it is desired to keep all the components on the top of the PCB if possible. The PCB is once again a 4-layer board, and requires the entire 30 in^2 to house 4 full-bridge converters and the analog signal conditioning topologies.

Since many of the parts and circuits used in the Prototype PCB are used in the UIFESS Driver Version 1 PCB, it is decided to make a copy of the Prototype PCB file to speed up the design process. The schematic layout already has the majority of the required parts and correct package sizes, as well as the proper supporting hardware and electrical connections in place. The board layout still requires significant redesign, but many of the parts will be grouped together, which reduce layout time.

Analog Hardware Results from the Prototype PCB determined the full-range distance sensor topology and the in-amp current sensor topology are best suited for use in the UIFESS. The short-range distance sensor topology and the op-amp current sensor topology are not included in this PCB design.

In-Amp Current Sensor Signal Conditioning Topology The in-amp current sensor topology requires a signal offset, so the REF102 precision voltage reference is required. There are 4 full-bridge DC-DC converters on the PCB, so 4 topologies are required. Texas Instruments offers the OPA2277, a dual package form of the OPA277. The current sensing topologies are placed in 2 groups of 2, and a single OPA2277 is used to provide the shifting voltage to each INA129. Using the OPA2277 gives the topology a smaller footprint and requires less bypass capacitors, simplifying the layout design.

Full-Range Distance Sensor Signal Conditioning Topology It is decided to place 2 full-range displacement topologies on the PCB. The distance sensors monitor displacements along the flywheel x-axis and y-axis. These displacements directly correlate to the status of the air gap between the machine rotor and stator. A single UIFESS Driver PCB has the ability to monitor both air gap axes. Recall the UIFESS requires control of 28 coils, so 7 UIFESS Driver PCBs are required. However, only 4 distance sensors are required for control. Not every UIFESS Driver PCB has its full-range distance topologies populated. Extra topologies may be populated to provide backup in case an issue arises.

The full-range distance topology requires the use of an op-amp before entering the in-amp for final signal conditioning. The Prototype PCB used the OPA277 to aid in stepping the Kaman displacement sensor output down to microcontroller ADC levels. Since two distance topologies are present, the dual package OPA2277 is used to save board space and simplify layout design.

Digital Hardware There are no significant changes made to the digital hardware used from the Prototype PCB. Each Full-Bridge DC-DC converter requires its own logic level shifter. It is decided to add voltage regulators capable of stepping +15 V down to 3.3 V or 5 V to the PCB. The logic level shifter can use the +15 V rail and regulators for its shifting instead of requiring additional voltage levels brought to each UIFESS Driver PCB, reducing the number of connections and voltage supplies required.

Full-Bridge DC-DC Converter One significant difference between the Prototype PCB and the UIFESS Driver PCB is the technique for connecting the full-bridge converters to the +24 V rail. The Prototype PCB brought the +24 V source onto the PCB and through a power plane. The converter then connected to the +24 V rail through the power plane. The commercial DC-DC converters ship with screw terminals in the package. Instead of introducing the additional path through the power plane, the +24 V and Ground could be brought to the converter through the terminals. It is hoped this would further decrease the amount of noise present in the PCB as well. The converter is grounded to the PCB though multiple ground connections through its header pin interface.

Common-Mode Choke and PCB Traces The choke is not placed on the UIFESS Driver PCB, since too much space is taken up and a clear advantage does not exist. In addition, it also required physically large traces carrying large currents in the top layer. By removing the choke, the converter can interface with the coil through the converter screw terminals.

Microcontroller Interface The interface between the PCB and the microcontroller is kept the same. Analog and digital signals are routed to male headers on the PCB. Female-female cables are used to connect the appropriate PCB signals to the header pins on the microcontroller Experimenter Kit.

For the UIFESS Driver PCB, the digital and analog interfaces are separated. There is no reason to place them in close proximity to one another. The Prototype PCB design proved the techniques used in Section 6.3.2 are valid. These principles are applied to the situation where a single device, such as a microcontroller, with analog and digital signals needed to be placed on the PCB. Separating the analog and digital interfaces only further separates the signals, ensuring the analog signals are not affected by noise.

Schematic Design Besides the new voltage regulators, all the parts required for the UIFESS Driver PCB are used in the Prototype PCB design. A custom library part had to be created for the voltage regulator. In addition, the Pololu Full-Bridge DC-DC converter library part had to be modified. The +24 V and power Ground connections are being brought into the screw terminals. There is no need for the +24 V and power Ground connections to be made to the PCB. The digital Ground connections on the header pin interface need to be enabled in the library part so they can be grounded to the digital ground in the PCB.

The same resistor and capacitor package sizes are used since the population process went smoothly. The same potentiometers are used since the values and ranges worked well for adjustments in the Prototype PCB. A copy of the Prototype PCB file is made, and specific parts are added or subtracted as needed to complete the schematic design. The schematic view of both distance signal conditioning topologies is shown in Figure 6.38. Note the OPA2277 scales down each Kaman sensor output voltage and sends the scaled voltage to the respective INA129. Compare the dual displacement topologies of Figure 6.38 to the Prototype PCB displacement topology of Figure 6.27. Each topology serves the same function, but the topology for the UIFESS Driver PCB conditions 2 signals at once.

Board Layout The Prototype PCB file is copied and modified to help speed up the design process. The physical board size is extended to take advantage of the full 30 in^2 size allowed by Advanced Circuits to obtain their special $66 4-layer PCB pricing. Time is spent considering layout options on how to best fit 4 full-bridge converters, where the analog and digital separation should take place, and how to configure the analog circuits to attempt to keep all components on the top layer of the PCB.

Layout Considerations The new analog circuit layouts are optimized to reduce the overall size and distance of electrical connections. The distance topologies are laid out. A group consisting of two current sensor topologies is laid out. A technique exists in EAGLE to copy and paste parts and specific trace connections in the layout view. This technique is used so both sets of the current topology layouts are identical to one another.

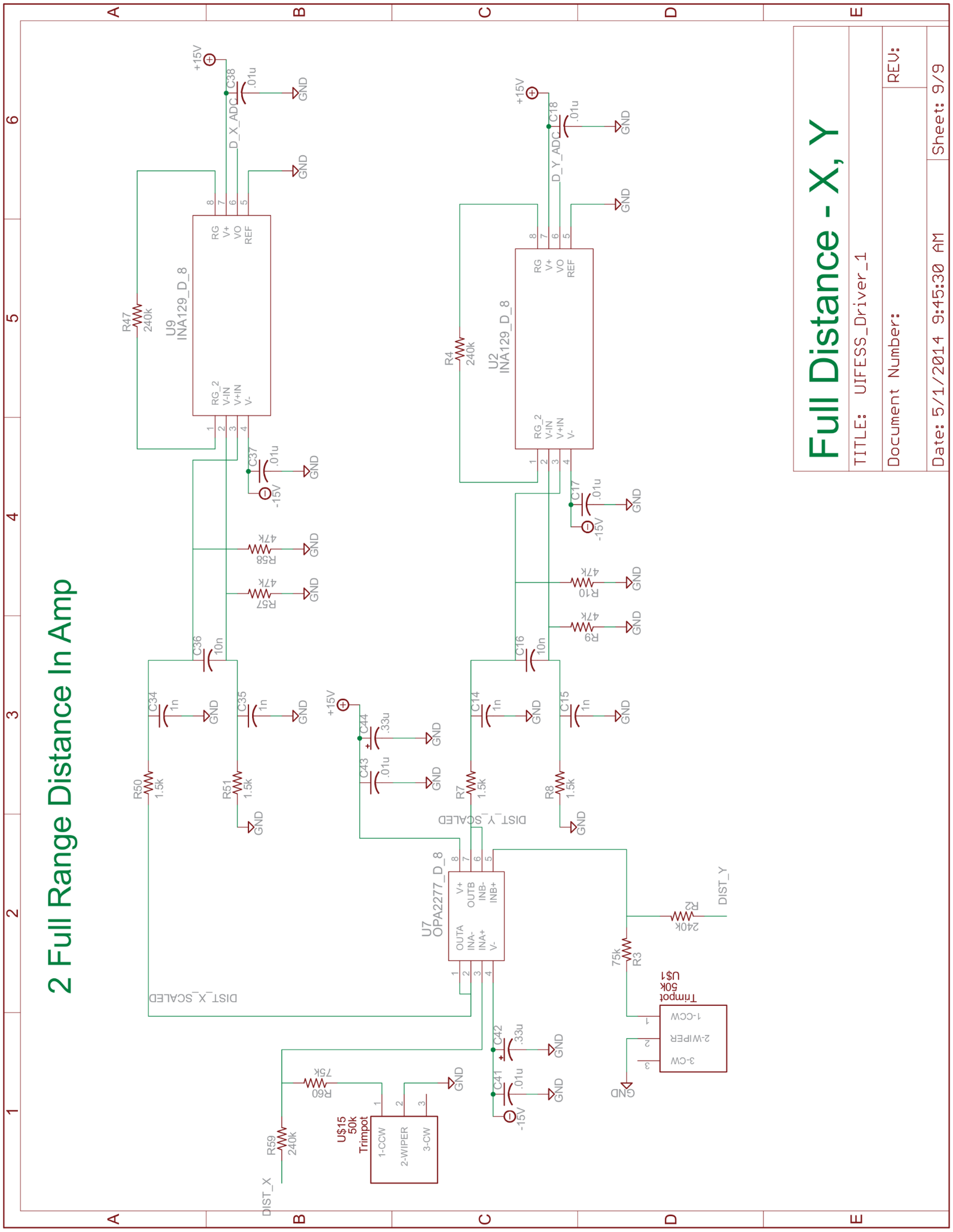

Figure 6.38: UIFESS Driver PCB Version 1 Schematic View of Full-Range Distance Sensor Topologies

The layout concept for the UIFESS Driver Version 1 PCB is shown in Figure 6.39. All of the components and PCB are all scaled relative to one other.

The block diagram is used to determine the basic layout of the board. The blocks are manipulated until an arrangement that fulfilled the mixed signal design requirements is found. It is seen that the DC-DC converters connect to the +24 V bus through the screw terminals. This reduces the amount of connections between the bus and converter. Each converter controls the current through a separate coil.

The Logic Level Shifters are placed between the converters and the microcontroller interface. The +3.3 V and +5 V regulators were placed on the digital side of the PCB. The +3.3 V voltage source is connected to the Logic Level Shifters through a power plane located in the second layer. The +5 V voltage source is connected to the Logic Level Shifter and the VCS pin of the converter. This provides power to the current sensor on each converter. The regulators are powered by the +15 V voltage source.

The ±15 V connections are placed on the analog side of the PCB. Each analog signal conditioning topology requires both voltage rails. The +10 V precision reference voltage delivers a voltage used for shifting the signals of the current sense topologies.

The configuration of the analog signal conditioning topologies is essentially dictated by the layout. The PCB width is set to house the 4 converters, and enough extra room for mounting holes, without any additional width. The PCB would have to made significantly longer to obtain a useful amount of board space, so it is decided to save the area for making the PCB longer instead. Since the current sensors are located on the converters, the signals are brought across the unofficial analog-digital separation line. The traces are routed towards the outside of the PCB to keep away from the shifting logic levels used to control the converters. This is similar to what was done in the Prototype PCB design. It is desired to keep these signal lengths as short at possible, but the inner converters are forced to take a longer route.

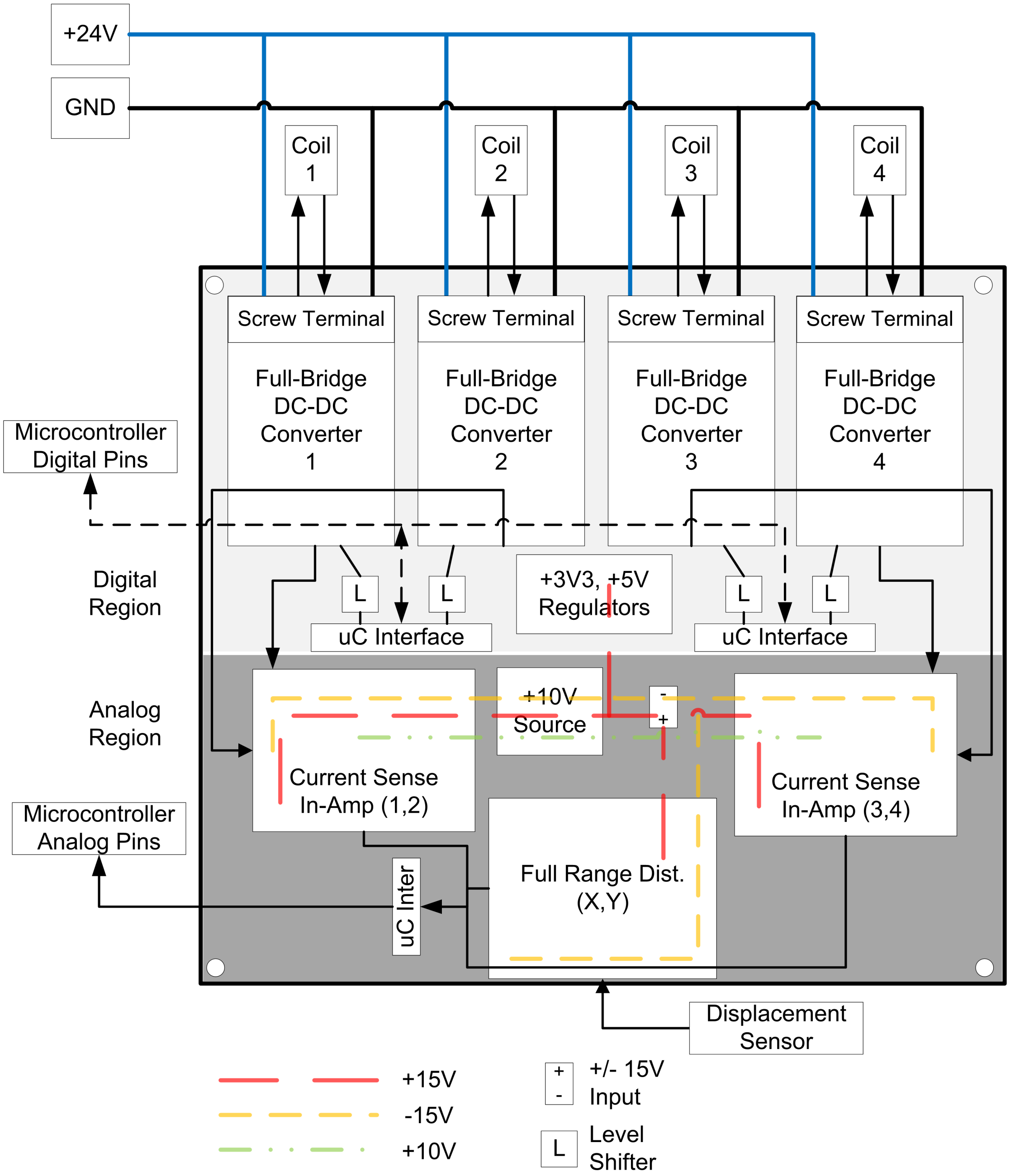

Figure 6.39: UIFESS Driver Version 1 PCB Layout Block Diagram Showing Approximate Placement of Major Hardware Components

After crossing into the analog side of the PCB, it is desired to have the signal enter the conditioning topology as soon as possible. Two current conditioning topologies are needed on the left and right hand side to minimize the signal path lengths. Each of these topologies requires the +10 V precision reference as well. The reference needs access to the +15 V source as well as the current conditioning topologies. The ±15 V source should be brought into the center of the analog region since all topologies require both rails. The distance topologies fit into the area that remained.

The expected current return paths that are of significant interest are shown in Figure 6.40. The converters are connecting to the +24 V bus and the coil through screw terminals for this design. The eliminates the need for passing high currents through the UIFESS Driver PCB at all. Any noise associated with switching the high currents is kept primarily in the converter PCB. A ground connection between the converter and UIFESS Driver PCB still exists, but minimal noise should transfer from the converter to the UIFESS Driver PCB.

The logic level shifters send high frequency signals back and forth between the microcontroller and the converter, so return currents in the ground plane are present. The return current of the current sensor signals is of interest. Current sensor 1 and current sensor 4 each take a short path to the conditioning topology, and a relatively short return path. The return paths have a potential to cross under the logic level shifters. However, current sensor 2 and current sensor 3 take a significantly longer path to reach the conditioning topology. The DC and low frequency current return path pass directly through two logic level shifters. This introduces noise and voltage drop into the current sensor signal. It is decided to place a cutout in the ground plane to steer the return currents from passing near so many logic traces. The return paths still pass through some logic traces, but the situation is unavoidable for the configuration.

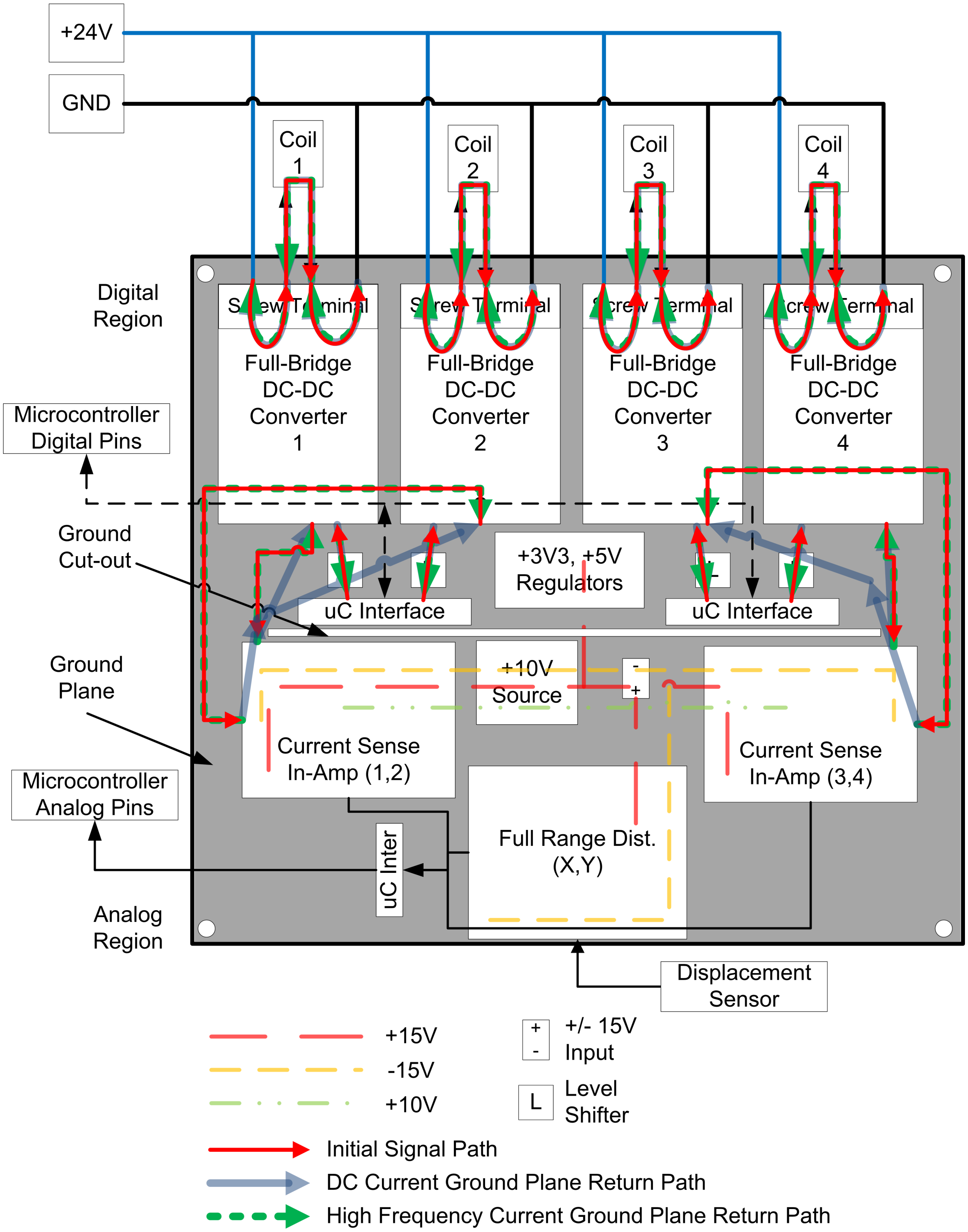

Figure 6.40: UIFESS Driver Version 1 PCB Block Diagram Showing Anticipated Major Current Return Paths

Each side of the logic level shifter channel sources approximately 5 μA of current when stepping the voltage from 3.3 V to 5 V [50]. This minimal amount of current creates minimal noise in the current sensor signal return path.

First Layer The top copper layer of the physical PCB is shown in Figure 6.41. The red lines are traces making electrical connections and the red polygons are solid copper. Note the location and orientation of the 4 full-bridge converters. The current sensor signals are implemented with guard traces in a similar fashion to the Prototype PCB. The microcontroller digital and analog interfaces work in the same manner as the Prototype PCB. The Kaman distance sensor outputs are brought to the PCB in the same method as the Prototype PCB. The +15 V copper plane crosses into the digital side of the PCB to power the voltage regulators. The -15 V plane is brought to the distance scaling topologies through the top layer since the topologies are positioned such that the voltage rails are not constrained to the second layer only.

The top layer contains all the components for the signal conditioning circuits. A group of two in-amp current sensor conditioning topologies are located on either side of the PCB, for a total of four current signal conditioning topologies. Two distance signal conditioning topologies are located near the bottom of the PCB.

The text that appears on the PCB is from the Silkscreen layer. The text is intended to help identify the PCB, as well as identify specific parts on the PCB.

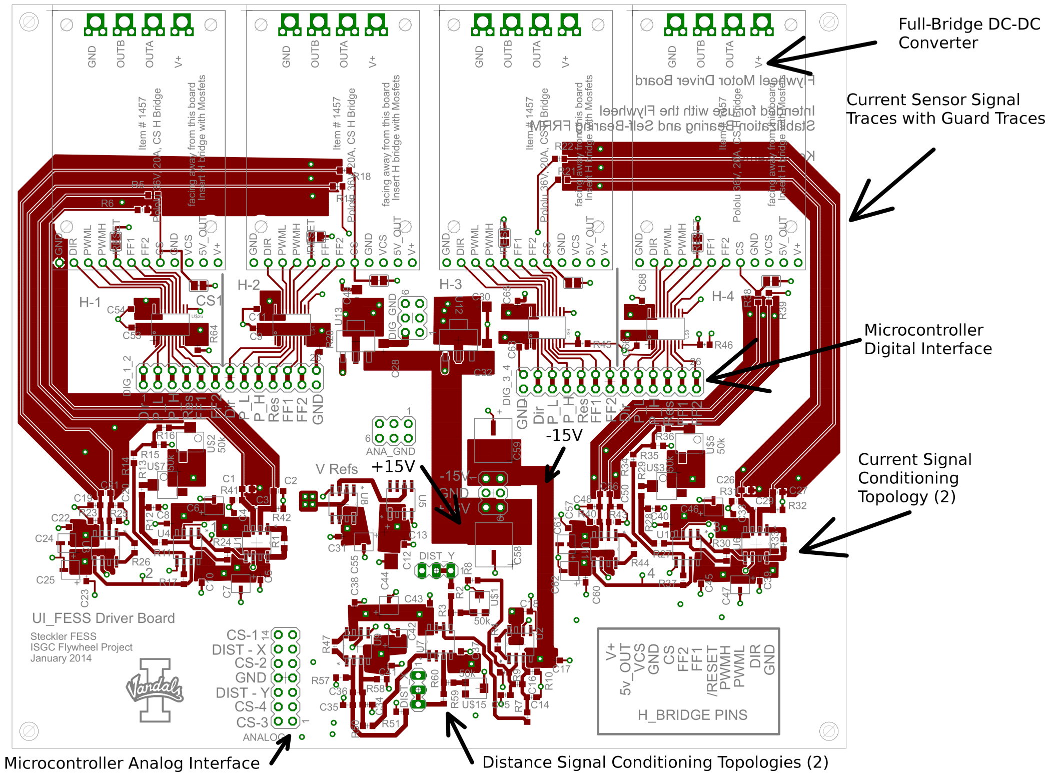

Figure 6.41: UIFESS Driver Version 1 PCB Top (Component) Layer

Second Layer The second layer of the PCB containing the ±15 V power planes and the +3.3 V and +5 V power planes that originate from the regulators is shown in Figure 6.42. The +5 V power plane can be seen making connections to the logic level shifters as well as the current sensor power input. The +3.3 V plane is connected to the logic level shifter.

The -15 V rail actually has two separate planes in the second layer. The plane closest to the digital side of the PCB delivers -15 V to the current signal conditioning topologies. The +15 V plane is able to deliver +15 V to all conditioning topologies. The -15 V plane could have wrapped around the +15 V plane and been able to deliver -15 V to the distance signal conditioning topologies, but the plane would be significantly long. A large enough area existed in the top layer to use a large copper trace to connect the -15 V planes in the second layer using vias.

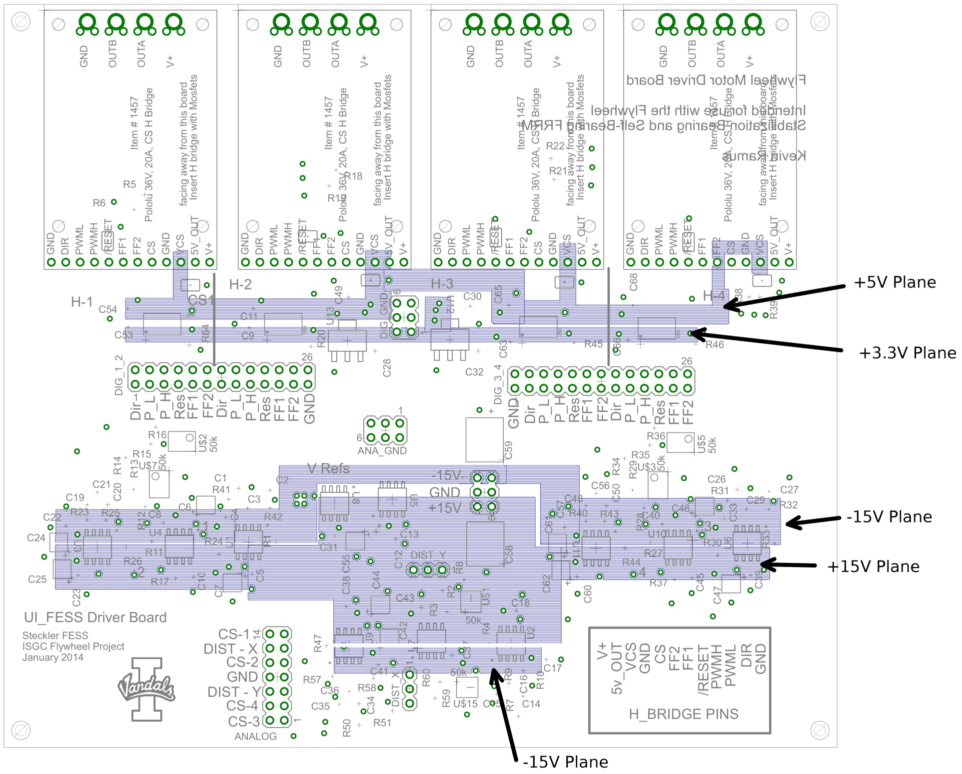

Figure 6.42: UIFESS Driver Version 1 PCB Second (Power Plane) Layer

Third Layer The ground plane of the PCB is shown in Figure 6.43. Note the ground plane is solid, except for the cutout in the center of the PCB. The cuts increase the length of the current signal low frequency return path, but steer the return path through a less noisy environment.

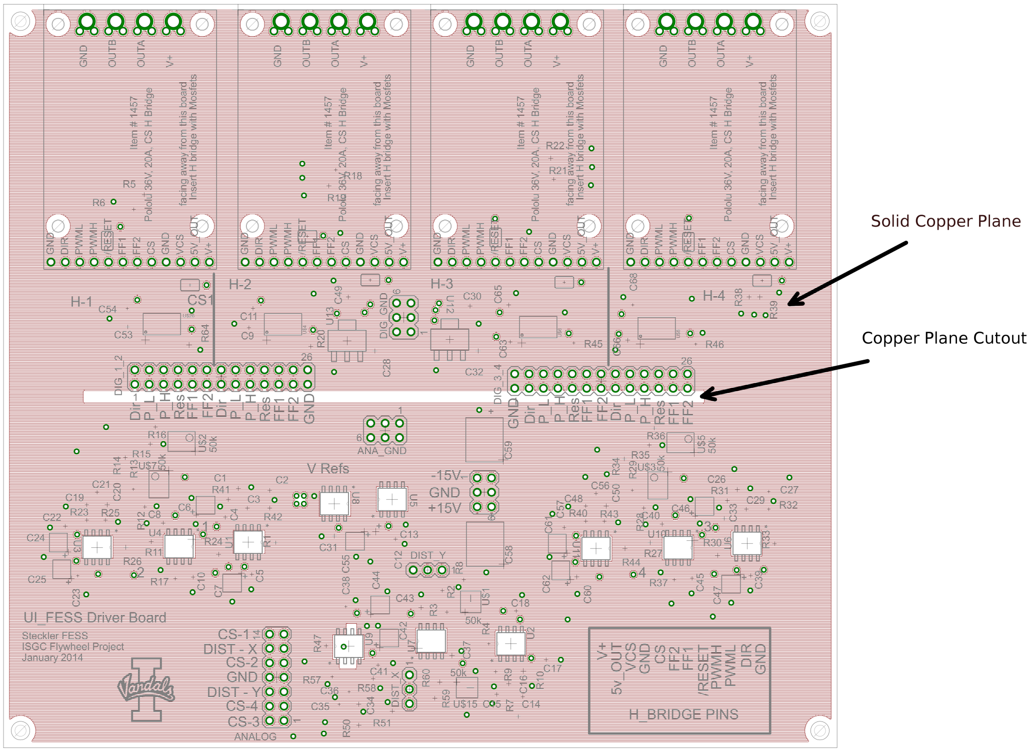

Figure 6.43: UIFESS Driver Version 1 PCB Third (Ground Plane) Layer

Fourth Layer The bottom copper layer of the PCB is shown in Figure 6.44. The +10 V precision voltage reference plane is brought down to this layer to reach the current sensor signal conditioning topologies. Much of the second layer area in the region is used for the ±15 V rails, and a simple orientation does not exist to deliver the +10 V to the desired areas. The fourth layer has plenty of space to house the +10 V plane.

The analog portion of the PCB houses the signal conditioning topologies as well as the analog interface with the microcontroller. The fully conditioned signals leave each conditioning topology and connect to the interface. Guard traces are implemented to help reduce cross talk between the conditioned signals that run near each other for extended lengths. The Prototype PCB uses a similar method with the conditioned analog traces being run on the bottom layer without issue, so it is decided to maintain this practice.

Additional information about the UIFESS Driver Version 1 PCB is shown in Appendix C. The bill of materials is shown in Appendix E. The actual populated

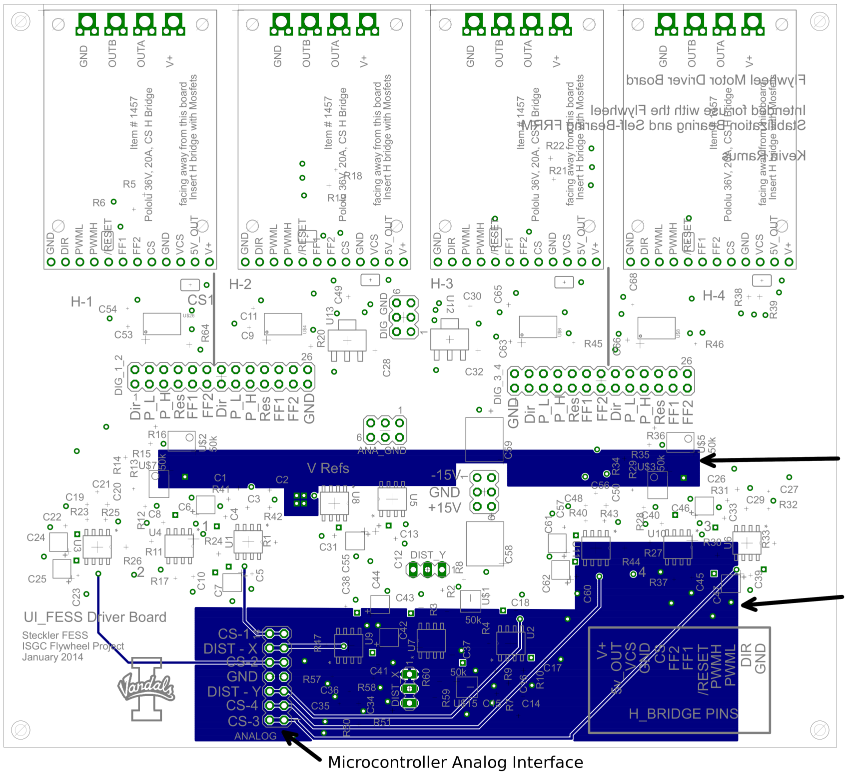

+10V Plane

Analog Signal Traces with Guard Traces

Microcontroller Analog Interface

Figure 6.44: UIFESS Driver Version 1 PCB Fourth (Solder Plane) Layer

UIFESS Driver Version 1 PCB is shown in Figure 6.45. The results are discussed in Section 7.3.

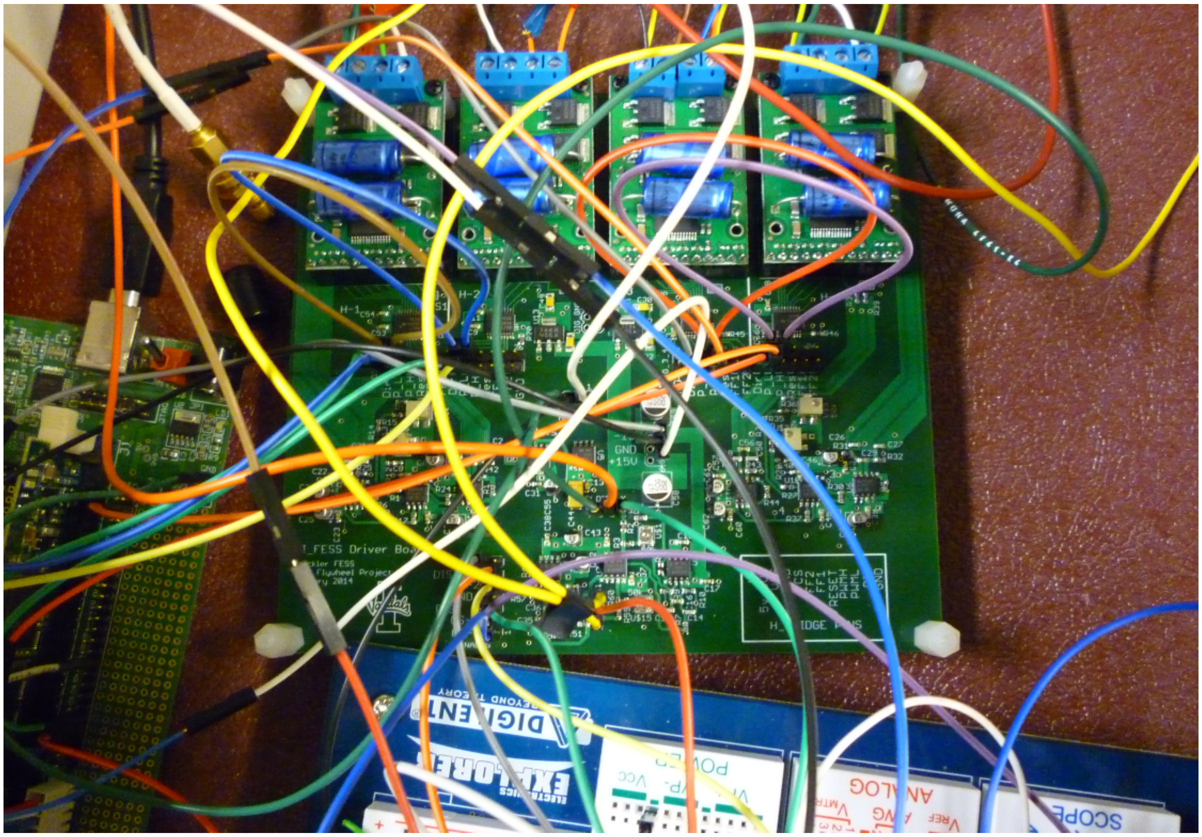

Figure 6.45: The Fully Populated and Functional UIFESS Driver Version 1 PCB. Note the Four Pololu Power Amplifiers are Installed on the PCB

6.3.3.3 UIFESS Driver Version 2

The purpose and design methodology for UIFESS Driver PCB Version 2 is the same as the UIFESS Driver PCB Version 1, as stated in Section 6.3.3.2. The UIFESS Driver Version 2 PCB corrects the few issues the UIFESS Driver Version 1 PCB had. Eight of these PCBs were purchased and enable all desired aspects of the UIFESS, rotation and air gap control. The UIFESS Driver PCB Version 2 has the same schematic connections and physical layout.

The GND pins on the Microcontroller Analog Interface were electrically connected to the PCB Ground. The Microcontroller Analog Interface labels are repositioned to avoid being covered when the male header pins are installed.

The four unnecessary stopmask cutouts present in the region near capacitors C5 and C7 are removed. The order of the silkscreen text box labels for the H-Bridge pins is corrected. Additional labels to identify the orientation of the connections for the H-Bridge screw terminals are added. A silkscreen box is added to enable assigning each PCB a specific number to allow future users to keep track of specific PCBs. A multiple layer view of the UIFESS Driver Version 2 PCB is shown in Figure 6.46. Note the copper filled polygons are not filled to keep the image simple to view. Additional information about the UIFESS Driver Version 2 PCB is found in Appendix D. The bill of materials is shown in Appendix E. The unpopulated PCB is shown in Figure 6.47. Results of the PCB are discussed in Section 7.4.

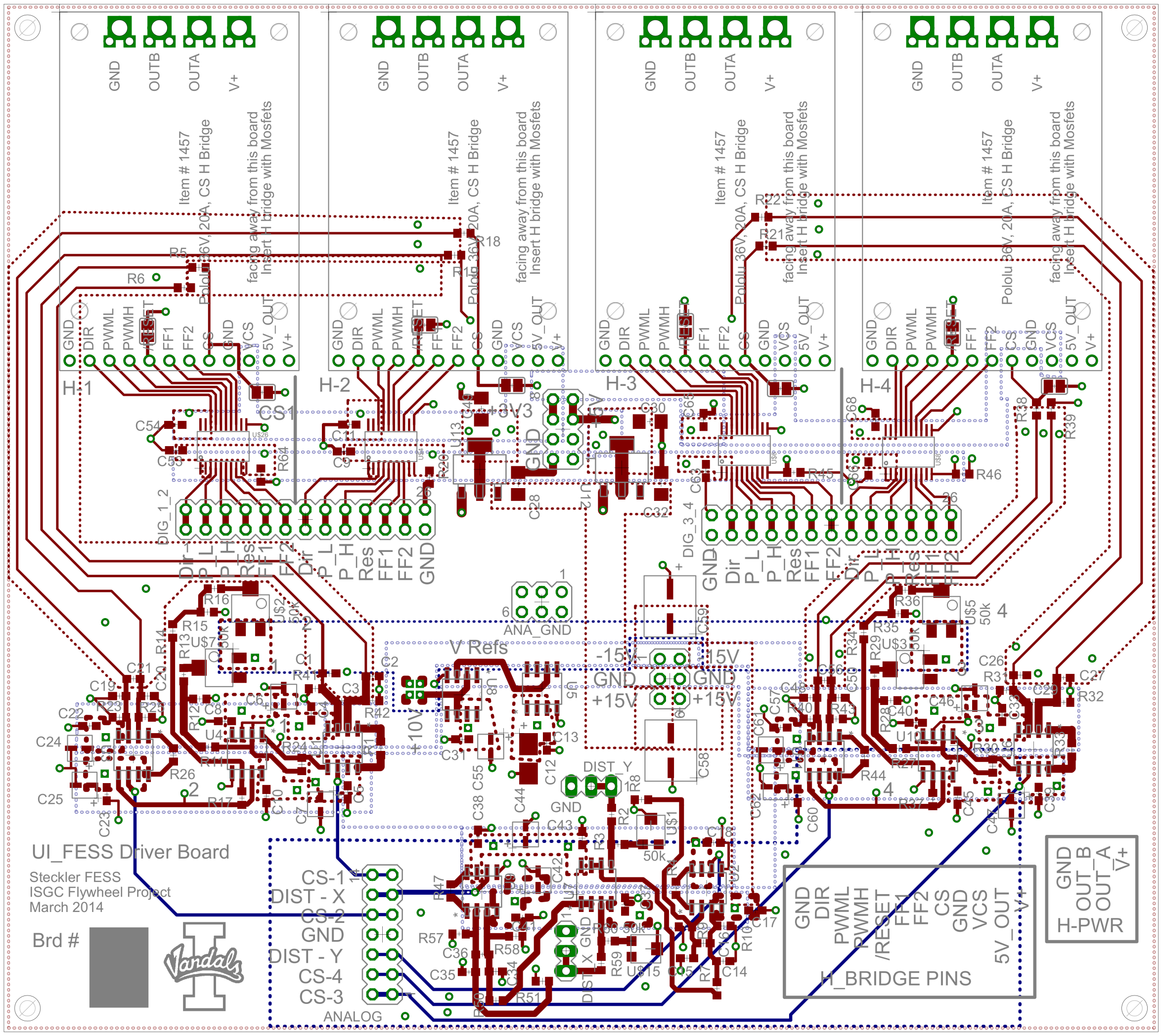

Figure 6.46: Multilayer View of UIFESS Driver PCB Version 2

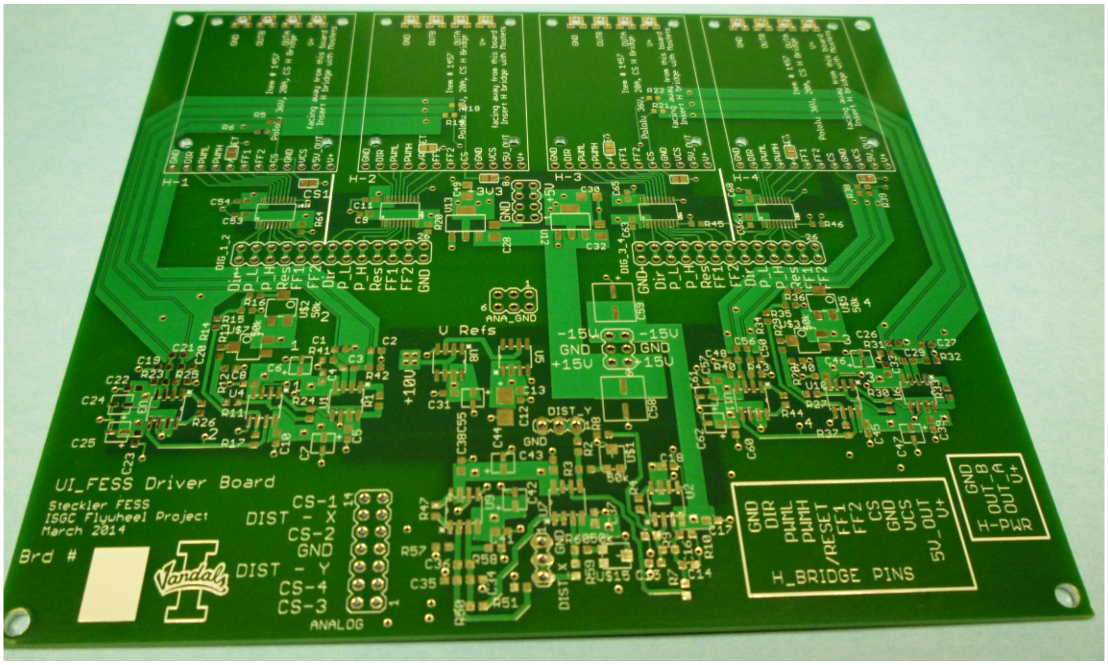

Figure 6.47: The Unpopulated UIFESS Driver PCB Version 2 PCB

Chapter 7

Hardware Implementation Results

7.1 Introduction

The results of the sensor signal conditioning topologies when placed on the custom designed PCBs are discussed. The Prototype PCB is first designed to investigate each of the signal conditioning topologies for the displacement sensor and the current sensor. These topologies are discussed in Section 6.2. The Prototype PCB is then used to test the air gap control algorithm on the Single Axis Single Bearing (SASB) demonstration unit that is discussed in Section 1.4. After successful air gap control, the UIFESS Driver #1 PCB is then designed. This board uses the design principles verified by the Prototype PCB. Two of these PCBs are purchased for use on the UIFESS itself. This PCB demonstrates successful 2-axis air gap control on the Stabilization Bearing (SB) of the UIFESS. Minor adjustments are made to the UIFESS Driver #2 PCB. A total of 8 of the UIFESS Driver #2 PCBs are purchased to enable air gap control and rotation of the flywheel. The major components and development path of the PCBs is shown in Figure 7.1.

7.2 Prototype PCB Results

7.2.1 Signal Conditioning Topology Results

The results of each sensor topology are presented. The sensor topologies discussed are located on the Prototype PCB.

7.2.1.1 Full Range Displacement Sensor Topology Results

The simulated circuit from Figure 6.7 is reproduced on the Prototype PCB. A Digilent Electronics Explorer Board with software enabling a network analyzer is used to conduct

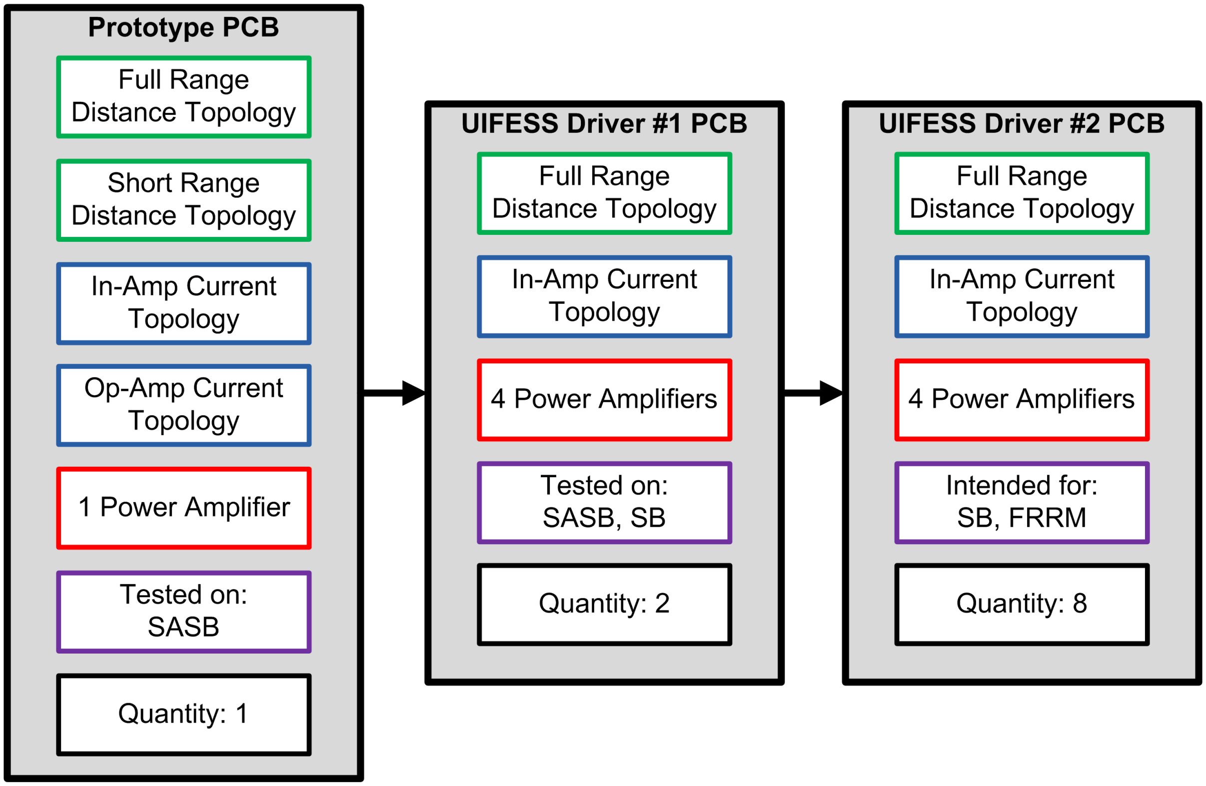

Figure 7.1: Major PCB Components and Order of Design

an AC frequency sweep of the circuit topology on the PCB. A comparison between the TINA simulation and the experimental network analyzer data is shown in Figure 7.2. Major specifications are highlighted in Table 7.1.

Table 7.1: Full Range Displacement Sensor Topology Comparison of Specifications

Specification	TINA Simulation	PCB Result	Error
Passband Gain [dB]	-10.9045	-11.1577	2.32%
Cutoff Frequency	5.248 kHz	5.417 kHz	3.21%
3-dB Down Magnitude [dB]	-13.9344	-14.197	1.88%
3-dB Down Phase	-45.7944°	-45.7267°	-0.15%
Propagation Delay [μs]	3.1802	3.1755	-0.15%

The PCB results closely match the TINA simulation results. The PCB passband gain is not exactly the same as the TINA simulation. Each PCB topology has a slightly different passband gain due to varying components. The actual passband gain is used to generate a custom equation for each distance topology. For this instance, the gain of the

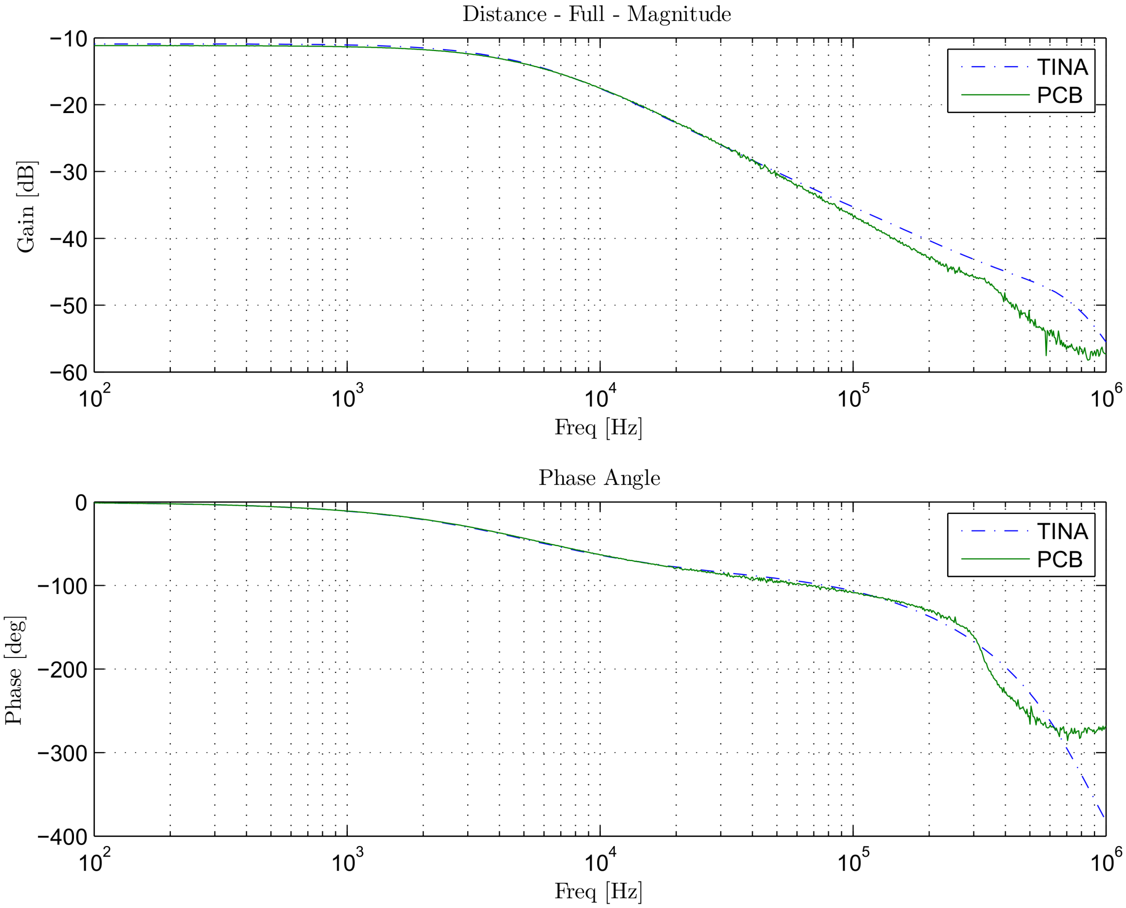

Figure 7.2: Full Range Displacement Sensor Topology Comparison of Simulation and PCB Results

specific Full Distance Topology on the first PCB created is shown in Equation (7.1). The ADC sampled reading is turned into a displacement by using Equation (7.2).

$$Gain_{FullDistancePCB} = -11.1577\,dB = 0.2768\,\frac{V}{V} \tag{7.1}$$

$$Displacement[mm] = 1.079757\left[\frac{mm}{V}\right] * ADC_{DistFullRange}[V] + 4.411644 * 10^{-3}[mm] \tag{7.2}$$

7.2.1.2 Short Range Displacement Sensor Topology Results

The circuit shown in Figure 6.9 is replicated on the Prototype PCB. Additional hardware is required to create adjustable bias voltages for the diodes to ensure the output is limited to 0 V to 3 V. A Digilent Electronics Explorer Board with software enabling a network analyzer is used to conduct an AC frequency sweep of the circuit topology on the PCB. A comparison between the TINA simulation and the experimental network analyzer data is shown in Figure 7.3 and Table 7.2.

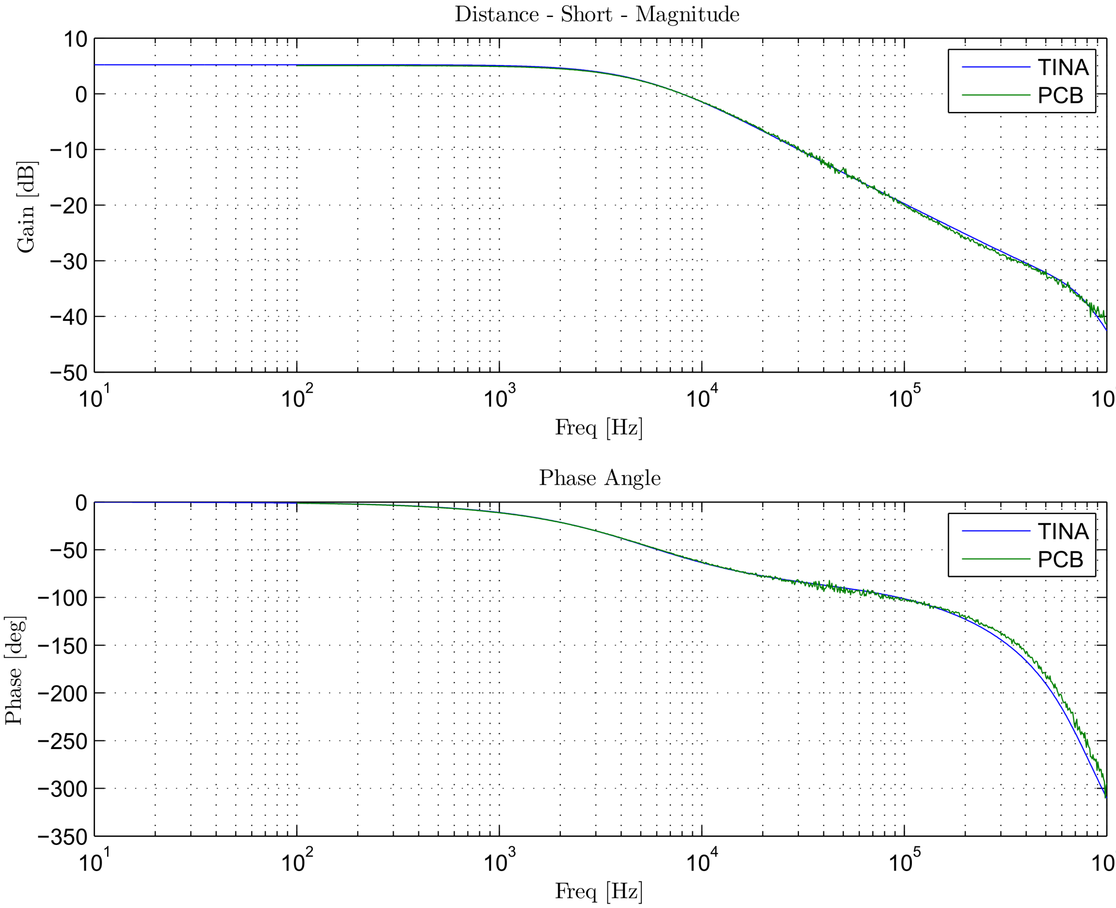

Figure 7.3: Short Range Displacement Sensor Topology Comparison of Simulation and PCB Results

The PCB results closely match the TINA simulation results. The PCB passband gain is not exactly the same as the TINA simulation. Each PCB topology has a slightly different passband gain due to varying components. The actual passband gain is used to generate a custom equation for each distance topology. The short-range ADC sampled output of Kaman Displacement Sensor #1 is turned into a distance in millimeters using

Table 7.2: Short Range Displacement Sensor Topology Comparison of Specifications

Specification	TINA Simulation	PCB Result	Error
Passband Gain [dB]	5.2196	5.0644	-2.97%
Cutoff Frequency	5.248 kHz	5.367 kHz	2.27%
3-dB Down Magnitude [dB]	2.184	2.0288	-7.13%
3-dB Down Phase	$-45.7151\,^{\circ}$	$-45.9246\,^{\circ}$	0.46%
Propagation Delay [μs]	3.1747	3.1892	0.46%

Equation (7.3).

$$Displacement[mm] = 0.163745\left[\frac{mm}{V}\right] * ADC_{DistShortRange}[V] + 0.757614[mm] \tag{7.3}$$

7.2.1.3 In-Amp Current Sensor Topology Results

The simulated circuit from Figure 6.15 is reproduced on the Prototype PCB. The data presented in this section pertains to the in-amp Current Sensor Topology on the UIFESS Driver Version 1 PCB of Section 7.4. Specific techniques of PCB implementation are discussed in Section 6.3.2. The Digilent Electronics Explorer Board network analyzer is used to conduct an AC frequency sweep of the circuit topology on the PCB. A comparison between the TI-TINA simulation and the experimental network analyzer data is shown in Figure 7.4 and major specifications are highlighted in Table 7.3.

Table 7.3: In-Amp Current Sensor Topology Comparison of Specifications

Specification	TINA Simulation	PCB Result	Error
Passband Gain [dB]	3.4680	3.4685	0.01%
Cutoff Frequency	77.983 kHz	78.505 kHz	0.67%
3-dB Down Magnitude [dB]	0.4529	4.6634	2.96%
3-dB Down Phase	$-52.84\,^{\circ}$	$-50.36\,^{\circ}$	-4.69%
Propagation Delay [μs]	3.67	3.50	-4.69%

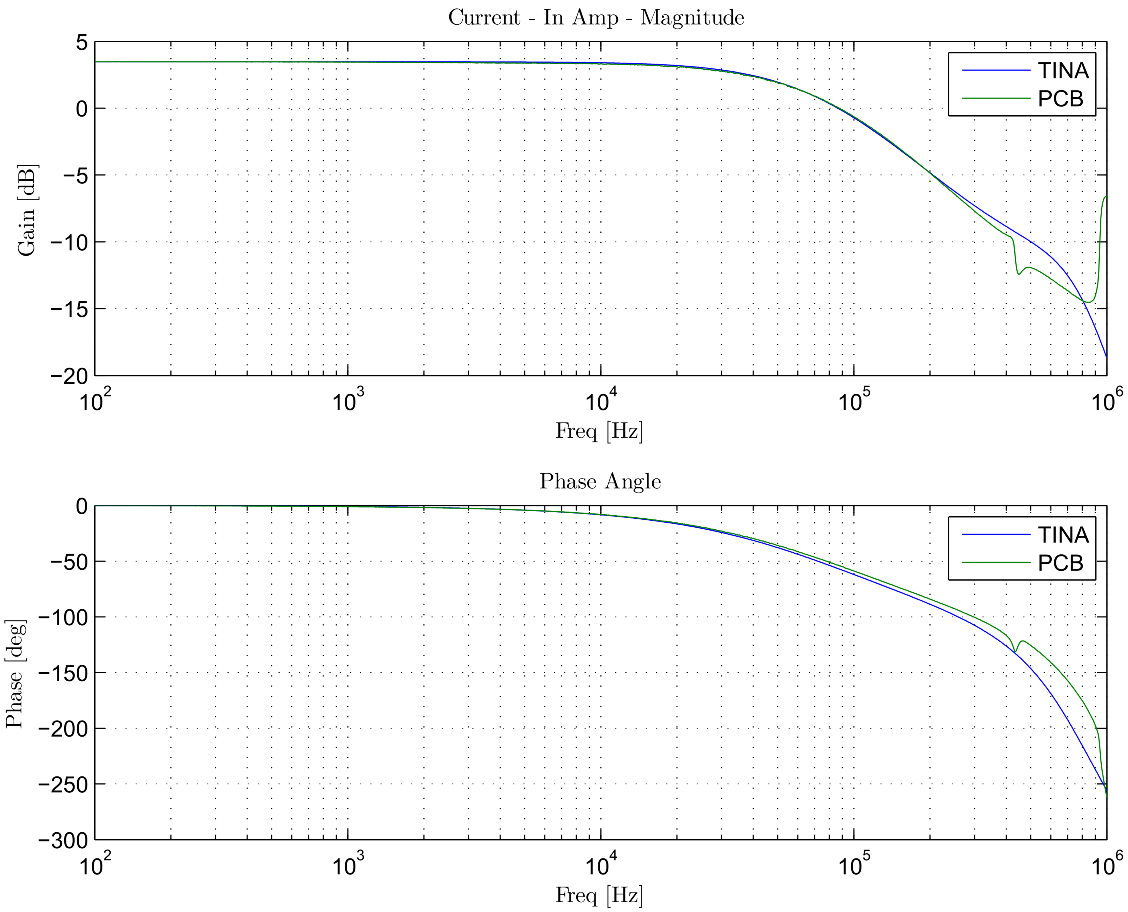

Figure 7.4: In-Amp Current Sensor Topology Comparison of Simulation and PCB Results

The PCB results closely match the TI-TINA simulation results. There are 28 current sensors, and significant time may be spent to obtain a specific gain for each individual sensor and develop its own custom equation for converting the ADC sample into a current. In addition, specific ADC channels would have to be attached to specific sensors. Instead, it is desired to have a universal equation for all current sensors that will give a close enough result.

Recall the measured current can be converted into an output voltage using Equation (6.11). An equation to relate the ADC sampled voltage into a current is desired. The gain from Equation (6.18) and offset from Equation (6.21) is used to convert Equation (6.11) into an equation that relates the ADC sampled voltage, V_{ADC}, to the current in the coil, I_{Coil}.

$$V_{ADC}[V] = \left[0.66\left[\frac{mV}{A}\right] * I_{Coil}[A] + 2.5[V]\right] * Gain_{INA129} + V_{Shift} \tag{7.4}$$

$$V_{ADC}[V] = 0.0986\left[\frac{mV}{A}\right] * I_{Coil}[A] + 3.735[V] + V_{Shift} \tag{7.5}$$

$$I_{Coil}[A] = 10.14158\left[\frac{A}{V}\right] * V_{ADC}[V] - 15.06024[A] \tag{7.6}$$

7.2.1.4 Op-Amp Current Sensor Topology Results

The circuit shown in Figure 6.17 is replicated on the Prototype PCB. Additional hardware is required to scale the shifting voltage. A Digilent Electronics Explorer Board with software enabling a network analyzer was used to conduct an AC frequency sweep of the circuit topology on the PCB. A comparison between the TI-TINA simulation and the experimental network analyzer data is shown in Figure 7.5 and Table 7.4.

Table 7.4: Op-Amp Current Sensor Topology Comparison of Specifications

Specification	TINA Simulation	PCB Result	Error
Passband Gain [dB]	3.5218	3.5466	0.70%
Cutoff Frequency	61.376 kHz	64.092 kHz	4.43%
3-dB Down Magnitude [dB]	0.4463	0.4934	10.55%
3-dB Down Phase	-95.40°	-78.4401°	-17.78%
Propagation Delay [μs]	6.63	5.4472	-17.78%

The PCB results match the simulation results in the lower frequency region. The PCB filter attenuation does not fall off as rapidly as the simulated results after the 3-db point is reached. At a frequency of approximately 350 kHz, the gain increases before attenuating again. When the op-amp current sense topology is attached to ADC channels with the diode suppression circuits present, an unknown condition occurs, and the signal being sampled by the ADC has a substantial 350 kHz component, which greatly reduced

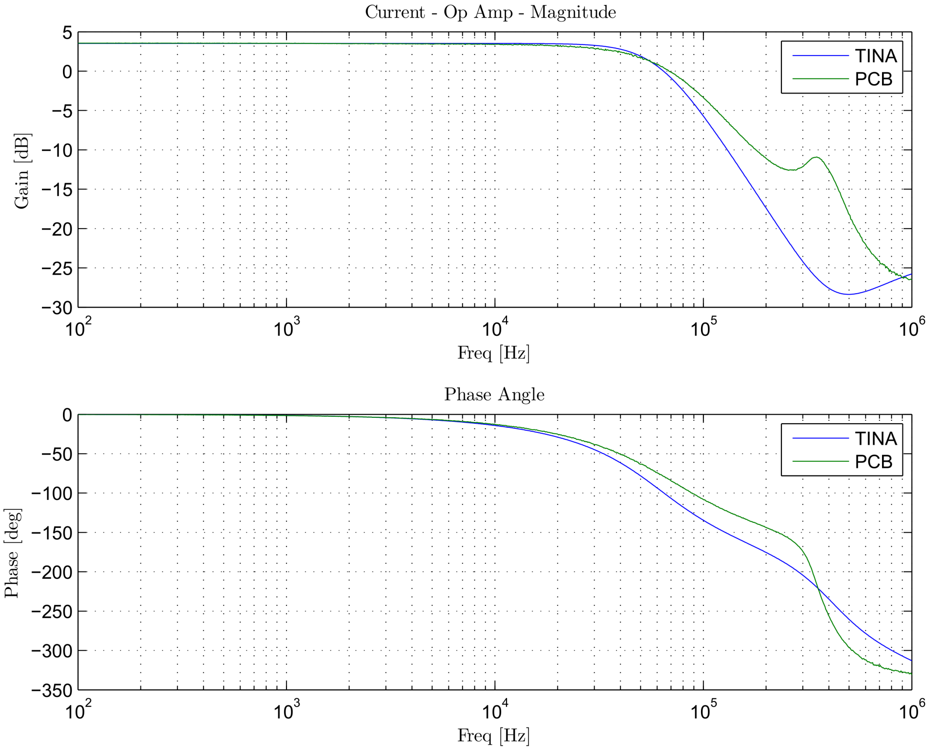

Figure 7.5: Op-Amp Current Sensor Topology Comparison of Simulation and PCB Results

performance. For these reasons, the op-amp current sensor conditioning circuit is not used on future designs.

The ADC sampled voltage is converted into a distance in millimeters using Equation 7.7.

$$I_{Coil}[A] = 10.10313 \left[\frac{A}{V}\right] V_{ADC}[V] - 15.14674[A] \tag{7.7}$$

7.2.2 Signal Conditioning Topology Comparison

Results It is now desired to test the Prototype PCB designs. A function generator was attached to each sensor topology. Expected voltage levels and various frequencies were sent through each topology to ensure the topology would not output a voltage that could harm or interfere with the microcontroller ADC.

After ensuring the topologies would not output voltages that would harm the microcontroller ADC, an attempt could be made using the prototype PCB and microcontroller to demonstrate control on the SASB demonstration unit. The microcontroller was programmed with the control algorithm[12], and the sensor topology outputs are connected to the ADC. The SASB electro-mechanical system is set up for a test, and air gap control is successfully demonstrated. The results show the controller algorithm itself is well-designed, and the sensor data the algorithm receives allows the controller to obtain an accurate portrayal of the electro-mechanical system current and distance.

Air gap control was successfully demonstrated using each combination of current and distance topologies. The current topology using either the in-amp or op-amp is demonstrated using the full-range distance topology as well as the short-range distance topology. A decision must be made on which topology should be used for the distance and current signals on later design iterations.

Distance Topology Comparison The air gap controller commands a step change in the desired distance to be maintained, shown in Figure 7.6. Initially, the controller has been maintaining a 1.000 mm air gap between the iron U-shaped bar and the flotor bar. The step change occurs, and the new commanded air gap to be maintained is 1.100 mm. A readily available redundant means of verifying the air gap down to single micrometers is not available. It is decided comparing the topology outputs to the output straight from the Kaman displacement sensor itself would suffice. The full-range distance sensor topology is used to maintain air gap control for the data in Figure 7.6. The Digilent Electronics Explorer Board oscilloscope is used to simultaneously capture the Kaman distance sensor output, the output from the full-range distance topology, and the output from the short-range topology.

Both the full-range and short-range topologies follow the Kaman sensor output very well. The solid (blue) line shows the Kaman distance senor output. The dotted-dashed (green) line shows the full-range topology output. During transients, such as the time

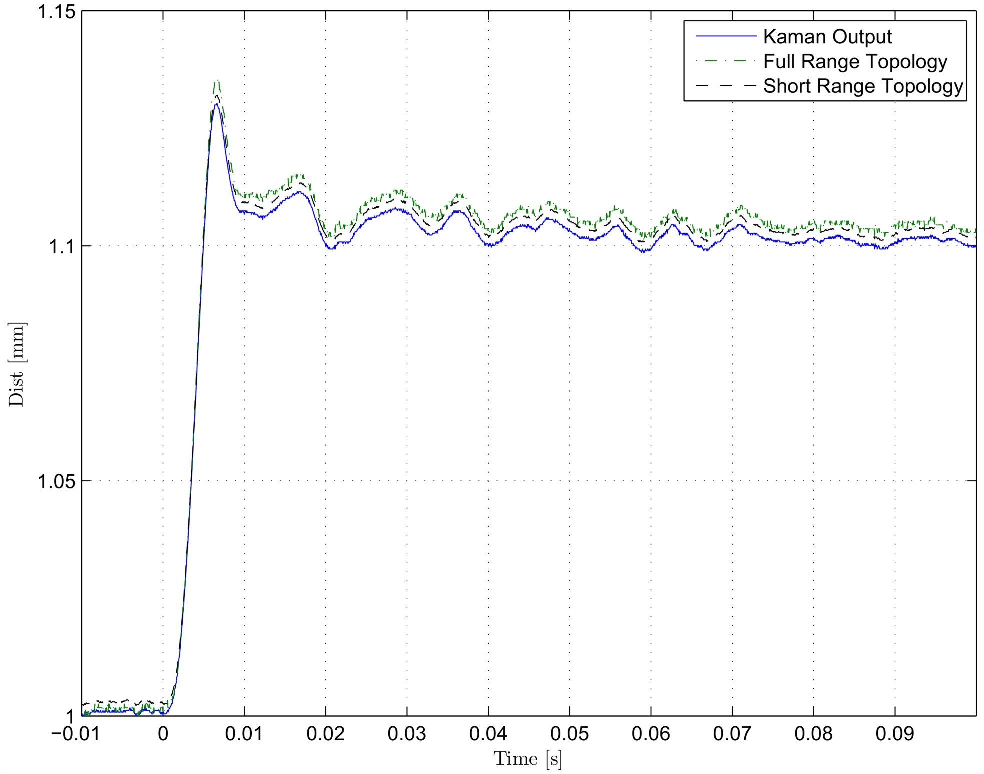

Figure 7.6: Prototype PCB Distance Sensor Topology Comparison

immediately following the step change, there is an approximate 6 μm difference between the full-range topology output and the Kaman output. When the system reaches a steady-state condition, such as the time before the step change, there is a near negligible difference in output. The dotted (red) line shows the short-range distance topology output. There is an approximate 3 μm difference between the short-range topology output and the Kaman output.

The short-range distance topology follows the Kaman output slightly better compared to the full-range topology. However, the difference in performance is not significant. The short-range distance topology requires significantly more hardware compared to the full-range distance topology, as well as only providing useful output over a significantly lower displacement range. It is decided the full range of the distance sensor is desired for yet-to-be-determined applications for the UIFESS, or other future applications, and the slightly better performance the short-range distance topology could offer is not worth the lack of range. It is decided to use the full-range distance topology for future PCB designs.

Current Topology Comparison A comparison between the op-amp and in-amp current sensing topolgies, as well as how each compares to the current as seen by the Tektronix AM503A Current Probe Amplifier, is shown in Figure 7.7. The Tektronix probe provides an entirely separate means of sensing the current in the coil, and will serve as a verification of the current sensor.

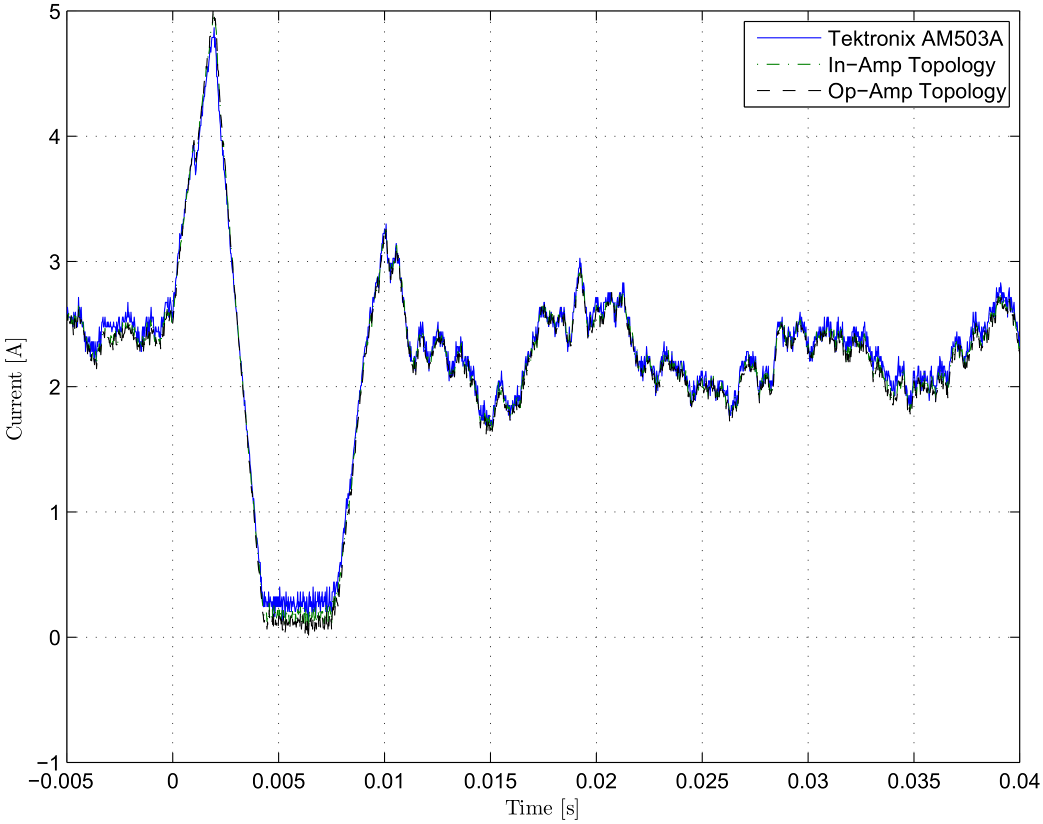

Figure 7.7: Prototype PCB Current Sensor Topology Comparison

The solid (blue) line is the current as seen by the Tektronix probe. The in-amp current topology is the dotted-dashed (green) line while the op-amp topology is the dotted (red) line. During the capture, the microcontroller ADC is reading the in-amp topology to determine the current in the coil. The PCB topologies closely follow the Tektronix probe output. Both topology outputs are typically within 100 mA of the Tektronix probe. At the worst, the currents are within 200 mA of each other. The in-amp and op-amp current sense topologies both output similarly shaped waveforms. No qualitative difference is determined while the control is active. The flotor bar behaved similarly to externally applied forces for each topology. Each topology offers similar performance, so either topology could be used.

However, additional testing discovered a scenario where the in-amp topology offered a distinct advantage. The TMS320F28335 has a 16 channel ADC. Clamping diode protection is present on 12 of the 16 channels. When the op-amp topology is connected to an ADC channel with the clamping diode protection, a situation occurs where a significant enough amount of high frequency noise can get through and skew the data. Control is still achievable, but controller stability and performance is significantly reduced.

The SASB demonstration unit only uses one coil. In order to control the flywheel, 24 coils are used on the FRRM self-bearing alone. There is significantly more noise in the flywheel environment due to the amount of coils and currents in close proximity. Additionally, the connections from the PCB to the microcontroller ADC may be longer and in closer proximity to multiple other ADC channels as well as digital switching lines. A significant amount of additional noise has the potential to be introduced to the current signal when the power electronics are applied for flywheel use. The in-amp topology's high CMRR may be required for successful implementation, and considerable time would have to be spent if a redesign is required. For these reasons, the in-amp topology is selected over the op-amp topology.

7.2.3 Other Considerations

Common-Mode Choke Comparison It is desired to determine if the common-mode choke improved controller performance in any way. The common-mode choke heavily attenuates high frequency noise that is picked up in the coil. Control is implemented with and without the choke and the distances and currents are shown in Figure 7.8 and 7.9. These captures are obtained for a step change command from 1.00 mm to 1.10 mm in the commanded air gap. The controller uses the full-range distance topology output to test control with and without the choke in place. The controller also uses the op-amp current sensor topology output.

It is observed that there is no significant difference between using the choke or eliminating it. The choke may prove to be useful when the power electronics are used on the actual flywheel. There are many coils and currents in close proximity, with substantial line lengths between the coil and the power electronics. However, the choke takes up significant board space on the PCB. It is decided to not include the choke in the next iteration of power electronic board design.

If significant high-frequency interference is present and it is believed the choke reduces the interference, it can be added after the fact. A commercially available choke that is not surface mount could be used off of the power electronic PCBs. If it is desired to use the same surface mount choke, a single PCB could be designed that would include multiple common-mode chokes on it. The design should allow the user to cut the PCB and separate the common-mode chokes after the board is received from the board-house.

Off-Board Interfaces Transferring analog and digital signals between the microcontroller and PCB is required. The microcontroller comes with an Experimenter Kit. The Kit brings the microcontroller analog and digital pins to male header pins. The PCB is designed to bring the desired signals to male header pins as well. These header pins had the typical 0.1” pitch spacing, and simple female-female cables could be used to make the appropriate connections. A cable harness should eventually be made to provide a quick means of connecting and disconnecting the signals. This interface allowed maximum flexibility in choosing connections between the microcontroller and the PCB. In addition, the signals could be routed through an oscilloscope to have the

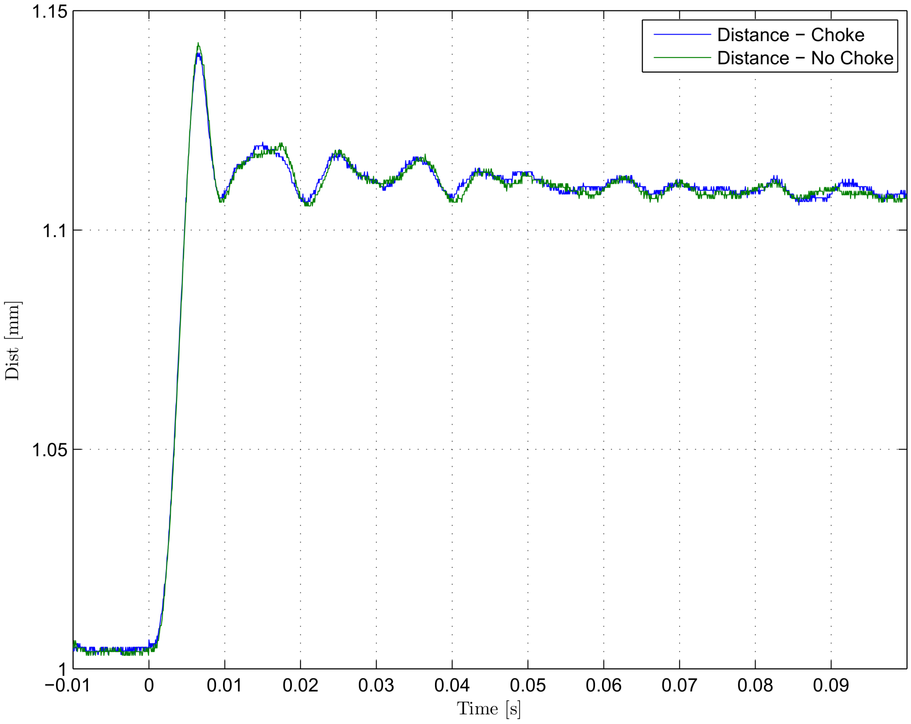

Figure 7.8: Prototype PCB Common-Mode Choke Comparison - Distance

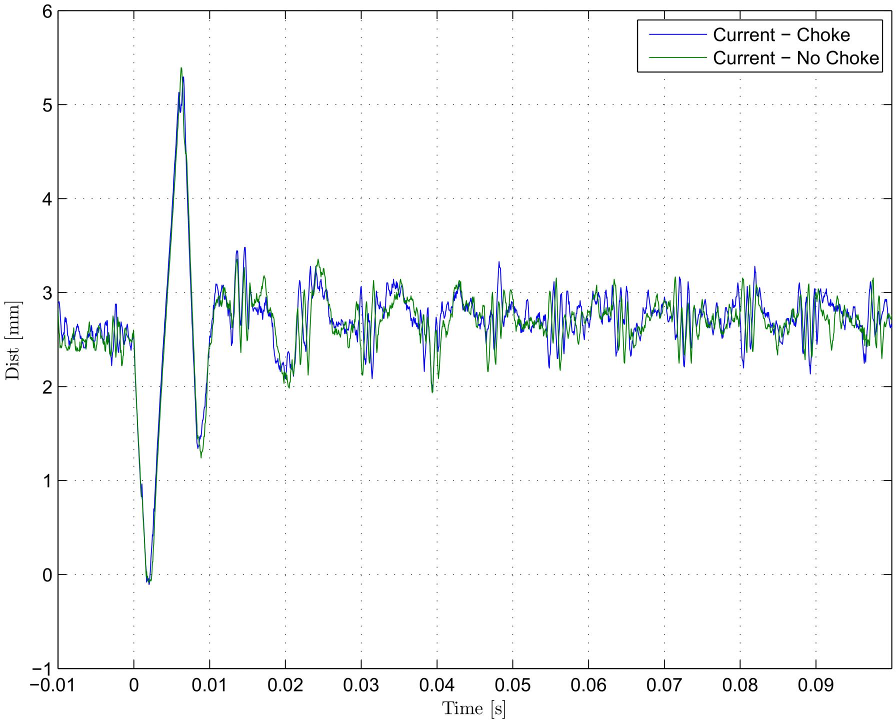

Figure 7.9: Prototype PCB Common-Mode Choke Comparison - Current

ability to see the signals the microcontroller is sending and receiving. This method works well in a prototype environment, but the extra connections have the potential to add noise to the analog signal lines before they reach the microcontroller ADC. Future design considerations to improve performance would see the elimination of the inter-board connections. Ideally, a PCB includes the microcontroller on board. The analog connections are ideally brought straight to the microcontroller ADC pins, and off-board connectors would are not required. Placing all of the required Full-Bridge DC-DC converters on a single PCB are not possible. The PCB with the microcontroller should include board to board connections to connect PCBs dedicated to housing the DC-DC converters and sensor signal conditioning topologies.

Summary The prototype PCB verified the mixed-signal design methodology. Similar design principles are applied to future PCB designs. In addition, the prototype PCB enabled investigation of various signal conditioning topologies, and provided experimental results. These results determined the full range distance signal topology and in-amp current signal topology is to be used on future UIFESS applications. It is determined the common-mode choke offered negligible affect on the SASB performance, and did not warrant the board space it would require. An off-board choke could be added to the power electronics for use in future applications. The inter-board connections for analog and digital signals between the PCB and microcontroller worked well for a prototype environment.

7.2.4 Control Results

The results of the SASB control algorithm test are shown. A step change is commanded adjust the air gap from 1.00 mm to 1.10 mm. The simulated response and the distance sensor output are compared in Figure 7.10. The current must change with the change in air gap, as shown in Figure 7.11. A more detailed analysis of the control algorithm results is discussed in Kisling[12].

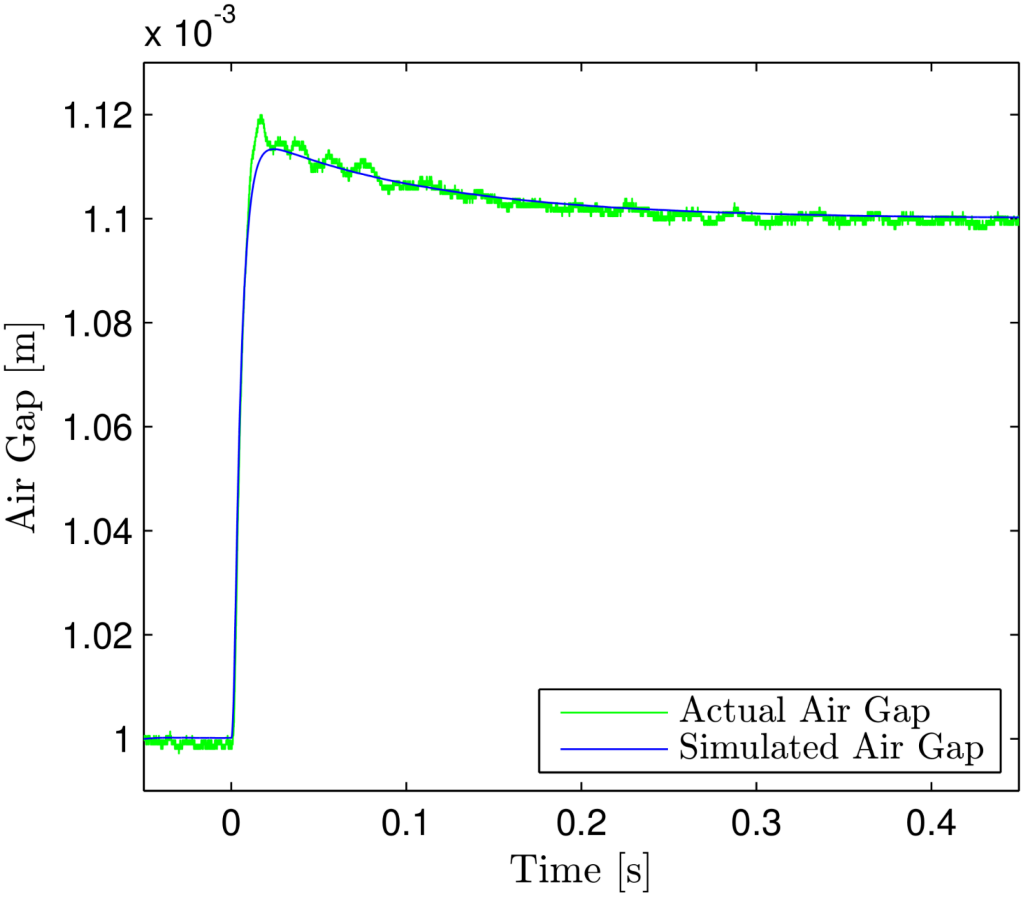

Figure 7.10: SASB Air Gap Control Distance Results

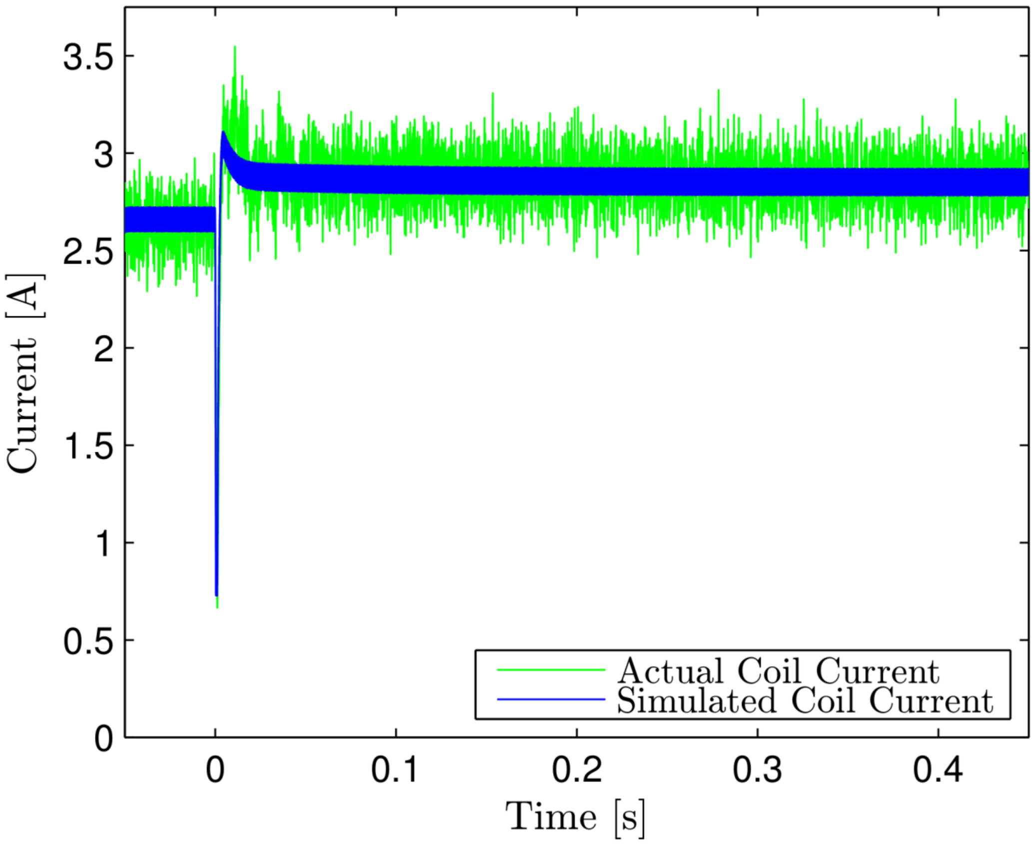

Figure 7.11: SASB Air Gap Control Current Results

7.3 UIFESS Driver Version 1 Results

The UIFESS Driver Board Version 1 is populated and ready for use. A function generator is attached to each sensor topology. Expected voltage levels and various frequencies are sent through each topology to ensure the topology does not output a voltage capable of harming or interfering with the microcontroller ADC.

After ensuring the topologies do not output voltages that would harm the microcontroller ADC, it is decided to verify control by using the SASB demonstration unit. The SASB unit's operation is well understood, and this knowledge would aid in troubleshooting any issues that may arise. The microcontroller is programmed with the same control algorithm used to test the Prototype PCB. The only difference between the tests would be the new PCB design. The test is successful, and no significant change in performance is discovered. Every combination of Full-Bridge DC-DC converter, current signal conditioning topology, and distance signal conditioning topology is tested to ensure every function on the PCB worked.

Air gap control is successful for all hardware combinations, so the UIFESS Driver 1 PCB design works controlling a single coil. The next step involves controlling multiple coils at once. A second coil with similar resistance and inductance is connected to a second Full-Bridge DC-DC converter. The control algorithm operates such that the distance sensor is read, and the current in one coil will increase or decrease as needed to maintain a distance reading of 1.00 mm. The other coil increases or decreases in the opposite direction. This is successfully demonstrated.

UIFESS Stabilization Bearing Single Axis Test With the successful demonstration of two coils on the SASB demonstration unit, control tests are conducted on the UIFESS itself. The first test on the UIFESS demonstrates control using the Stabilization Bearing in a single axis. The stabilization bearing has a non-salient rotor and a stator that contains 8 individual coils. A cross-sectional view of the stabilization bearing is shown in Figure 7.12. The non-rotating stator is located in the inner region. Coils of wire are wound around each stator leg. There are a total of 8 coils, and each coil winding is represented by the alternating light or dark trapezoidal regions on either side of the stator leg. The 1.00 mm air gap is between the outermost part of the stator and the rotor. The coils are connected in pairs, effectively creating only 4 coils that need to be controlled. Additional information about the SB is found in Section 1.3 or by referring to Kisling[12].

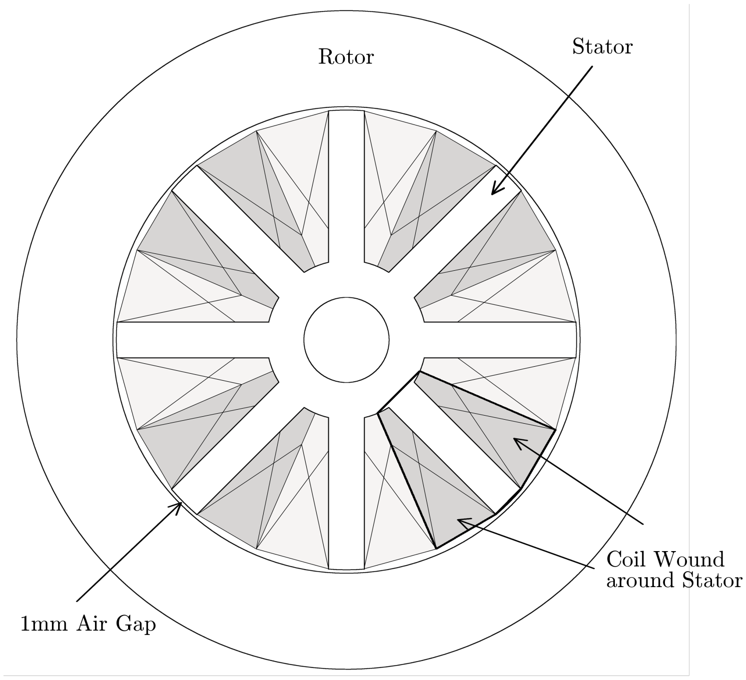

Figure 7.12: Cross-Sectional View of UIFESS Stabilization Bearing Identifying Rotor, Stator, Air Gap, and Coils

The rotor is controlled in the x axis and the y axis. A displacement sensor detects the rotor's movement along each axis, and a coil on each side of the stator pulls on either side of the rotor to maintain the spacing between the rotor and the stator. The stabilization bearing test setup is shown in Figure 7.13. Position Sensor 1 is used to measure rotor displacement in the x-axis. Coil 6 and Coil 7 are connected together in series, and is controlled by one full-bridge converter. Coil 2 and Coil 3 are connected and controlled by a second full-bridge converter.

If Position Sensor 1 determines the rotor is moving away from the sensor, in the positive x direction, then the controller will command the current in Coil 6 and Coil 7 to decrease, and command an equal increase in current in Coil 2 and Coil 3. The increased current in Coil 2 and Coil 3 creates a larger pulling force on the rotor, pulling it in the

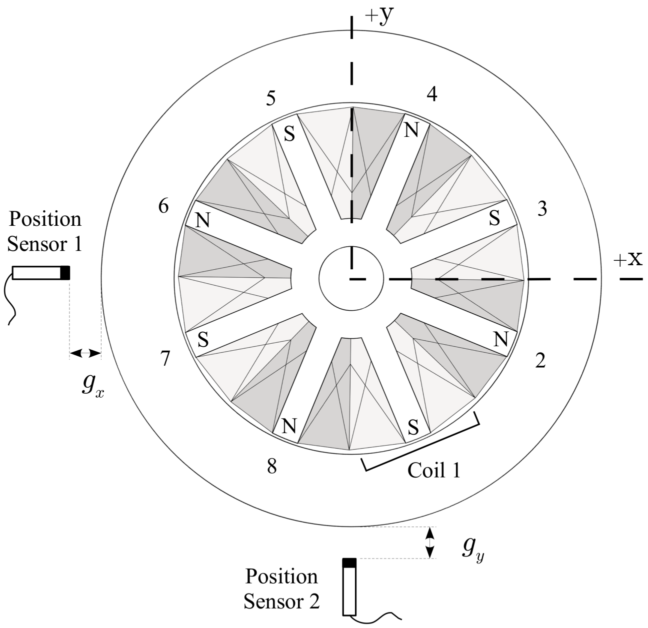

Figure 7.13: Cross-Sectional View of UIFESS Stabilization Bearing with Distance Sensors and Numbered Coils

negative x direction, and the air gap is maintained. The current flowing in Coil 2 and Coil 3 generates the flux path that results in the pulling force, as shown in Figure 7.14.

The simulated and actual results of the test are compared shown in Figure 7.15, Figure 7.16, and Figure 7.17. Control of the air gap on the SB of the UIFESS was considered successful. Additional information about the results can be found in Kisling[12].

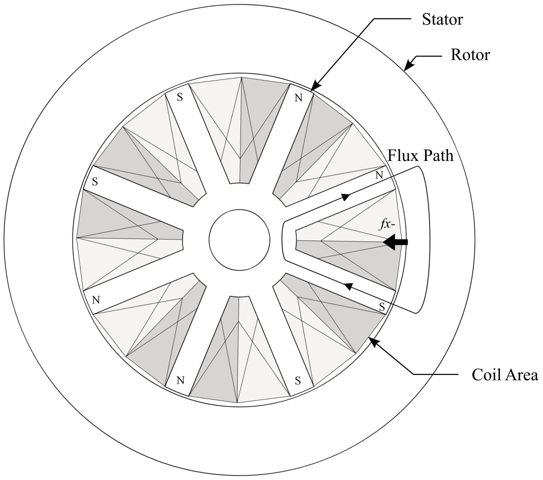

Figure 7.14: Overhead View of UIFESS Stabilization Bearing Demonstrating a Pulling Force Being Exerted on the Rotor

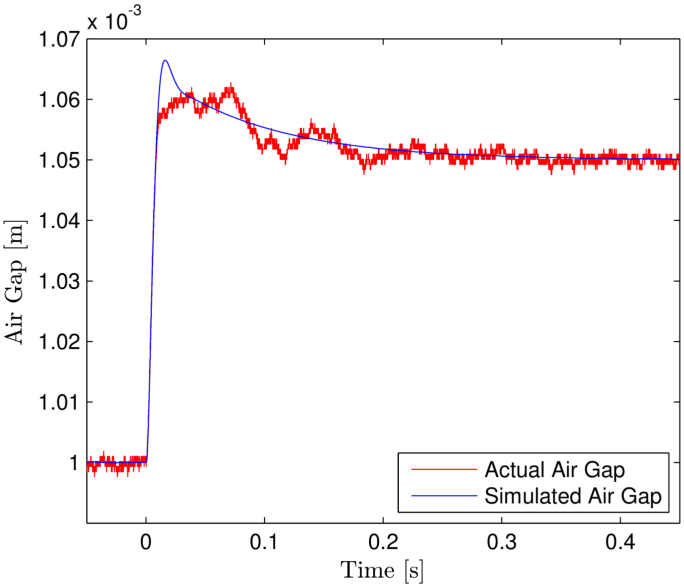

Figure 7.15: SB Air Gap Simulated and Actual Control Results for the X axis

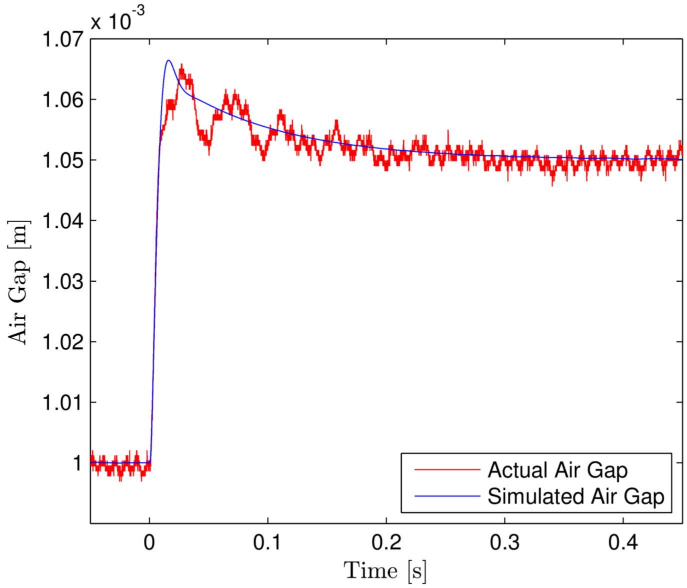

Figure 7.16: SB Air Gap Simulated and Actual Control Results for the Y axis

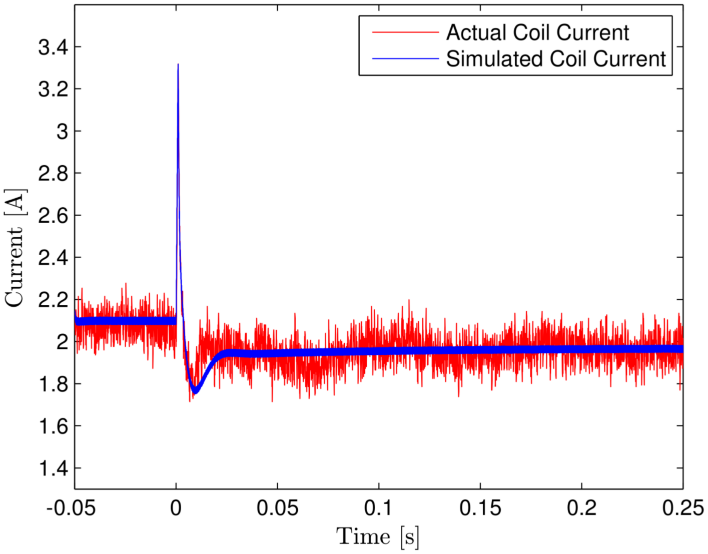

Figure 7.17: SB Air Gap Simulated and Actual Control Results for the Current flowing in Coil 6 and Coil 7

Issues Upon receiving the PCB from the board-house, multiple minor issues were discovered. None of the issues caused any reduction in the performance of the PCB. These issues are resolved on the next iteration of PCB design. Two UIFESS Driver PCB Version 1 PCBs are ordered to ensure the design works and to have the chance to correct any errors before ordering the all of the required PCBs.

The pins labeled GND on the Microcontroller Analog Interface are not grounded. These pins are not electrically connected to anything, and should not be used. In addition, the silk screen labels for the Microcontroller Analog Interface are shifted from their intended positions, and portions of the labels are covered when the male header pins are soldered in place.

The silkscreen text box labels for the pins on the Full-Bridge DC-DC converter, or H-bridge, have the incorrect orientation. The H-bridges must be placed with the MOSFET side facing upwards, away from the PCB. With the H-bridge in this orientation, the silkscreen text box labels should have GND on the left and V+ on the right to match the layout of the H-Bridge.

A stop mask layer from the Prototype PCB is accidentally carried over into the UIFESS Driver Version 1 PCB file. In the region near capacitors C5 and C7, four rectangular areas are cut out of the green soldermask. This did not affect any electrical connections, but should be removed for later iterations of PCB design.

7.4 UIFESS Driver Version 2 Results

These boards are designed, fabricated, and populated. The issues associated with the UIFESS Driver Version 1 PCB have been resolved. There are no significant differences in the results when compared to conducting air gap control with the UIFESS Driver Version 1 PCB.

Chapter 8

UIFESS Rotation Speed and Future High Speed Hardware

8.1 Introduction

The rotational speed enabled by the UIFESS power electronics is investigated. Only the power electronics and hardware controller will be investigated. It is assumed the rotor continues to behave as a rigid body at higher speeds. In reality, the rotor requires a flexible rotor model. The faster the rotor rotates, the rotor itself will begin to bend and warp, based on material properties and rotor construction[18].

A brief discussion of the possible hardware requirements to achieve 500,000 rpm are discussed. Examples of current and near future technology are presented.

8.2 UIFESS Hardware Limits

There are many considerations to take into account for determining how fast a flywheel can be rotated. The rotor itself must be designed to withstand the forces it will undergo at higher rotations. The UIFESS rotor is expected to be safe for operation up to 2,000 rpm. The machine has only been designed for 1,800 rpm[11]. The sensors must be able to provide useful data at these higher speeds. For instance, the displacement sensor must be able to accurately pick up radial oscillations the rotor will undergo as it speeds up and reaches its desired idling speed.

The power electronics face limitations. Sensor bandwidth and microcontroller speed are limiting factors. The Full-Bridge DC-DC converter must switch faster for higher rotational speeds. The self-bearing FRRM coil inductance also limits how quickly current magnitude can be changed. The coils of the self-bearing FRRM must shift their function depending on the rotor position. Each coil must transition from a positive or negative direct axis current, I_d, to a negative or positive quadrature axis current, I_q.

8.2.1 Full-Bridge DC-DC Converter Limits

Switching Speed Limits The Full-Bridge DC-DC converter introduces multiple limits for rotation consideration. As shown in Section 5.2, the converter operates in the locked-antiphase operation. Recall this is where the opposite switches of the converter are operated in pairs. A dead time is introduced where all four of the switches are open for a short time before a pair of switches close to ensure the power supply is not shorted. The dead time is set by an external resistor and the driver IC. The dead time resistor is located on the Pololu PCB. The default resistance value that comes on the commercial product is approximately 47 kΩ, giving a dead time of about 1.4 μs, which limits the switching speed[24]. Switching speeds above 80 kHz begin to dominate the power losses of the converter. The dead time resistor is shown in Figure 8.1.

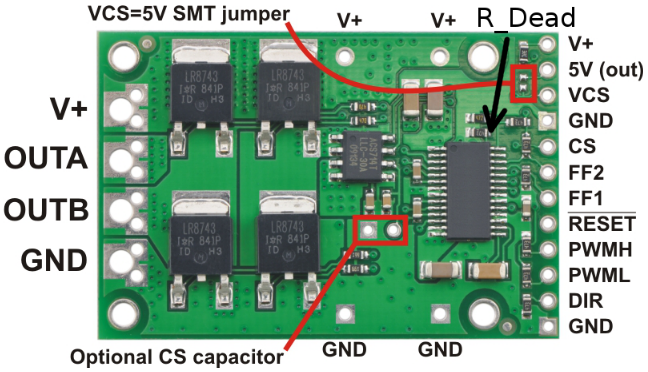

Figure 8.1: Dead Time Resistor Identified on Power Amplifier

The switching speed depends parameters specific to the Allegro A3941 MOSFET driver IC and the Infineon IPD048N06L3 G OptiMOS 3 Power-Transistor. The time required to fully cycle the MOSFET switches requires knowing the timing parameters summarized in Table 8.1. The total switching time, and switching frequency, is calculated using values from the device datasheets and application guides, as shown in Equation 8.1 and 8.2. For a factor of safety, it is desired to allow the MOSFETs to be in the on or off position for as long as the t_{dead} time, which effectively doubles the $t_{SwitchCycle}$ time, and reduces the frequency to approximately 150 kHz, shown in Equation 8.3. This is the practical switching speed to be considered. This means the MOSFETs can change direction every 6.67 μs maximum.

Device	Parameter	Symbol	Value
A3941 Driver	Turn-on Propagation Delay[24]	t_{pOn}	150 ns
A3941 Driver	Turn-off Propagation Delay[24]	t_{pOff}	150 ns
A3941 Driver	Standard Dead Time[24][22]	t_{dead}	1.5 μs
Infineon IPD048N06L3	Turn-off Delay Time[21]	t_{dOff}	56 ns
Infineon IPD048N06L3	Turn-on Delay Time[21]	t_{dOn}	11 ns
Infineon IPD048N06L3	Current Rise Time[21]	t_{ri}	5 ns
Infineon IPD048N06L3	Current Fall Time[21]	t_{fi}	12 ns
Infineon IPD048N06L3	Voltage Rise Time[51]	t_{rv}	1.07 ns
Infineon IPD048N06L3	Voltage Fall Time[51]	t_{fv}	0.48 ns

Table 8.1: Power Amplifier Timing and Operational Parameters

$$t_{SwitchCycle} = t_{pOn} + t_{dead} + t_{dOff} + t_{ri} + t_{rv} + t_{pOff} + t_{dead} + t_{dOn} + t_{ri} + t_{fv} = 3.39\mu s \quad (8.1)$$

$$f_{SwMax} = (t_{SwitchCycle})^{-}1 = 295kHz \quad (8.2)$$

$$f_{Sw} = 150kHz \quad (8.3)$$

Thermal Limits It is desired to determine the power amplifier power loss. It is crucial to ensure the switching losses do not generate so much heat that the MOSFETs or MOSFET driver IC would be permanently damaged. Values for the power losses are shown in Table 8.2. The losses are calculated with a bus voltage of 44V, assuming a direct axis current of 1.75 A, and a switching frequency of 150 kHz for a worst-case scenario. A simple thermal model equivalent circuit is used to relate the power loss to the junction temperature. At these conditions, the MOSFET is extremely warm, but not in danger of device failure.

Thermal limits on the A3941 Driver IC are also considered. The device characteristics and temperatures are shown in Table 8.3.

Table 8.2: Theoretical Power Amplifier MOSFET Power Losses for 150 kHz Switching Frequency, Bus Voltage of 44 V, and Current of 1.75 A

Device	Characteristic	Symbol	Value
IPD048N06L3	MOSFET Switching Loss	P_{swM}	0.527 W
IPD048N06L3	MOSFET Conduction Loss	P_{condM}	0.025 W
IPD048N06L3	Anti-Parallel Diode Switching Loss	P_{swD}	.003 W
IPD048N06L3	Anti-Parallel Diode Conduction Loss	P_{condD}	.340 W
IPD048N06L3	Total Full-Bridge Converter Loss	P_{HLoss}	.894 W
IPD048N06L3	Junction-Ambient Thermal Impedance	R_{ja}	50°C / W
Air	Ambient Temperature	T_A	30°C
IPD048N06L3	Junction Temperature	T_j	74.7°C
IPD048N06L3	Max Junction Temperature	T_{jMax}	175°C

Table 8.3: Theoretical Power Amplifier Driver IC Power Losses for 150 kHz Switching Frequency, Bus Voltage of 44 V, and Current of 1.75 A

Device	Characteristic	Symbol	Value
A3941 Driver	Bias Power Loss	P_{bias}	0.88 W
A3941 Driver	Charge Pump Power Loss	P_{CPump}	0.908 W
A3941 Driver	Switching Power Loss	$P_{swDriver}$	0.368 W
A3941 Driver	Total Driver IC Power Loss	P_{LossD}	2.156 W
A3941 Driver	Junction-Ambient Thermal Impedance	R_{jaD}	32°C / W
Air	Ambient Temperature	T_A	30°C
A3941 Driver	Junction Temperature	T_{jD}	99°C
A3941 Driver	Max Junction Temperature	T_{jMaxD}	150°C

A simple thermal model equivalent circuit is used to relate the power loss to the junction temperature. At these conditions, the A3941 Driver is extremely warm, but not in danger of device failure. The A3941 Driver IC is most likely be the limiting device on the commercial power amplifier, unless a heat sink is added to the system. The temperatures of the MOSFETs and Driver IC while switching at a 100 kHz, 60% Duty Cycle Switching Frequency, resulting in 0.9 A average current being supplied to the load is shown in Figure 8.2. The switching waveform and current flow to the load is shown in Figure 8.3. The 1.5 μs dead time in the current waveform can be seen after each change in the Direction Pin.

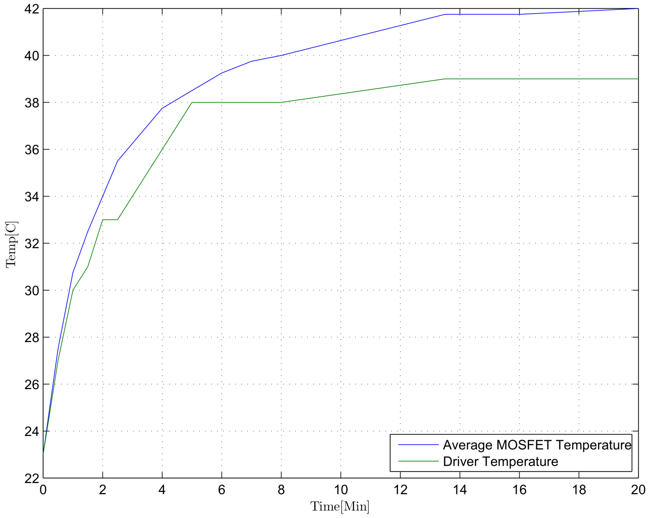

Figure 8.2: Thermal Analysis of Power Amplifier for a 100 kHz, 60% Duty Cycle Switching Frequency, Providing a 0.9 A Current

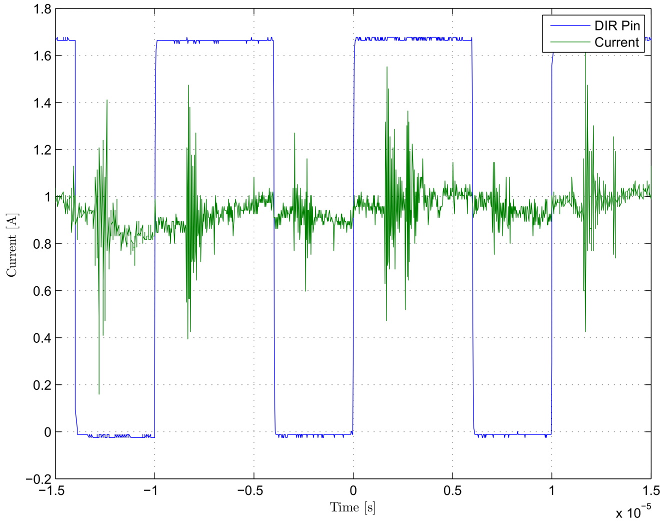

Figure 8.3: Power Amplifier Switching Signal and Current Flow Highlighting Switching Dead Time

Power Bandwidth The self-bearing FRRM coils is modeled as an inductive load as seen by the converter. The converter has a maximum voltage that it can place across the coil. The smallest voltage to be used for the UIFESS will be 12 V. This voltage and the coil inductance determines how quickly the current can change over time. The current is limited to 10 A for this calculation, shown in Equation (8.4). As stated in [12], a bias current chosen based on machine parameters is selected, shown in Equation (8.5). The bias current should be some fraction, γ, of the total current. Practical values for γ range from 0.2 to 0.5 [18]. The UIFESS has a γ of 0.26, a practical value. The bias current allows the control algorithm to operate in the linear region of the magnetic iron B-H curve. This allows linear assumptions made in the control system to be valid.

$$i_{max} = 10A \tag{8.4}$$

$$i_{bias} = 2.6A \tag{8.5}$$

At low frequencies, the current drawn by the coil will primarily be based on the coil resistance. As the frequency is increased, the impedance due to the inductance increases. The increasing frequency eventually reaches the point where the converter voltage becomes saturated, and the dynamic behavior of the converter becomes nonlinear, which is highly undesirable. The worst case saturation frequency, assuming a bus voltage of only 12 V, is shown in Equation 8.6 [18].

$$f_{sat} = 2 * \pi * \sqrt{\frac{\left(\frac{V_{bus}}{(1-\gamma)i_{max}}\right)^2 - (R_{DB})^2}{(L_{DB})^2}} = 17.34kHz \tag{8.6}$$

The current in the coil, i_{mag}, is limited by the relationship shown in Equation (8.7) for frequencies below the saturation frequency, and is limited by the relationship shown in Equation (8.8) for frequencies above the saturation frequency. The linear operation region of the power amplifier is the area under both the horizontal line of Equation (8.7) and the area under the curve of Equation (8.8), as shown in Figure 8.4.

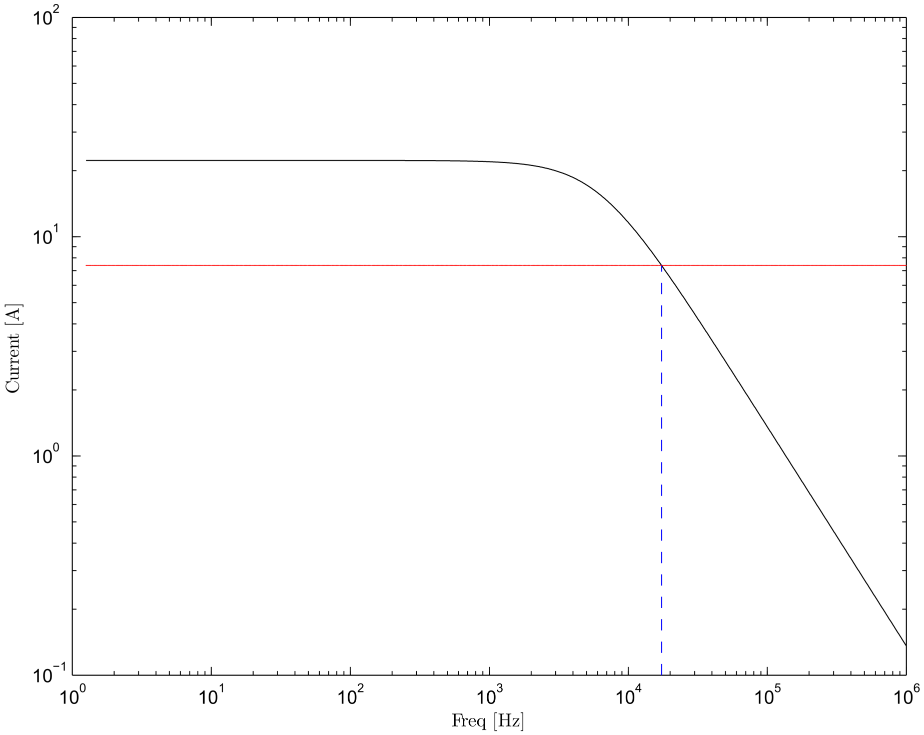

Figure 8.4: Power Bandwidth for a 12 V, 10 A Power Amplifier with a 2.6 A bias current

$$i_{mag1} = (1 - \gamma) i_{max} = 7.4A \tag{8.7}$$

$$i_{mag2} = \frac{V_{bus}}{\sqrt{(L_{DB})^2 (2\pi f)^2 + (R_{DB})^2}} \tag{8.8}$$

The vertical line represents the saturation frequency, f_{sat}. For frequencies below the saturation frequency, the power amplifier is able to supply i_{mag1}, which is 7.4 A for 12 V. At frequencies above f_{sat}, currents are supplied up to, but not exceeding, i_{mag2} for linear operation [18]. The power amplifier is switched at a frequency of 80 kHz up to 150 kHz. The inductor impedance is based on this frequency region. Also, different bus voltage levels may be used in the future. A list displaying the currents the power amplifier is capable of supplying for various frequencies and bus voltages is shown in Table 8.4.

Table 8.4: Power Amplifier Maximum Output Current for Various Power Amplifier Conditions

Frequency	Bus Voltage	Max Current
80 kHz	12 V	1.695 A
100 kHz	12 V	1.358 A
125 kHz	12 V	1.087 A
150 kHz	12 V	0.906 A
80 kHz	24 V	3.391 A
100 kHz	24 V	2.716 A
125 kHz	24 V	2.174 A
150 kHz	24 V	1.812 A
80 kHz	44 V	6.217 A
100 kHz	44 V	4.979 A
125 kHz	44 V	3.986 A
150 kHz	44 V	3.323 A

This table shows that if V_{bus} is 12 V, the amplifier is not able to properly source the I_D or I_Q current levels. The FRRM design, as discussed in Wimer[11], uses a 12 V bus. Additional analysis is required to determine what impact a higher bus voltage will have.

Ultimately, the power amplifier is responsible for inducing a pulling force on the rotor. The power amplifier is limited on how quickly its exerted force can be changed. [18]. The force slew rate is shown in Equation (8.9). The air gap distance is labeled g, and θ is the component of force pulling on the rotor. For a direct axis coil, the coil responsible for control, all the force generated will result in pulling the rotor towards the stator, so θ is equal to 0°. Aspects from Section 8.2.2 and Section 8.2.3 must also be considered to determine rotational speed. Higher voltages extend the linear operating region of the power amplifier.

$$F_{SlewRate} = i_{max} V_{bus} \left(\frac{2\gamma \cos(\theta)}{g} \right) = 62.4 \frac{N}{ms} \tag{8.9}$$

8.2.2 Self-Bearing FRRM Limits

Coil Inductance The self-bearing FRRM introduced rotational speed limits. The inductance and the resistance of the self-bearing FRRM coils is calculated. The inductance of a single coil is found using Equation (8.10), where A_{cross}, the stator face cross sectional area, is 2 inches by 0.226 inches, N is 55 turns, and g is the desired air gap of 1 mm.

$$L_{DB} = \mu_0 N^2 \frac{A_{cross}}{2g} = 0.554mH \tag{8.10}$$

The resistance of the coil is found by estimating the length of a single turn, multiplying by the 55 turns to get the length and using the resistivity of 18 gauge copper wire. The resistance is estimated to be 0.539 Ω. The resulting coil time constant is 1.028 ms. A voltage placed across the coil induces a current. The current does not change instantaneously, but ramps up, as shown in Equation (8.11), where $i(0)$ is the initial current flowing in the inductor.

$$i_t = \frac{V_{bus}}{R_{DB}} \left(1 - e^{-\frac{R_{DB}}{L_{DB}}t} + i(0)e^{-\frac{R_{DB}}{L_{DB}}t}\right) \tag{8.11}$$

An approximation is used to relate the voltage applied to the coil to the change in current over time, as shown in Equation 8.12.

$$\Delta t = \frac{L_{DB}\Delta i}{V_{bus}} \tag{8.12}$$

Theory of Rotation Knowledge of the rotation is required to understand how the self-bearing FRRM coil inductance limits rotational speed. The proposed rotational control algorithm is out of the scope of this thesis, but discussed in Kisling[12]. A cross-section of the self-bearing FRRM iron laminations and coils is shown in Figure 8.5.

Coils 21, 22, 23, and 24 have the direct axis current, I_D, flowing in them. These coils produce flux that generates a north pole on the upper rotor pole. Flux flows from the north rotor pole, across the air gap, and to each of the south pole rotors. Coils 1 and 2 have the quadrature axis current, I_Q, flowing in them. The portion of the coils directly under the upper north pole have a current flowing in a magnetic, B, field. A force is

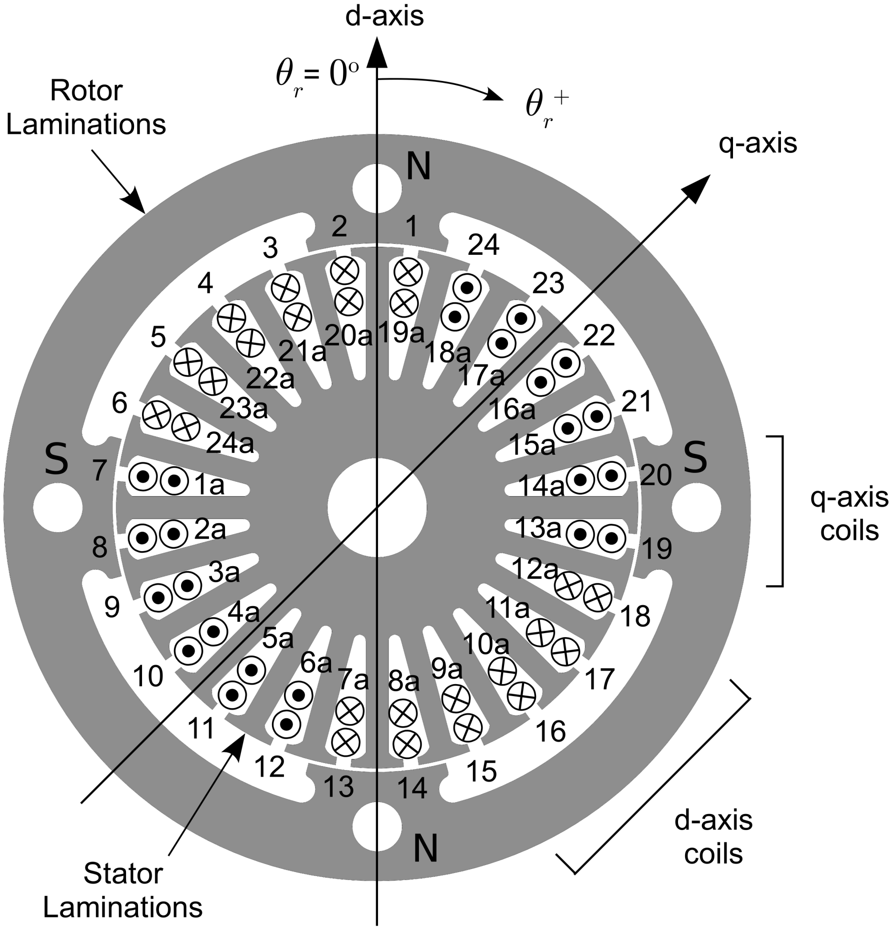

Figure 8.5: Cross Section of Self-Bearing FRRM Iron Laminations and Coils with Current Flow and Rotation Direction. Note this view is from looking from the bottom of the stator

exerted on the coil in the direction of the cross product between i and B. The conductors have a counter-clockwise force exerted on them. The coils are held in place, and an equal but opposite force is exerted on the rotor. The rotor is subjected to a clock-wise force, and rotates in that direction. The same concepts apply to the other coils and poles for the machine.

For the instance the rotor is in the position as shown in Figure 8.5, a q-axis current must be flowing in the coils under the rotor poles to create torque for rotor rotation. A q-axis current must be flowing in coils 1, 2, 7, 8, 13, 14, 19, and 20. As the rotor moves clockwise, the coils 2, 8, 14, and 20 are no longer under the rotor pole, and must transition into carrying a d-axis current to maintain the rotating magnetic field. Coils 24, 18, 12, and 6 carry q-axis current to continue exerting a torque on the rotor. However, the transition between the d-axis and q-axis currents is not instantaneous, as shown in Equation (8.12). Coil #1 functions with respect to the rotor pole positions are shown in Figure 8.6. This shows the coil functions for one full mechanical rotor rotation. Coil #2 has the same waveform, just shifted by one function cycle, and Coil #3 is shifted by two function cycles.

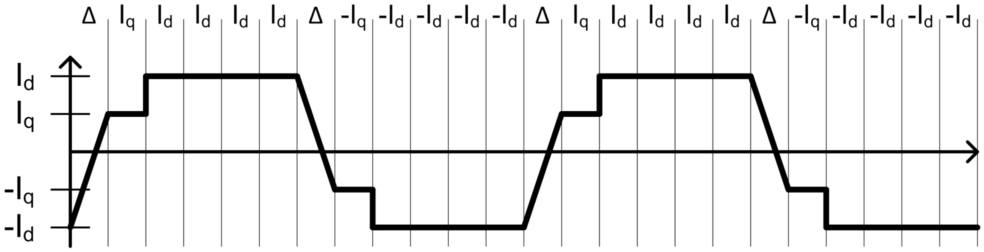

Figure 8.6: Coil #1 Functions With Respect to Rotor Pole Position for One Mechanical Rotation

Assume that current headed into the page is positive for Figure 8.5. For the rotor position shown in the Figure 8.5, Coil #1 is in the midst of transitioning from a negative direct current to a positive quadrature current. Coil #2 is already a positive quadrature current, providing torque to the rotor. As the rotor moves clockwise by one twenty-fourth of a rotation, Coil #2 transitions to a positive direct axis current and Coil #1 has reached the quadrature current level. Coil #24 begins to transition from a negative direct axis current to a positive quadrature current.

If the rotation algorithm is constrained to requiring one coil being at the quadrature current, the other coil has time to reach the desired quadrature level. In the time required to transition the current, the rotor cannot move more than one twenty-fourth of a rotation.

The bus voltage determines how quickly the current in the coil can change. The large current transition is always from a positive or negative direct axis current to a negative or positive quadrature current. This change of current is shown in Equation (8.13).

$$\Delta i = I_D + I_Q = 3.42A \tag{8.13}$$

Using Equation (8.13) and various bus voltages, the transition time required by the coil and the associated parameters are calculated and shown in Table 8.5.

Table 8.5: Theoretical Coil Transition Times Determine Mechanical Rotation Speeds, Applied Electrical Frequency, and Minimal Requirements for Current and Position Control Algorithm Rates
* As many current control algorithms will be run in the time allowed

Bus Voltage	Δt_{Calc}	Δt	N_s	f_e	Pos. Ctrl	Curr. Ctrl
12 V	158 μs	160 μs	15,625 rpm	521 Hz	6.25 kHz	*
24 V	78.98 μs	80 μs	31,250 rpm	1.042 kHz	12.5 kHz	*
44 V	43.08 μs	50 μs	50,000 rpm	1.667 kHz	20 kHz	*

When the rotor is rotating at its maximum speed, N_s, a coil must undergo the large Δi transition of Equation (8.13) every Δt. The electrical frequency, f_e, is the effective AC frequency supplied to each coil. A sinusoidal waveform is shown in Figure 8.6. Note that the electrical frequency is double the mechanical rotational frequency.

It was decided to require one position reading and control for each coil function cycle. The position PID controller for each axis has to be conducted every coil function cycle. The current control loops should be conducted as many times as possible in between each coil function cycle after the position controller had been conducted. The values listed are theoretical, and based solely on the timing required to adjust the current in the machine coils. Aspects from Section 8.2.1 and Section 8.2.3 must also be considered to determine rotational speed.

The FRRM is a type of Synchronous Machine, and the equation for synchronous speed can be used to relate mechanical rotation speed to the required electrical frequency, shown in Equation (8.14). Note that p is equal to 4, the number of poles in the FRRM[11].

$$N_s = \frac{120 f_e}{p} \tag{8.14}$$

8.2.3 Microcontroller Capabilities

It must be determined how many position and current controls the microcontroller can do for the given coil transition time, Δt. Successful control of the stabilization bearing is demonstrated using the TMS320F28335 microcontroller. The self-bearing FRRM uses the TMS320F28377D microcontroller, which is considerably faster. The position and current control algorithms for air gap control are the same for each bearing. The microcontroller for the self-bearing FRRM has to conduct current control for 24 coils instead of only 4 coils as in the stabilization bearing. The algorithms are demonstrated with the TMS320F28335 and an approximate time is calculated to conduct the same control algorithms with the TMS320F28377D, shown in Table 8.6. Current control for 24 coils was estimated based on timing requirements for fewer coils.

Table 8.6: Microcontroller Processing Time for Various Control Algorithms

Algorithm	F28335 Time	Clock Cycles	Est. F28377D Time
Position PID and Dig. Filter	3 μs	450	2.25 μs
1 Coil Current Control	345 ns	52	259 ns
2 Coil Current Control	530 ns	80	398 ns
4 Coil Current Control	910 ns	137	683 ns
24 Coil Current Control		680	3.39 μs

After calculating estimates for the control algorithms, it is determined how many control algorithms are conducted in the time for one twenty-fourth of a mechanical rotation, as shown in Table 8.5. The fastest rotating case, with a bus voltage of 44 V, is analyzed. The position control must be conducted every 20 kHz, once every coil function cycle. The 24 coil current control is conducted at a 150 kHz rate as many times as possible during the coil function cycle. The position and current control algorithm rates and calculation time is shown in Figure 8.7.

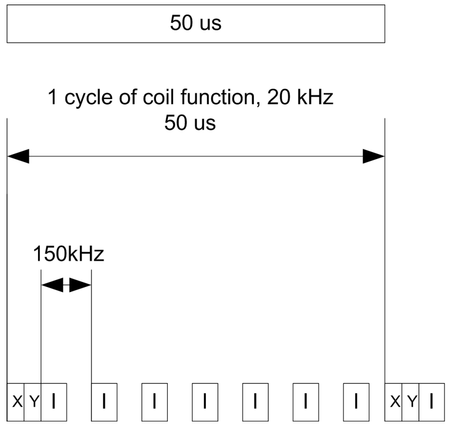

Figure 8.7: Position and Current Control Algorithm Rates for a Rotation of 50,000 rpm

A dynamic model analysis must be done to see if a single x-axis and y-axis position update and control per coil function cycle is capable of maintaining the air gap. At the maximum rotational speed, one x-axis position control algorithm, one y-axis position control algorithm, and seven coil control algorithms are run during one coil function cycle.

The TMS320F28377D is capable of sampling 24 analog channel at a speed of 14 MSPS. During one coil function cycle, up to 700 analog samples are taken. If each current control algorithm block from Figure 8.7 requires three sets of 24 readings, a total of 504 readings are required. The position sensor analog readings are taken with a different microcontroller, and communicated to the controller connected to all of the FRRM coils. The second microcontroller, most likely a TMS320F28335, can use its ADC to read the x-axis and y-axis displacement sensors. After the ADC sampling, a 12-bit number will represent the distance. This number is sent to the master TMS320F28377D microcontroller to be used in the displacement control algorithm. The master TMS320F28377D microcontroller interfaces with six of the UIFESS Driver Version 2 PCBs, as well as interface with the rotational sensor and parallel communication channels with the other microcontroller, shown in Figure 8.8. The UIFESS project has the power electronics necessary to rotate the flywheel at at least

50,000 rpm. A dynamic model of the rotor is required to determine how many air gap position algorithms must be run for a given rotational speed.

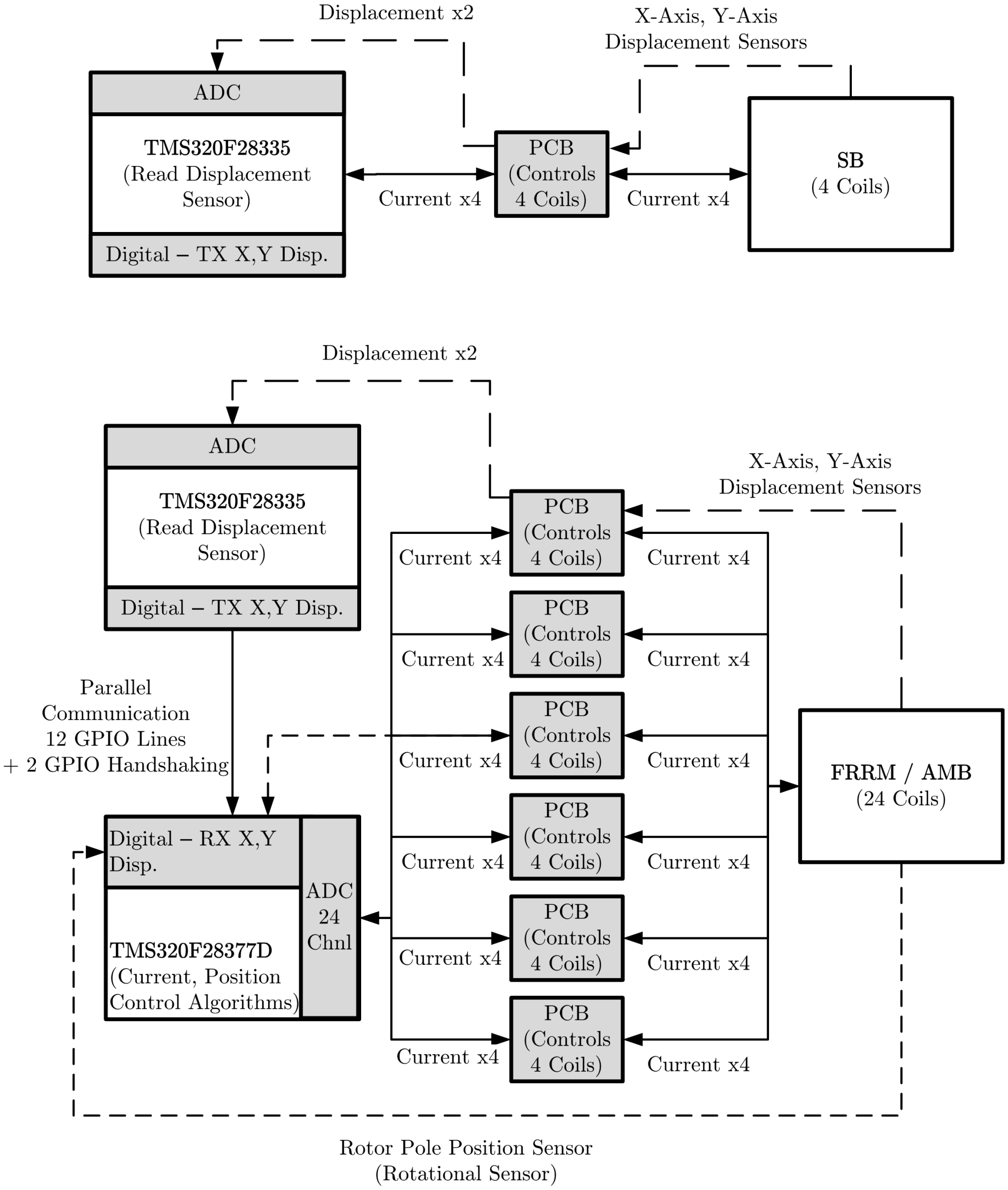

Figure 8.8: Proposed Microcontroller Configuration to Obtain Required Analog and Digital Readings

8.3 Today's High Speed Hardware

Many FESS research groups use a similar power electronics topology. These groups typically have a dedicated motor-generator that is used to add or remove energy from the rotor. Separate AMBs are used to maintain air gap control. The UIFESS is attempting to use a single AMB in conjunction with a motor/generator that doubles as an AMB.

NASA Glenn used synchronous machines in their flywheel designs. A voltage sourced inverter controls the motor/generator [9]. The inverter is constructed of IGBTs, though MOSFETs would have been preferred in one instance [2]. Multiple flywheels associated with NASA Glenn are developed, and range in speeds from 1,000 rpm up to 60,000 rpm [9] [10] [2]. These flywheels are controlled using a real-time control development system from dSPACE. Future plans intend to replace the dSPACE hardware with an embedded system using a combination of multiple digital signal processors (DSP) that would possibly interface with analog control hardware [2]. Implementation of FPGAs is also possible [9].

The McTronX research group at the North-West University of South Africa have developed a FESS that would be capable of reaching 30,000 rpm [16]. Safety concerns significantly reduced the actual rotational speed. However, the power electronics are capable of enabling rotation up to the desired 30,000 rpm. McTronX also used the dSPACE real-time control development system. Advanced Motion Controls' model 12A8 servo amplifiers are used as the power amplifiers. This device uses MOSFETs and is capable of switching speeds up to 36 kHz. This FESS utilized a dedicated motor/generator and separate AMB for air gap control [16].

AFS Trinity Power Corporation has developed a flywheel system that is capable of reaching 40,800 rpm. This system also featured a dedicated motor/generator and separate AMB. Separate systems control the motor/generator and the AMB. A proprietary DSP utilizing custom hardware and software enables control. A three-phase H-Bridge power converter utilizes IGBTs for control [17].

Many institutions have made use of the real-time control development system from dSPACE. The modular hardware system features options for a processor board, several options for ADC acquisitions, digital I/O, digital waveform outputs, and analog outputs. The system is also capable of integrating with Matlab Simulink, making it ideal in research and development real-time applications. The DS1005 processor board features an IBM PowerPC 750GX 1 GHz chip, and well suited for applications requiring high sampling rates and many inputs and outputs. The DS2004 high-speed A/D board has a 16 channel, 16-bit ADC with an input voltage range of ±10 V per channel and capable of 800 ns conversion time [16]. The dSPACE real-time control development system would greatly increase the rate of development of FESS.

8.4 Power Electronics for High-Speeds

A brief investigation to consider rotating the UIFESS at 500,000 rpm is conducted. The investigation assumes the UIFESS rotor is capable of spinning at these speeds, and the displacement sensors have a high enough frequency response to maintain control of the rotor. As the rotor increases in rotational speeds, different vibrational frequencies will be experienced, and the displacement sensors must be capable of reflecting these vibrations [18]. It is desired to determine how often the displacement and current control algorithms have to be conducted to achieve a similar rate of control as discussed in Section 8.2.3.

The UIFESS still operates on the same principles and has the same number of coils. The effective electrical frequency supplied to each coil is calculated using Equation (8.14), shown in Equation (8.15).

$$f_{e500k} = \frac{500000 \cdot p}{120} = 16.667kHz \tag{8.15}$$

One electrical frequency still requires 12 coil function shifts. The time alloted for one coil function cycle is shown in Equation (8.16). This is the time required to ramp the current from the $\pm I_D$ to $\mp I_Q$.

$$\Delta t_{500k} = \frac{2\pi(500,000rpm)^{-1}}{24} = 5\mu s \tag{8.16}$$

A bus voltage of 380 V is required to achieve the desired change in current for the present coil inductance. A higher power machine is required to achieve this rotational speed. The machine could be redesigned to change the inductance of the coils, the required change in current required, and the number of coils as well.

If dynamic modeling of the rotor shows that still only one displacement control algorithm per axis is required per coil function cycle, a 200 kHz rate is required. This would require conducting two displacement control algorithms during the 5 μs span. A faster processor would be required to achieve this. The current control algorithms must be done as well. A single controller is only capable of working primarily in series. To achieve such a high speed, a significant portion of the control will have to be conducted in parallel [2]. The estimated timing assuming a 1 GHz processor is used is shown in Figure 8.9.

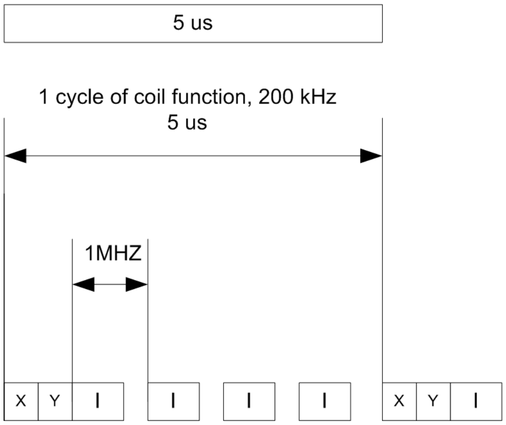

Figure 8.9: Estimated Position and Current Control Algorithm Rates for a Rotation of 500,000 rpm using a 1 GHz processor

The Texas Instruments DaVinci Digital Media Processor which features a 1.35 GHz processor. This processor has to interface with an off-board ADC and could be capable of doing the position control algorithms, but not be able to do 24 current control algorithms as well. The position control algorithm output could be sent to multiple other processors which would each be responsible for a number of current control algorithms only. The current control algorithms may be realized using only analog hardware, as shown in Figure 8.10. An FPGA in another possible solution, since it is capable of running multiple tasks in parallel.

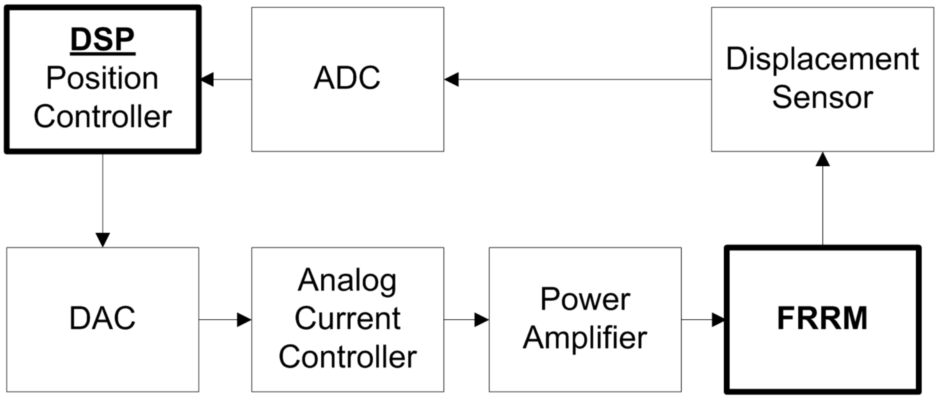

Figure 8.10: Estimated Position and Current Control Algorithm Rates for a Rotation of 500,000 rpm using a 1 GHz processor

The power amplifier hardware needs to be switched at considerably higher speeds to maintain air gap control. A new technology, Gallium nitride (GaN) Power Transistors, is a new development in the power conversion field[19][52][53]. GaN transistors first appeared in 2004 [19]. These devices have a lower gate capacitance and lower on-resistance, which allow for significantly higher switching frequencies compared to traditional silicon transistors. Omura has implemented a GaN device in a power supply topology capable of switching at 27.1 MHz [52]. The GaN transistors have some implementation issues, but are expected to become a dominant technology in power conversion over the next decade. GaN transistors have the potential to improve switching frequencies and efficiency in areas typically dominated by MOSFETs, and could offer a significant improvement to flywheel power electronic development[5].

Commercial H-Bridge Driver ICs exist that are capable of switching in the Megahertz range. The Intersil HIP4081 and the IXYS IXD604 offer quick rise and fall times and can provide a large peak gate current [54] [55]. Research conducted has demonstrated a driver IC capable of driving a 100-V 1-A GaN HFET switching at 10 MHz.

8.5 Conclusion

The constructed power electronics hardware is capable of rotating the UIFESS at approximately 50,000 rpm. Higher speeds are possible if the switching limits of the power amplifier are pushed further, and the dead resistance of the driver IC is modified. Improved heat sinks, possibly involving the liquid nitrogen cooling system already in place for the UIFESS HTS, could be utilized to cool down the power amplifiers. Additional analysis must be done using a dynamic model of the rotor to determine how many position readings and control algorithms must be run for each coil function cycle. The present UIFESS rotor/flywheel is only rated for rotational speeds up to approximately 2,000 rpm. The power electronics are certainly capable of achieving this speed. It is hoped that the next iteration of machine design can utilize these power electronics and achieve a higher desired rotational speed.

Future FESS power electronic control systems may include multiple processors, analog control hardware, and FPGAs. New discrete power components are being designed to enable faster switching with less power losses.

Chapter 9

Summary and Conclusions

9.1 Summary

The University of Idaho is currently developing a flywheel energy storage system. As of the spring 2014, rotation of the UIFESS has not been demonstrated, however the work conducted on the UIFESS has built a foundation for future researchers at the University of Idaho to build on. The goal of the UIFESS project is to create a low-speed flywheel that is capable of demonstrating numerous technologies associated with flywheel energy storage.

The work presented in this thesis discussed hardware which enabled control of the UIFESS. The air gap control system and the FRRM require power electronics. Sensors, filtering and sensor signal conditioning, microcontrollers, power amplifiers and a reliable interface between these elements was required for a successful demonstration of the work conducted by Wimer[11] and Kisling[12].

A commercial power amplifier was selected. The full-bridge DC-DC converter enables four quadrant control of the voltage and current in a coil. This enables motoring and generation of the FRRM, allowing energy to be transferred to and from the flywheel. The power amplifier operation, switching times, power bandwidth, power losses, and microcontroller interfacing logistics were discussed. The FRRM and SB coils needed to be brought outside the vacuum chamber using electrical feedthroughs to connect to the power amplifiers. The power amplifier requires 5 V logic to change the switch positions, while the microcontroller was only capable of 3 V digital output.

The commercial power amplifier included a current sensor that was used for determining the current in each individual coil associated with the UIFESS. The Hall effect-based linear current sensor is capable of sensing bi-directional AC and DC currents. Having the current sensor integrated with the power amplifier was a great convenience. The power amplifiers were located outside of the vacuum chamber, so vacuum feedthroughs for the current sensors were not required.

Displacement sensors for determining rotor movement in the x-y plane were chosen. These sensors were responsible for determining the air gap between the rotor and the stator. The sensors operate on an eddy current principle, and are accurate down to the sub-micrometer level. The sensors have a 0 mm to 3 mm range. The sensor probes must use a stainless steel target. The sensor probe signals were brought out of the vacuum chamber using feedthroughs. The probe signals were connected to an electronics box that linearizes the output before any signal conditioning takes place.

The rotational sensor will be used to keep track of the rotor pole positions. This will allow the control system to know when a change in coil function cycle must take place. The sensor was not chosen due to time constraints and unresolved integration issues with the rotor itself.

Thermocouples were installed in various windings of the stabilization bearing and the FRRM. Type K thermocouples will be used to create a thermal model of the UIFESS during normal operation to ensure the winding insulation will not overheat. Type T thermocouples will be used to monitor the HTS temperatures and ensure the HTS and cold plate stay in the required temperature range. Multiple thermocouples are brought through the vacuum chamber using feedthroughs.

Microcontrollers to enable control were selected. A summary of the input and output requirements the SB and the self-bearing FRRM were discussed. The Texas Instruments' TMS320F28335 microcontroller was used with the Single Axis Single Bearing demonstration unit and the SB. The self-bearing FRRM requires additional speed, input, and output channels, resulting in using the new TI TMS320F28377D. Each system will be separate, and will not have any interaction. Separate systems will enable decentralized control, as stated in Kisling[12]. Successful control was demonstrated with the TMS320F28335 on the SASB demonstration unit as well as basic testing on the SB of the flywheel itself. The TMS320F28335 microcontroller successfully demonstrated interfacing with the UIFESS Driver #1 PCB, the power amplifier, and the ability to obtain accurate sensor data from the signal conditioning topologies.

The microcontrollers are responsible for reading displacement sensor data and coil current data. Each of these analog sensors had a voltage output range that was not directly compatible with the microcontroller ADC range. Signal conditioning circuits were designed to provide signal filtering, shifting, and scaling of the sensor outputs before the signal was sampled by the ADC. Two different topologies were design, built, and demonstrated for each sensor.

The topologies for the distance sensor dealt with adjusting the effective sensing range. The displacement sensors have a 0 mm to 3 mm range. The full range displacement topology shifted the entire sensing range of the sensor output. The sensor would output a signal in the range of approximately 0 V to 11 V. This had to be brought down to a 0 V to 3 V signal. An instrumentation amplifier was used to aid in the filtering and shifting of the signal.

It was not clear how much resolution and noise would be present with the full sensor topology. As a precaution, a short range displacement topology that only scaled output over a 0.5 mm range was designed. The output of the topology would give a 0 V to 3 V reading for only the 0.5 mm range. After demonstration of each topology on the SASB demonstration unit, it was decided the full range sensor gave enough resolution to use for the UIFESS, and the convenience of being able to read the entire 0 mm to 3 mm range would be useful during installation and setup on the UIFESS itself.

Analysis between a cheaper and a more expensive solution for current sensing was investigated. The current sensor on the commercial power amplifier give a 0.5 V to 4.5 V signal for currents ranging from -30 A to 30 A. The UIFESS will use an absolute maximum of ±12 A, so the current signal needed to be shifted and scaled so the ±12 A range would result in a 0 V to 3 V output for the microcontroller ADC to sample. Topologies utilizing an operational amplifier and an instrumentation amplifier were analyzed. The op-amp topology was a cheaper solution, but the in-amp would provide better performance. During demonstration on the SASB unit, it was discovered the op-amp topology had an issue when it was connected to the microcontroller ADC channels that included transient protection. The op-amp topology output had significant noise, drastically reducing the accuracy of the current. In addition, it was believed the in-amp's high common-mode rejection ratio would be of use in the actual UIFESS application, so the in-amp current topology was selected.

A custom printed circuit board was used to interface the sensor signal outputs, the analog signal conditioning topologies, the digital input and output signals for the power amplifier, and the microcontroller. The PCBs house the power amplifiers and the signal conditioning topologies. A device to shift the 3 V microcontroller logic to 5 V was placed on the PCB. The displacement sensor outputs, microcontoller ADC channels, digital inputs, and digital outputs were connected to the PCB, as shown in Figure 6.1.

The PCB contains digital signals switching at high rates as well as the analog sensor signals. The PCB design ensured high frequency digital switching signals did not add noise to the analog signals. The robustness of the control system depends on obtaining accurate displacement distance and currents. Mixed signal PCB design techniques were utilized to ensure interference would not be an issue.

The Prototype PCB was designed as a proof of concept. The Prototype PCB holds one power amplifier, contains the four signal conditioning topologies to be analyzed, and the 3 V to 5V logic level shifter. The Prototype PCB was used with the SASB demonstration unit. Implementation with the SASB unit offered a conceptually simpler route for researchers to gain an intuition on AMBs, air gap control algorithms, and the interface with the power electronics hardware before attempting control on the actual UIFESS. A single prototype PCB was populated to ensure the desired design was obtained.

The Prototype PCB allowed the evaluation of the various sensor topologies. The full range distance sensor topology and the in-amp current sensor topology were selected with results from the Prototype PCB. Successful demonstration of air gap control concluded the mixed signal design methodology allowed minimal interference to the analog signals. The prototype PCB also allowed verification of the 3 V to 5 V logic level shifter. The Prototype PCB verified physical package sizes for designed components. The population technique for placing the surface mount components was successfully demonstrated, and allowed the researchers to feel comfortable using this method to populate all the PCBs for the project.

After the successful demonstration of the prototype PCB, the UIFESS driver PCBs were designed. These PCBs utilized the same design principles and components as the prototype PCB. Only the full-range distance signal conditioning topology and the in-amp current sensor signal topology were placed on the UIFESS driver boards. The driver boards house 4 power amplifiers per PCB. This would push the PCB to its largest manufacturing size for academic pricing.

The driver boards were designed, and 2 PCBs were purchased. One PCB was populated and successfully demonstrated on the SASB unit as well as the SB. The SB test utilized all 4 power amplifiers, 4 in-amp current sensor topologies, 2 displacement sensor topologies, and logic level shifting.

Some minor aesthetic issues were resolved in the final iteration of design. Eight (8) of the UIFESS Driver Board Version 2 were purchased. These boards are populated and ready for future work on the UIFESS.

Analysis was conducted to estimate the power electronic system's rotational speed. Without modification, the power electronics are capable of achieving 50,000 rpm. A look at future rotational speeds and the power electronic hardware requirement and layout to achieve such a speed was investigated. Technology will continuously attempt to push flywheel rotational speeds higher. The specific energy of a storage device is a crucial factor in applying the technology for space applications. Power electronics continue to increase in speed and abilities. Future control systems will most likely feature a combination of high speed digital signal processors, analog controllers, and FPGAs. Power amplifier technology will continue to improve the switching speed and efficiency of power electronics. Gallium Nitride Power Transistors are beginning to gather interest for use in power amplifiers.

9.2 Conclusions

The major conclusions and highlights of this thesis are summarized.

- The primary objective of this work was to enable air gap and rotational control of the UIFESS. To achieve this objective, displacement sensors, power amplifiers, current sensors, and microcontrollers were selected. Custom printed circuit boards were designed to interface the power electronic elements. Compatible vacuum feedthroughs were selected for use with the power electronics and other hardware.

- Signal conditioning circuits were designed and built to filter, scale, and shift sensor signal outputs. These topologies were placed on Printed Circuit Boards and successfully demonstrated in practice by enabling air gap control of the SASB demonstration unit and the UIFESS stabilization bearing.

- Mixed-signal PCB design techniques were successfully implemented. The air gap control system's robustness is heavily dependent on the sensor inputs. The mixed-signal design methodologies enabled the control system to obtain accurate sensor inputs. The thesis attempts to document the design methodology for future students to reference.

- The UIFESS Driver PCB Version 2 successfully interfaces all power electronic hardware components. The microcontroller was able to obtain high quality sensor readings. The microcontroller was also able to interface with each power amplifier. The PCB and hardware components have demonstrated air gap control using the stabilization bearing of the UIFESS. High confidence in the ability to successfully demonstrate air gap control and rotation using the self-bearing FRRM exists.

- Without any modification, the power electronics can allow speed up to at least 50,000 rpm. With additional cooling and slight modification of hardware, faster rotational speeds could be achieved. It is desired to have the power electronics be utilized for the next phase of the project.

- Hardware used to obtain high rotational speeds and efficiency will most likely include the use of Gallium Nitride Power Transistors, several high speed processors, analog controllers, and/or Field Programmable Gate Arrays. These types of hardware will enable higher switching speeds and higher efficiencies, and could be capable of rotating flywheels at 500,000 rpm.

Chapter 10

Recommendations for Future Work

This chapter discusses topics to further development of the UIFESS. Several items are closely integrated with work conducted by Wimer[11] and Kisling[12].

- The integration issues surrounding the rotational position sensor must be resolved. A counter wheel mounted to the flywheel was discussed. This option introduces issues when the rotor has to be lowered after the HTS have cooled. A separate solution discussed would utilize placing markings on the plastic spacer of the flywheel. The composition of the marking material and color, the size of the mark, and accuracy in placing the markings need to be considered. An optical sensor that is capable of distinguishing alternating light and dark markings will most likely be utilized. Devices listed in the electrical component distributor Digikey's reflective optical sensors, logic output product area will most likely have a solution.

- A new solution is required to mount the displacement sensors on the UIFESS. The present solution had the sensors mounted on thin metal rings. The sensors had extensive vibration, which fed back into the control system. The vibration did not accurately portray the air gap, and the air gap control was compromised. A make-shift solution offered marginal air gap control capabilities to verify the PCB and power electronics on the stabilization bearing.

- Each of the UIFESS Driver #2 PCBs will need to demonstrate air gap control. Initial testing should be conducted on the SASB to ensure the signal conditioning topologies are operating correctly.

- The UIFESS Driver Board Version 2 PCBs can then be used to demonstrate 2-axis air gap control on the self-bearing FRRM. This would verify the air gap control algorithm in Kisling[12] and demonstrate the microcontroller, sensors, and

PCB interface for use on the UIFESS. The air gap control system could implement PWM signals for the PWMH and PWML pins to enable coasting and braking operations, which would enable a more efficient current control algorithm. Each PCB design discussed in Chapter 6.3.3 offer access to all power amplifier pins. Successful demonstration of 2-axis air gap control would verify the proposed hardware setup discussed in Section 5.4.5.

- The vacuum chamber electrical feed throughs must be installed. Additional wiring is required to connect the coil leads to the 24 pin sockets that will be located inside the vacuum chamber. Connections outside the vacuum chamber will have to interface with the power amplifiers.

- It must be determined how many distance sensor samples per axis are required to ensure air gap control once the flywheel is rotating. The mechanical system, the flywheel, will move much slower than the electrical control system, but adequate distance and current sensor acquisition rates must be maintained. If the flywheel is not sampled at a high enough rate, the microcontroller samples will not accurately portray the system. It is hoped that work by Wimer will aid in answering this question[11].

- The assumption from Section 8.2.2 that one q-axis current coil can be transitioning for one twenty-fourth of a rotation must be verified. One of the q-axis coils will always be providing a torque to the rotor, which will have consequences for rotation speeds.

- The power amplifiers are four-quadrant devices, capable of moving power to and from the load. The UIFESS researchers to date have focused only on the motoring aspects of the UIFESS. A control algorithm will need to be developed to enable the FRRM to act as a generator. Since both the direct and quadrature currents can be controlled, the voltage and power out of the power amplifier can be specified. The direct axis current can be adjusted to regulate the output voltage, and the quadrature current can be adjusted to control the power out of the amplifier. Considerable details are involved in the implementation of this feature. The addition of this feature will enable demonstration of motoring and generation, as shown in Figure 1.2

References

[1] Haisheng Chen et al. "Progress in electrical energy storage system: A critical review". In: Progress in Natural Science 19.3 (2009), pp. 291–312.

[2] Kascak. P. "Fully Levitated Rotor Magnetically Suspended by Two Pole-Pair Separated Conical Motors". Doctoral Thesis. Case Western Reserve University, 2010. URL: https://etd.ohiolink.edu/rws_etd/document/get/case1278530250/inline.

[3] Daryl R Brown and William D Chvala. "Flywheel energy storage: an alternative to batteries for UPS systems". In: Energy engineering 102.5 (2005), pp. 7–26. URL: http://smartenergy.illinois.edu/pdf/Archive/FlywheelEnergyStorage.pdf.

[4] Björn Bolund, Hans Bernhoff, and Mats Leijon. "Flywheel energy and power storage systems". In: Renewable and Sustainable Energy Reviews 11.2 (2007), pp. 235–258.

[5] G. Roe. "Boeing Flywheel Energy Storage Technology". In: (2012). URL: http://www.uaf.edu/files/acep/BoeingFlywheelOverview_06_20_2012.pdf.

[6] F.A. Bhuiyan and A. Yazdani. "Energy storage technologies for grid-connected and off-grid power system applications". In: Electrical Power and Energy Conference (EPEC), 2012 IEEE. Oct. 2012, pp. 303–310. DOI: 10.1109/EPEC.2012.6474970.

[7] Valerie Lyons and et al. "Space Power and Energy Storage Roadmap". In: (2012). URL: http://www.nasa.gov/pdf/501328main_TA03-ID_rev7_NRC_wTASR.pdf.

[8] A. Smith. "Breakthrough in Ricardo Kinergy 'second generation' high-speed flywheel technology". In: (2011). URL: http://www.ricardo.com/en-GB/News--Media/Press-releases/News-releases1/2011/Breakthrough-in-Ricardo-Kinergy-second-generation-high-speed-flywheel-technology/.

[9] Ralph Jansen et al. "Single axis flywheel IPACS@ 1300w, 0.8 nm". In: Space Power Workshop, Manhattan Beach, CA (2005).

[10] F. Wolff. "Flywheel Energy Storage Technology Being Developed". In: NASA Technical Reports Server (Mar. 2001). URL: http://nix.nasa.gov/search.jsp?R=20050195881&qs=N=4294967061+4294724640&No=60.

[11] B. Wimer. "Dynamic Model and Design of an Integrated Flywheel Energy Storage System". Master's Thesis. University of Idaho, 2014.

[12] B. Kisling. "Active Magnetic Bearing Control for an Experimental Flywheel Energy Storage System". Master's Thesis. University of Idaho, 2014.

[13] R. Larsonneur. "Design and Control of Active Magnetic Bearing Systems for High Speed Rotation". Doctoral Thesis. Swiss Federal Institute of Technology Zurich, 1990. URL: http://www.mecos.com/pdf/PHD_0003.PDF.

[14] Hannes Bleuler et al. "Application of digital signal processors for industrial magnetic bearings". In: Control Systems Technology, IEEE Transactions on 2.4 (1994), pp. 280–289.

[15] N. Eastman. "Considerations for Mixed analog/digital PCB design". In: WESCON/96. IEEE. 1996, pp. 297–301.

[16] S. Myburgh. "The development of a fully suspended AMB system for a high-speed flywheel application". Master's Thesis. North-West University, South Africa, 2007. URL: http://dspace.nwu.ac.za/handle/10394/2314.

[17] M. Reading. "Flywheel Energy Storage System Consultant Report". In: AFS Trinity Power Corporation (Feb. 2004). URL: http://www.energy.ca.gov/reports/2004-04-07_500-04-014.PDF.

[18] G. Schweitzer, E. H. Maslen, et al. Magnetic Bearings: Theory, Design, and Application to Rotating Machinery. Springer, 2009.

[19] A. Lidow. Is it the End of the Road for Silicon in Power Conversion? Efficient Power Conversion Corporation. 2010. URL: http://www.digikey.com/Web%20Export/Supplier%20Content/EfficientPowerConversion_917/PDF/EPC_Appnote_Si_endofroad.pdf?redirected=1.

[20] N. Mohan, U. Undeland, and W. Robbins. Power Electronics: Converters, Applications, and Design. John Wiley & Sons, Inc., 2003.

[21] IPD048N06L3 G. Infineon, Inc. Dec. 2008. URL: http://www.infineon.com/dgdl/IPD048N06L3_Rev2.0.pdf?folderId=db3a30431441fb5d01148ca9f1be0e77&fileId=db3a30431ddc9372011e2b4f496e4db0.

[22] Pololu High-Power Motor Driver 36v20 CS. Pololu Robotics and Electronics, Inc. URL: http://www.pololu.com/product/1457.

[23] N. Mohan. Power Electronics: A First Course. John Wiley & Sons, Inc., 2012.

[24] Automotive Full Bridge MOSFET Driver. 5th ed. Allegro Microsystems, Inc. Aug. 2011. URL: http://www.allegromicro.com/Products/Motor-Driver-And-Interface-ICs/Brush-DC-Motor-Drivers/A3941.aspx.

[25] Kaman Aerospace. Inductive Technology Handbook. Kaman Precision Products / Measuring. URL: http://www.kaman.com/files/file/Kaman_Applications_Handbook_WEB.pdf.

[26] Kaman Aerospace. KD-2446 Sensor Data Sheet. Kaman Precision Products / Measuring. URL: http://www.kamansensors.com/pdf_files/Kaman_KD-2446_data_sheet_web.pdf.

[27] Kaman Aerospace. KD-2306 Instrument Data Sheet. Kaman Precision Products / Measuring. URL: http://www.kamansensors.com/pdf_files/Kaman_KD-2306_data_sheet_web.pdf.

[28] Eddy-Current Displacement Sensor ECL101 - Single Channel DIN Rail Mount, ECL110 - Multi-Channel (No Enclosure). Lion Precision, Inc. URL: http://www.lionprecision.com/inductive-sensors/ecl101.html.

[29] Eddy current sensors for displacement and position. Micro-Epsilon Messtechnik GmbH & Co. KG. URL: http://www.micro-epsilon.com/displacement-position-sensors/eddy-current-sensor/index.html.

[30] 3300 XL 11mm Proximity Transducer System. General Electric, Measurement and Control, Bently-Nevada. URL: http://www.ge-mcs.com/download/sensors-and-transducers/146256.pdf.

[31] Automotive Grade, Fully Integrated, Hall Effect-Based Linear Current Sensor IC with 2.1 kVRMS Voltage Isolation and a Low-Resistance Current Conductor. Allegro Microsystems, Inc. Oct. 2011. URL: http://www.pololu.com/file/0J196/ACS714-Datasheet.pdf.

[32] Spero M. "Thermocouple Temperature Measurements for Twin Jet Thermal Mixing". Master's Thesis. University of Tennessee, 2011. URL: http://trace.tennessee.edu/utk_gradthes/1090.

[33] H. Duckworth. Electricity and Magentism. New York: Holt, Rinehart and Winston, Inc., 1960.

[34] OM-CP-QUADTEMP-A. OMEGA Engineering, Inc. URL: http://www.omega.com/DAS/pdf/OM-CP-QUADTEMP-A.pdf.

[35] TMS320F28335 Experimenter Kit. Texas Instruments, Inc. URL: http://www.ti.com/tool/tmdsdock28335.

[36] TMS320F28335, TMS320F28334, TMS320F28332 TMS320F28235, TMS320F28234, TMS320F28232 Digital Signal Controllers (DSCs). Texas Instruments, Inc. Aug. 2012. URL: http://www.ti.com/lit/ds/symlink/tms320f28335.pdf.

[37] TMS320F28377D. Texas Instruments, Inc. URL: http://www.ti.com/product/tms320f28377d.

[38] F28377D Delfino Experimenter Kit. Texas Instruments, Inc. URL: http://www.ti.com/tool/tmdxdock28377d.

[39] P. Shinde. Hardware Design Guidelines for TMS320F28xx and TMS320F28xxx DSCs. Texas Instruments, Inc. Aug. 2011. URL: http://www.ti.com/lit/an/spraas1b/spraas1b.pdf.

[40] LM118, LM218, LM318 Fast General-Purpose Operational Amplifiers. Texas Instruments, Inc. Dec. 2002. URL: http://www.ti.com/product/lm318.

[41] A Designer's Guide to Instrumentation Amplifiers. Analog Devices, Inc. 2006. URL: http://www.analog.com/static/imported-files/design_handbooks/5812756674312778737Complete_In_Amp.pdf.

[42] INA128 INA129 Precision , Low Power Instrumentation Amplifiers. Texas Instruments, Inc. Feb. 2005. URL: http://www.ti.com/product/ina129.

[43] MT-070 Tutorial In-Amp Input RFI Protection, Protecting In-Amps Against RFI. Analog Devices, Inc., 2009. URL: http://www.analog.com/static/imported-files/tutorials/MT-070.pdf.

[44] M. Duff. "Five basic mistakes to avoid when using instrumentation amplifiers". In: Planet Analog (June 2007). URL: http://www.planetanalog.com/document.asp?doc_id=527518.

[45] Tektronix AM503A Current Probe Amplifier Service Manual. Tektronix, Inc. Dec. 1993. URL: http://energy.ece.illinois.edu/equipment/am503a_service.pdf.

[46] R. Sanapala. "Characterization of FR-4 Printed Circuit Board Laminates Before and After Exposure to Lead-free Soldering Conditions". Master's Thesis. University of Maryland, 2008. URL: http://hdl.handle.net/1903/8362.

[47] EAGLE Easily Applicable Graphical Layout Editor Manual Version 6. Cadsoft Computer, Inc. 2011. URL: http://www.cadsoftusa.com/training/manuals/.

[48] M. Fortunato. Successful PCB grounding with mixed-signal chips - Part 1: Principles of current flow. Maxim Integrated Products. Aug. 2012. URL: http://www.edn.com/design/analog/4394761/Successful-PCB-grounding-with-mixed-signal-chips---Part-1--Principles-of-current-flow.

[49] M. Stoehr. Avoid PC-Layout Gotchas in ISM-RF Products. Maxim Integrated Products. Apr. 2011. URL: http://www.maximintegrated.com/app-notes/index.mvp/id/4636.

[50] 8-Bit Bidirectional Voltage-Level Translator with Auto-Direction Sensing and ±15 -kV ESD Protection. Texas Instruments, Inc. May 2012. URL: http://www.ti.com/product/txb0108.

[51] D. Graovac. MOSFET Power Losses Calculation Using the Data- Sheet Parameters. infineon, Inc. July 2006. URL: http://www.btipnow.com/library/white_papers/MOSFET%20Power%20Losses%20Calculation%20Using%20the%20Data-Sheet%20Parameters.pdf.

[52] Ichiro Omura et al. "Gallium Nitride power HEMT for high switching frequency power electronics". In: Physics of Semiconductor Devices, 2007. IWPSD 2007. International Workshop on. IEEE. 2007, pp. 781–786.

[53] GaN Based Power Devices: Cost-Effective Revolutionary Performance. International Rectifier. 2008. URL: http://www.irf.com/pressroom/articles/560pee0811.pdf.

[54] HIP4081, 80V High Frequency H Bridge Driver. Intersil. 2003. URL: http://www.hvlabs.com/files/HIP4081application.pdf.

[55] IXD604 4 Ampere Dual Low Side Ultrafast MOSFET Drivers. IXYS Integrated Circuits Division. 2012. URL: http://www.clare.com/home/pdfs.nsf/www/IXD_604.pdf/$file/IXD_604.pdf.

Appendix A

Prototype PCB Schematic and Board Layout

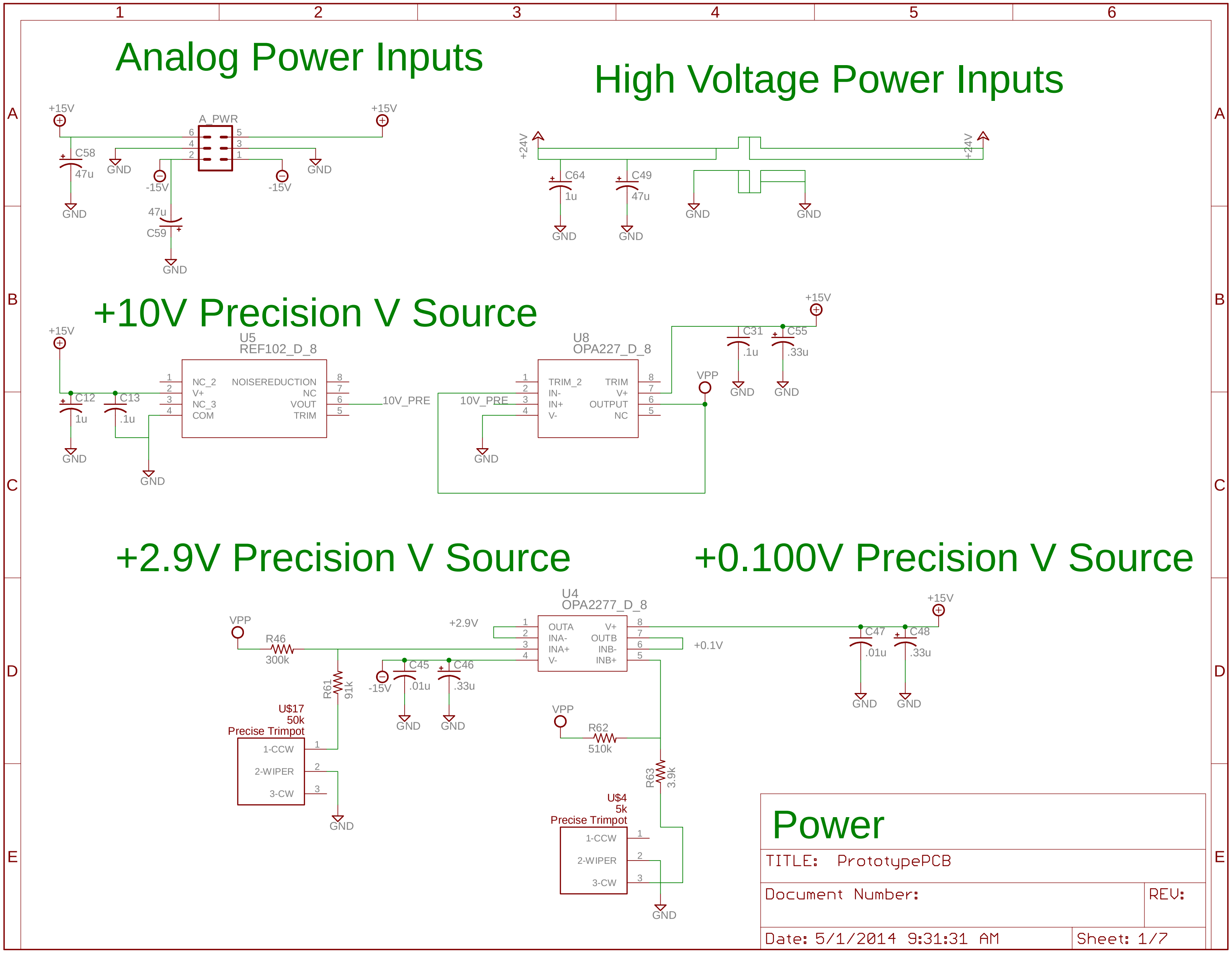
1
2
3
4
5
6
A
B
C
D
E
Analog Power Inputs
+15V
C58
47u
GND
A_PWR
6
4
2
5
3
1
GND
-15V
-15V
GND
+15V
47u
C59
GND
High Voltage Power Inputs
+24V
C64
1u
GND
C49
47u
GND
GND
GND
+24V
+10V Precision V Source
+15V
C12
1u
GND
C13
.1u
GND
U5
REF102_D_8
NC_2
V+
NC_3
COM
NOISEREDUCTION
NC
VOUT
TRIM
1
2
3
4
8
7
6
5
10V_PRE
U8
OPA227_D_8
10V_PRE
TRIM_2
IN-
IN+
V-
TRIM
V+
OUTPUT
NC
GND
VPP
+15V
C31
.1u
GND
C55
.33u
GND
+2.9V Precision V Source
+0.100V Precision V Source
VPP
R46
300k
R61
91k
U$17
50k
Precise Trimpot
1-CCW
2-WIPER
3-CW
GND
+2.9V
-15V
C45
.01u
GND
C46
.33u
GND
U4
OPA2277_D_8
OUTA
INA-
INA+
V-
V+
OUTB
INB-
INB+
+0.1V
VPP
R62
510k
R63
3.9k
U$4
5k
Precise Trimpot
1-CCW
2-WIPER
3-CW
GND
+15V
C47
.01u
GND
C48
.33u
GND
Power
TITLE: PrototypePCB
Document Number:
REV:
Date: 5/1/2014 9:31:31 AM
Sheet: 1/7

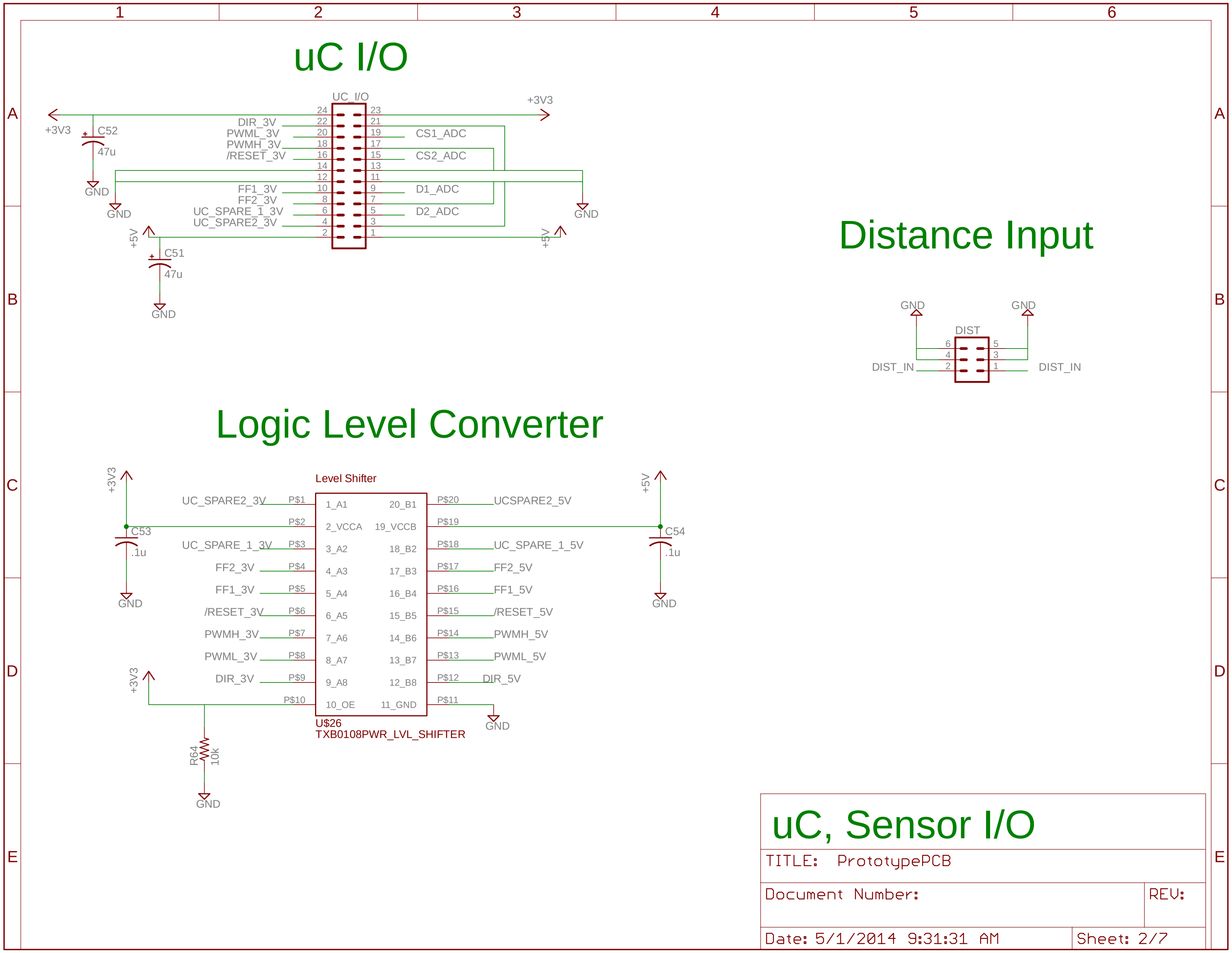
uC I/O
UC_I/O
+3V3
C52
47u
GND
DIR_3V
PWML_3V
PWMH_3V
/RESET_3V
FF1_3V
FF2_3V
UC_SPARE_1_3V
UC_SPARE2_3V
CS1_ADC
CS2_ADC
D1_ADC
D2_ADC
+5V
C51
47u
Distance Input
DIST
GND
DIST_IN
Logic Level Converter
Level Shifter
U$26
TXB0108PWR_LVL_SHIFTER
1_A1
2_VCCA
3_A2
4_A3
5_A4
6_A5
7_A6
8_A7
9_A8
10_OE
20_B1
19_VCCB
18_B2
17_B3
16_B4
15_B5
14_B6
13_B7
12_B8
11_GND
UCSPARE2_5V
UC_SPARE_1_5V
FF2_5V
FF1_5V
/RESET_5V
PWMH_5V
PWML_5V
DIR_5V
C53
C54
.1u
R64
10k
uC, Sensor I/O
TITLE: PrototypePCB
Document Number:
REV:
Date: 5/1/2014 9:31:31 AM
Sheet: 2/7

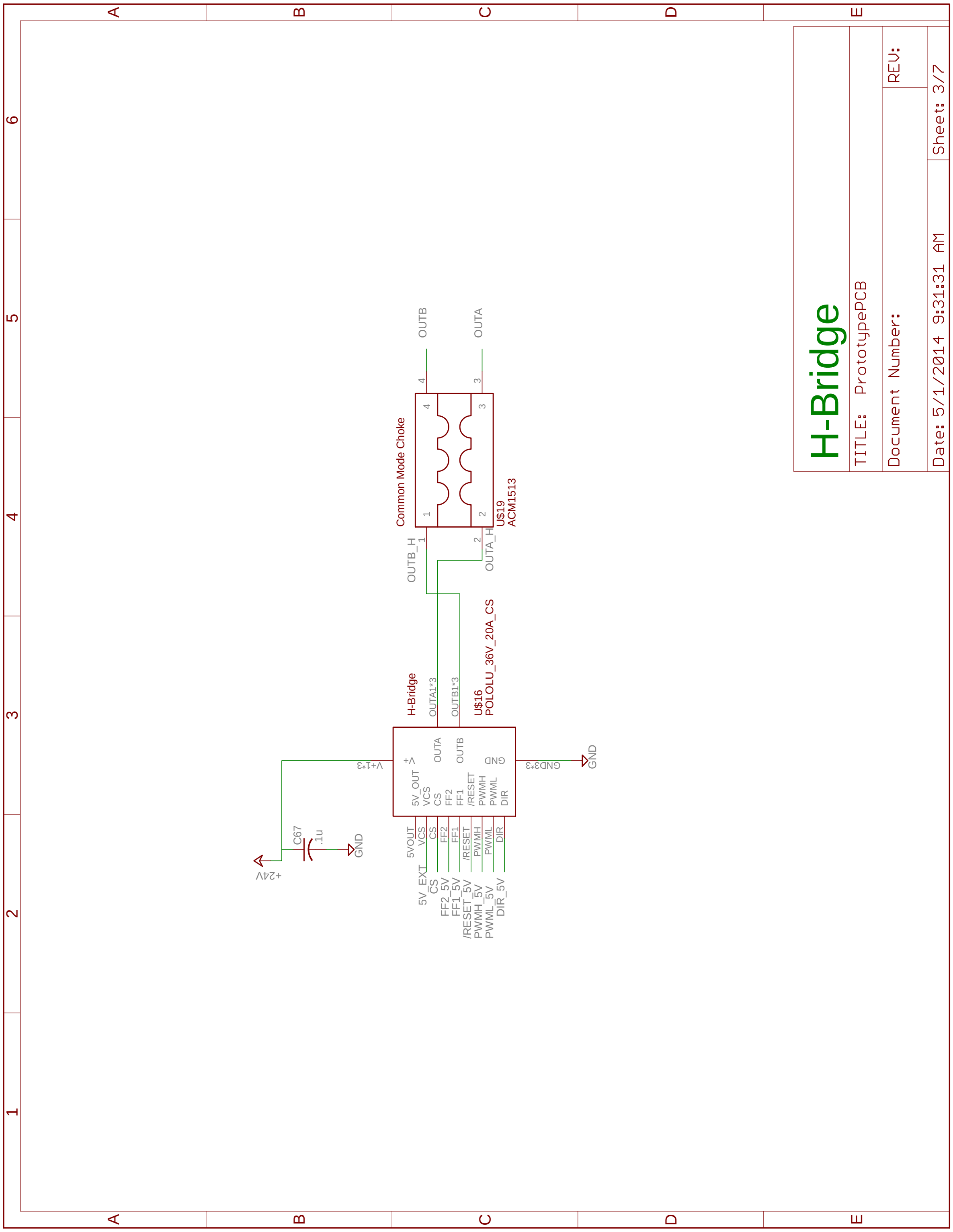
H-Bridge
TITLE: PrototypePCB
Document Number:
REV:
Date: 5/1/2014 9:31:31 AM
Sheet: 3/7
Common Mode Choke
U$19
ACM1513
OUTB
OUTA
OUTB_H
OUTA_H
H-Bridge
U$16
POLOLU_36V_20A_CS
OUTA1*3
OUTB1*3
V+
OUTA
OUTB
GND
5V_OUT
VCS
CS
FF2
FF1
/RESET
PWMH
PWML
DIR
V+1*3
GND3*3
GND
C67
.1u
GND
+24V
5VOUT
5V_EXT
CS
FF2_5V
FF1_5V
/RESET_5V
PWMH_5V
PWML_5V
DIR_5V
A
B
C
D
E
1
2
3
4
5
6

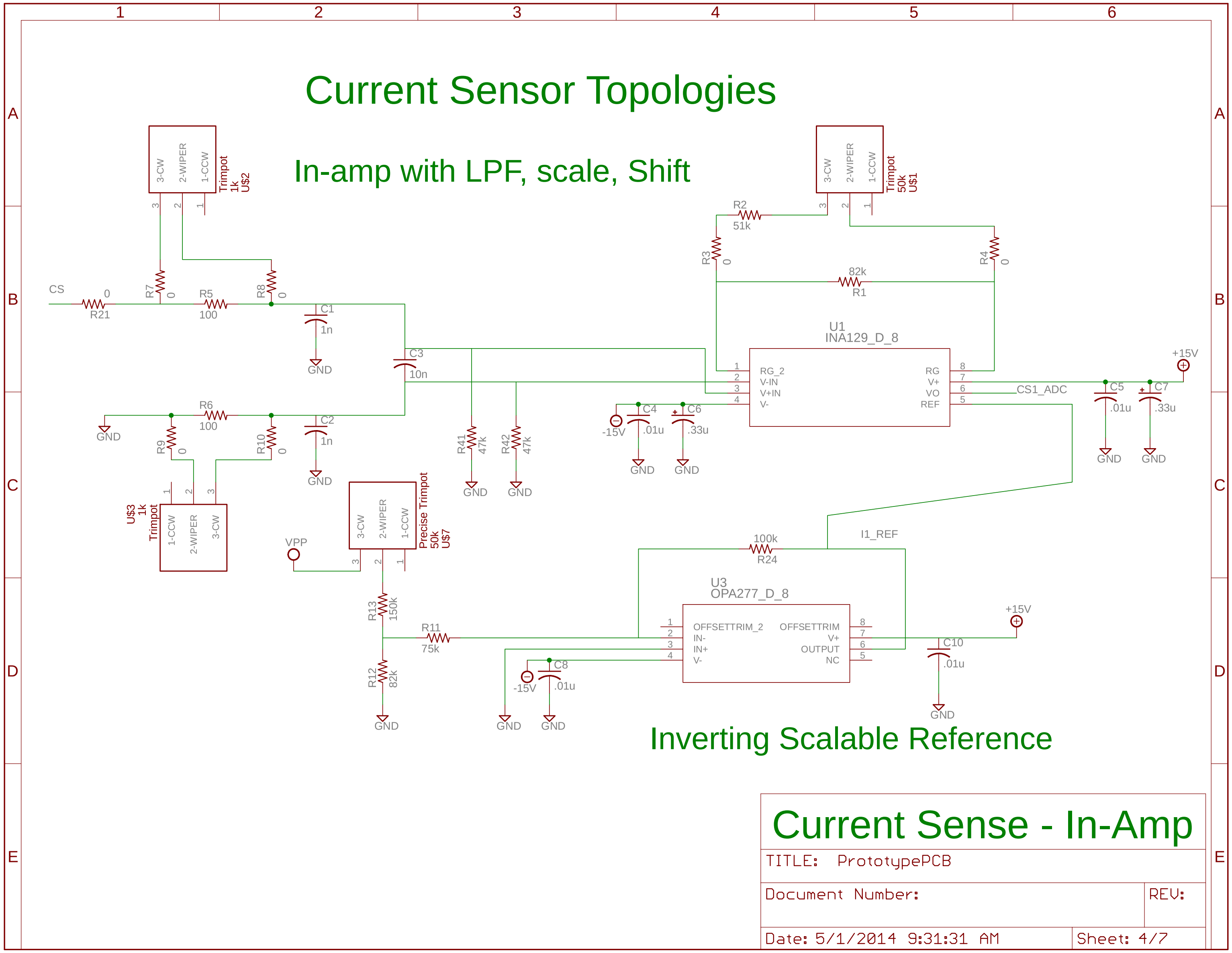
Current Sensor Topologies
In-amp with LPF, scale, Shift
Inverting Scalable Reference
Current Sense - In-Amp
TITLE: PrototypePCB
Document Number:
REV:
Date: 5/1/2014 9:31:31 AM
Sheet: 4/7
1
2
3
4
5
6
A
B
C
D
E
CS
R21
0
R7
0
R5
100
R8
0
C1
1n
C2
1n
C3
10n
R6
100
R9
0
R10
0
GND
Trimpot
1k
U$2
3-CW
2-WIPER
1-CCW
Trimpot
1k
U$3
Precise Trimpot
50k
U$7
VPP
R13
150k
R11
75k
R12
82k
R41
47k
R42
47k
Trimpot
50k
U$1
R2
51k
R3
0
R4
0
R1
82k
U1
INA129_D_8
RG_2
V-IN
V+IN
V-
RG
V+
VO
REF
CS1_ADC
+15V
-15V
C4
.01u
C6
.33u
C5
.01u
C7
.33u
R24
100k
I1_REF
U3
OPA277_D_8
OFFSETTRIM_2
IN-
IN+
V-
OFFSETTRIM
V+
OUTPUT
NC
C8
.01u
C10
.01u

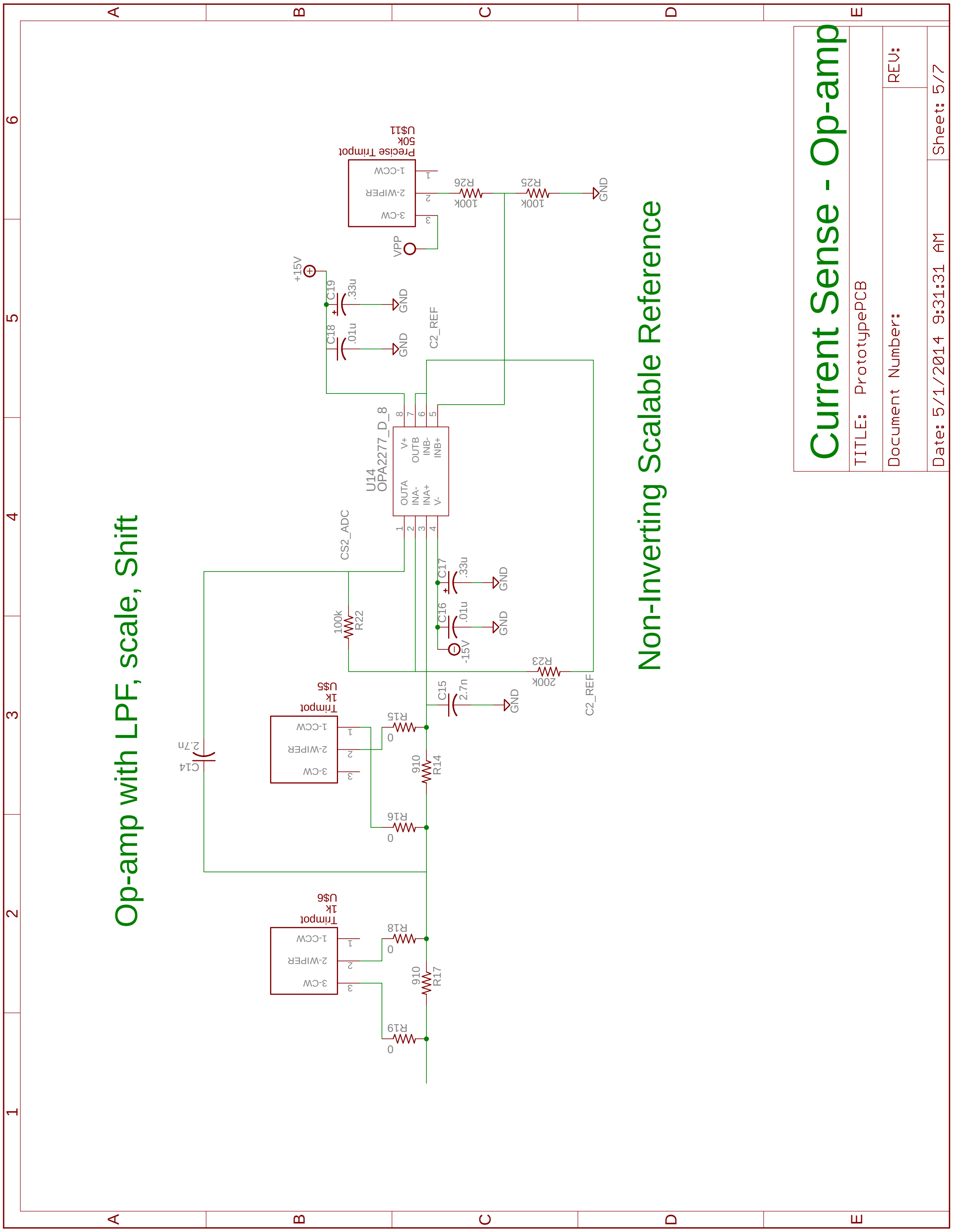
Op-amp with LPF, scale, Shift
Non-Inverting Scalable Reference
U14
OPA2277_D_8
OUTA
INA-
INA+
V-
V+
OUTB
INB-
INB+
CS2_ADC
C2_REF
C2_REF
+15V
-15V
VPP
GND
C19
.33u
C18
.01u
C17
.33u
C16
.01u
C15
2.7n
C14
2.7n
R22
100k
R23
200k
R25
100k
R26
100k
R14
910
R17
910
R15
0
R16
0
R18
0
R19
0
Precise Trimpot
50K
U$11
Trimpot
1K
U$5
Trimpot
1K
U$6
1-CCW
2-WIPER
3-CW
Current Sense - Op-amp
TITLE: PrototypePCB
Document Number:
REV:
Date: 5/1/2014 9:31:31 AM
Sheet: 5/7

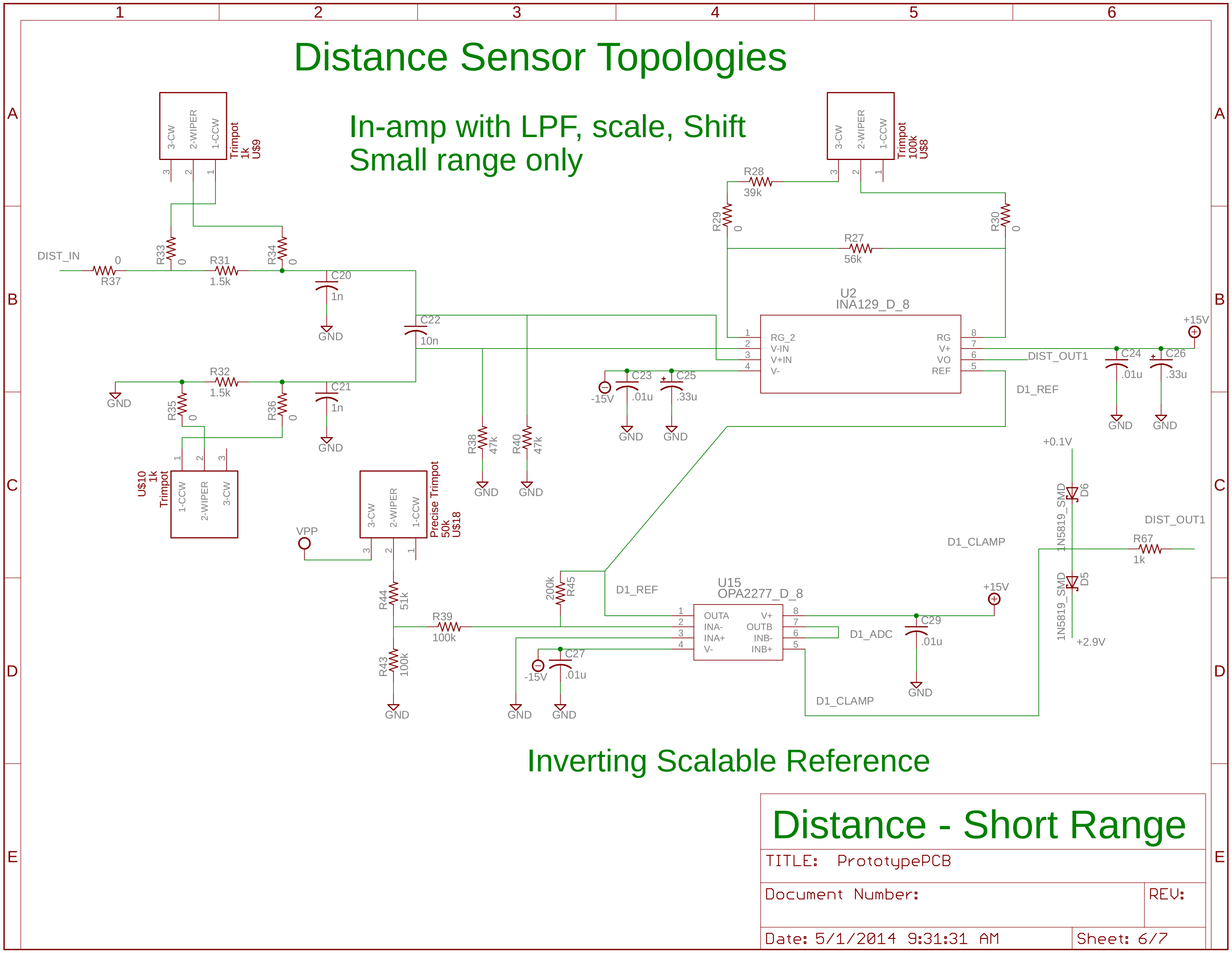
Distance Sensor Topologies
In-amp with LPF, scale, Shift
Small range only
Inverting Scalable Reference
Distance - Short Range
TITLE: PrototypePCB
Document Number:
REV:
Date: 5/1/2014 9:31:31 AM
Sheet: 6/7
DIST_IN
R37 0
R33 0
R31 1.5k
R34 0
R32 1.5k
R35 0
R36 0
C20 1n
C21 1n
C22 10n
Trimpot 1k U$9
Trimpot 1k U$10
Trimpot 100k U$8
Precise Trimpot 50k U$18
1-CCW
2-WIPER
3-CW
R28 39k
R29 0
R30 0
R27 56k
U2 INA129_D_8
RG_2
V-IN
V+IN
V-
RG
V+
VO
REF
R38 47k
R40 47k
C23 .01u
C25 .33u
C24 .01u
C26 .33u
+15V
-15V
GND
DIST_OUT1
D1_REF
VPP
R44 51k
R43 100k
R39 100k
R45 200k
C27 .01u
U15 OPA2277_D_8
OUTA
INA-
INA+
V-
V+
OUTB
INB-
INB+
C29 .01u
D1_ADC
D1_CLAMP
+0.1V
+2.9V
D6 1N5819_SMD
D5 1N5819_SMD
R67 1k

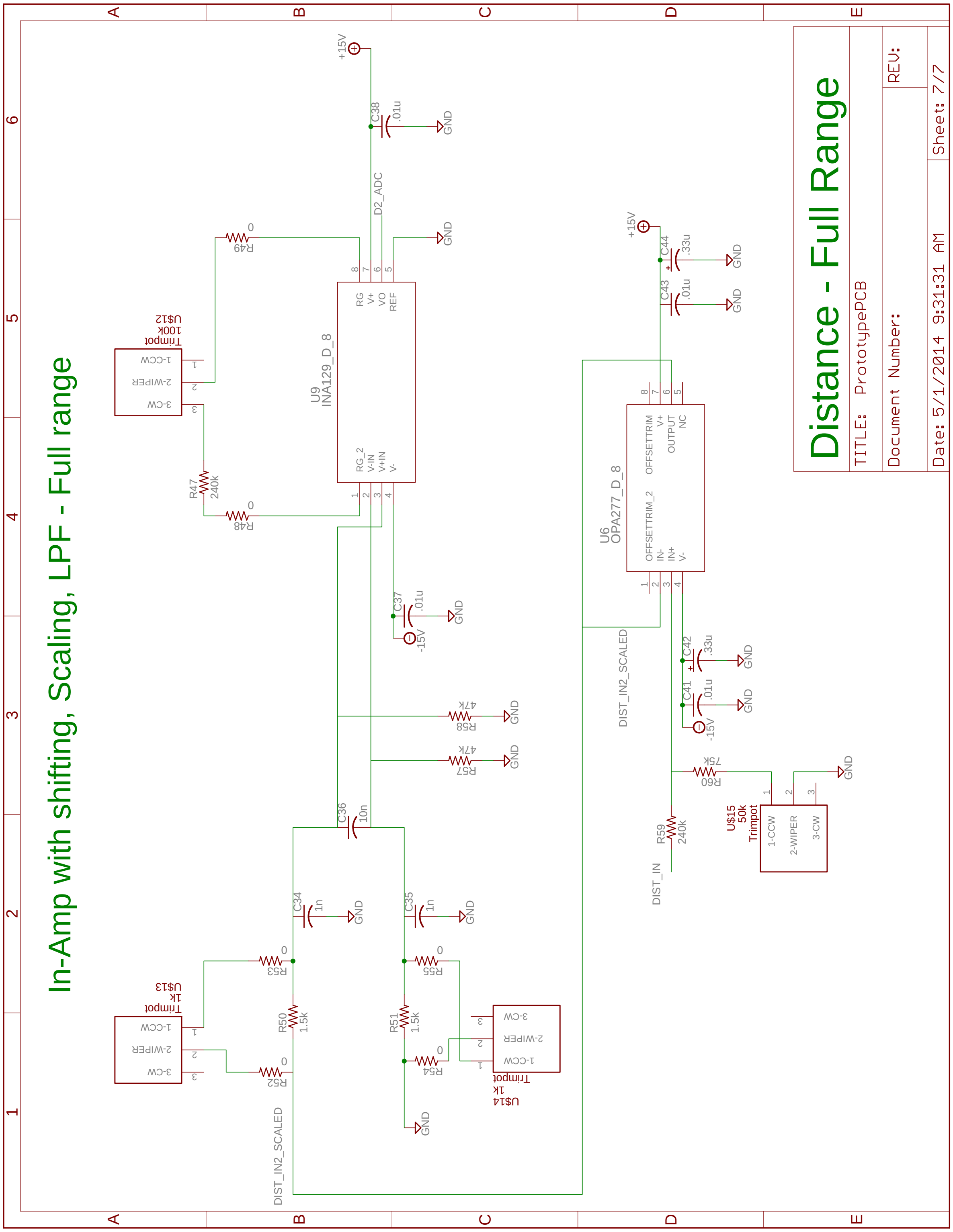
In-Amp with shifting, Scaling, LPF - Full range
Distance - Full Range
TITLE: PrototypePCB
Document Number:
REV:
Date: 5/1/2014 9:31:31 AM
Sheet: 7/7
U9
INA129_D_8
RG_2
V-IN
V+IN
V-
RG
V+
VO
REF
U6
OPA277_D_8
OFFSETTRIM_2
IN-
IN+
V-
OFFSETTRIM
V+
OUTPUT
NC
U$12
100K
Trimpot
U$13
1K
Trimpot
U$14
1k
Trimpot
U$15
50k
Trimpot
1-CCW
2-WIPER
3-CW
R47
240k
R48
0
R49
0
R50
1.5k
R51
1.5k
R52
0
R53
0
R54
0
R55
0
R57
47K
R58
47K
R59
240k
R60
75K
C34
1n
C35
1n
C36
10n
C37
.01u
C38
.01u
C41
.01u
C42
.33u
C43
.01u
C44
.33u
+15V
-15V
GND
D2_ADC
DIST_IN2_SCALED
DIST_IN
A
B
C
D
E
1
2
3
4
5
6

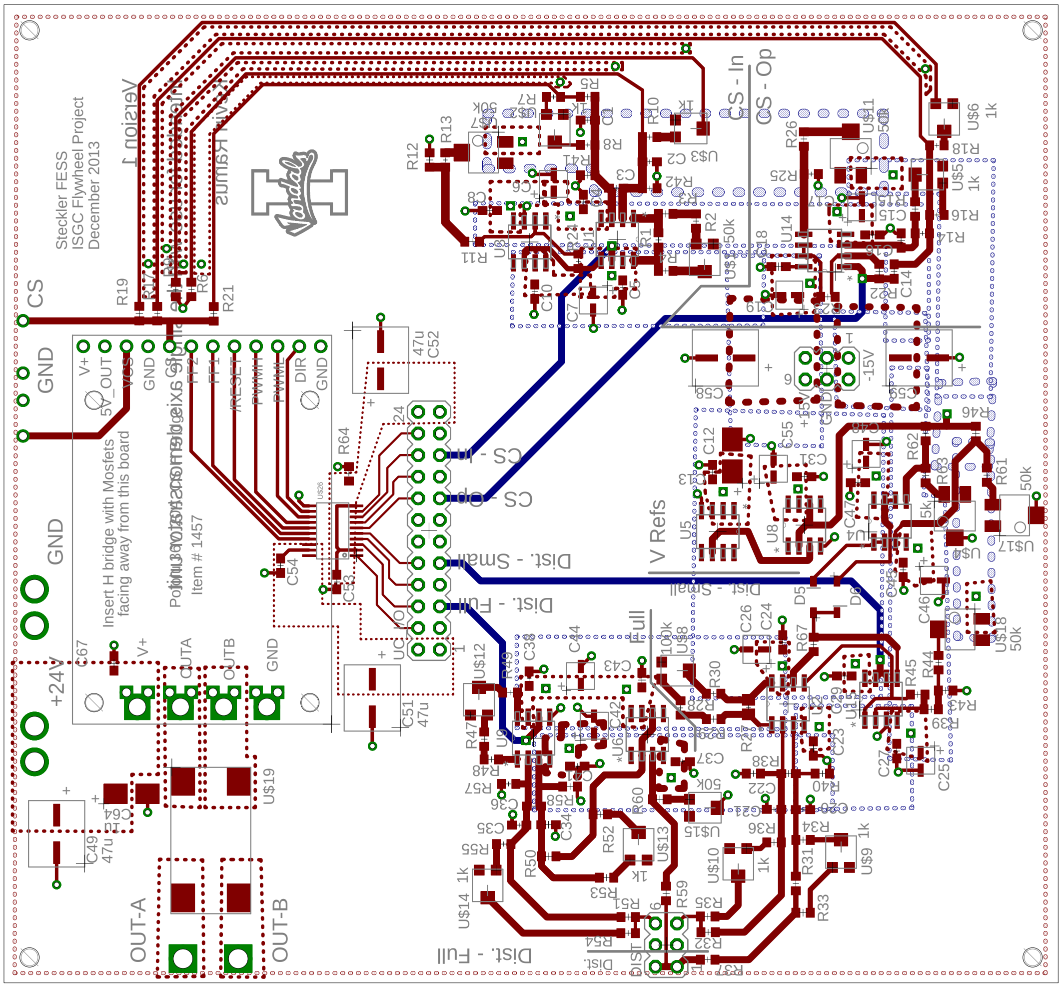
Steckler FESS
ISGC Flywheel Project
December 2013
Version 1
CS
GND
+24V
OUT-A
OUT-B
Insert H bridge with Mosfets
facing away from this board
Item # 1457
CS - In
CS - Op
Dist. - Small
Dist. - Full
V Refs
-15V
+15V
V+
OUTA
OUTB
DIR
PWM
RESET
47u
50k
1k
100k

Appendix B

Prototype PCB Bill of Materials

Part Name	**Part Number**	**Supplier**
CAP CER 1000PF 50V 1% NP0 0603	490-6377-1-ND	Digikey
CAP CER 10000PF 50V 5% X7R 0603	399-1092-1-ND	Digikey
CAP ALUM 0.33UF 50V 20% SMD	PCE3939CT-ND	Digikey
CAP TANT 1UF 50V 10% 2413	399-10241-1-ND	Digikey
CAP CER 0.1UF 50V 10% X7R 0603	1276-1000-1-ND	Digikey
CAP CER 2700PF 50V 10% X7R 0603	399-7890-1-ND	Digikey
CAP ALUM 47UF 50V 20% SMD	399-6690-1-ND	Digikey
DIODE SCHOTTKY 40V 1A SOD123	1N5819HW-FDICT-ND	Digikey
RES 82K OHM 1/10W 1% 0603	RMCF0603FT82K0CT-ND	Digikey
RES 75K OHM 1/10W 5% 0603	RMCF0603JT75K0CT-ND	Digikey
RES 0.0 OHM 1/10W JUMP 0603	RMCF0603ZT0R00CT-ND	Digikey
RES 100 OHM 1/10W .1% 0603 SMD	P100DBCT-ND	Digikey
RES 150K OHM 1/10W 5% 0603	RMCF0603JT150KCT-ND	Digikey
RES 910 OHM 1/10W 1% 0603 SMD	P910HCT-ND	Digikey
RES 100K OHM 1/16W .5% 0603 SMD	RR08P100KDCT-ND	Digikey
RES 200K OHM 1/16W .5% 0603 SMD	RR08P200KDCT-ND	Digikey
RES 62K OHM 1/10W .5% 0603 SMD	311-62KDCT-ND	Digikey
RES 56.0K OHM 1/16W .5% 0603 SMD	RR08P56.0KDCT-ND	Digikey
RES 39K OHM 1/10W 5% 0603	RMCF0603JT39K0CT-ND	Digikey
RES 1K OHM 1/10W 1% 0603	RMCF0603FT1K00CT-ND	Digikey
RES 47K OHM 1/10W 1% 0603	RMCF0603FT47K0CT-ND	Digikey
RES 51K OHM 1/10W 5% 0603	RMCF0603JT51K0CT-ND	Digikey
RES 91K OHM 1/10W 5% 0603	RMCF0603JT91K0CT-ND	Digikey
RES 510 OHM 1/10W 5% 0603	RMCF0603JT510RCT-ND	Digikey
RES 1.5K OHM 1/10W .1% 0603 SMD	P1.5KDBCT-ND	Digikey
RES 240K OHM 1/10W 1% 0603	RMCF0603FT240KCT-ND	Digikey
RES 300K OHM 1/10W 5% 0603	RMCF0603JT300KCT-ND	Digikey
RES 510K OHM 1/10W 5% 0603 SMD	P510KGCT-ND	Digikey
RES 3.9K OHM 1/10W 5% 0603	RMCF0603JT3K90CT-ND	Digikey
RES 10K OHM 1/10W 5% 0603	RMCF0603JT10K0CT-ND	Digikey
TRIMMER 50K OHM 0.1W SMD	TC33X-503ECT-ND	Digikey
TRIMMER 1K OHM 0.1W SMD	TC33X-102ECT-ND	Digikey
TRIMMER 100K OHM 0.1W SMD	TC33X-104ECT-ND	Digikey
TRIMMER 5K OHM 0.1W SMD	TC33X-502ECT-ND	Digikey
TRIMMER 50K OHM 0.25W SMD	3214X-1-503ECT-ND	Digikey
TRIMMER 5K OHM 0.25W SMD	3214X-1-502ECT-ND	Digikey

Part Name	**Part Number**	**Supplier**
CHOKE COMM MODE 10A SMD	445-2211-1-ND	Digikey
IC 8-BIT TRNSTR 15KV ESD 20TSSOP	296-21527-1-ND	Digikey
INA129 In-amp	INA129UA-ND	Digikey
IC OPAMP GP 1MHZ 8SOIC	296-23667-1-ND	Digikey
IC VREF SERIES PREC 10V 8-SOIC	REF102AU-ND	Digikey
IC OPAMP GP 1MHZ 8SOIC	OPA277UA-ND	Digikey
IC OPAMP GP 8MHZ 8SOIC	OPA227UA-ND	Digikey
HEX STANDOFF 4-40 NYLON 1/2”	4802K-ND	Digikey
SOLDERPASTE NO CLEAN 63/37 35GM	KE1507-ND	Digikey
PLUNGER 10CC FOR 35GR SYRINGE	10LL4-ND	Digikey

Appendix C

UIFESS Driver 1 PCB Schematic and Board Layout

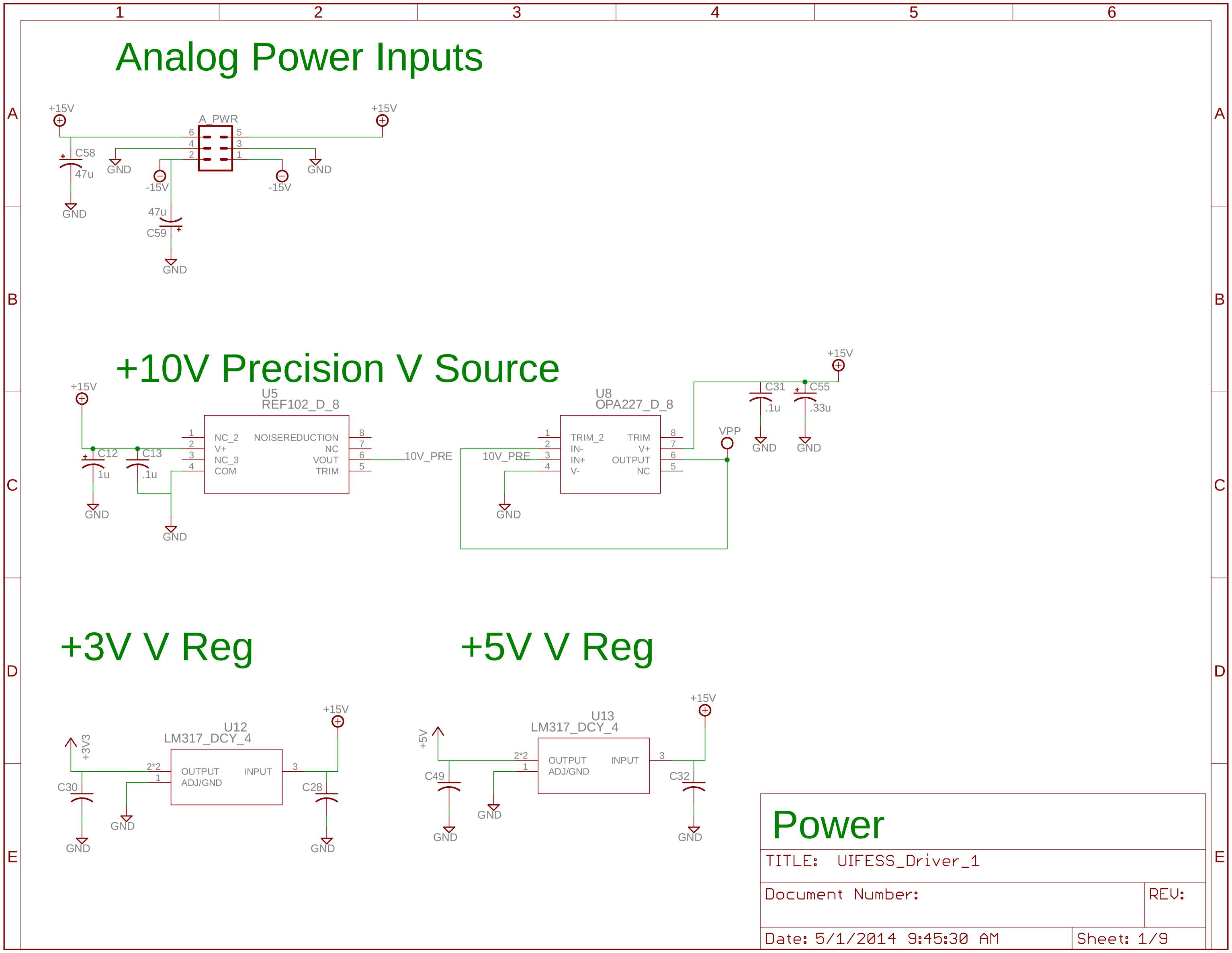
Analog Power Inputs
+15V
C58
47u
GND
A_PWR
6 4 2 5 3 1
GND
-15V
-15V
47u
C59
GND
+15V
GND
+10V Precision V Source
+15V
C12
1u
C13
.1u
GND
GND
U5
REF102_D_8
NC_2
V+
NC_3
COM
NOISEREDUCTION
NC
VOUT
TRIM
10V_PRE
U8
OPA227_D_8
TRIM_2
IN-
IN+
V-
TRIM
V+
OUTPUT
NC
10V_PRE
GND
VPP
C31
.1u
C55
.33u
+15V
GND
GND
+3V V Reg
+3V3
C30
GND
U12
LM317_DCY_4
OUTPUT
ADJ/GND
INPUT
2*2
1
3
GND
C28
+15V
GND
+5V V Reg
+5V
C49
GND
U13
LM317_DCY_4
OUTPUT
ADJ/GND
INPUT
GND
C32
+15V
GND
Power
TITLE: UIFESS_Driver_1
Document Number:
REV:
Date: 5/1/2014 9:45:30 AM
Sheet: 1/9

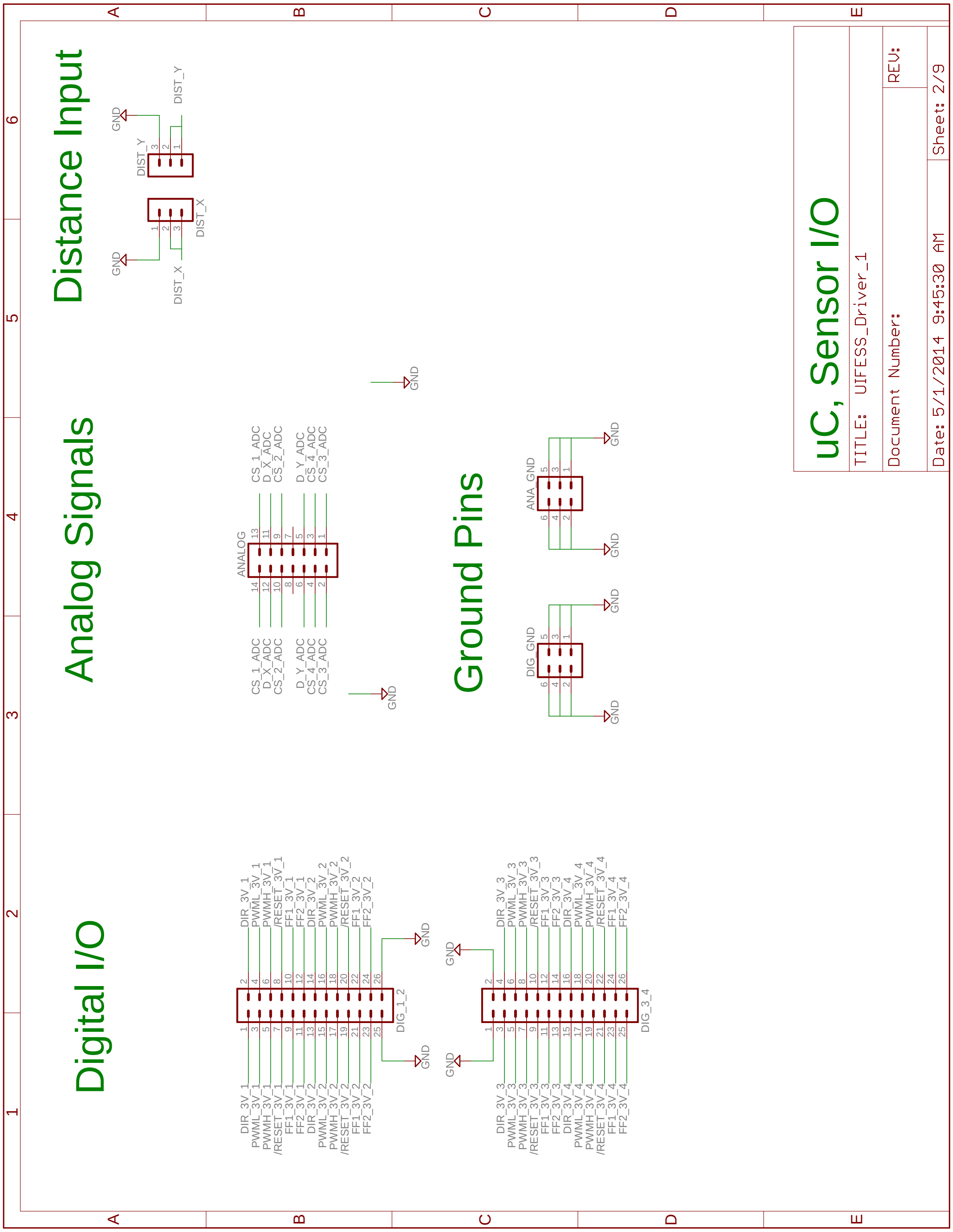
Distance Input
DIST_X
DIST_Y
GND
Analog Signals
ANALOG
CS_1_ADC
D_X_ADC
CS_2_ADC
D_Y_ADC
CS_4_ADC
CS_3_ADC
Ground Pins
DIG_GND
ANA_GND
Digital I/O
DIG_1_2
DIG_3_4
DIR_3V_1
PWML_3V_1
PWMH_3V_1
/RESET_3V_1
FF1_3V_1
FF2_3V_1
DIR_3V_2
PWML_3V_2
PWMH_3V_2
/RESET_3V_2
FF1_3V_2
FF2_3V_2
DIR_3V_3
PWML_3V_3
PWMH_3V_3
/RESET_3V_3
FF1_3V_3
FF2_3V_3
DIR_3V_4
PWML_3V_4
PWMH_3V_4
/RESET_3V_4
FF1_3V_4
FF2_3V_4
uC, Sensor I/O
TITLE: UIFESS_Driver_1
Document Number:
REV:
Date: 5/1/2014 9:45:30 AM
Sheet: 2/9

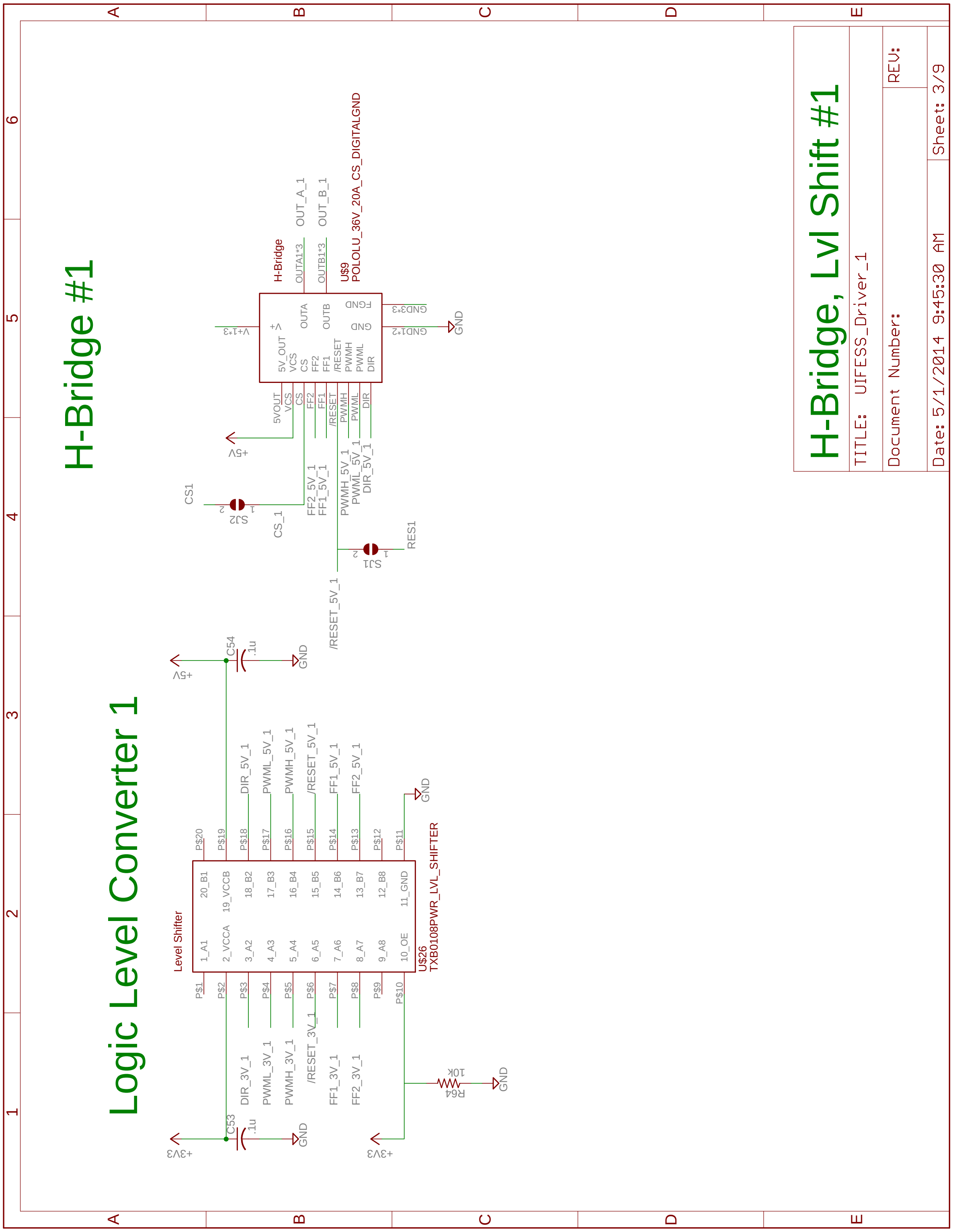
H-Bridge #1
Logic Level Converter 1
H-Bridge
U$9
POLOLU_36V_20A_CS_DIGITALGND
5V_OUT
VCS
CS
FF2
FF1
/RESET
PWMH
PWML
DIR
V+
OUTA
OUTB
GND
FGND
V+1*3
OUTA1*3
OUTB1*3
GND1*2
GND3*3
5VOUT
OUT_A_1
OUT_B_1
+5V
GND
CS1
SJ2
CS_1
FF2_5V_1
FF1_5V_1
PWMH_5V_1
PWML_5V_1
DIR_5V_1
RES1
SJ1
/RESET_5V_1
C54
.1u
C53
Level Shifter
U$26
TXB0108PWR_LVL_SHIFTER
1_A1
2_VCCA
3_A2
4_A3
5_A4
6_A5
7_A6
8_A7
9_A8
10_OE
20_B1
19_VCCB
18_B2
17_B3
16_B4
15_B5
14_B6
13_B7
12_B8
11_GND
P$1
P$2
P$3
P$4
P$5
P$6
P$7
P$8
P$9
P$10
P$20
P$19
P$18
P$17
P$16
P$15
P$14
P$13
P$12
P$11
DIR_3V_1
PWML_3V_1
PWMH_3V_1
/RESET_3V_1
FF1_3V_1
FF2_3V_1
/RESET_5V_1
+3V3
R64
10K
A
B
C
D
E
1
2
3
4
5
6
H-Bridge, Lvl Shift #1
TITLE: UIFESS_Driver_1
Document Number:
REV:
Date: 5/1/2014 9:45:30 AM
Sheet: 3/9

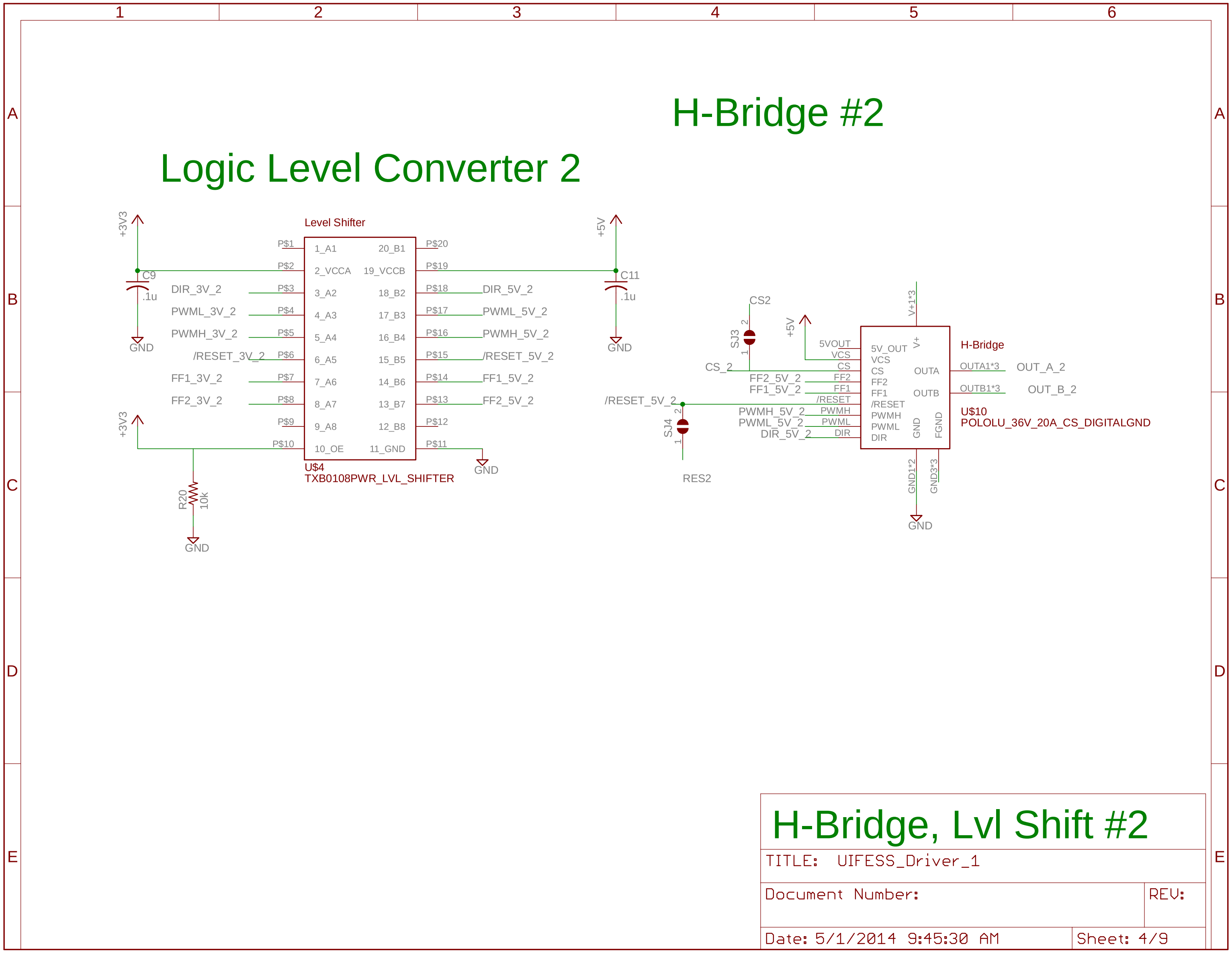
Logic Level Converter 2
H-Bridge #2
Level Shifter
U$4
TXB0108PWR_LVL_SHIFTER
1_A1
2_VCCA
3_A2
4_A3
5_A4
6_A5
7_A6
8_A7
9_A8
10_OE
20_B1
19_VCCB
18_B2
17_B3
16_B4
15_B5
14_B6
13_B7
12_B8
11_GND
P$1
P$2
P$3
P$4
P$5
P$6
P$7
P$8
P$9
P$10
P$20
P$19
P$18
P$17
P$16
P$15
P$14
P$13
P$12
P$11
DIR_3V_2
PWML_3V_2
PWMH_3V_2
/RESET_3V_2
FF1_3V_2
FF2_3V_2
DIR_5V_2
PWML_5V_2
PWMH_5V_2
/RESET_5V_2
FF1_5V_2
FF2_5V_2
+3V3
+3V3
+5V
+5V
C9
.1u
C11
.1u
GND
R20
10k
H-Bridge
U$10
POLOLU_36V_20A_CS_DIGITALGND
5V_OUT
VCS
CS
FF2
FF1
/RESET
PWMH
PWML
DIR
V+
OUTA
OUTB
GND
FGND
5VOUT
V+1*3
OUTA1*3
OUTB1*3
GND1*2
GND3*3
OUT_A_2
OUT_B_2
CS2
SJ3
CS_2
SJ4
RES2
/RESET_5V_2
PWMH_5V_2
PWML_5V_2
DIR_5V_2
1
2
A
B
C
D
E
1
2
3
4
5
6
H-Bridge, Lvl Shift #2
TITLE: UIFESS_Driver_1
Document Number:
REV:
Date: 5/1/2014 9:45:30 AM
Sheet: 4/9

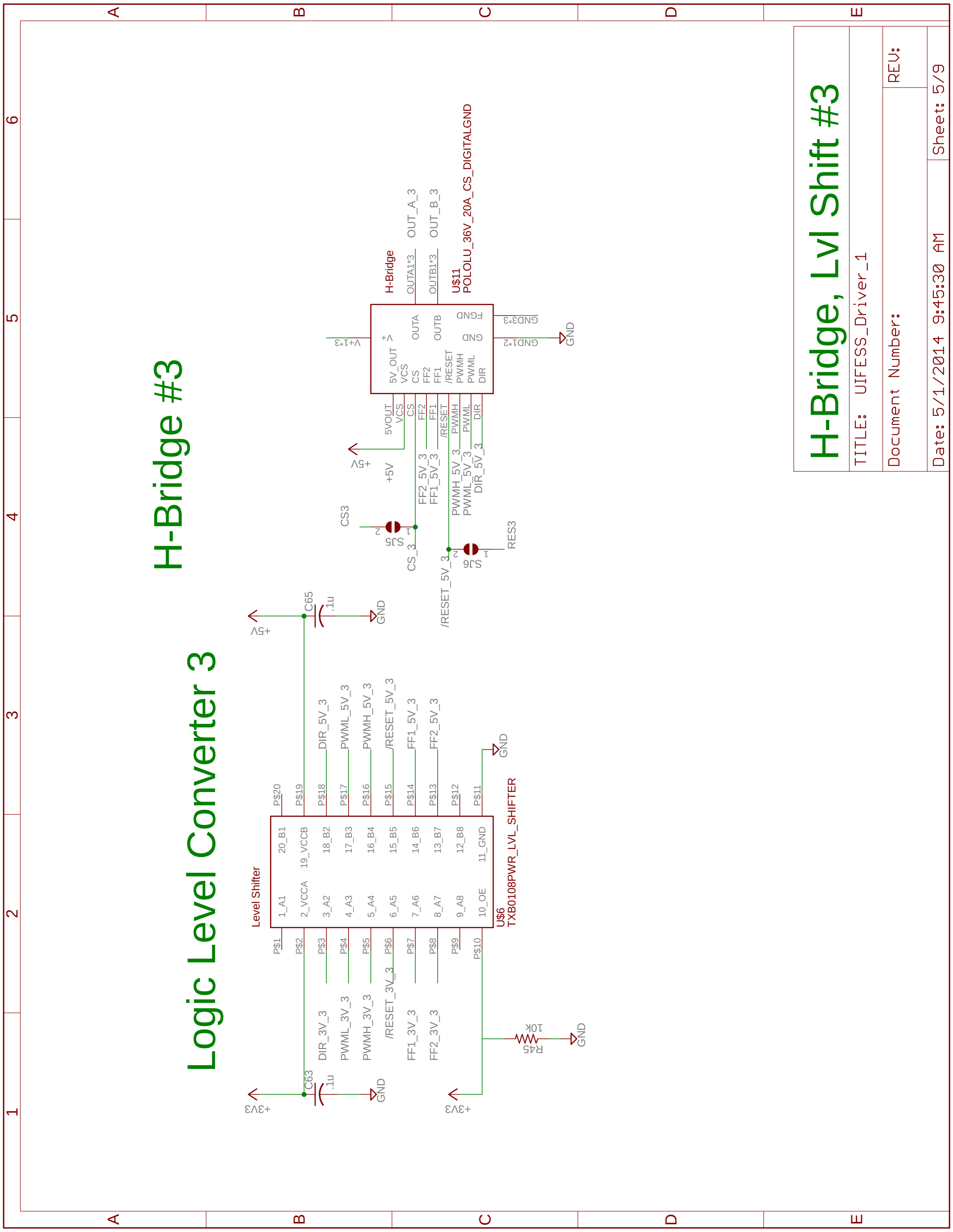
H-Bridge #3
Logic Level Converter 3
H-Bridge
U$11
POLOLU_36V_20A_CS_DIGITALGND
5V_OUT
VCS
CS
FF2
FF1
/RESET
PWMH
PWML
DIR
V+
OUTA
OUTB
GND
FGND
OUTA1*3
OUTB1*3
OUT_A_3
OUT_B_3
V+1*3
GND1*2
GND3*3
GND
+5V
5VOUT
FF2_5V_3
FF1_5V_3
PWMH_5V_3
PWML_5V_3
DIR_5V_3
CS3
SJ5
CS_3
SJ6
RES3
/RESET_5V_3
C65
.1u
Level Shifter
U$6
TXB0108PWR_LVL_SHIFTER
1_A1
2_VCCA
3_A2
4_A3
5_A4
6_A5
7_A6
8_A7
9_A8
10_OE
20_B1
19_VCCB
18_B2
17_B3
16_B4
15_B5
14_B6
13_B7
12_B8
11_GND
P$1
P$2
P$3
P$4
P$5
P$6
P$7
P$8
P$9
P$10
P$20
P$19
P$18
P$17
P$16
P$15
P$14
P$13
P$12
P$11
DIR_3V_3
PWML_3V_3
PWMH_3V_3
/RESET_3V_3
FF1_3V_3
FF2_3V_3
DIR_5V_3
PWML_5V_3
PWMH_5V_3
/RESET_5V_3
FF1_5V_3
FF2_5V_3
C63
.1u
+3V3
R45
10K
H-Bridge, Lvl Shift #3
TITLE: UIFESS_Driver_1
Document Number:
REV:
Date: 5/1/2014 9:45:30 AM
Sheet: 5/9
A
B
C
D
E
1
2
3
4
5
6

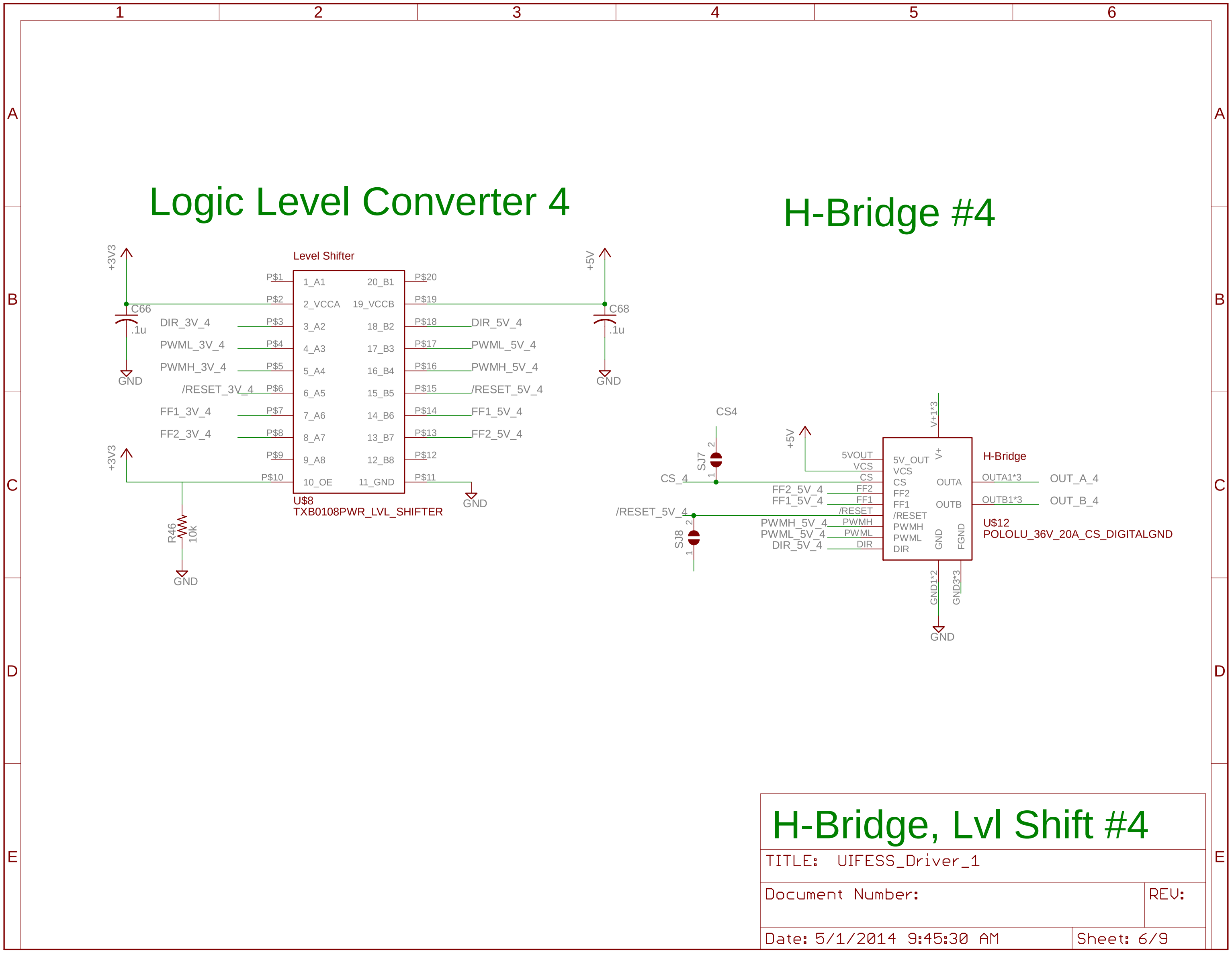
Logic Level Converter 4
H-Bridge #4
Level Shifter
+3V3
C66
.1u
GND
DIR_3V_4
PWML_3V_4
PWMH_3V_4
/RESET_3V_4
FF1_3V_4
FF2_3V_4
+3V3
R46
10k
GND
P$1
P$2
P$3
P$4
P$5
P$6
P$7
P$8
P$9
P$10
1_A1
2_VCCA
3_A2
4_A3
5_A4
6_A5
7_A6
8_A7
9_A8
10_OE
20_B1
19_VCCB
18_B2
17_B3
16_B4
15_B5
14_B6
13_B7
12_B8
11_GND
P$20
P$19
P$18
P$17
P$16
P$15
P$14
P$13
P$12
P$11
U$8
TXB0108PWR_LVL_SHIFTER
GND
DIR_5V_4
PWML_5V_4
PWMH_5V_4
/RESET_5V_4
FF1_5V_4
FF2_5V_4
+5V
C68
.1u
GND
CS4
SJ7
CS_4
/RESET_5V_4
SJ8
+5V
FF2_5V_4
FF1_5V_4
PWMH_5V_4
PWML_5V_4
DIR_5V_4
5VOUT
VCS
CS
FF2
FF1
/RESET
PWMH
PWML
DIR
V+1*3
5V_OUT
VCS
CS
FF2
FF1
/RESET
PWMH
PWML
DIR
V+
OUTA
OUTB
GND
FGND
GND1*2
GND3*3
GND
H-Bridge
OUTA1*3
OUTB1*3
OUT_A_4
OUT_B_4
U$12
POLOLU_36V_20A_CS_DIGITALGND
H-Bridge, Lvl Shift #4
TITLE: UIFESS_Driver_1
Document Number:
REV:
Date: 5/1/2014 9:45:30 AM
Sheet: 6/9
1
2
3
4
5
6
A
B
C
D
E

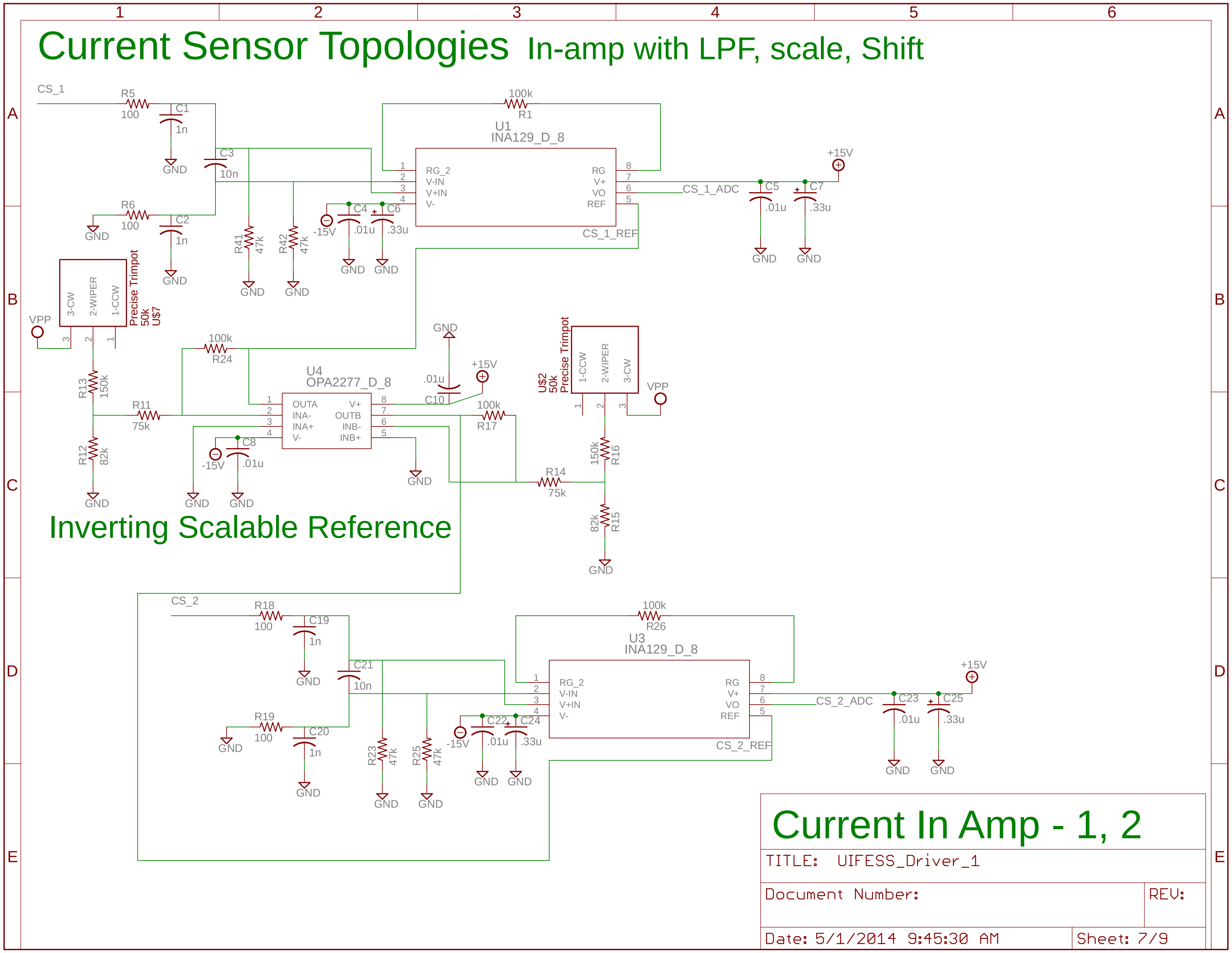
Current Sensor Topologies In-amp with LPF, scale, Shift
Inverting Scalable Reference
1
2
3
4
5
6
A
B
C
D
E
CS_1
R5
100
C1
1n
C3
10n
R6
100
C2
1n
GND
R1
100k
U1
INA129_D_8
RG_2
V-IN
V+IN
V-
RG
V+
VO
REF
CS_1_ADC
CS_1_REF
C5
.01u
C7
.33u
+15V
-15V
C4
.01u
C6
.33u
R41
47k
R42
47k
Precise Trimpot
50k
U$7
3-CW
2-WIPER
1-CCW
VPP
R13
150k
R12
82k
R11
75k
R24
100k
U4
OPA2277_D_8
OUTA
INA-
INA+
V-
V+
OUTB
INB-
INB+
C8
.01u
C10
.01u
R17
100k
R14
75k
U$2
Precise Trimpot
R16
150k
R15
82k
CS_2
R18
100
C19
1n
C21
10n
R19
100
C20
1n
R26
100k
U3
INA129_D_8
CS_2_ADC
CS_2_REF
C23
.01u
C25
.33u
C22
.01u
C24
.33u
R23
47k
R25
47k
Current In Amp - 1, 2
TITLE: UIFESS_Driver_1
Document Number:
REV:
Date: 5/1/2014 9:45:30 AM
Sheet: 7/9

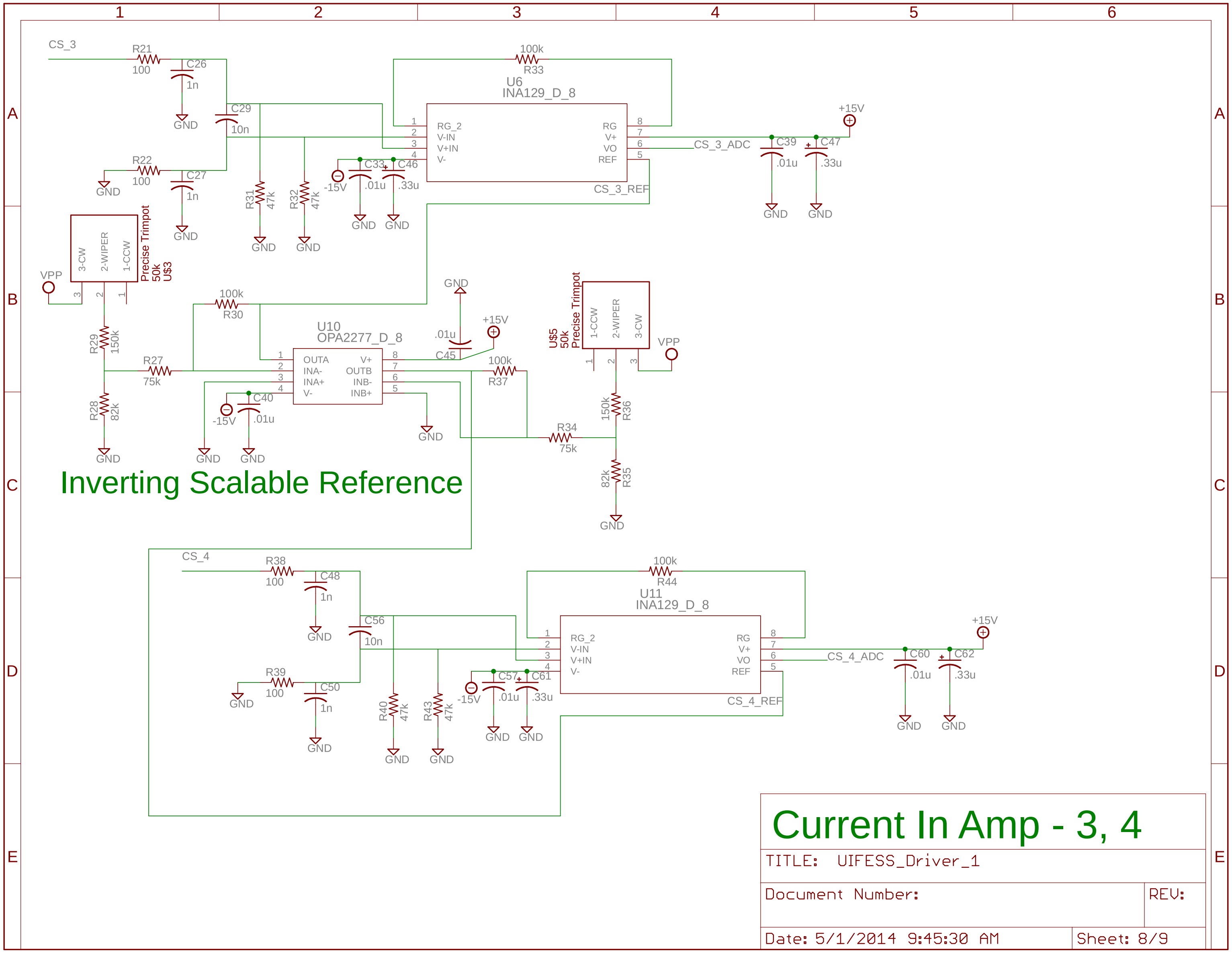

Current In Amp - 3, 4

TITLE: UIFESS_Driver_1

Document Number:

REV:

Date: 5/1/2014 9:45:30 AM

Sheet: 8/9

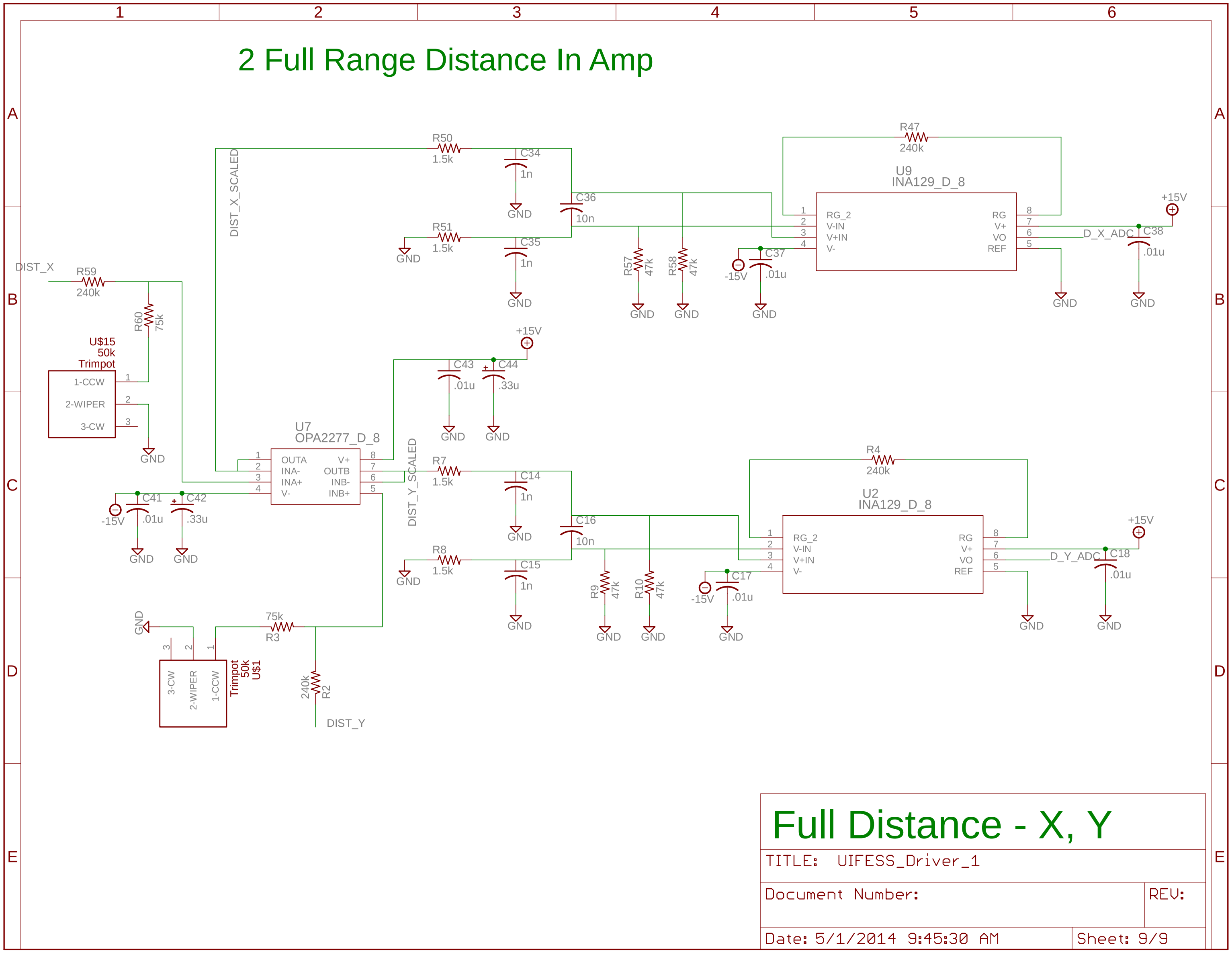
2 Full Range Distance In Amp
U9
INA129_D_8
U2
INA129_D_8
U7
OPA2277_D_8
RG_2
V-IN
V+IN
V-
RG
V+
VO
REF
OUTA
INA-
INA+
OUTB
INB-
INB+
R47 240k
R4 240k
R50 1.5k
R51 1.5k
R7 1.5k
R8 1.5k
R57 47k
R58 47k
R9 47k
R10 47k
R59 240k
R60 75k
R3 75k
R2 240k
C34 1n
C35 1n
C14 1n
C15 1n
C36 10n
C16 10n
C37 .01u
C38 .01u
C17 .01u
C18 .01u
C41 .01u
C42 .33u
C43 .01u
C44 .33u
U$15 50k Trimpot
U$1 50k Trimpot
1-CCW
2-WIPER
3-CW
+15V
-15V
GND
DIST_X
DIST_Y
DIST_X_SCALED
DIST_Y_SCALED
D_X_ADC
D_Y_ADC
Full Distance - X, Y
TITLE: UIFESS_Driver_1
Document Number:
REV:
Date: 5/1/2014 9:45:30 AM
Sheet: 9/9

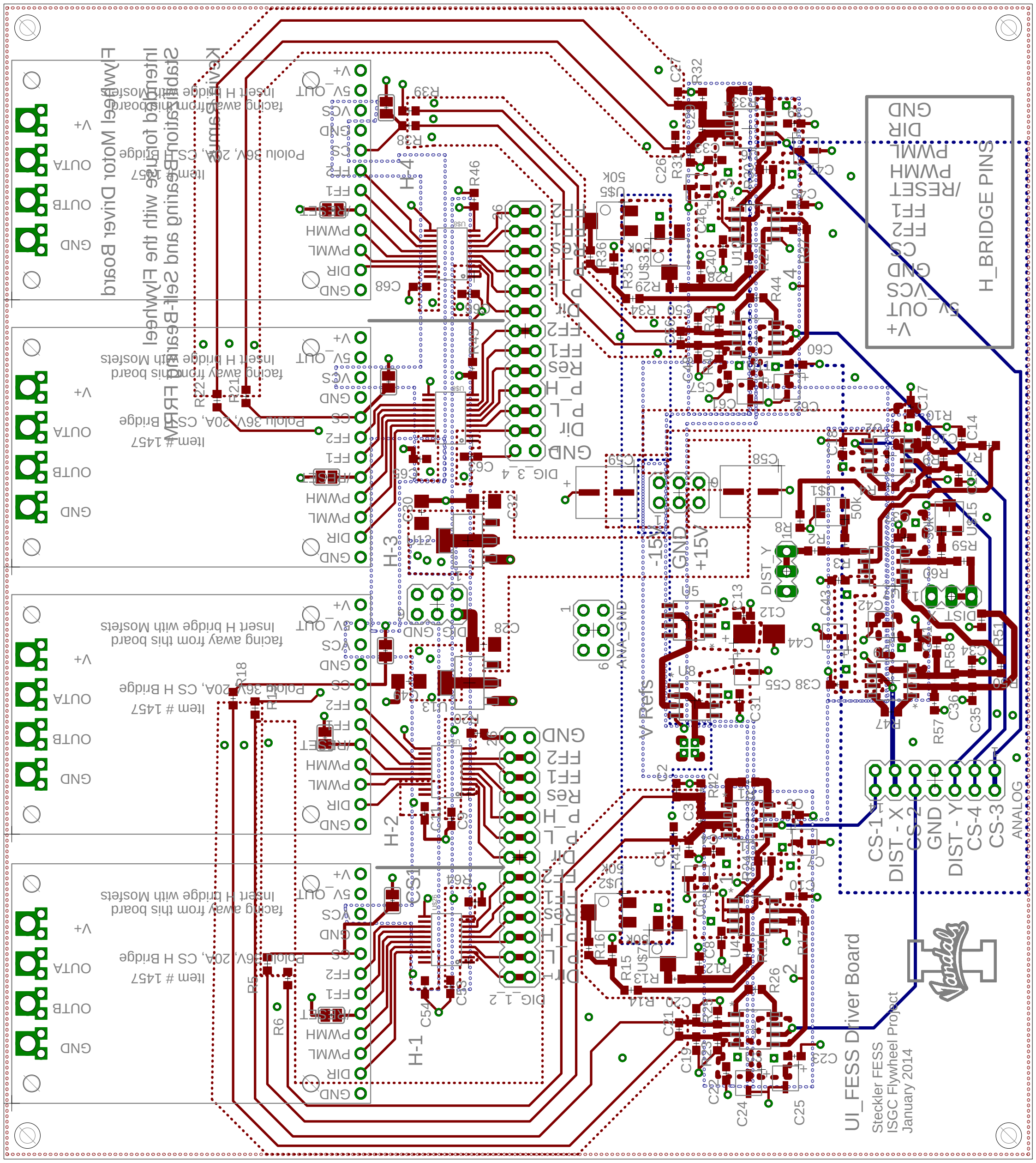
UI_FESS Driver Board
Steckler FESS
ISGC Flywheel Project
January 2014
Flywheel Motor Driver Board
Internal Bearing with the Flywheel
Stabilization for the Flywheel
H_BRIDGE PINS
GND
DIR
PWML
PWMH
/RESET
FF1
FF2
CS
GND
VCS
5V_OUT
V+
H-1
H-2
H-3
H-4
DIG_1_2
DIG_3_4
ANA_GND
V-Refs
-15V
GND
+15V
CS-1
DIST - X
CS-2
GND
DIST - Y
CS-4
CS-3
ANALOG
DIST_Y
DIST
Pololu 36V, 20A, CS H Bridge
Item # 1457
Insert H bridge with Mosfets facing away from this board
V+
OUTA
OUTB
GND

Appendix D

UIFESS Driver 2 PCB Schematic and Board Layout

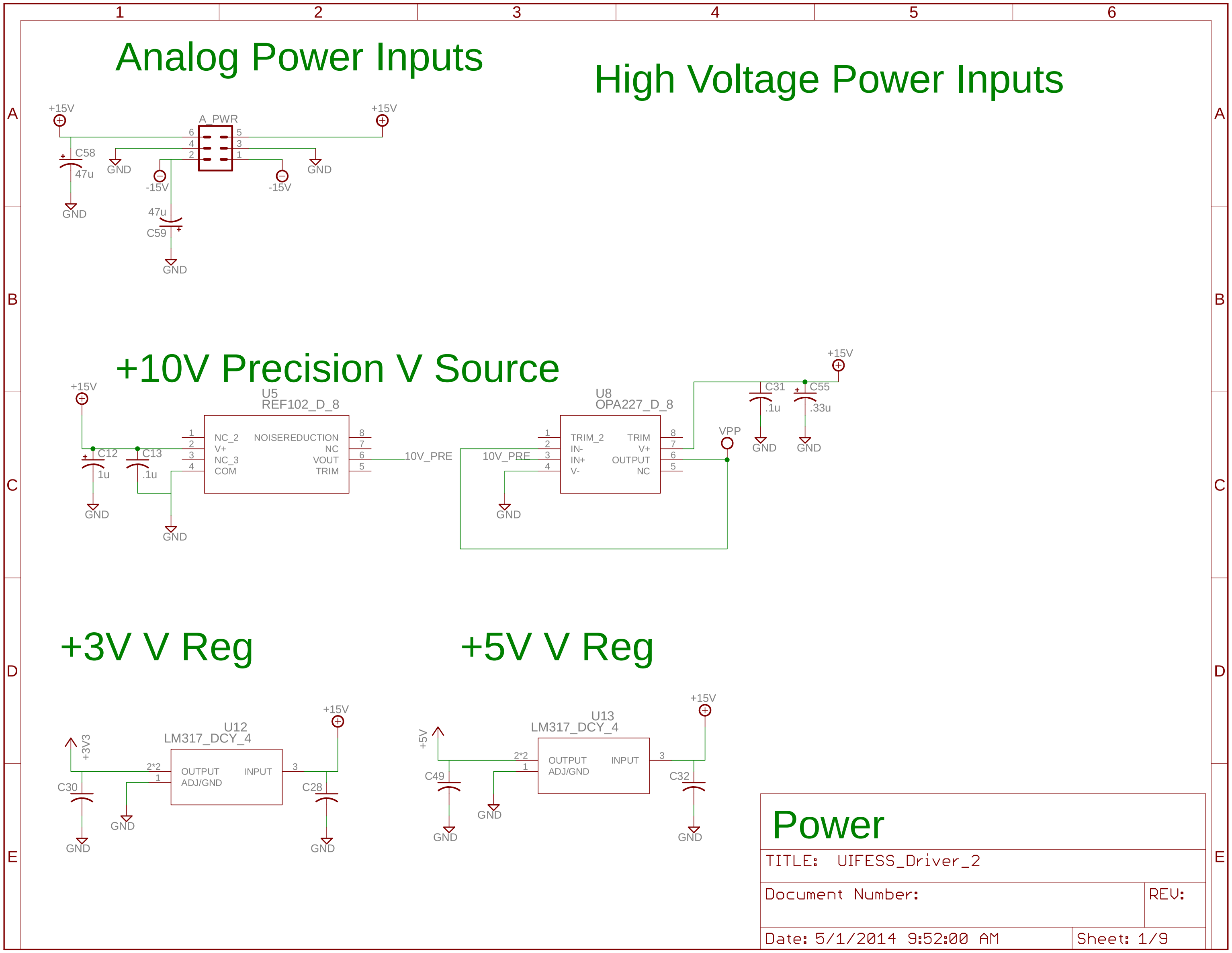
Analog Power Inputs
High Voltage Power Inputs
+10V Precision V Source
+3V V Reg
+5V V Reg
A_PWR
+15V
-15V
GND
C58
47u
C59
47u
U5
REF102_D_8
NC_2
V+
NC_3
COM
NOISEREDUCTION
NC
VOUT
TRIM
C12
1u
C13
.1u
10V_PRE
U8
OPA227_D_8
TRIM_2
IN-
IN+
V-
TRIM
V+
OUTPUT
NC
VPP
C31
.1u
C55
.33u
U12
LM317_DCY_4
OUTPUT
ADJ/GND
INPUT
+3V3
C30
C28
U13
LM317_DCY_4
+5V
C49
C32
2*2
1
2
3
4
5
6
7
8
A
B
C
D
E
Power
TITLE: UIFESS_Driver_2
Document Number:
REV:
Date: 5/1/2014 9:52:00 AM
Sheet: 1/9

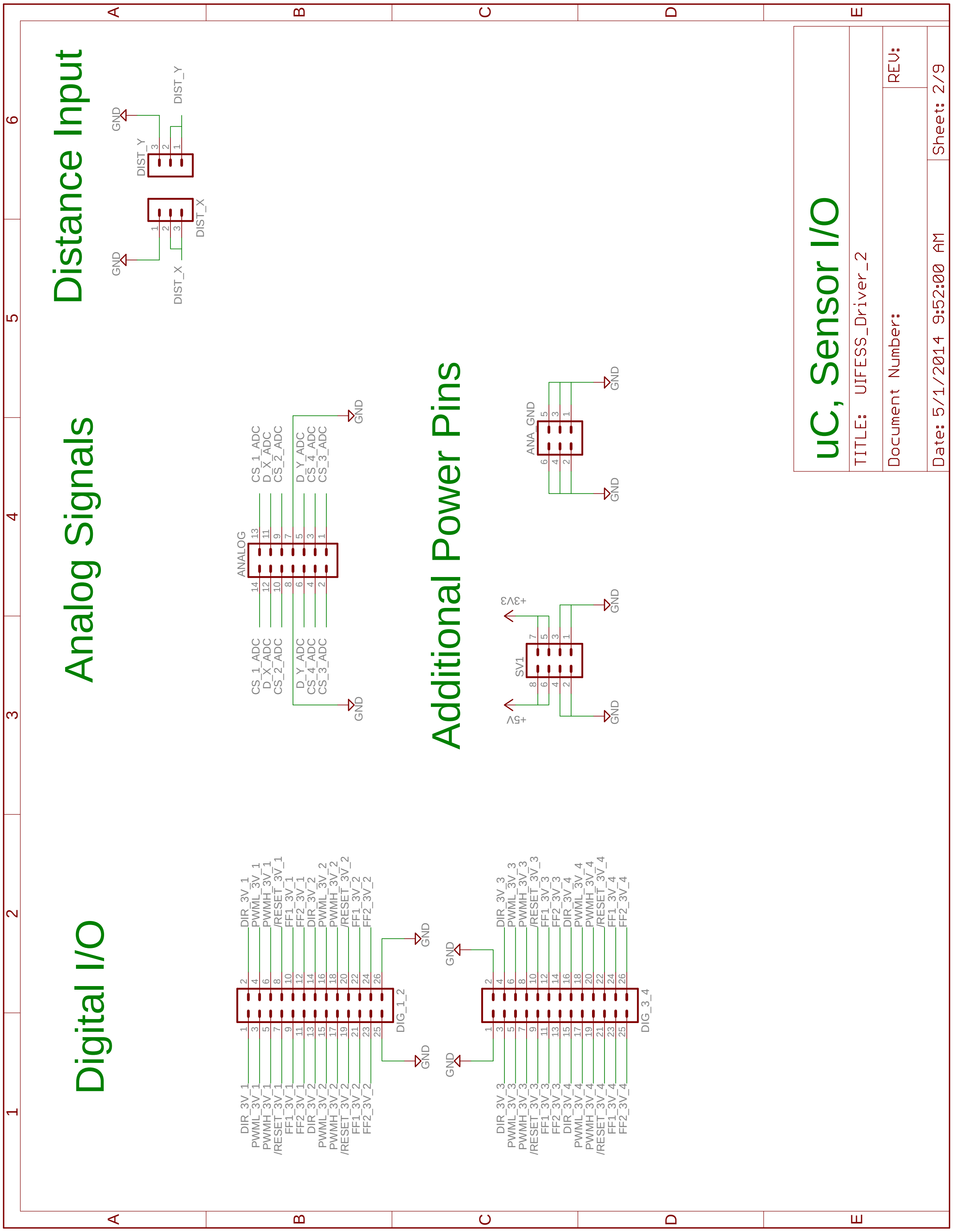
Distance Input
DIST_X
DIST_Y
GND
Analog Signals
ANALOG
CS_1_ADC
D_X_ADC
CS_2_ADC
D_Y_ADC
CS_4_ADC
CS_3_ADC
Additional Power Pins
SV1
+5V
+3V3
ANA_GND
Digital I/O
DIG_1_2
DIG_3_4
DIR_3V_1
PWML_3V_1
PWMH_3V_1
/RESET_3V_1
FF1_3V_1
FF2_3V_1
DIR_3V_2
PWML_3V_2
PWMH_3V_2
/RESET_3V_2
FF1_3V_2
FF2_3V_2
DIR_3V_3
PWML_3V_3
PWMH_3V_3
/RESET_3V_3
FF1_3V_3
FF2_3V_3
DIR_3V_4
PWML_3V_4
PWMH_3V_4
/RESET_3V_4
FF1_3V_4
FF2_3V_4
uC, Sensor I/O
TITLE: UIFESS_Driver_2
Document Number:
REV:
Date: 5/1/2014 9:52:00 AM
Sheet: 2/9

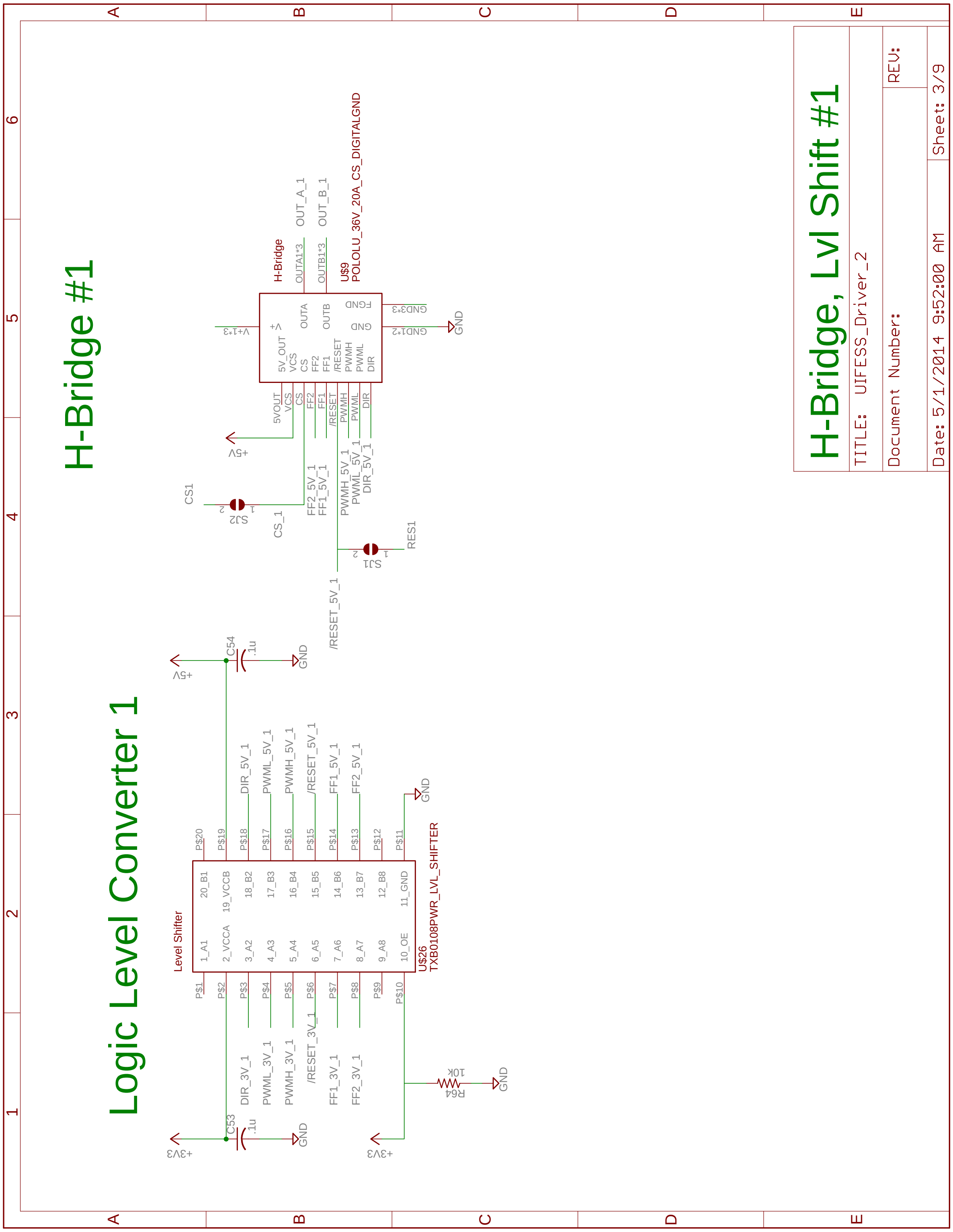
H-Bridge #1
Logic Level Converter 1
H-Bridge
U$9
POLOLU_36V_20A_CS_DIGITALGND
5V_OUT
VCS
CS
FF2
FF1
/RESET
PWMH
PWML
DIR
V+
OUTA
OUTB
FGND
GND
V+1*3
OUTA1*3
OUTB1*3
GND1*2
GND3*3
OUT_A_1
OUT_B_1
5VOUT
+5V
GND
FF2_5V_1
FF1_5V_1
PWMH_5V_1
PWML_5V_1
DIR_5V_1
CS_1
CS1
SJ2
RES1
SJ1
/RESET_5V_1
C54
.1u
Level Shifter
U$26
TXB0108PWR_LVL_SHIFTER
1_A1
2_VCCA
3_A2
4_A3
5_A4
6_A5
7_A6
8_A7
9_A8
10_OE
20_B1
19_VCCB
18_B2
17_B3
16_B4
15_B5
14_B6
13_B7
12_B8
11_GND
P$1
P$2
P$3
P$4
P$5
P$6
P$7
P$8
P$9
P$10
P$20
P$19
P$18
P$17
P$16
P$15
P$14
P$13
P$12
P$11
DIR_3V_1
PWML_3V_1
PWMH_3V_1
/RESET_3V_1
FF1_3V_1
FF2_3V_1
C53
+3V3
R64
10K
H-Bridge, Lvl Shift #1
TITLE: UIFESS_Driver_2
Document Number:
REV:
Date: 5/1/2014 9:52:00 AM
Sheet: 3/9
A
B
C
D
E
1
2
3
4
5
6

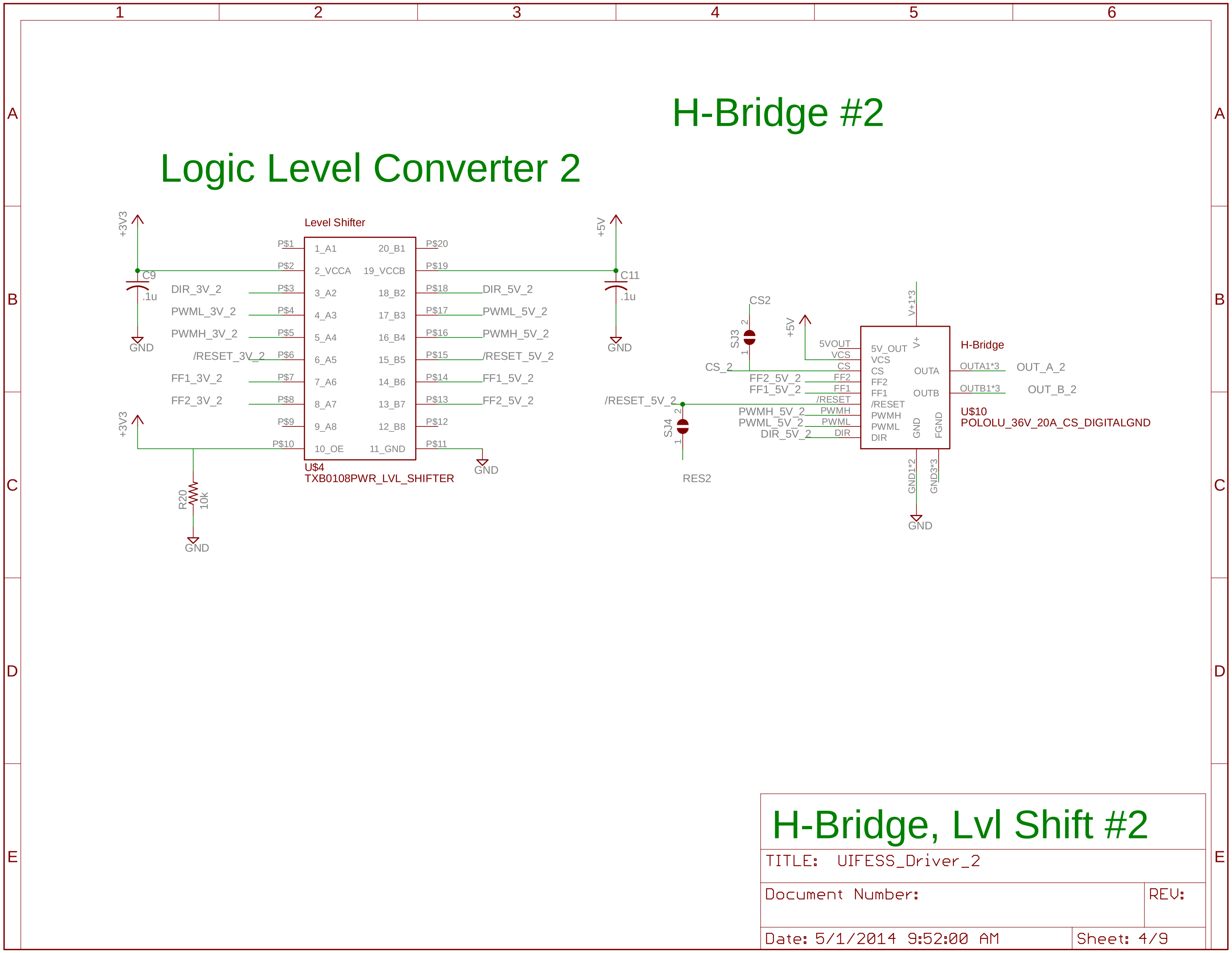

H-Bridge, Lvl Shift #2

TITLE: UIFESS_Driver_2

Document Number:

REV:

Date: 5/1/2014 9:52:00 AM

Sheet: 4/9

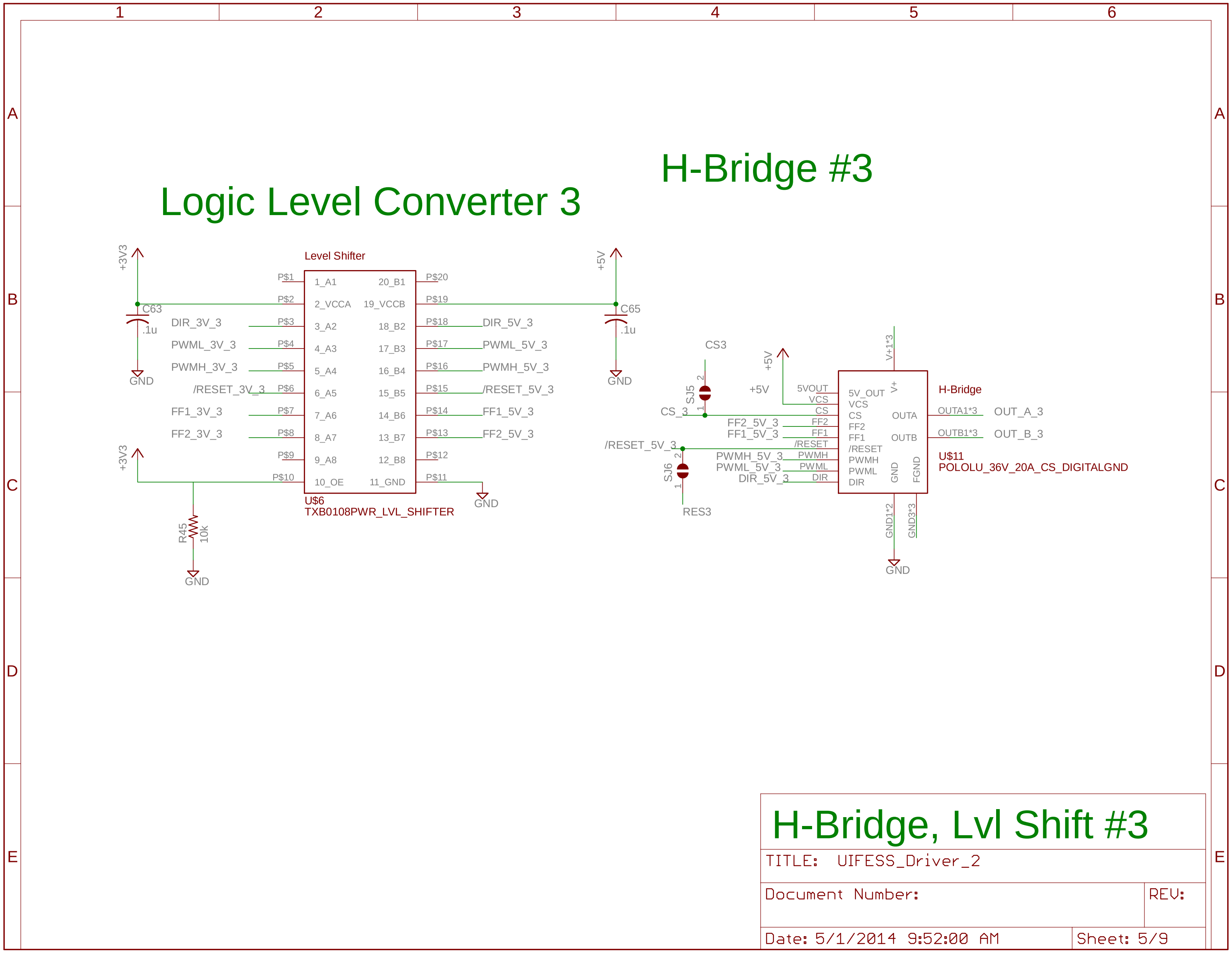

Logic Level Converter 3
H-Bridge #3
Level Shifter
U$6
TXB0108PWR_LVL_SHIFTER
1_A1
2_VCCA
3_A2
4_A3
5_A4
6_A5
7_A6
8_A7
9_A8
10_OE
20_B1
19_VCCB
18_B2
17_B3
16_B4
15_B5
14_B6
13_B7
12_B8
11_GND
P$1
P$2
P$3
P$4
P$5
P$6
P$7
P$8
P$9
P$10
P$20
P$19
P$18
P$17
P$16
P$15
P$14
P$13
P$12
P$11
+3V3
C63
.1u
GND
DIR_3V_3
PWML_3V_3
PWMH_3V_3
/RESET_3V_3
FF1_3V_3
FF2_3V_3
+3V3
R45
10k
GND
DIR_5V_3
PWML_5V_3
PWMH_5V_3
/RESET_5V_3
FF1_5V_3
FF2_5V_3
GND
+5V
C65
.1u
GND
CS3
SJ5
+5V
+5V
CS_3
FF2_5V_3
FF1_5V_3
/RESET_5V_3
SJ6
PWMH_5V_3
PWML_5V_3
DIR_5V_3
RES3
5VOUT
VCS
CS
FF2
FF1
/RESET
PWMH
PWML
DIR
5V_OUT
VCS
CS
FF2
FF1
/RESET
PWMH
PWML
DIR
V+
V+1*3
OUTA
OUTB
GND
FGND
GND1*2
GND3*3
GND
H-Bridge
OUTA1*3
OUTB1*3
OUT_A_3
OUT_B_3
U$11
POLOLU_36V_20A_CS_DIGITALGND
H-Bridge, Lvl Shift #3
TITLE: UIFESS_Driver_2
Document Number:
REV:
Date: 5/1/2014 9:52:00 AM
Sheet: 5/9
1
2
3
4
5
6
A
B
C
D
E

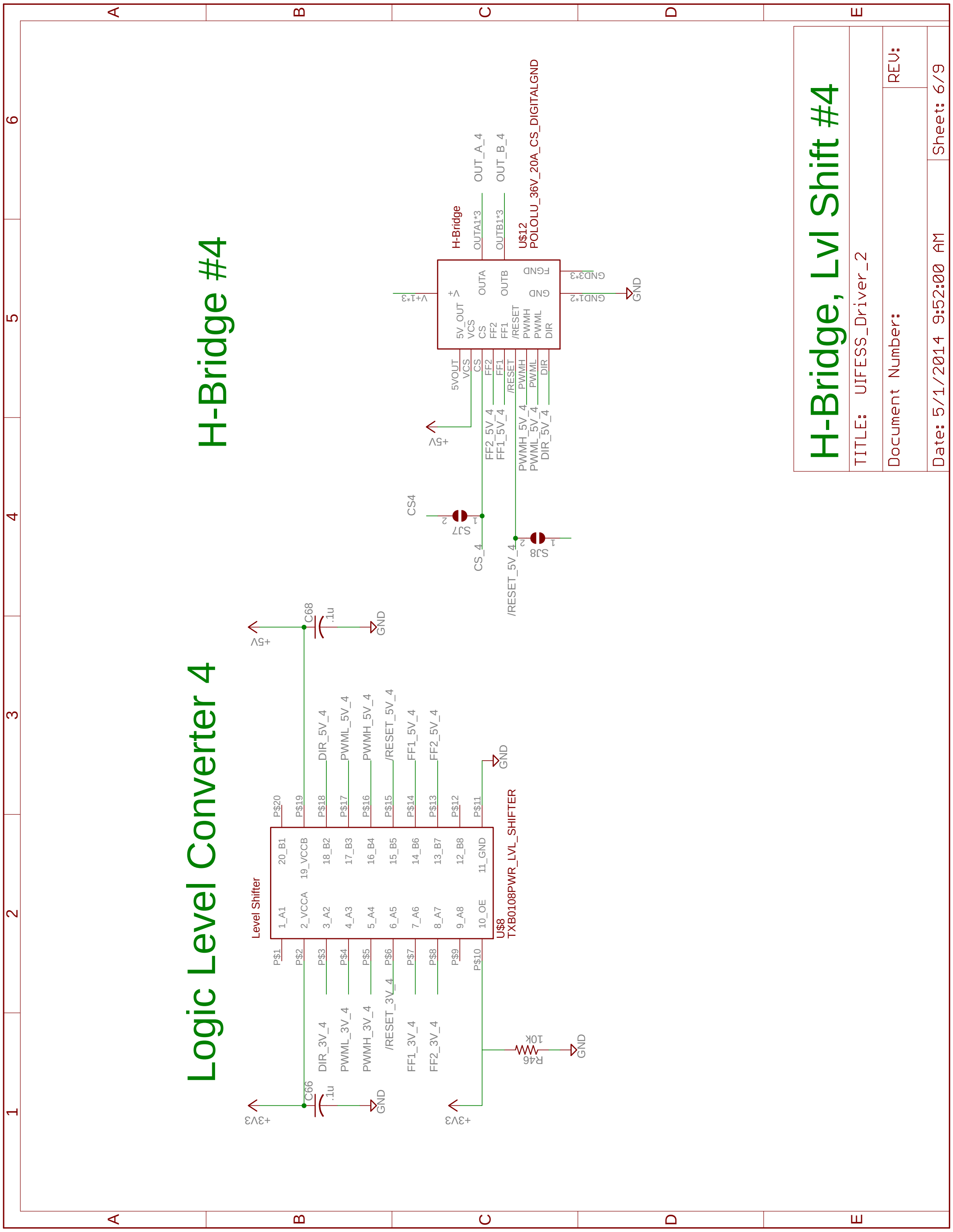
H-Bridge #4
Logic Level Converter 4
H-Bridge
U$12
POLOLU_36V_20A_CS_DIGITALGND
OUTA1*3
OUTB1*3
OUT_A_4
OUT_B_4
V+1*3
V+
5V_OUT
VCS
CS
FF2
FF1
/RESET
PWMH
PWML
DIR
OUTA
OUTB
FGND
GND
GND3*3
GND1*2
GND
5VOUT
+5V
FF2_5V_4
FF1_5V_4
PWMH_5V_4
PWML_5V_4
DIR_5V_4
CS4
SJ7
CS_4
SJ8
/RESET_5V_4
C68
.1u
Level Shifter
U$8
TXB0108PWR_LVL_SHIFTER
1_A1
2_VCCA
3_A2
4_A3
5_A4
6_A5
7_A6
8_A7
9_A8
10_OE
20_B1
19_VCCB
18_B2
17_B3
16_B4
15_B5
14_B6
13_B7
12_B8
11_GND
P$1
P$2
P$3
P$4
P$5
P$6
P$7
P$8
P$9
P$10
P$20
P$19
P$18
P$17
P$16
P$15
P$14
P$13
P$12
P$11
DIR_5V_4
PWML_5V_4
PWMH_5V_4
/RESET_5V_4
FF1_5V_4
FF2_5V_4
DIR_3V_4
PWML_3V_4
PWMH_3V_4
/RESET_3V_4
FF1_3V_4
FF2_3V_4
C66
.1u
+3V3
R46
10K
H-Bridge, Lvl Shift #4
TITLE: UIFESS_Driver_2
Document Number:
REV:
Date: 5/1/2014 9:52:00 AM
Sheet: 6/9
A
B
C
D
E
1
2
3
4
5
6

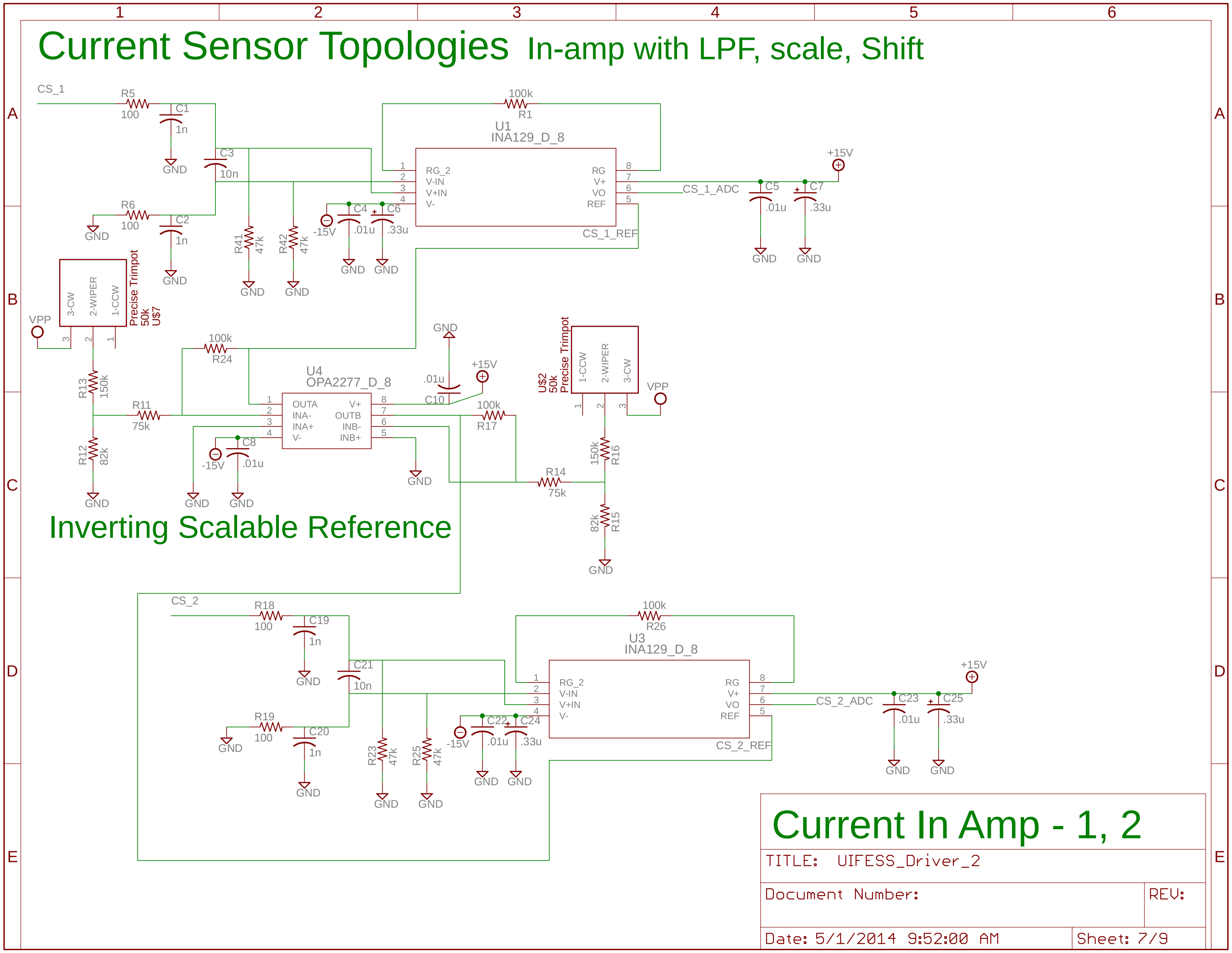
Current Sensor Topologies In-amp with LPF, scale, Shift
Inverting Scalable Reference
1
2
3
4
5
6
A
B
C
D
E
CS_1
R5
100
C1
1n
C3
10n
R6
100
C2
1n
GND
100k
R1
U1
INA129_D_8
RG_2
V-IN
V+IN
V-
RG
V+
VO
REF
CS_1_ADC
CS_1_REF
C4
.01u
C6
.33u
-15V
C5
.01u
C7
.33u
+15V
R41
47k
R42
47k
Precise Trimpot
50k
U$7
3-CW
2-WIPER
1-CCW
VPP
R13
150k
R12
82k
R11
75k
100k
R24
U4
OPA2277_D_8
OUTA
INA-
INA+
V-
V+
OUTB
INB-
INB+
C8
.01u
C10
.01u
100k
R17
R14
75k
Precise Trimpot
50k
U$2
150k
R16
82k
R15
CS_2
R18
100
C19
1n
C21
10n
R19
100
C20
1n
R23
47k
R25
47k
100k
R26
U3
INA129_D_8
C22
.01u
C24
.33u
CS_2_ADC
CS_2_REF
C23
.01u
C25
.33u
Current In Amp - 1, 2
TITLE: UIFESS_Driver_2
Document Number:
REV:
Date: 5/1/2014 9:52:00 AM
Sheet: 7/9

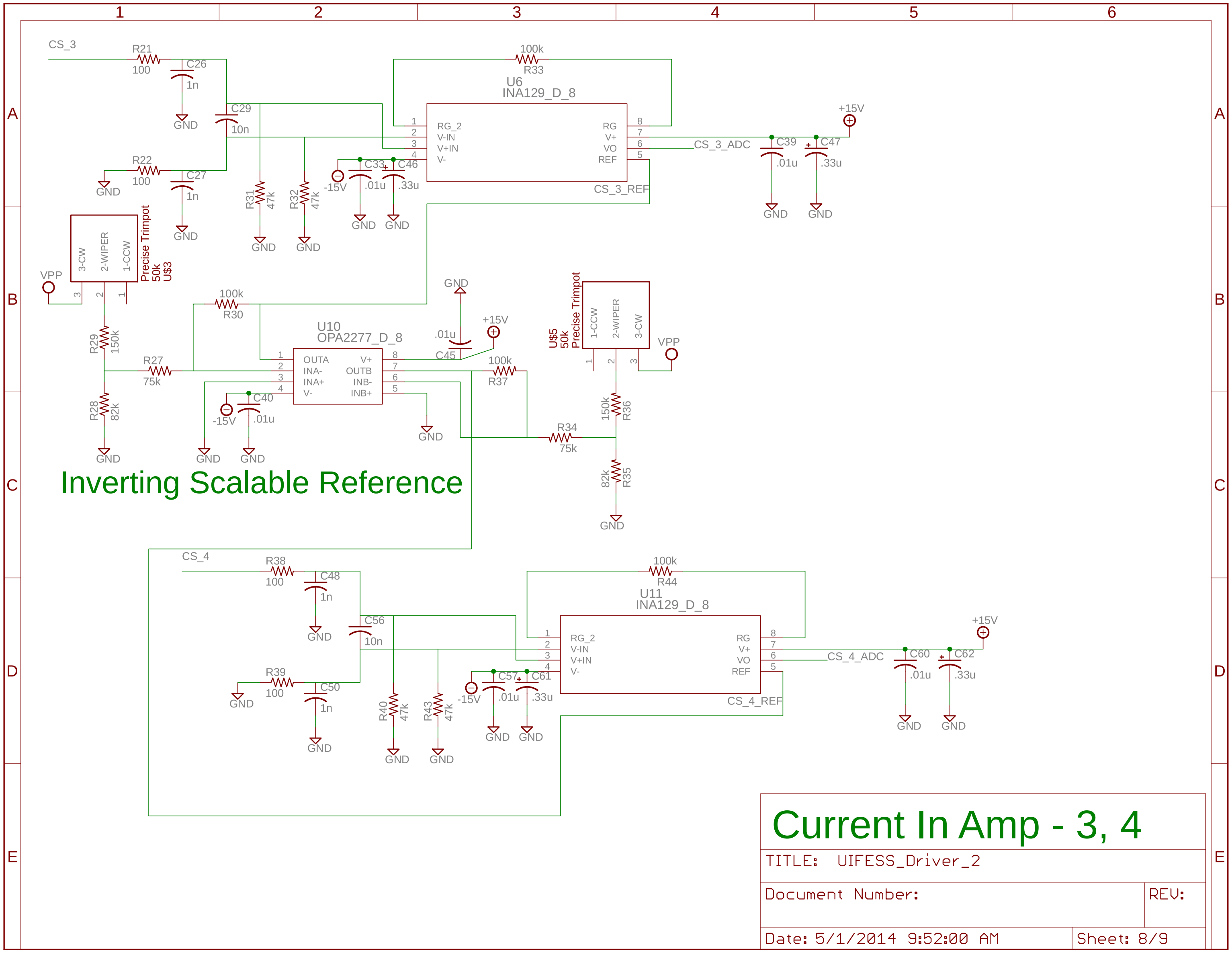
Current In Amp - 3, 4
TITLE: UIFESS_Driver_2
Document Number:
REV:
Date: 5/1/2014 9:52:00 AM
Sheet: 8/9
Inverting Scalable Reference
1
2
3
4
5
6
A
B
C
D
E
CS_3
R21
100
C26
1n
C29
10n
R22
100
C27
1n
GND
U6
INA129_D_8
R33
100k
RG_2
V-IN
V+IN
V-
RG
V+
VO
REF
CS_3_ADC
CS_3_REF
C39
.01u
C47
.33u
+15V
-15V
C33
.01u
C46
.33u
R31
47k
R32
47k
Precise Trimpot
50k
U$3
3-CW
2-WIPER
1-CCW
VPP
R29
150k
R27
75k
R28
82k
R30
100k
U10
OPA2277_D_8
OUTA
INA-
INA+
OUTB
INB-
INB+
C40
.01u
C45
.01u
R37
100k
U$5
R36
150k
R34
75k
R35
82k
CS_4
R38
100
C48
1n
R39
100
C50
1n
C56
10n
R40
47k
R43
47k
U11
INA129_D_8
R44
100k
C57
.01u
C61
.33u
CS_4_ADC
CS_4_REF
C60
.01u
C62
.33u

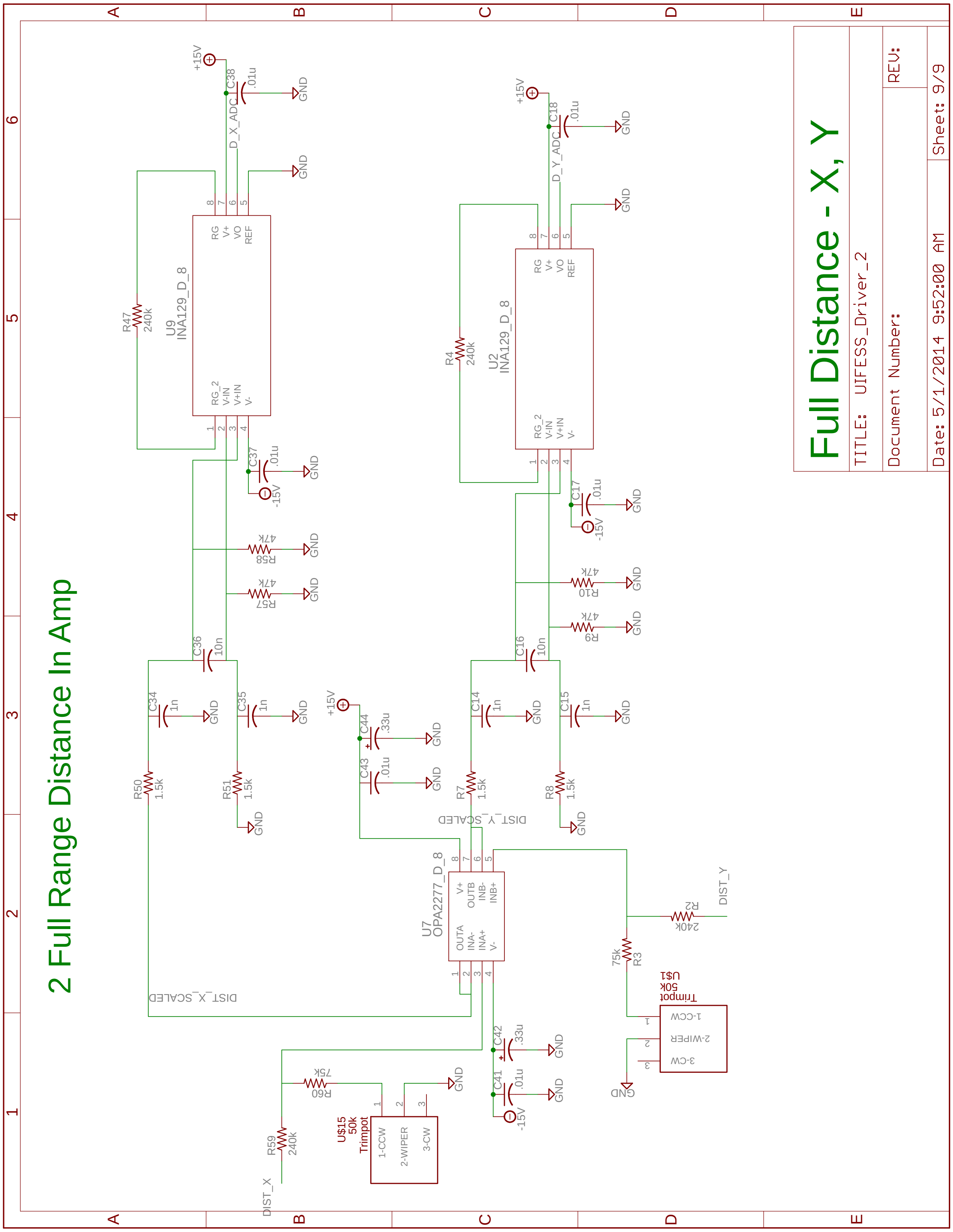
2 Full Range Distance In Amp
Full Distance - X, Y
TITLE: UIFESS_Driver_2
Document Number:
REV:
Date: 5/1/2014 9:52:00 AM
Sheet: 9/9
U9
INA129_D_8
U2
INA129_D_8
RG_2
V-IN
V+IN
V-
RG
V+
VO
REF
R47
240k
R4
240k
C38
.01u
C18
.01u
C37
.01u
C17
.01u
D_X_ADC
D_Y_ADC
+15V
-15V
GND
R58
47K
R57
47K
R10
47K
R9
47K
C36
10n
C16
10n
C34
1n
C35
1n
C14
1n
C15
1n
C44
.33u
C43
.01u
C42
.33u
C41
.01u
R50
1.5k
R51
1.5k
R7
1.5k
R8
1.5k
DIST_Y_SCALED
DIST_X_SCALED
U7
OPA2277_D_8
OUTA
INA-
INA+
OUTB
INB-
INB+
R2
240K
DIST_Y
R3
75k
Trimpot
50K
U$1
1-CCW
2-WIPER
3-CW
R60
75K
R59
240k
DIST_X
U$15
50k
Trimpot
A
B
C
D
E
1
2
3
4
5
6

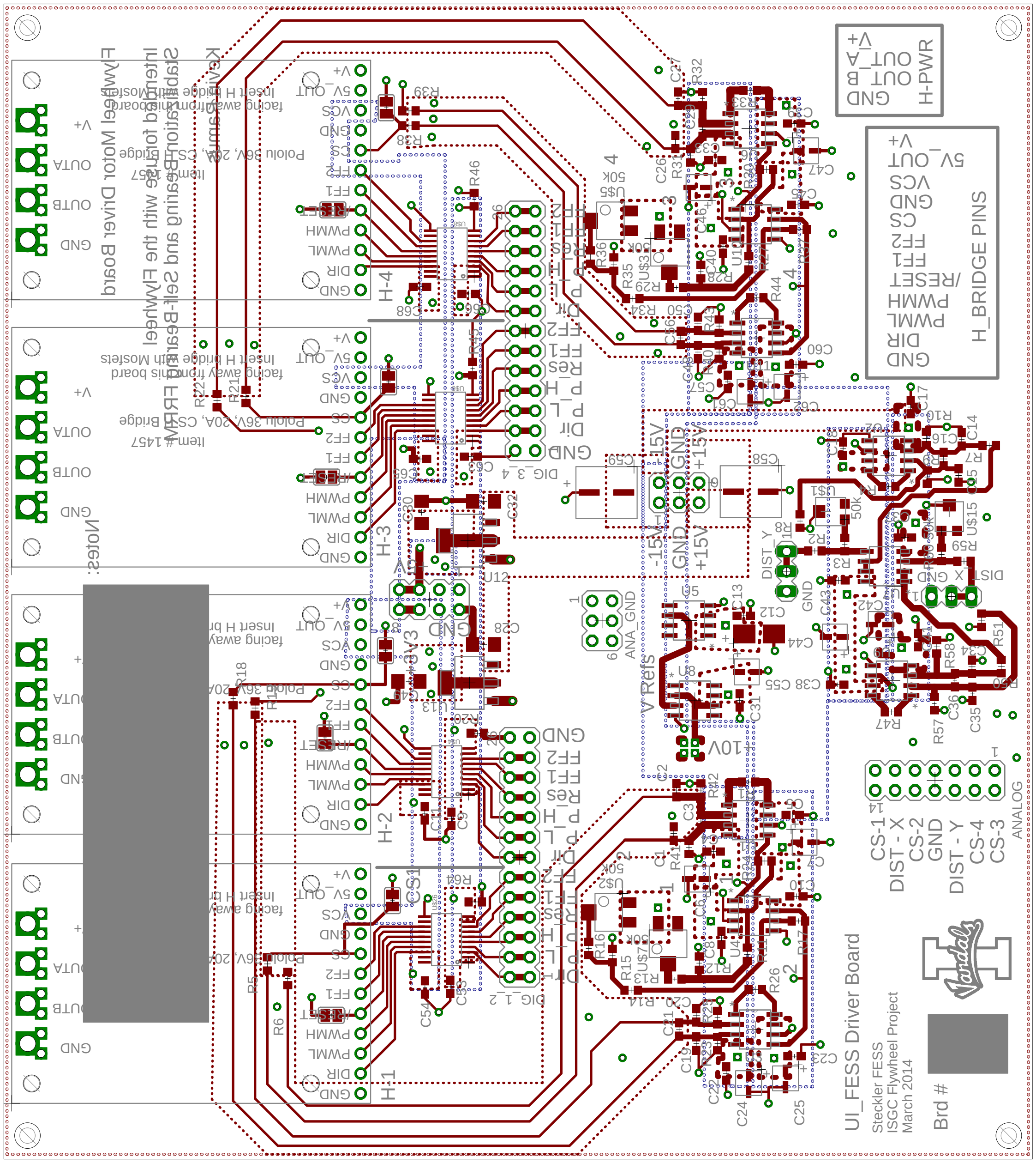
UI_FESS Driver Board
Steckler FESS
ISGC Flywheel Project
March 2014
Brd #
H_BRIDGE PINS
V+
5V_OUT
VCS
GND
CS
FF2
FF1
/RESET
PWMH
PWML
DIR
GND
H-PWR
V+
OUT_A
OUT_B
GND
CS-1
DIST - X
CS-2
GND
DIST - Y
CS-4
CS-3
ANALOG
H-1
H-2
H-3
H-4
-15V
GND
+15V
ANA_GND
DIST_Y
DIST_X
Notes:

Appendix E

UIFESS Driver PCB Bill of Materials

Part Name	**Part Number**	**Supp.**
CAP CER 1000PF 50V 1% NP0 0603	490-6377-1-ND	Digikey
CAP CER 10000PF 50V 5% X7R 0603	399-1092-1-ND	Digikey
CAP ALUM 0.33UF 50V 20% SMD	PCE3939CT-ND	Digikey
CAP TANT 1UF 50V 10% 2413	399-10241-1-ND	Digikey
CAP CER 0.1UF 50V 10% X7R 0603	1276-1000-1-ND	Digikey
CAP ALUM 47UF 50V 20% SMD	399-6690-1-ND	Digikey
CAP TANT 10UF 25V 10% 1206	478-8494-1-ND	Digikey
RES 82K OHM 1/10W 1% 0603	RMCF0603FT82K0CT-ND	Digikey
RES 75K OHM 1/10W 5% 0603	RMCF0603JT75K0CT-ND	Digikey
RES 100 OHM 1/10W .1% 0603 SMD	P100DBCT-ND	Digikey
RES 150K OHM 1/10W 5% 0603	RMCF0603JT150KCT-ND	Digikey
RES 100K OHM 1/16W .5% 0603 SMD	RR08P100KDCT-ND	Digikey
RES 47K OHM 1/10W 1% 0603	RMCF0603FT47K0CT-ND	Digikey
RES 91K OHM 1/10W 5% 0603	RMCF0603JT91K0CT-ND	Digikey
RES 1.5K OHM 1/10W .1% 0603 SMD	P1.5KDBCT-ND	Digikey
RES 240K OHM 1/10W 1% 0603	RMCF0603FT240KCT-ND	Digikey
RES 10K OHM 1/10W 5% 0603	RMCF0603JT10K0CT-ND	Digikey
TRIMMER 50K OHM 0.1W SMD	TC33X-503ECT-ND	Digikey
TRIMMER 50K OHM 0.25W SMD	3214X-1-503ECT-ND	Digikey
IC 8-BIT TRNSTR 15KV ESD	296-21527-1-ND	Digikey
INA129 In-amp	INA129UA-ND	Digikey
IC OPAMP GP 1MHZ 8SOIC	296-23667-1-ND	Digikey
IC VREF SERIES PREC 10V 8-SOIC	REF102AU-ND	Digikey
IC OPAMP GP 8MHZ 8SOIC	OPA227UA-ND	Digikey
IC REG LDO 5V 0.8A SOT223	LM1117MPX-5.0/NOPBCT-ND	Digikey
IC REG LDO 3.3V 0.8A SOT223	LM1117MPX-3.3/NOPBCT-ND	Digikey
HEX STANDOFF 4-40 NYLON 1/2”	4802K-ND	Digikey
HEX STANDOFF 4-40	4813K-ND	Digikey
HEX NUT 3/16” NYLON 2-56	H612-ND	Digikey
MACHINE SCREW PAN 2-56	H534-ND	Digikey
CONN HEADER FEM 12POS.1” SGL	S6100-ND	Digikey
ROUND SPACER M3 NYLON 9MM	952-2016-ND	Digikey
BERGSTIK II .100” SR STRAIGHT	609-3465-ND	Digikey
36V_20A H_Bridge	#1457	Pololu